REPORT ONR-CR215-237-2

12

MODERN METHODS OF AIRCRAFT STABILITY AND CONTROL ANALYSIS

Robert F. Stengel
John R. Broussard
Paul W. Berry
James H. Taylor

THE ANALYTIC SCIENCES CORPORATION
Six Jacob Way
Reading, Massachusetts 01867

Contract N00014-75-C-0432
ONR Task 215-237

27 MAY 1977

ANNUAL TECHNICAL REPORT FOR PERIOD 1 FEBRUARY 76 - 31 JANUARY 77

PREPARED FOR THE

OFFICE OF NAVAL RESEARCH ● 800 N. QUINCY ST. ● ARLINGTON ● VA ● 22217

Organizations receiving reports on the initial distribution list should confirm correct address. This list is located at the end of the report. Any change of address of distribution should be conveyed to the Office of Naval Research, Code 211, Washington, D.C. 22217.

When this report is no longer needed, it may be transmitted to other authorized organizations. Do not return it to the originator or the monitoring office.

The findings in this report are not to be construed as an official Department of Defense or Military Department position unless so designated by other official documents.

UNCLASSIFIED

SECURITY CLASSIFICATION OF THIS PAGE (When Data Entered)

REPORT DOCUMENTATION PAGE	READ INSTRUCTIONS BEFORE COMPLETING FORM
1. REPORT NUMBER: ONR - CR215-237-2	2. GOVT ACCESSION NO. / 3. RECIPIENT'S CATALOG NUMBER
4. TITLE (and Subtitle): Modern Methods of Aircraft Stability and Control Analysis.	5. TYPE OF REPORT & PERIOD COVERED: Annual - Technical, 1 Feb 1976-31 Jan 1977.
	6. PERFORMING ORG. REPORT NUMBER: TR-612-2
7. AUTHOR(s): Robert F. Stengel, John R. Broussard, Paul W. Berry and James H. Taylor	8. CONTRACT OR GRANT NUMBER(s): N00014-75-C-0432
9. PERFORMING ORGANIZATION NAME AND ADDRESS: The Analytic Sciences Corporation, 6 Jacob Way, Reading, Massachusetts 01867	10. PROGRAM ELEMENT, PROJECT, TASK AREA & WORK UNIT NUMBERS: 61153N-14, RR014-11-84, 1-12, RMS 1411-840
11. CONTROLLING OFFICE NAME AND ADDRESS: Office of Naval Research, Technology Projects Division, Code 211, Arlington, Virginia 22217	12. REPORT DATE: 27 May 1977
	13. NUMBER OF PAGES: 256
14. MONITORING AGENCY NAME & ADDRESS (If different from Controlling Office)	15. SECURITY CLASS. (of this report): Unclassified
	15a. DECLASSIFICATION/DOWNGRADING SCHEDULE

16. DISTRIBUTION STATEMENT (of this Report)

Approved for public release; Distribution unlimited.

17. DISTRIBUTION STATEMENT (of the abstract entered in Block 20, if different from Report)

18. SUPPLEMENTARY NOTES

19. KEY WORDS (Continue on reverse side if necessary and identify by block number)

Aircraft Stability and Control, Atmospheric Flight Mechanics, Modern Control Theory, Human Operator Dynamics, Nonlinear System Analysis, MULCAT

20. ABSTRACT (Continue on reverse side if necessary and identify by block number)

This report presents new methodologies and results in the study of aircraft stability and control, including detailed consideration of piloting effects on the aircraft's motion. The potential for "departure" (i.e., loss of control) in transonic and supersonic flight is addressed using

(cont.)

DD FORM 1 JAN 73 1473 EDITION OF 1 NOV 65 IS OBSOLETE

UNCLASSIFIED

SECURITY CLASSIFICATION OF THIS PAGE (When Data Entered)

20. ABSTRACT (Continued)

linear, time-invariant dynamic models which incorporate longitudinal-lateral-directional coupling. Optimal and sub-optimal piloting techniques are examined; and a minimum-control-effort (MCE) adaptation model for pilot behavior is formulated. This model presents a rationale for high angle-of-attack piloting style, including conscious switching from one command mode to another. A method for designing departure-prevention command augmentation systems (DPCAS) is developed and is applied to a subsonic model of the F-14A aircraft. This design technique can provide excellent flying qualities for the aircraft throughout its flight envelope. A multivariable limit cycle analysis technique (MULCAT) is used to predict possible self-induced nonlinear oscillations, and the results of this prediction are evaluated using a direct simulation of the nonlinear dynamic model. The methods and results presented here can have substantial impact on the development, analysis, and testing of high-performance aircraft, enhancing safety, reliability, and effectiveness of flight operations.

PREFACE

This investigation was conducted by The Analytic Sciences Corporation, Reading, Massachusetts, from 1 February 1975 under Contract N00014-75-C-0432 for the Office of Naval Research, Washington, D.C. This report is the second annual technical report, and includes results through 31 January 1977. The sponsoring office was the Vehicle Technology Program, headed by Mr. David Siegel. CDR P.R. "Bob" Hite served as the Navy Technical Monitor for the program.

We would like to thank the Langley Research Center of the National Aeronautics and Space Administration, the Naval Air Development Center, and the Grumman Aerospace Company for providing data and discussions which were helpful in conducting this research.

The study was directed by Dr. Robert F. Stengel, who was assisted by Mr. John R. Broussard, Mr. Paul W. Berry, and Dr. James H. Taylor.

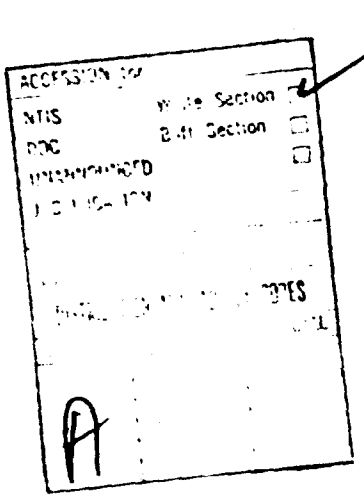

TABLE OF CONTENTS

TABLE OF CONTENTS (Continued)

LIST OF FIGURES

LIST OF FIGURES (Continued)

LIST OF FIGURES (Continued)

LIST OF FIGURES (Continued)

LIST OF TABLES

LIST OF TABLES (Continued)

1. INTRODUCTION

1.1 BACKGROUND

There is a continuing need to develop and apply new methods for analyzing the stability and designing the control systems of aircraft. This need is brought about by requirements for operating aircraft within expanded flight envelopes, by aircraft configurations with reduced inherent stability, and by the need to meet safety, reliability, and cost objectives.

Recent research has extended stability and control analysis techniques, and it has demonstrated the results of analysis using mathematical models of two contemporary high-performance aircraft. Fully coupled linear, time-invariant equations of motion are derived in Ref. 1. The characteristics of a small, supersonic fighter are investigated using eigenvalues, eigenvectors, transfer functions, and time histories of control response, and logic is developed for a departure-prevention stability augmentation system (DPSAS). In Ref. 2, a mathematical model of the F-14A is analyzed in similar manner, and several additional analysis methods are investigated. These include evaluation of piloting effects on aircraft stability, evaluation of the effects of deceleration on aircraft stability, and presentation of a new numerical technique for analyzing limit cycles in nonlinear dynamic models.

The present work is a continuation of the types of analysis established in Ref. 2. Using the same mathematical model of the aircraft, new methods of predicting pilot-aircraft

stability boundaries are presented, and contours of equal tracking performance and control effort are defined. Linear-optimal control theory is employed to design logic for a departure-prevention command augmentation system (DPCAS), and the limit cycle analysis technique is investigated further. A new mathematical model of the aircraft, which contains Mach-dependent effects and simplified lateral-directional aerodynamics, is used to examine the effects of compressibility on high angle-of-attack dynamics. Thus, the results presented in this report expand on the earlier analyses, demonstrating the relationship between modern control theory and the practical evaluation of aircraft stability and control.

1.2 SUMMARY OF RESULTS

The results obtained in this investigation fall into four categories:

- Effects of Compressibility on Stability and Control
- Prediction of Pilot-Aircraft Stability Boundaries and Performance Contours
- Design of Command Augmentation Systems for Improved Flying Qualities
- Analysis of Limit Cycles in Aircraft Models with Multiple Nonlinearities

Numerical results are based upon comprehensive aerodynamic and inertial models of the F-14A aircraft. Extensive use is made of linear, time-invariant dynamic models which incorporate the major coupling effects that occur in asymmetric flight. For example, stability derivatives are evaluated at non-zero sideslip and high angle-of-attack trim conditions when appropriate. For analyses in the first three

categories cited above, the stability derivatives are based on the aerodynamic slopes at the generalized trim condition. For the fourth category, the "stability derivatives" are quasi-linear, i.e., they represent amplitude-dependent nonlinear effects in the vicinity of the generalized trim condition using an extension of sinusoidal-input describing function theory.

The examination of compressibility effects highlighted the importance of basing stability and control analyses on the best, most consistent set of aerodynamic data available for a particular aircraft configuration. As no comparison of the two data sets with flight test data was intended or undertaken, no comment can be made on the validity of either data set; however, it is clear that the analytical results obtained with the two sets are qualitatively different in their overlapping region (subsonic flight, with wings swept forward). This does not impact the current research effort, which is directed at new methodology development and the demonstration of trends which depend on flight condition, but data validity is a major concern in most applications.

The Mach-dependent data set indicates overall stability at subsonic and supersonic speeds, with sideslip and speed divergences in the transonic regions for angles of attack beyond 5 deg. Rapid roll rate couples these transonic instabilities into a divergent speed-sideslip-angle of attack oscillation. As known previously, constant roll rate can have the effect of transferring damping from one axis to another, and that effect is particularly noticeable in supersonic flight. Our earlier work with subsonic data (Refs. 1 and 2) suggested that sideslipping "into" a constant rolling motion tends to destabilize an aircraft; that effect also occurs in supersonic flight. In addition, sideslipping "out of" the roll introduces a different mode of instability in

the supersonic case studied here. The net effect is that tight control of sideslip angle is indicated for supersonic flight.

The highlight of the pilot-aircraft stability and performance analysis is the definition of a minimum-control-effort (MCE) adaptation model for the human pilot. As in our earlier work, the pilot is characterized (mathematically) as a stochastic optimal regulator which attempts to minimize a weighted sum of state and control perturbations in flying the aircraft. The potentially destabilizing effect which the pilot could have if he adopts a fixed control strategy was noted previously, and the current work endeavors to expand upon this result by examining the effects of a set of mismatched pilot models on pilot-aircraft characteristics. In addition, predictions of rms tracking accuracy and control effort within the stable regions were investigated. It was noted that optimal piloting did not necessarily correspond with minimum control effort, and that if the pilot adapted his control strategy to minimize his effort, he could be directed to regions in which even small piloting errors could lead to system instability. The MCE model further predicts when a pilot who has more than one control at his disposal (e.g., lateral stick and foot pedal deflections) is likely to switch from one control mode to another. Limited validation of the model is afforded by comparison of MCE model predictions with the result of a manned simulation.

A departure-prevention command augmentation system (DPCAS) design methodology is established in our third category of work, and the method is applied to the design of an advanced control system for the subsonic model of the F-14A aircraft. The DPCAS design, illustrated by Fig. 1, provides precision response to pilot commands (normal acceleration, stability-axis roll rate, and sideslip angle), with "Level 1" flying

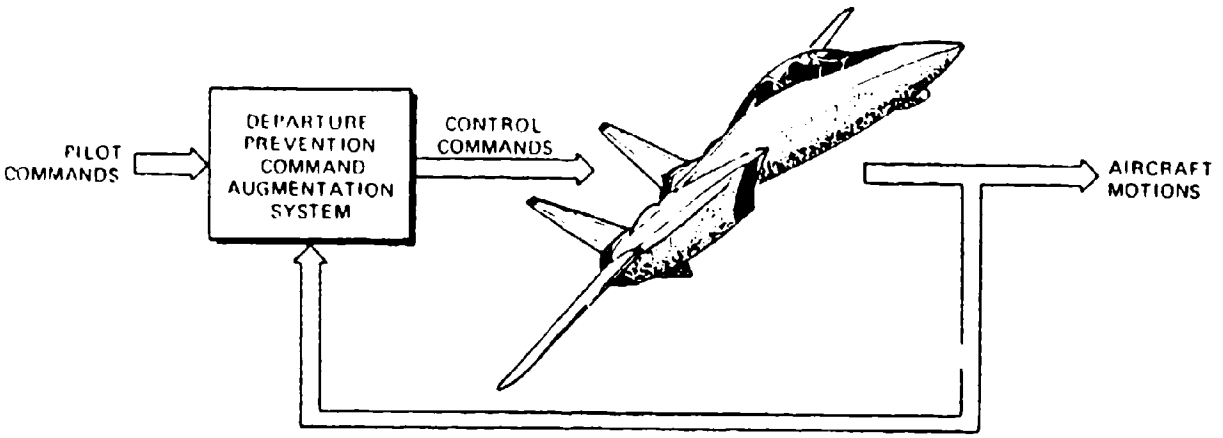

Figure 1 Departure-Prevention Command Augmentation System (DPCAS) for F-14A

qualities (as defined by military specification) at the 25 flight conditions used for design. The design points represent the following range of nominal flight conditions:

- True Airspeed: 122 to 244 m/s (400 to 800 fps)
- Angle of Attack: 10 to 34 deg
- Stability-Axis Roll Rate: 0 to 100 deg/sec
- Altitude: 6096 m (20,000 ft)

This DPCAS design technique is directly applicable to the design of advanced active control laws, e.g., those associated with control-configured vehicles (CCV), and an analysis of the unmodified F-14A's ability to be flown in various CCV modes was conducted. It was found that separate-surface control deflections could provide independent fuselage pointing, direct lift, and direct side force to a small degree; however, the major improvements which can be made to the unmodified aircraft's maneuverability arise from the basic 3-command DPCAS described above.

A unique feature of the DPCAS design approach, which is based upon linear-optimal control theory, is that equivalent "Type 0" and "Type 1" controllers can be designed concurrently. (A Type 1 controller has one pure integrator in each command path; a Type 0 controller has no pure integration in the forward loop.) The two implementations have virtually identical step response characteristics when the design model and the actual aircraft are matched; however, their responses to turbulence and state measurement errors are different, and steady-state response is not the same when the design model and actual aircraft are mismatched. The Type 0 implementation has superior disturbance rejection, and the Type 1 controller guarantees zero steady-state command error in the presence of model mismatch.

The multivariable limit cycle analysis technique (MULCAT) investigated in the final category of our work is an iterative process for identifying flight regimes in which self-induced nonlinear oscillations in the aircraft's motions are likely to occur. Beginning near a point of neutral stability, as defined by the aircraft's linear dynamic model, a succession of neighboring quasi-linear models is analyzed. The quasi-linear models are similar to the linear models, except that potentially significant nonlinear terms (which are approximated by slopes or "small signal" gains in the linear case) are represented by dual-input describing functions. These describing functions reflect the scaling changes and trim shifts which occur when sinusoidal oscillations of varying amplitude are present in the nonlinear system model (which includes both aerodynamic and inertial effects). In general, the eigenvalues and eigenvectors of the quasi-linear model are decidedly different from those of the linear model if the assumed amplitudes of oscillation are large. Using MULCAT, potential limit cycles are identified by the combination of state variable amplitudes and oscillation frequency which forces the quasi-linear dynamic model to a point of neutral stability (as defined by the quasi-linear eigenvalues).

The results of the MULCAT investigation are promising, in that the procedure converged to limit cycle predictions in several cases involving the subject aircraft. As expected, the combination of large-amplitude oscillations and nonlinearities caused a significant shift in the aircraft's trim condition, as well as in the effective eigenvalues and eigenvectors. Direct simulations of the corresponding nonlinear dynamic equations confirmed the existence of persistent oscillations with the predicted amplitudes and frequency. The simulations could not confirm the long-term "locked-in" nature of oscillation amplitude which is characteristic of limit cycles, because there are also slow unstable modes present in the aircraft dynamics. The simulated initial conditions always forced these additional modes of motion, and this led to eventual changes in the flight condition. Nevertheless, MULCAT provided significant new insights regarding nonlinear oscillations, and it should receive further testing with alternate dynamic models.

The methods and results presented here can have substantial impact on the development and testing of future high-performance aircraft, on the analysis and modification of existing aircraft, and on the training of aviators. As a consequence of a better understanding of the dynamic coupling which occurs during maneuvering flight and of the use of modern control theory, stall/spin-related accidents can be minimized, and operational effectiveness of aircraft can be improved. The mathematical models of pilot-aircraft dynamics can identify flight regimes which may be departure-prone, as well as control procedures which must be used to avoid difficulty. The net effect can be to enhance the safety, reliability, and performance of flight operations, particularly those involving high-performance aircraft.

1.3 ORGANIZATION OF THE REPORT

This report presents analyses of coupled aircraft dynamics (with emphasis on transonic and supersonic flight), pilot-aircraft interactions, control system design, and nonlinear aerodynamic and inertial phenomena. Chapter 2 employs a Mach-dependent aerodynamic model of the F-14A aircraft to investigate the possibilities for departure and control difficulty throughout the aircraft's flight regime. Chapter 3 develops the minimum-control-effort (MCE) adaptation model for pilot behavior, illustrating the stability boundaries and performance contours of the pilot-aircraft system. A departure-prevention command augmentation system (DPCAS) design for the subsonic F-14A model is developed in Chapter 4. Results of the multivariable limit cycle analysis technique (MULCAT) are presented in Chapter 5, and conclusions and recommendations are presented in Chapter 6. Symbols and abbreviations are given in Appendix A. The Mach-dependent aerodynamic model is summarized in Appendix B. Pilot command modes for the DPCAS, including so-called "CCV Modes," are presented in Appendix C, while the theory of proportional-integral, linear-optimal regulators used in DPCAS design appears in Appendix D.

2. COMPRESSIBILITY EFFECTS ON FIGHTER AIRCRAFT STABILITY AND CONTROL

2.1 OVERVIEW

Previous high angle-of-attack stability and control developments have detailed many of the significant dynamic characteristics of a mathematical model of the F-14A (Ref. 2). The model used in the previous study was restricted to subsonic flight with wings fixed in the forward position. This chapter presents stability boundary and control variation results for an aircraft model which includes the effects of Mach number. The aerodynamic model is described in Appendix B. All of these results are for the "unaugmented airframe" model only; handling qualities of the aircraft as flown are greatly influenced by the SAS, CAS, ARI, and other elements of the flight control system.

As in the previous work reported in Ref. 2, the analysis approach is based on the formation of linear aircraft models which include longitudinal-lateral-directional coupling. Linear, time-invariant models describe small perturbation stability in the vicinity of a single flight condition and can be useful for practical approximation of system dynamics, for sensitivity analyses, and for control system design.

The linearized aircraft model, derived as it is from a Taylor series expansion of the complete nonlinear model about a reference flight condition, is valid for small perturbations about that reference condition. Reference 1 compared time histories generated by nonlinear and properly linearized models in a highly dynamic trajectory (a rudder roll) and found good agreement between the two types of models.

In this chapter the linear system eigenvalues, evaluated along a series of flight conditions, are used to construct stability boundaries as functions of the flight condition variables. Other stability comparisons are made on the basis of damping ratio or specific damping. Damping ratio, defined only for oscillatory modes, is the ratio between the actual damping and the critical damping (i.e., the damping for which the mode no longer oscillates). Specific damping is the real part of the eigenvalue, and it describes the rate of convergence (or, if positive, divergence) of that mode.

Three different Mach-altitude regimes are examined in this chapter; they have been chosen so that the dynamic pressures at the subsonic, transonic, and supersonic flight conditions are identical. Figure 2 illustrates the three regimes and also indicates the wing sweep regions modeled. To give an indication of the maneuverability involved, approximate 1-g and 8-g curves for 25-deg angle of attack (α) are plotted. The subsonic and transonic regimes represent regions in which air combat maneuvering (ACM) is likely to occur. The supersonic regime could occur in a long-range, high-altitude intercept. The variable-geometry aircraft adapts to each of these regimes through wing sweep and glove vane extension.

This chapter examines the stability and control characteristics of this airframe in these regimes. Even in the subsonic regime, compressibility effects are shown to be important. The stability decrease inherent in transonic flight is examined, and stable (but lightly damped) modes appear in the supersonic regime.

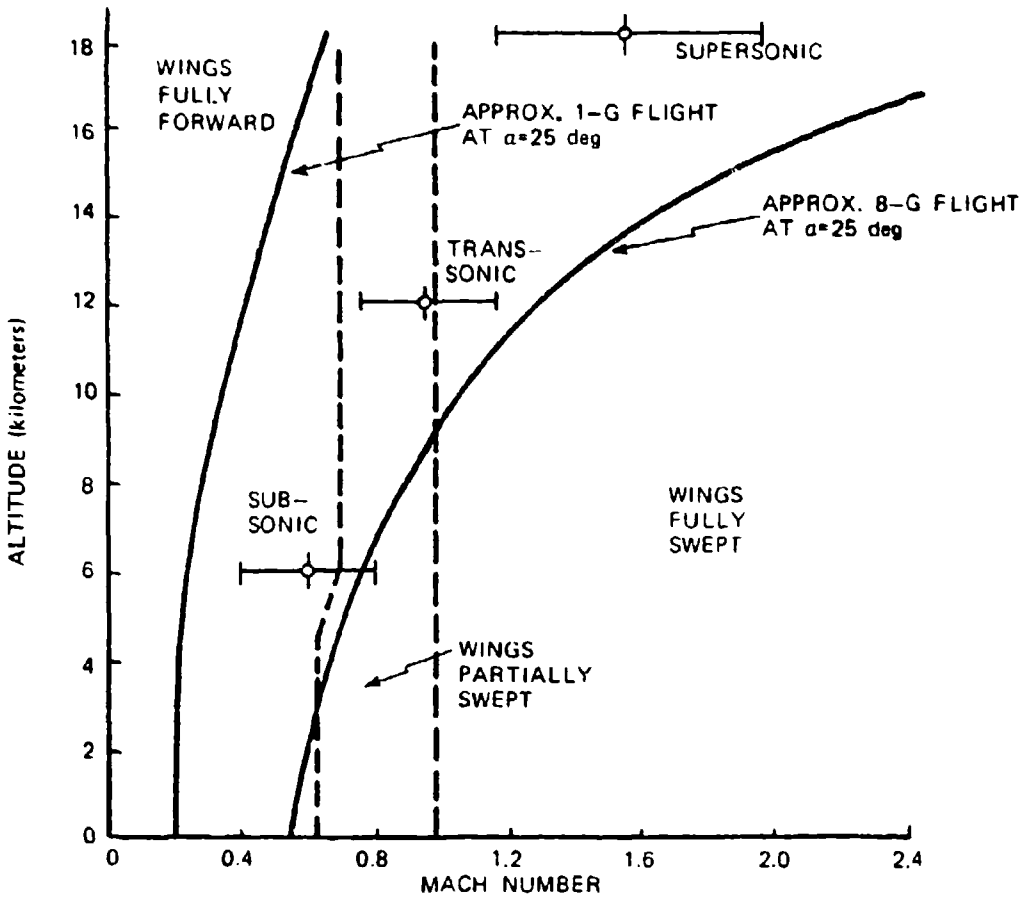

Figure 2 Flight Conditions for Stability Analysis of Compressibility Effects

2.2 SUBSONIC BASELINE CHARACTERISTICS

2.2.1 Description of the Subsonic Regime

The altitude (6,096 m (20,000 ft)), angle of attack, and Mach number (M) ranges chosen for use in the subsonic analysis are ones where many air combat engagements occur, so the stability and control characteristics of the aircraft in maneuvering flight are important. The subsonic regime

spans Mach numbers from 0.4 (where compressibility has a minor effect) to 0.8, where Mach effects are quite large.

The variables describing straight-and-level trimmed flight are plotted in Fig. 3. The wing sweep adapts to the flight regime, remaining fully forward for flight efficiency over most of this regime and only beginning its rearward sweep when compressibility becomes important. Trim throttle and stabilator are small relative to the total control deflections available, and trim α in 1-g flight is small. Trim α decreases with increasing Mach number as dynamic presure increases and the required lift coefficient for 1-g flight is reduced.

The low subsonic Mach number (M=0.4) results presented here are somewhat different from the results derived from the imcompressible-flow model used in Ref. 2. The high-α unstable roll-spiral mode (shown in Fig. 4) is the same in both models, but the Dutch roll instability near 20-deg α in the incompressible-flow model is not exhibited by the compressible-flow model at M=0.4.

2.2.2 Subsonic Stability Boundaries of the Aircraft

The lateral mode damping variation with α for M=0.4 is illustrated in Fig. 4. Two major effects are apparent: the roll mode slows dramatically in the α band associated with outer wing panel stall (10-20 degrees), and the Dutch roll damping consistently increases with angle of attack. There is a mild roll-spiral oscillation at high α.

The same α sweep at higher Mach number (M=0.8) exhibits significantly different mid-α characteristics, as shown in Fig. 5. The roll mode slows at an even lower angle

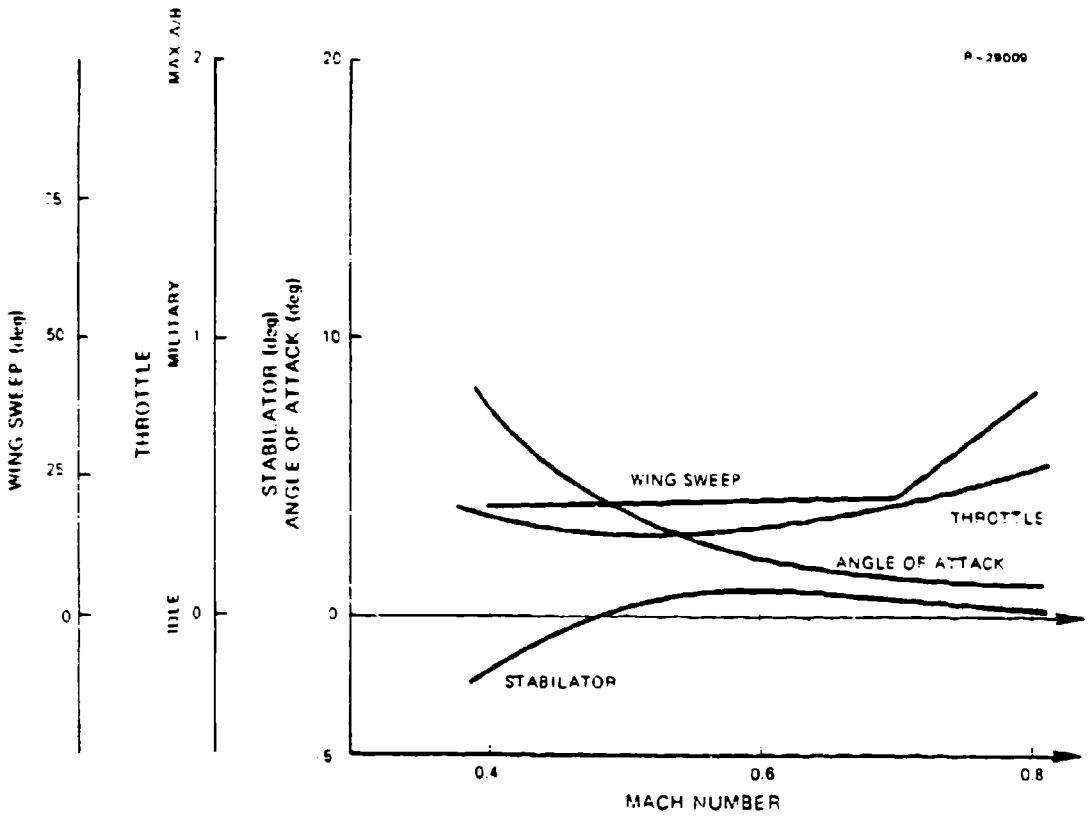

Figure 3 Trim at 6,096 m in 1-g Flight

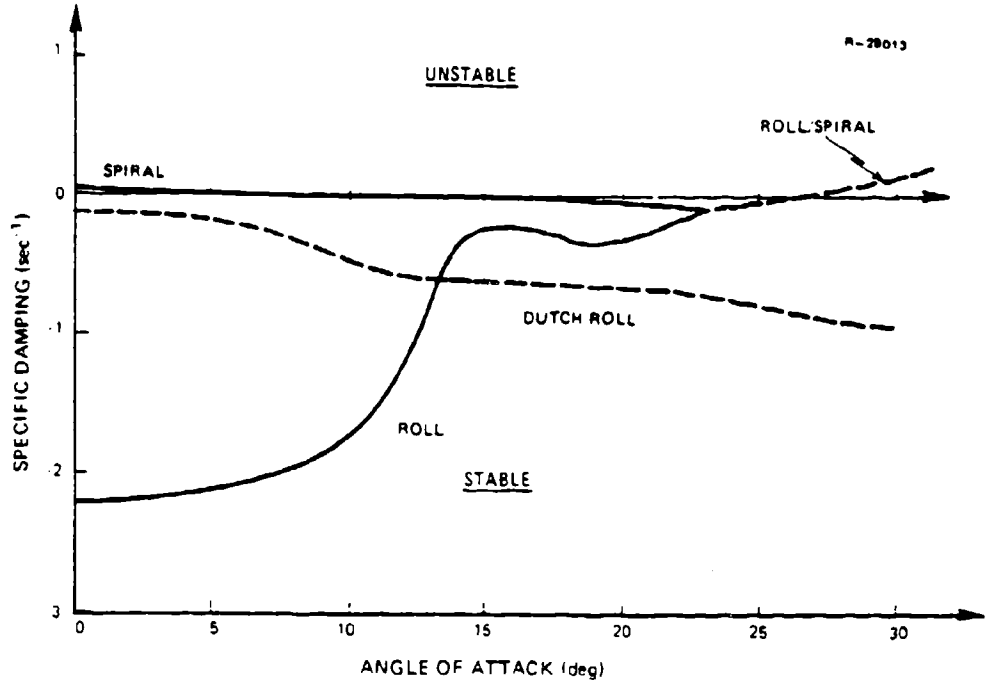

Figure 4 Specific Damping of the Lateral Modes (M=0.4)

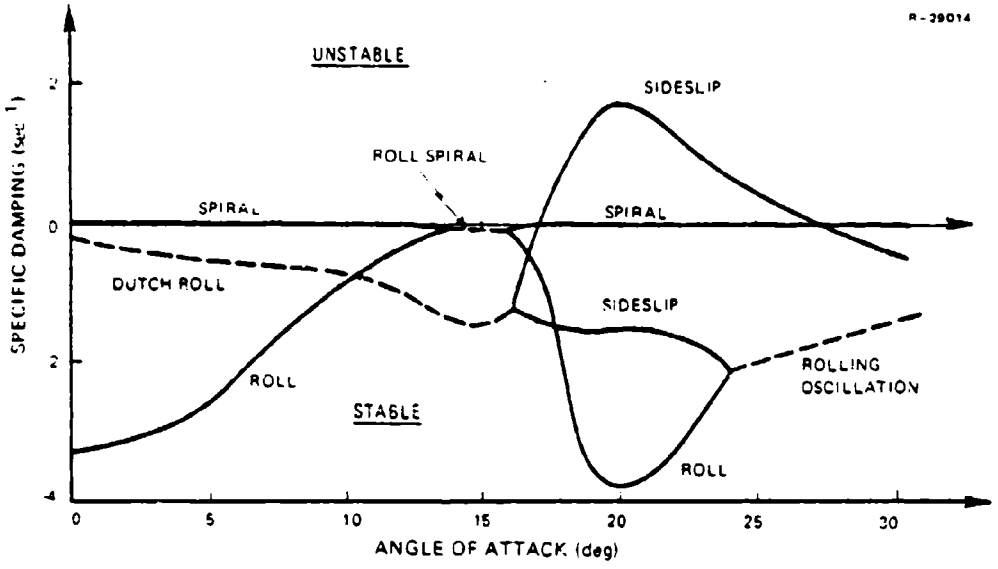

Figure 5 Specific Damping of the Lateral Modes (M=0.8)

of attack, and the Dutch roll mode decomposes into two real modes exhibiting large sideslip motions at about 16-deg α. One of these modes is very unstable. In the same α range, the roll-spiral decomposes to roll and spiral convergences. At moderately high α, the roll mode and one of the sideslip modes combine to form a rolling oscillation.

Mode shapes for the α range from 10 to 30 deg are detailed by the eigenvectors illustrated in Fig. 6. The large amount of sideslip in the roll mode at 10- and 20-deg α is apparent, and it illustrates the difficulty of discerning between the roll and Dutch roll modes at 10-deg α. The sideslip modes are apparent at 20 deg, and the rolling oscillation appears above 24 deg. As α increases beyond 24 deg, the rolling oscillation begins to approach the Dutch roll shape (as indicated by the magnitudes and phase angles of the eigenvectors).

The sideslip divergence appears in different angle-of-attack regions for different Mach numbers. Figure 7 illustrates this effect; increased Mach number tends to delay this

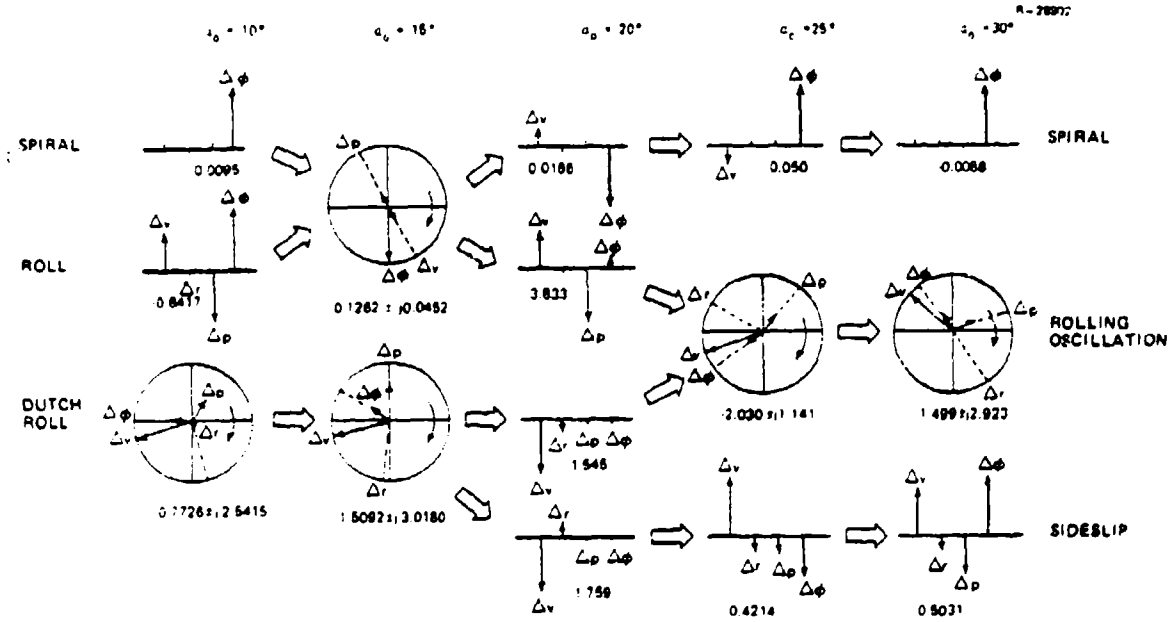

Figure 6 Eigenvector Evolution with Angle of Attack (M=0.8)

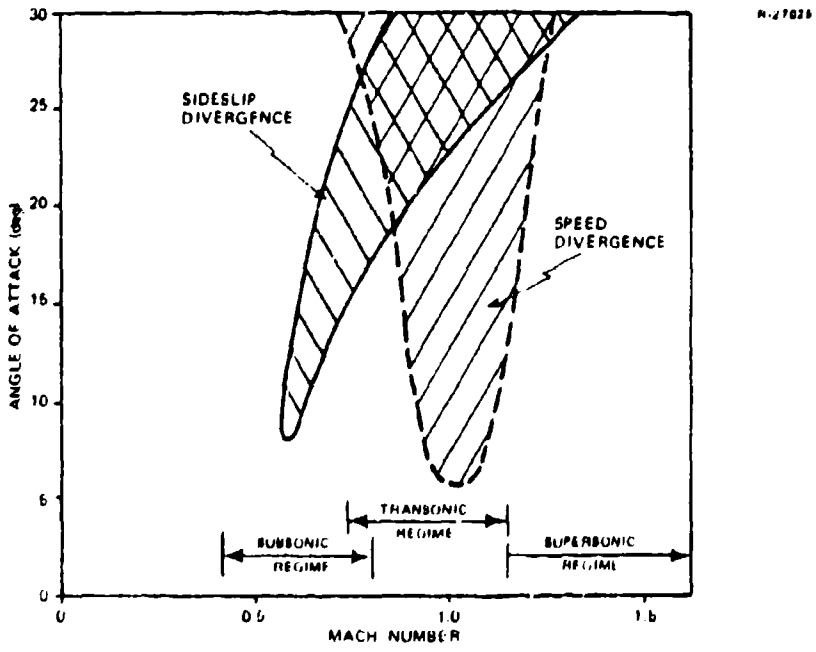

Figure 7 Effects of Compressibility on Stability Boundaries

effect to higher angles of attack. This trend follows, to some extent, the increase in wing sweep angle which occurs in the same Mach number range.

Time histories of the aircraft's lateral-directional motion are shown in Figs. 8 and 9. The low-α roll response is dominated by the fast roll convergence mode (Fig. 8), and relatively small yaw-sideslip motions ensue. The directional motion illustrates the low Dutch roll damping. At higher α (Fig. 9), the roll mode dominates both the roll and yaw responses, but it is much slower than at low angle of attack. The well-damped Dutch roll oscillation appears in the first few seconds of the response.

Even at those flight conditions where the Dutch roll mode is stable, its damping varies greatly. Figure 10 plots contours of equal Dutch roll damping ratio in constant altitude flight. There are a number of areas in this plot where relatively small Mach number or angle of attack changes result in significant changes in Dutch roll damping. Overlayed on the plot are contours of constant maneuver load factor, and it is instructive to trace the Dutch roll damping exhibited by the aircraft as its load factor increases. At a constant Mach number of 0.75, the Dutch roll damping increases up to a load factor of 4, decreases up to a load factor of 6.5, and then increases rapidly for load factors up to 8. The model exhibits significantly different lateral-directional characteristics as load factor varies in the high subsonic regime.

In this analysis, the pitch rate effects of maneuvering flight have been deleted to concentrate on the angle of attack effects. Steady pitch rate causes a redistribution of the available damping among the lateral-directional modes

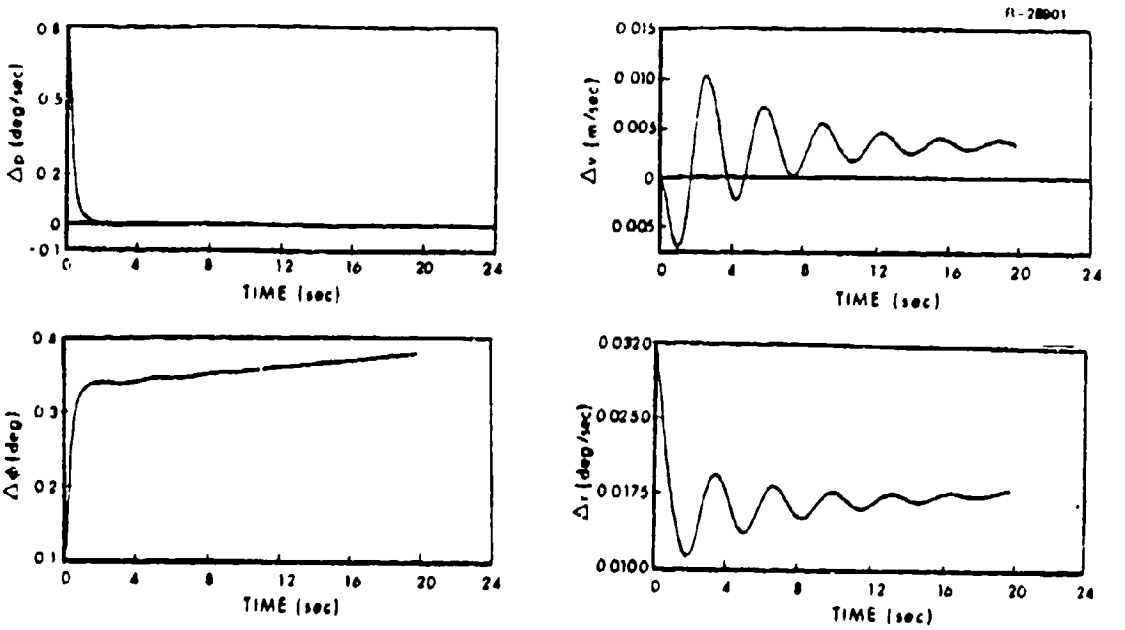

Figure 8 Lateral Response to Roll Rate Initial Condition (p_W = 1 deg/sec, M = 0.6, α_O = 2.03 deg)

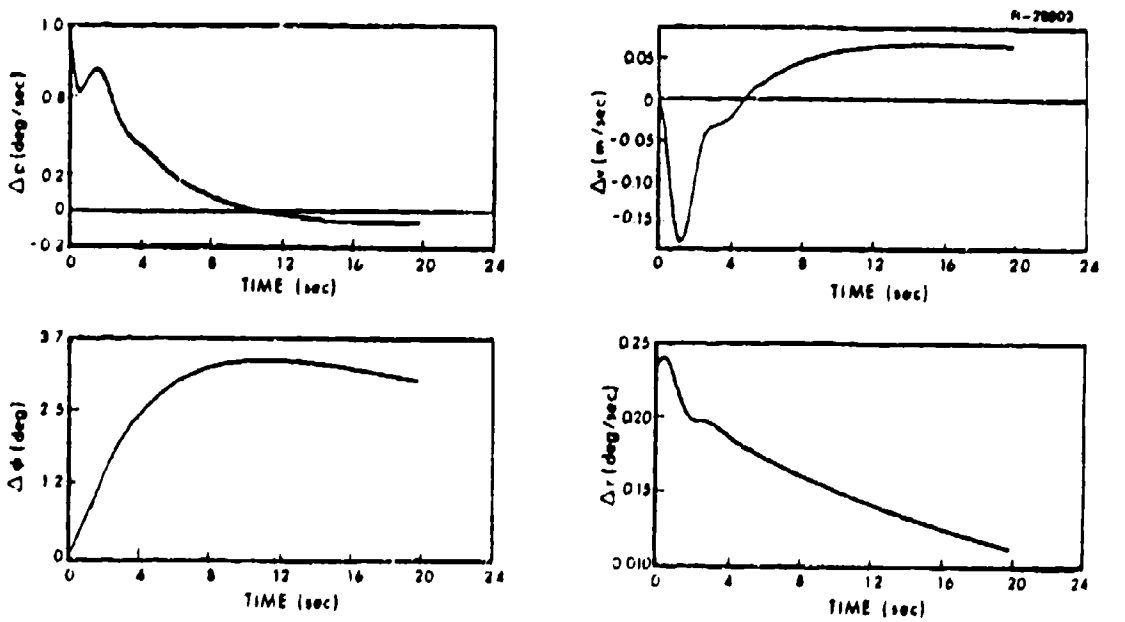

Figure 9 Lateral Response to Roll Rate Initial Condition (p_W = 1 deg/sec, M = 0.6, α_O = 15 deg)

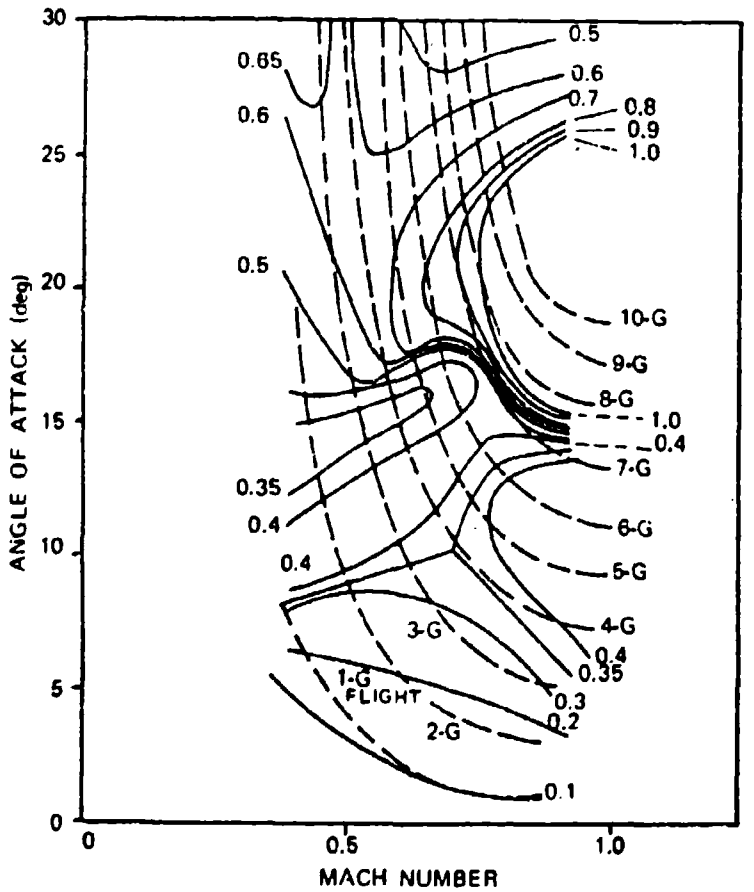

Figure 10 Effects of Compressibility on Dutch Roll Damping Ratio at Constant Altitude (h = 6,096 m)

without significantly changing the total specific damping. Figure 11 illustrates that the roll mode is stabilized while the Dutch roll mode becomes less well damped with increasing pitch rate. This effect is mild and relatively independent of flight condition, and the same result was observed in the incompressible model (Ref. 2). In the longitudinal modes, there is a general increase in short period damping accompanied by a decrease in phugoid damping. Increasing pitch rate can cause the phugoid mode to split into two real modes, one of which may become unstable.

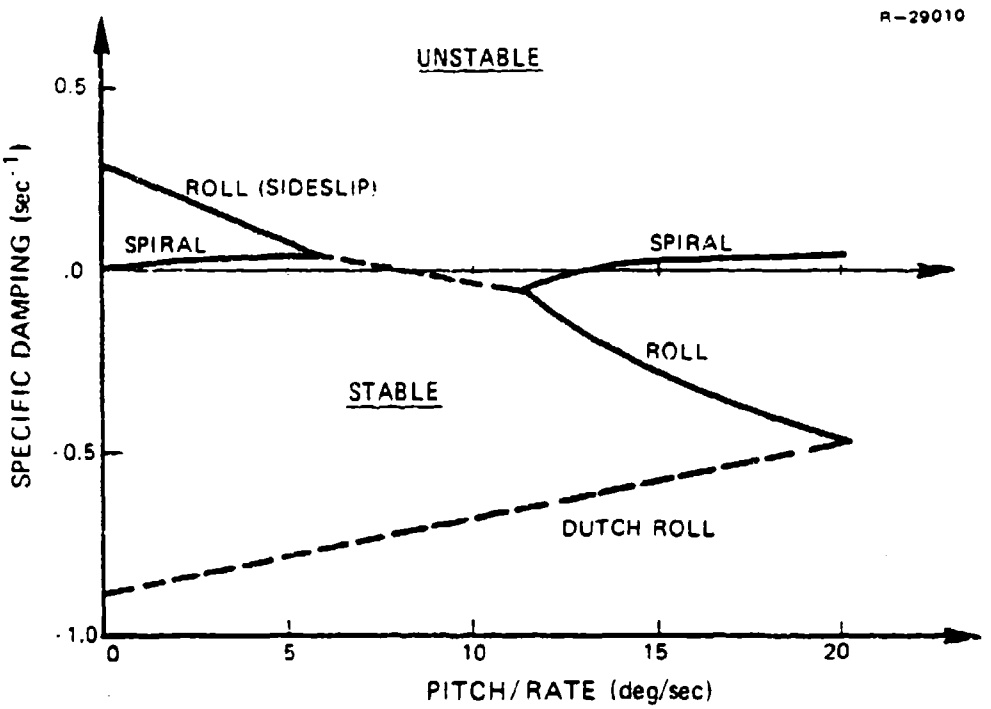

Figure 11 Specific Damping of the Lateral Modes as a Function of Pitch Rate (M=0.6, h=6,096 m, α_o=10 deg)

2.2.3 Control Power Variations in the Subsonic Regime

The longitudinal control set of this aircraft consists of throttle position, stabilator position, and maneuvering flap position. The latter two controls provide both pitch moments and normal forces, and they can be mixed (at least conceptually) to illustrate the extent to which pitch and angle of attack can be independently controlled. Figure 12 shows the normalized control ratio between stabilator and maneuvering flap necessary to initiate a vertical translation at constant pitch angle.

"Normalized control ratio" indicates that the control effectiveness derivatives used in this calculation have been

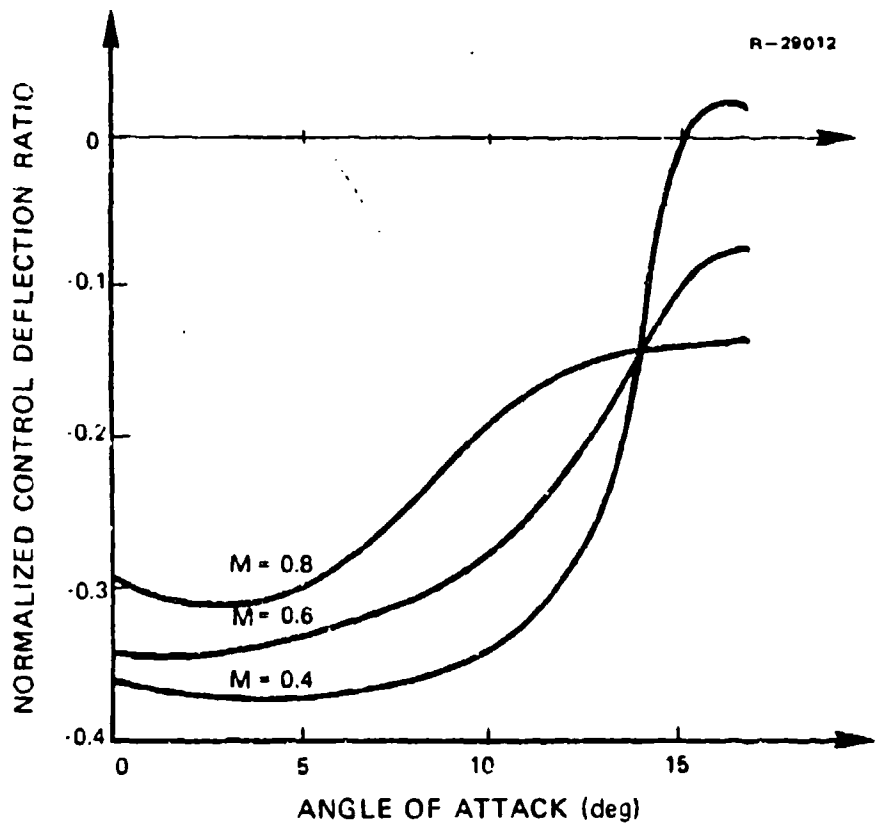

Figure 12 Normalized Stabilator/Maneuver Flap Deflection Ratio for Vertical Translation (Constant Pitch Attitude)

divided by the maximum control deflections. (Maneuver flap can be deflected 10 degrees, and ±12 degrees is used as the limit on stabilator available for maneuvering.) Hence, a normalized ratio of 1.0 implies that the controls deflect in equal proportions of full deflection. These ratios are only valid for the initial deflections; the actual control history necessary to achieve constant pitch angle depends on the vehicle response characteristics. Chapter 4 details a control approach which can produce the complete desired response time history.

Figure 12 indicates that the stabilator is much more powerful than the maneuvering flap, and there should be no difficulty producing (at least initially) a pure normal force. The magnitude of the normal force produced in this way is limited by the fairly small normal force due to maneuvering flap deflection and by the fact that the maneuvering flaps and the stabilator both have effective centers of pressure behind the center of gravity. As Mach number increases, the maneuvering flaps become less powerful relative to the stabilator.

An alternative longitudinal control interconnect is one which produces a pitch moment (and hence a normal acceleration) at constant angle of attack. This combination is referred to as direct lift control (Ref. 3), and Fig. 13 illustrates the normalized maneuver flap-to-stabilator ratio that initiates this motion. The maneuver flap is not powerful enough in normal force to enable full stabilator deflections to be used in this mode.

These longitudinal control results indicate that this aircraft's ability to operate as a control configured vehicle (CCV) with existing control surfaces is limited, as would be expected. The maneuver flap is powerful enough, however, to have a significant beneficial effect on handling qualities. This capability is examined in detail in Chapter 4, where the design of an advanced command augmentation system is illustrated.

The lateral control effectors of this aircraft are conventional rudders and differential stabilator, with spoilers used for additional roll control in the subsonic regime. Figure 14 details the differential stabilator roll and yaw specific moments over the angle of attack range from 0 to 30 deg. Adverse yaw from the differential stabilator above

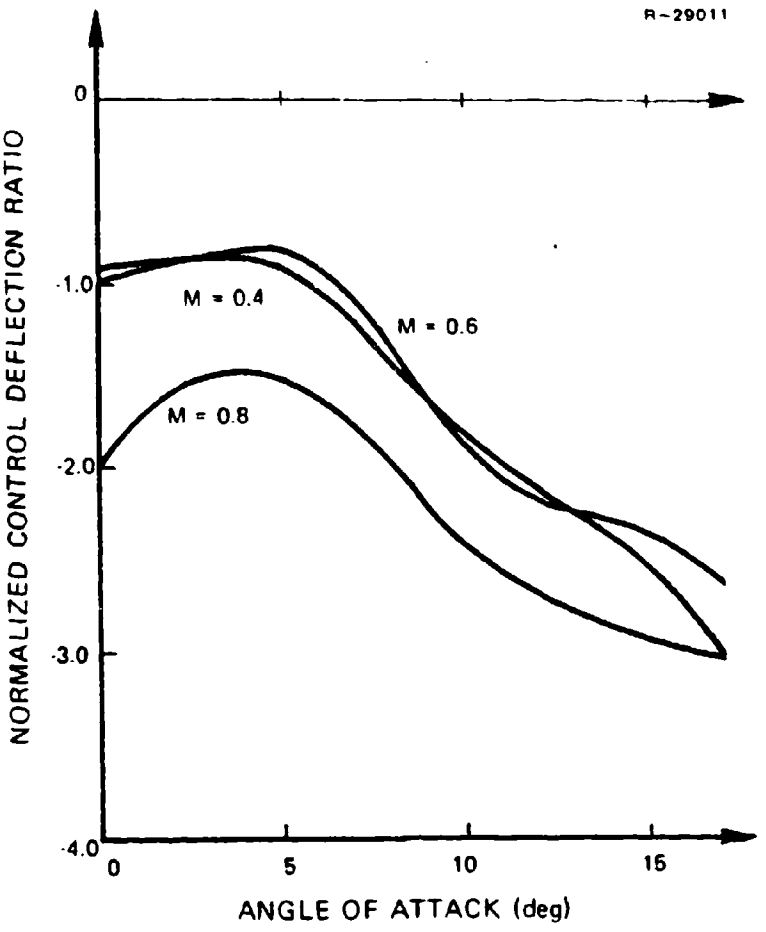

Figure 13 Normalized Maneuver Flap/Stabilator Deflection Ratio for Direct Lift Control (Constant α)

17-deg α can be expected to cause control difficulties in the high-α regime (as is the case for most aircraft configurations). Although the yaw moment is much smaller than the roll moment, it still has an important effect due to the smaller magnitude of most yawing motions.

The rudder creates a large, fairly constant yawing moment and a highly variable roll moment, as shown in Fig. 15. Combining differential stabilator and rudder to provide a

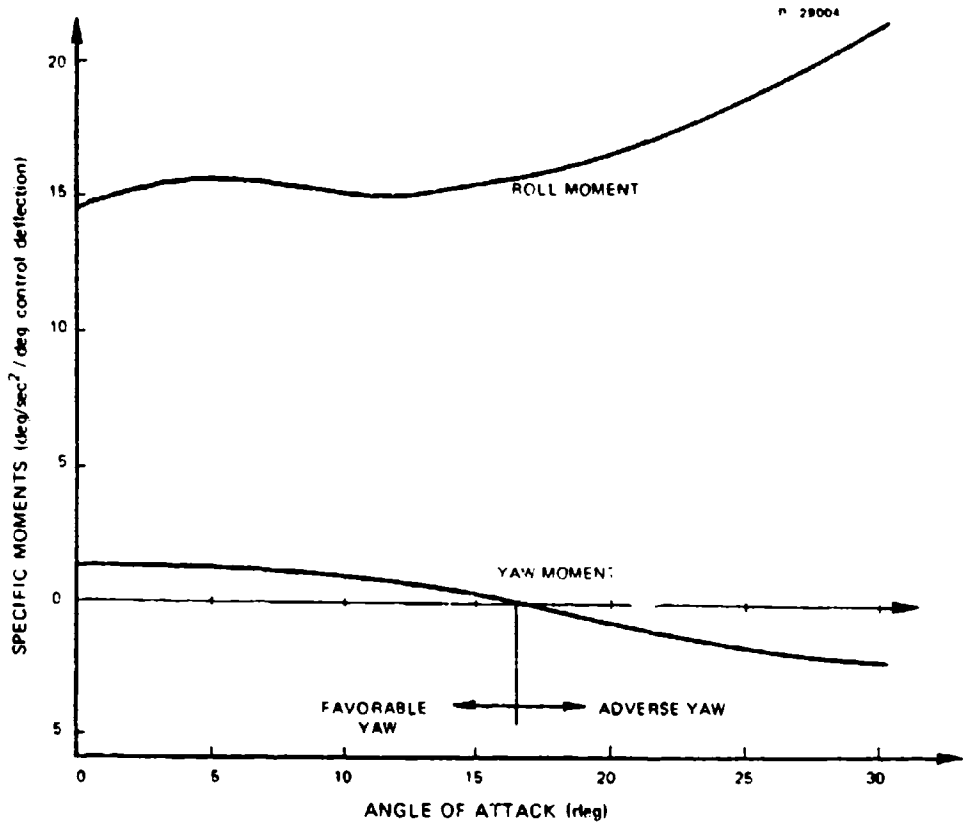

Figure 14 Differential Stabilator Specific Moments (M=0.6)

rolling moment about the velocity vector ($\dot{p}_W$) results in the normalized rudder-to-differential stabilator ratio shown in Fig. 16. Above 19-deg α, it is no longer possible to produce a pure velocity-vector rolling moment at full differential stabilator deflection. This is due to the increased amount of adverse wind-axis yaw moment from the differential stabilator at high α.

Figure 16 also indicates the differential stabilator-to-rudder ratio which is needed for pure yaw moment. The ratio varies by a factor of four from 5- to 15-deg α. This

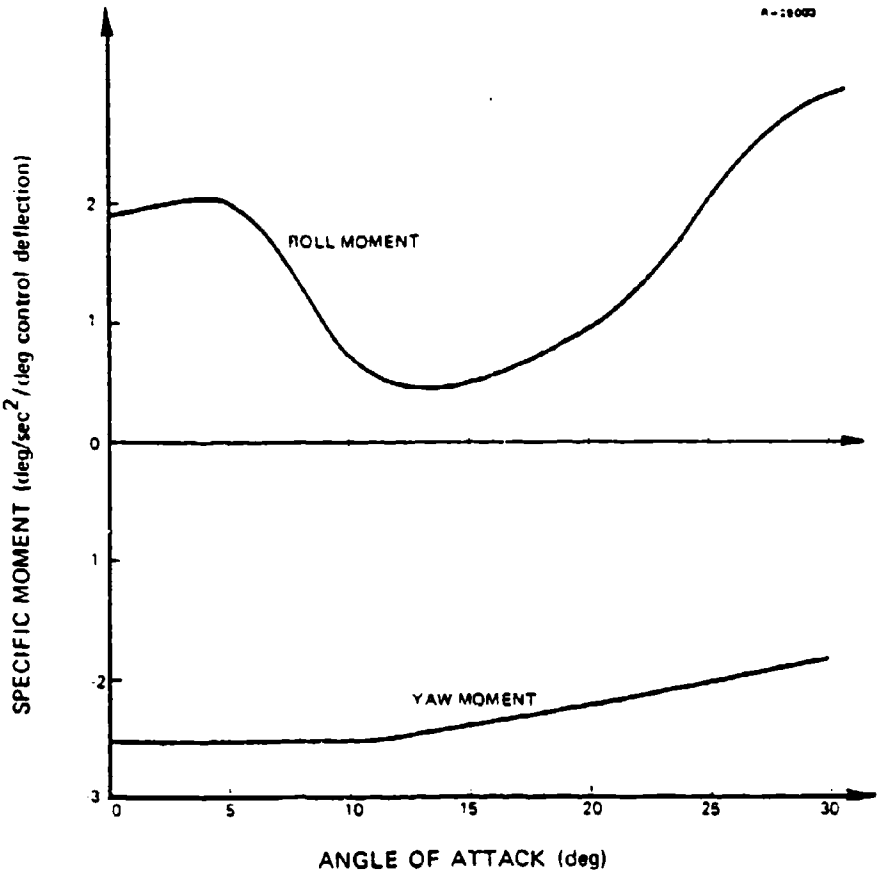

Figure 15 Rudder Specific Moments (M=0.6)

is significant, because any deflection error would produce unwanted rolling, which, along an accelerated trajectory, could result in large tracking errors.

Spoilers are used to augment the roll control moment in the subsonic regime. Figure 17 compares the roll moment due to spoiler with that of the differential stabilator. At low α and low M, the spoilers create more roll moment than the differential stabilator does, but spoiler effectiveness drops to zero at about 16-deg α. Compressibility reduces spoiler effectiveness significantly, and they are not used at all in the transonic and supersonic regimes.

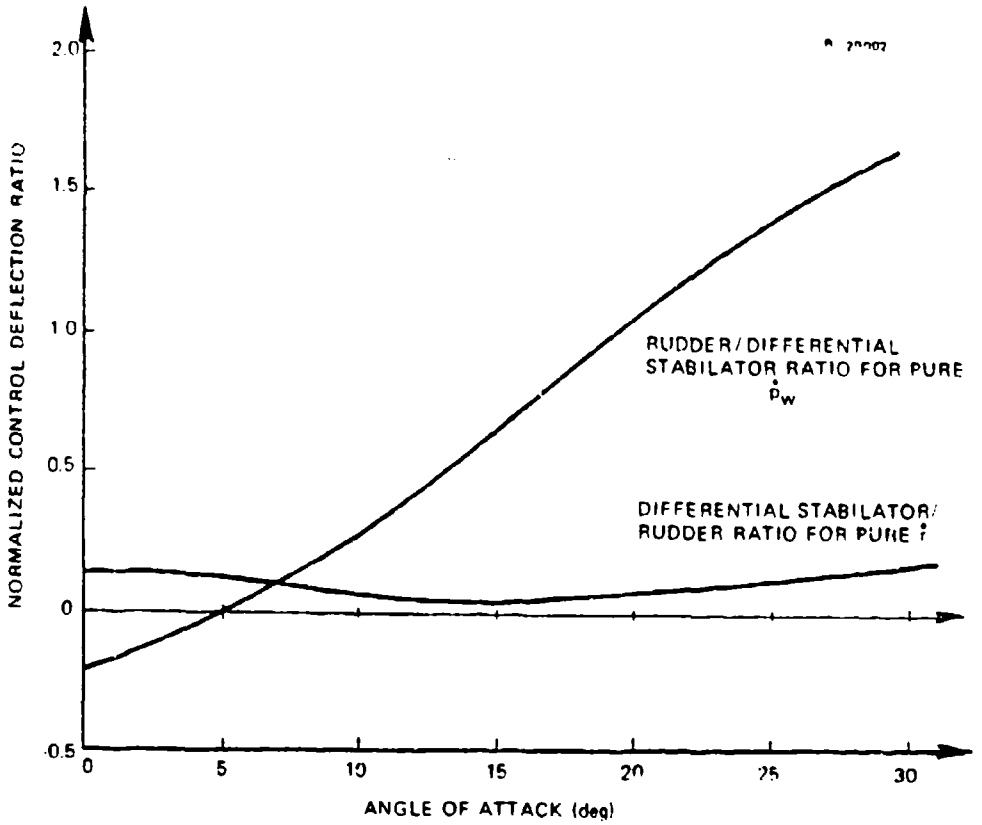

Figure 16 Lateral Control Deflection Ratios for Pure Yaw Acceleration and for Pure Wind-Axis Roll Acceleration

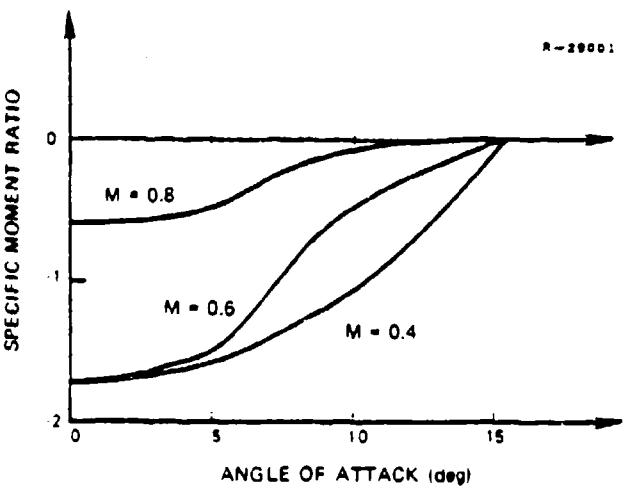

Figure 17 Spoiler-to-Differential Stabilator Roll Moment Ratio at Full Deflection

2.3 TRANSONIC AIRCRAFT CHARACTERISTICS

2.3.1 Transonic Flight Regime Characteristics

Transonic characteristics are examined at an altitude of 12,192 m (40,000 ft), providing the same range of dynamic pressures that is treated in Section 2.2. The dynamic pressure at the central transonic flight condition (M=0.95, h=12,192 m) is the same as at the central subsonic flight condition (h=6,096 m, M=0.6).

The aircraft configuration goes through a substantial transition in the transonic flight regime. The aircraft's variable geometry feature matches the wing sweep to the flight Mach number, as shown by the trim plot in Fig. 18. Significant changes in aircraft stability and lift-curve characteristics are evident in the shapes of the trim stabilator deflection and trim angle of attack, respectively. The large drag increases associated with this regime lead to increased trim throttle position.

2.3.2 Critical Transonic Stability Boundaries

Two aspects of transonic flight are of concern in all modern fighter aircraft. A longitudinal instability could result from the significant shift in aerodynamic center which accompanies Mach number variations. The second concern involves directional stability in the transonic regime, where the destabilizing influence of the fuselage is larger than in other regimes, and where the vertical fin effectiveness is decreasing (especially at large α).

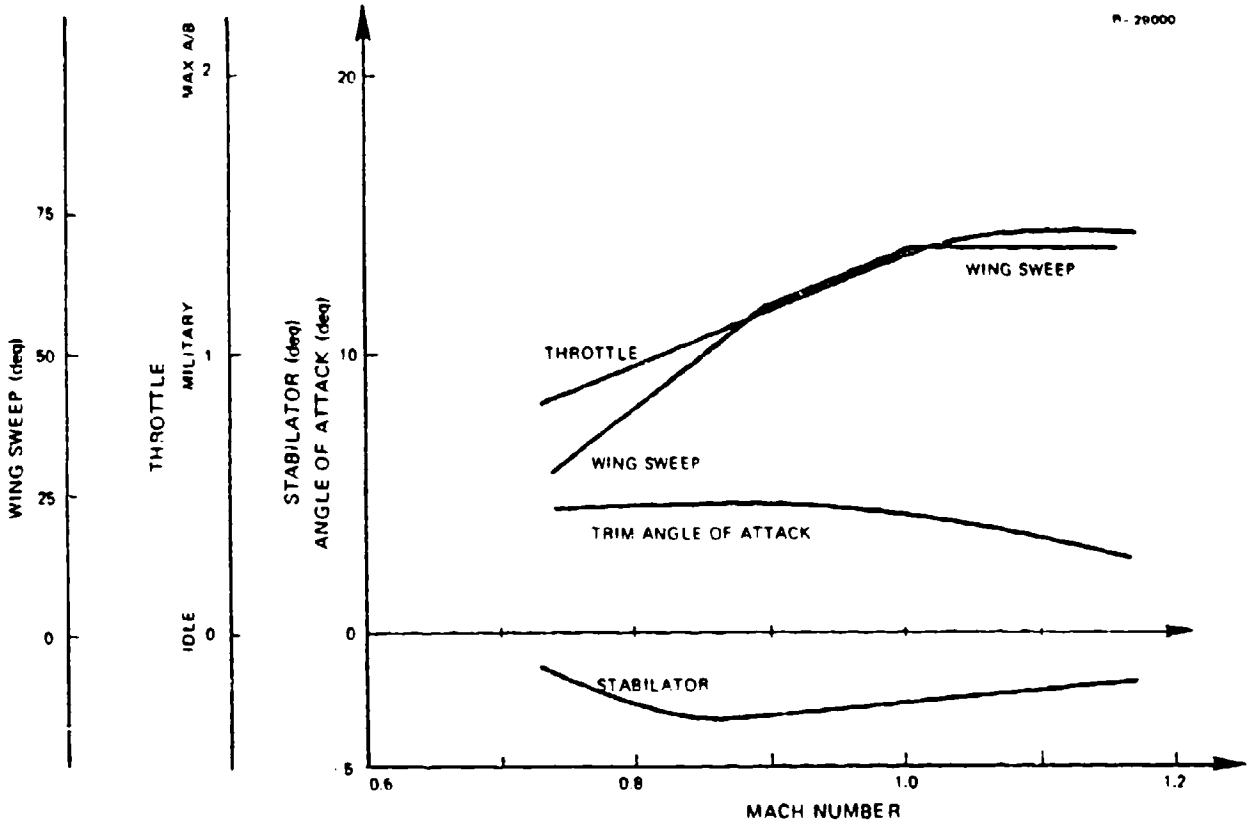

Figure 18 Trim at 12,192 m in 1-g Flight

The dynamic model used in this chapter exhibits both lateral and longitudinal transonic divergences at moderate to high angles of attack, as shown in Fig. 7. The longitudinal instability spans a larger Mach range at higher angles of attack, and it takes the form of a pitch-speed instability. Any change in Mach number in the regime leads to a change in longitudinal force which increases the Mach variation. At the same time, the aircraft pitches in such a way that the Mach variation is enlarged. Both specific longitudinal force due to speed variation ($\partial \dot{u}/\partial u$) and specific pitch moment due to speed variation ($\partial \dot{q}/\partial u$) change sign above 10-deg α in the transonic regime. The general shape of this motion involves 1-deg pitch change for every 3 m/s speed change, and the

doubling time can be as small as one-half second at high α. As shown in Fig. 7, the speed divergence disappears at low angle of attack.

The transonic lateral divergence is associated with a loss of static directional stability. Inspection of the dynamic model in high-α transonic flight reveals negative (unstable) values of specific yaw moment due to sideslip ($\partial\dot{r}/\partial v$) at high α. Additionally, as observed in other modern, supersonic, fuselage-heavy, fighter designs, the roll-sideslip coupling is important. The size of the specific roll moment due to sideslip ($\partial\dot{p}/\partial v$) is a major cause of this, with the coriolis coupling of roll rate to lateral acceleration a contributing factor. The decrease in roll mode speed at high-α is not caused by a drop in roll damping ($\partial\dot{p}/\partial p$ is fairly steady) but is due to the transfer of this damping to the Dutch roll mode by the roll-sideslip coupling terms. As shown in Fig. 7, the directional divergence disappears at moderate angles of attack.

The lateral oscillation (the Dutch roll mode) is stable in the transonic regime, although it exhibits large variations in damping. Figure 19 illustrates these changes, assuming constant dynamic pressure. (Altitude and Mach number increase together to maintain this condition.) The Dutch roll damping increases with maneuver load factor in a fairly predictable manner over much of the α range, although large damping changes can occur with small flight condition variations in the high-α region. It should be noted that the Dutch roll damping at low α is very low.

The rolling pull-up is a common maneuver in air combat. This involves a combination of rapid rolling (to orient the maneuver in the correct plane) and a hard pull-up (producing large normal acceleration). This combination is of

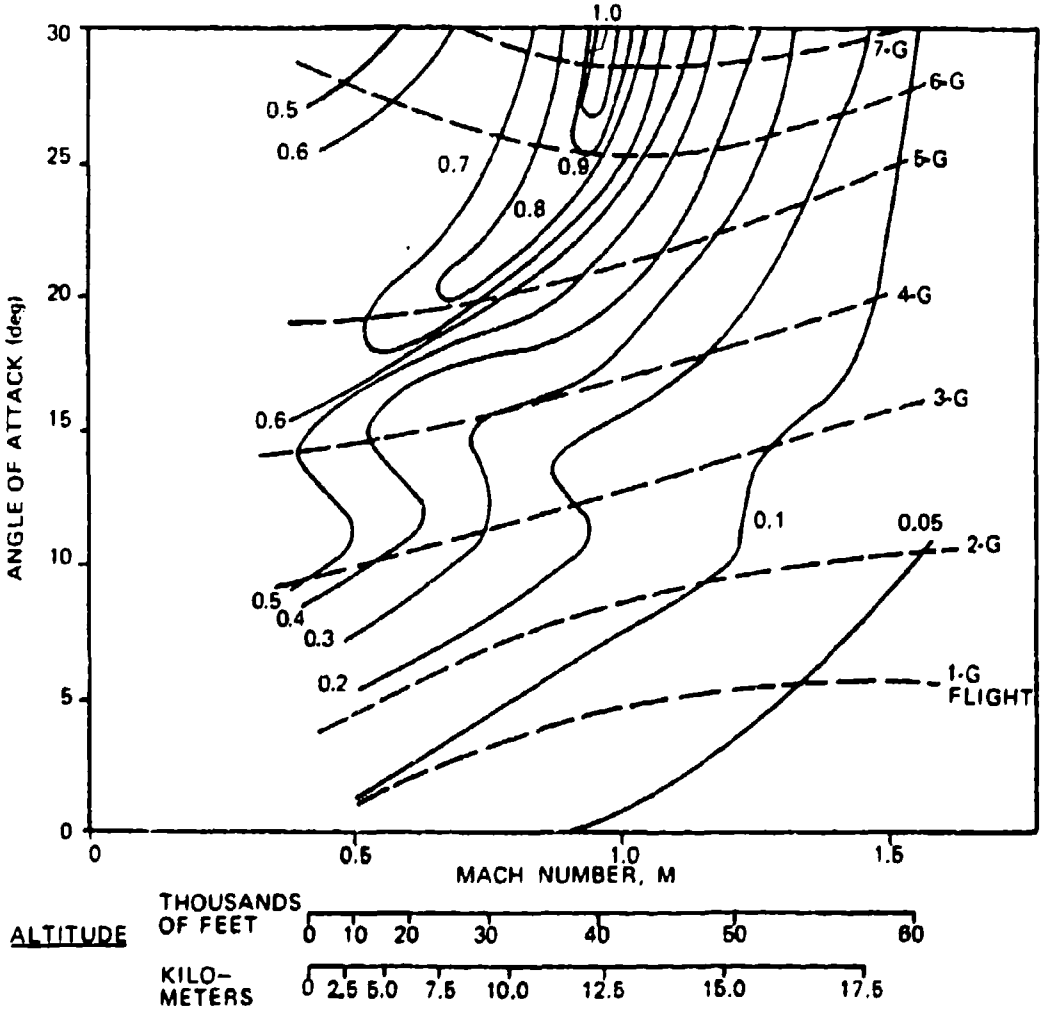

Figure 19 Effects of Compressibility on Dutch Roll Damping Ratio at Constant Dynamic Pressure ($q_\infty = 11.9 \times 10^3$ Nm^{-2} (248 psf))

interest because it combines the effects of lateral-longitudinal coupling and high angle-of-attack aerodynamics. Figure 20 shows the rolling pull-up stability boundaries for the subsonic, transonic, and supersonic regimes. The subsonic regime exhibits a mild roll-pitch angular instability, while the supersonic regime shows unstable oscillations at extreme rolling-pull up combinations.

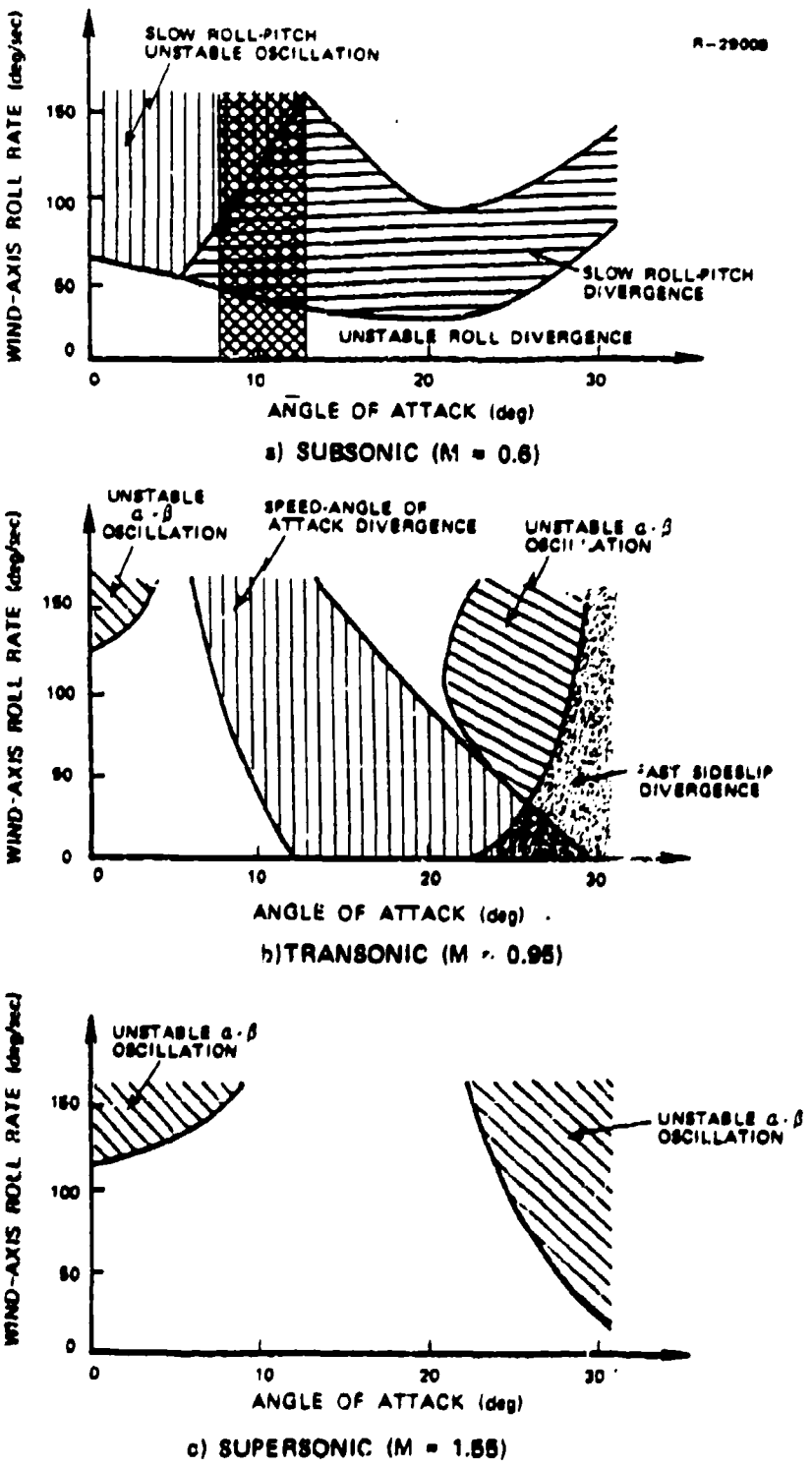

Figure 20 Angle of Attack-Wind Axis Roll Rate Stability Boundaries in All Mach Regimes

The transonic rolling pull-up stability boundary is much more complex. At low roll rates, the sideslip and speed divergences appear as before, but increasing roll rate causes these two modes to couple into an unstable α-β oscillation. At about 20-deg α, the steady rolling stabilizes the longitudinal oscillation. As observed before, steady angular rates do not add damping to the aircraft but only redistribute it, and this stabilized longitudinal oscillation is accompanied by reduced damping in the short period mode.

The short period damping ratio variations in the rolling pull-up are shown in Fig. 21. Below 26-deg α, short period damping ratio drops as roll rate increases. At high roll rates, the damping ratio is very low.

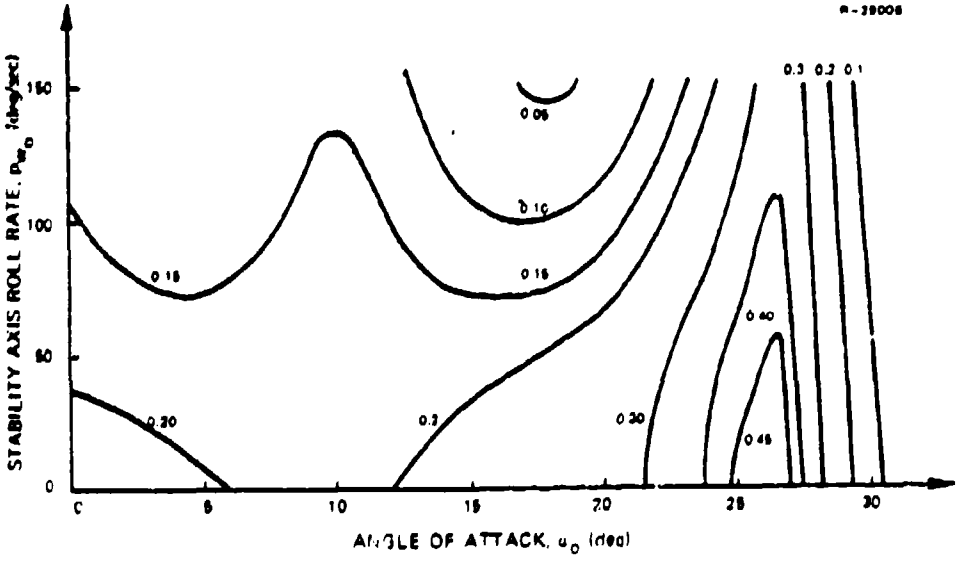

Figure 21 Short Period Damping Ratio in the Angle of Attack-Roll Rate Plane (M=0.95, h=12,192 m)

The damping interchange due to roll rate is illustrated in Fig. 22, which shows how the total specific damping is

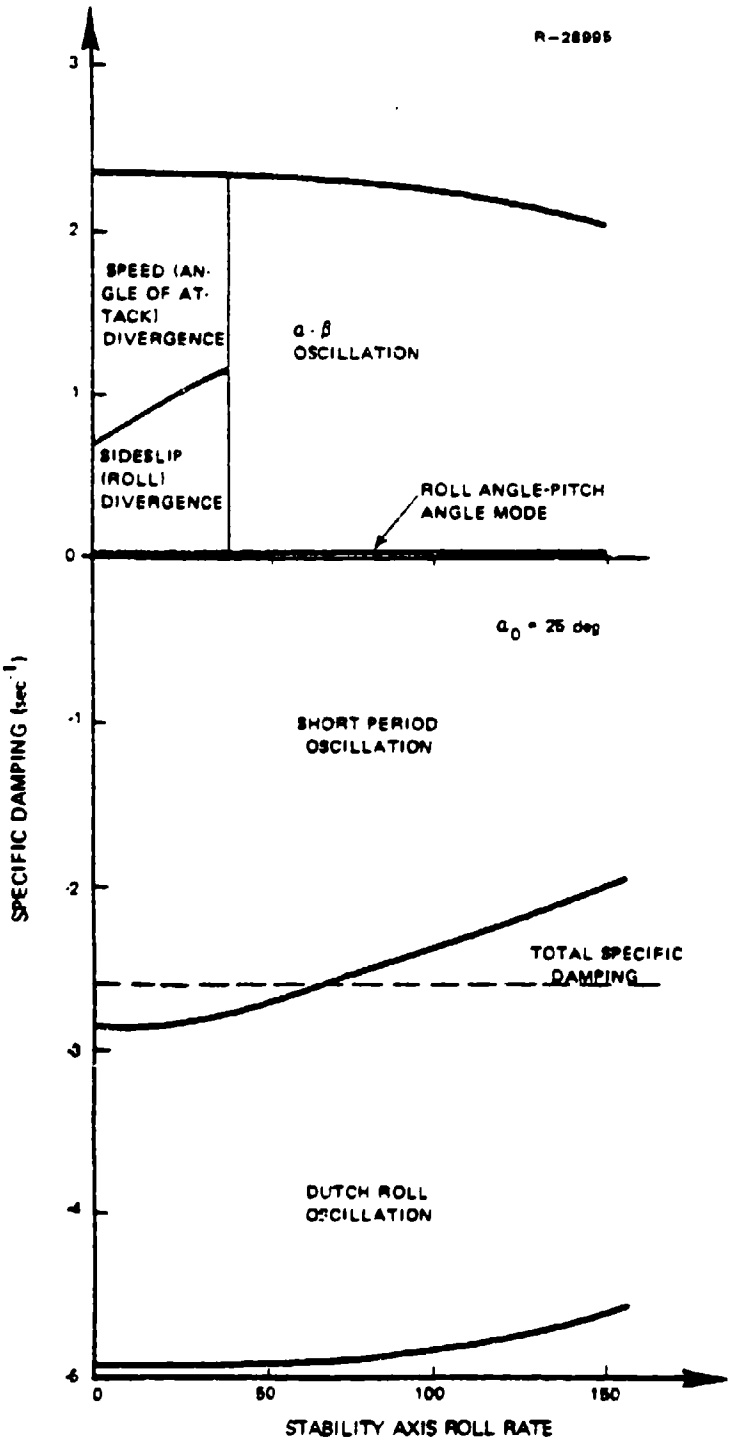

Figure 22 Specific Damping Allocation Variation Due to Roll Rate

allocated among the various modes. There is a drop in short period damping and an increase in Dutch roll damping. The unstable α-β oscillation (formed from the directional and longitudinal divergences at 40 deg/sec roll rate) becomes less unstable as roll rate increases. The total damping (noted by the dotted line) is constant.

2.3.3 Transonic Control Power Variations

Symmetric stabilator and differential stabilator are the major pitch and roll moment control surfaces in the transonic regime, and the rudders supply yaw control. The spoilers and maneuver flaps are disengaged as the wing sweeps aft. The trim plot (Fig. 18) shows that the stabilator retains significant control power at transonic speeds.

The differential stabilator exerts large roll moments throughout the angle of attack range, as shown by Fig. 23. There is a significant amount of adverse yaw, which appears at α = 14 deg. The small α range within which the differential stabilator switches from favorable to adverse yaw indicates that a change in yaw-moment-neutralizing rudder deflection strategy is necessary in the low to mid-α range.

Rudder control power varies with angle of attack as illustrated in Fig. 24. The yaw moment available decreases steadily as α increases, and the roll moment drops as lift increases up to about 14-deg α. The effect reverses through mid-α so that the roll moment due to rudder becomes large in the 25-deg α region.

The interactions between control power and aircraft stability lead to aircraft rudder responses which vary significantly with flight condition. Figure 25 shows the linear

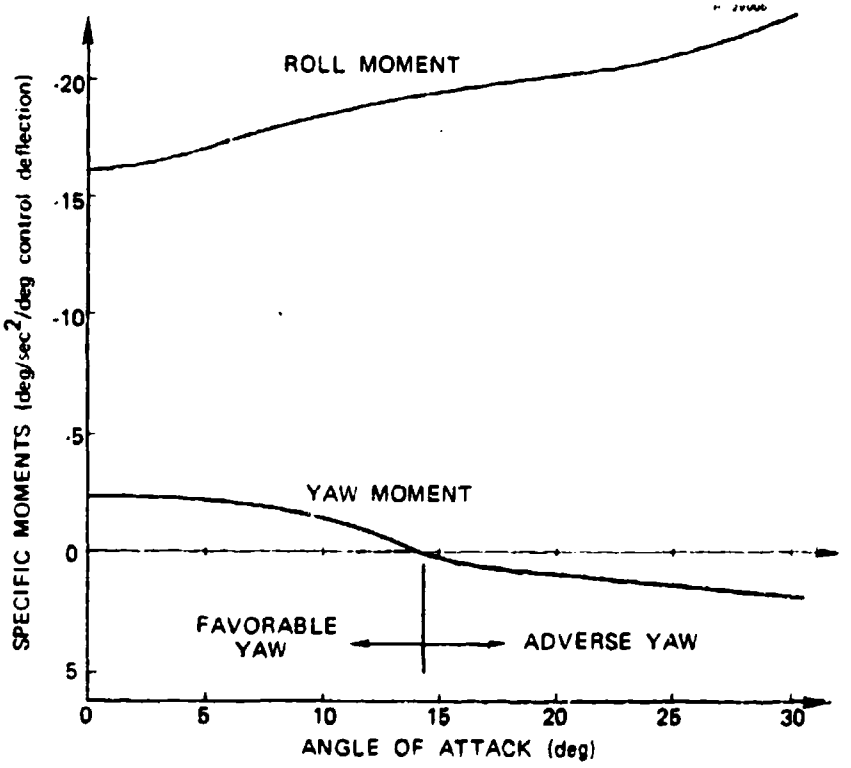

Figure 23 Differential Stabilator Specific Moments (M=0.95)

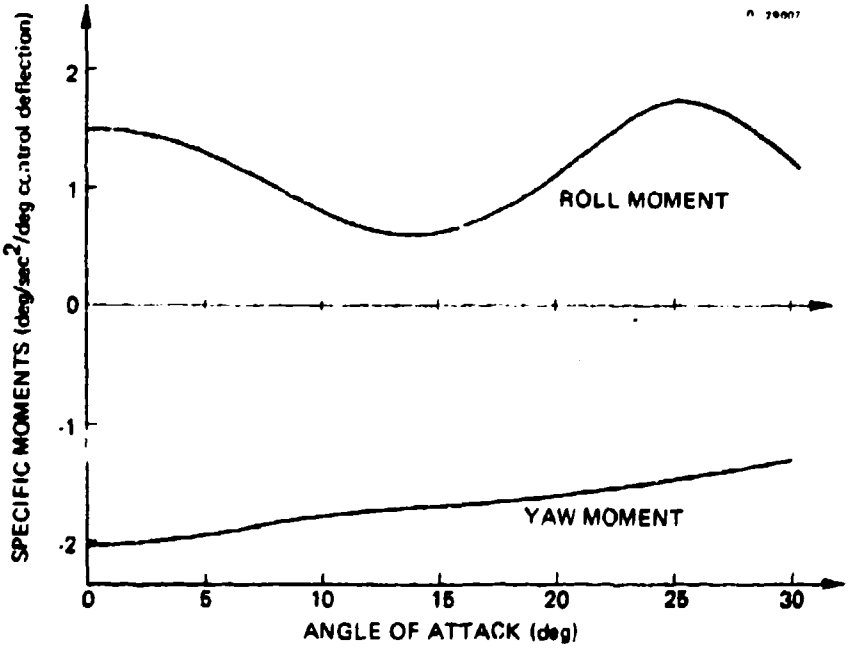

Figure 24 Rudder Specific Moments (M=0.95)

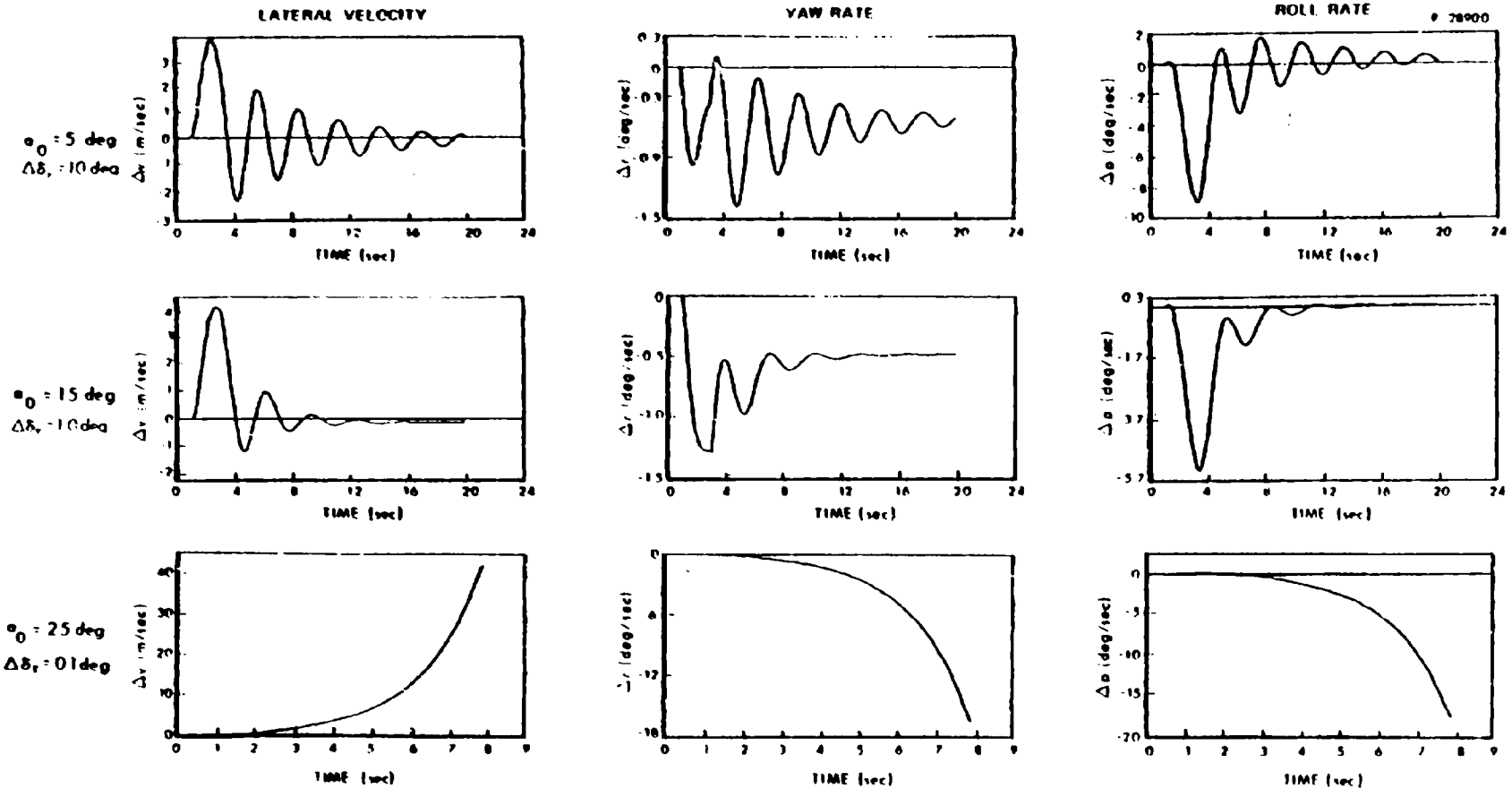

Figure 25 Rudder Response Variations at Different Angles of Attack (M=0.95)

aircraft model response to rudder deflection at three different angles of attack in the transonic regime. At low α, the Dutch roll damping is low, and the response is highly oscillatory. The large amount of rolling motion in the Dutch roll mode, which is typical of fuselage-heavy aircraft, is apparent.

At 15-deg α, the Dutch roll damping is much better, and there is significantly less roll involved in the Dutch roll mode. The damping interchange continues at higher angles of attack, and a sideslip divergence appears. At 25 deg α, the unstable mode dominates the aircraft response.

The control power variations in the transonic regime are smooth, suggesting that stability augmentation logic can readily account for the "open-loop" divergences exhibited by this transonic model.

2.4 SUPERSONIC STABILITY AND CONTROL CHARACTERISTICS

2.4.1 The Supersonic Flight Regime

The central supersonic flight condition (M = 1.55, h = 18,288 m (60,000 ft)) is chosen to have the same dynamic pressure as the subsonic and transonic central flight conditions. The aircraft trim conditions are shown in Fig. 26 for the supersonic regime. The relatively large trim angle of attack reflects the reduced lift slope of the aircraft in this flight regime, and the large trim stabilator angle results from the well-known aft shift of the center of pressure at supersonic velocities. All of these trim effects have a relatively minor effect on the aircraft flying qualities, which are examined next.

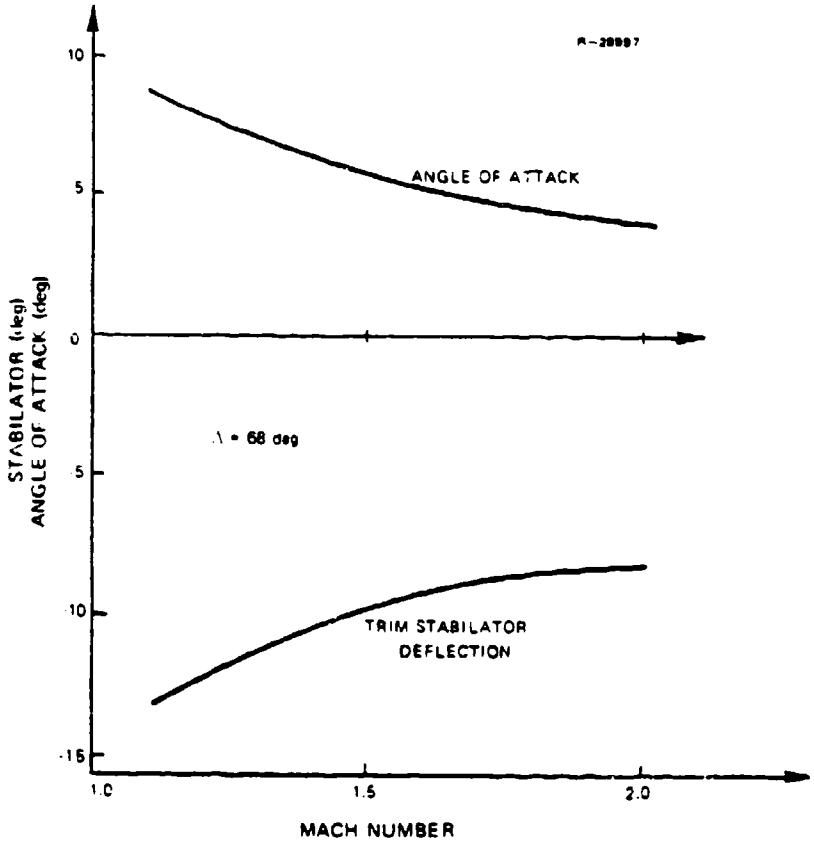

Figure 26 Trim at 18,288 m in 1-g Flight

2.4.2 Supersonic Stability Boundaries

The supersonic regime is characterized by stable (but lightly damped) natural modes. Variations with flight condition (with the usual exception of roll rate effects) are well-behaved and gradual. Figure 27 plots the specific damping (real part) of the lateral modes as a function of flight condition, and the trends are similar to those found at low Mach number. A drop in roll damping occurs in the 10-to-20-deg α region; this is accompanied by an increase in Dutch roll damping. A roll-spiral oscillation is formed at about 18-deg α, and the Dutch roll mode shape at high α exhibits in-phase roll and yaw motion. Thus, the Dutch roll mode appears as a

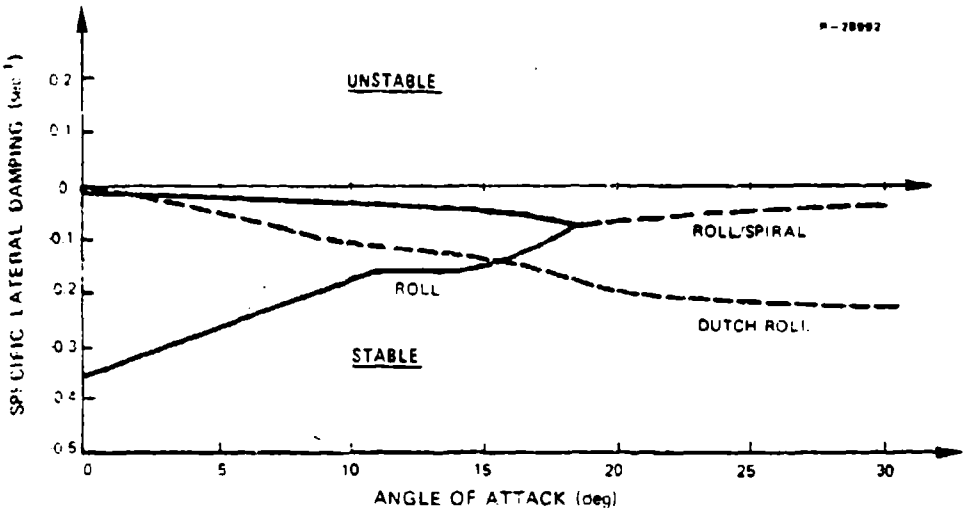

Figure 27 Specific Damping of the Lateral Modes (M=1.55)

rolling oscillation rather than the roll-yaw interchange typical of the low angle-of-attack Dutch roll mode.

Pitch rate has a destabilizing effect on the Dutch roll mode, and this effect is especially large in the supersonic regime. Figure 28 describes this effect. As noted before, large nominal angular rates do not change total aircraft damping, but only reapportion it, and the low level of damping in the supersonic regime accentuates this effect. Relatively low pitch rates lead to a Dutch roll instability in the supersonic regime. An actual pull-up combines both high α and pitch rate, which have opposite effects on the Dutch roll damping in this flight regime.

During a steady roll, it may be difficult to control sideslip accurately. The effects of non-zero sideslip and steady rolling on aircraft stability are of interest, and Fig. 29 illustrates the aircraft stability regions as functions of sideslip and roll rate. Any significant roll rate

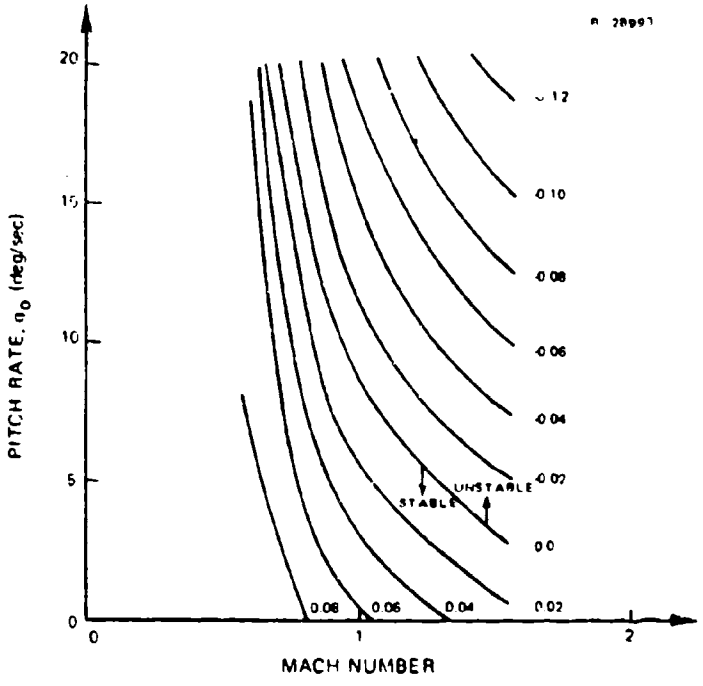

Figure 28 Dutch Roll Damping Ratio (Constant Dynamic Pressure, Low Angle of Attack)

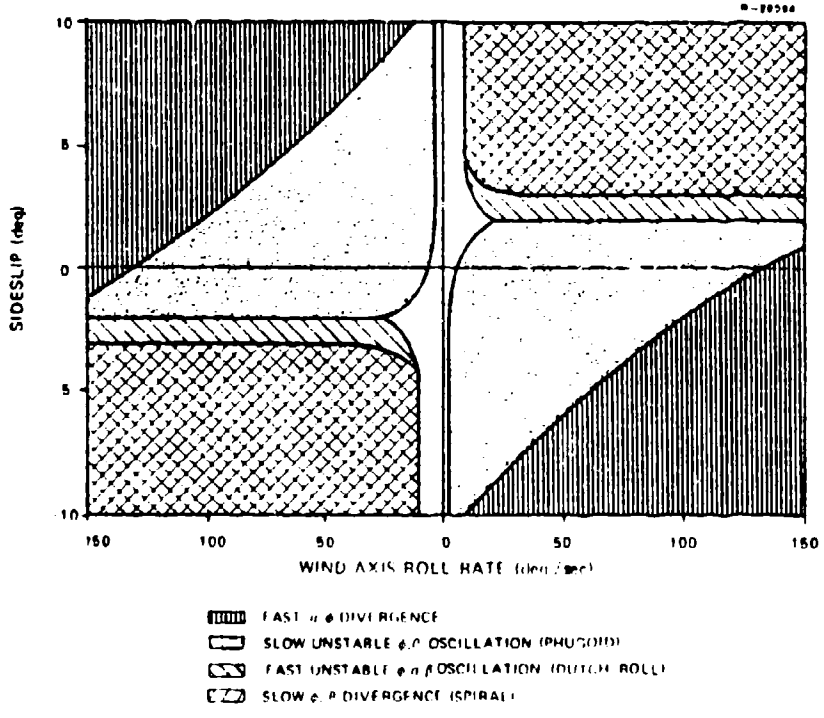

Figure 29 Sideslip - Wind-axis Roll Rate Stability Boundary ($M = 1.55$, $\alpha_o = 5.7$ deg)

leads to a slow, unstable angular oscillation at zero sideslip angle; sideslip out of the roll (roll rate and sideslip of the same sign) causes a fast unstable α-ξ oscillation.

Sideslip into the roll leads to an instability only at high roll rates or large sideslip angles, and the instability takes the form of a fast angular divergence. This root is part of the short period mode, which is decomposed and destabilized by roll rate. In all of these cases, the coupled nominal motion and the complex shape of the instabilities makes accurate control of these modes difficult.

2.4.3 Supersonic Control Capabilities

Reduced stabilator power in pitch is a characteristic of supersonic flight. Figure 30 shows the trim stabilator deflections for various angles of attack in the three Mach regimes. The increased stabilator deflections necessary in supersonic flight are due to the increased pitch stability in this region, which underlines the basic conflict in the longitudinal plane between stability and control effectiveness.

Available control moments tend to decrease with M. The rudder roll and yaw specific moments (Fig. 31) decrease as M increases (as is true in the transonic region), although there is less rudder roll-moment variation with angle of attack for supersonic M. The differential stabilator produces lower rolling moments in the supersonic regime than at lower M (Fig. 32). There is considerable variation in rolling moment in the low-α area. The differential stabilator yaw moment is as large in the supersonic regime as at low M, with the transition to adverse yaw occurring at a higher α, about 19 degrees.

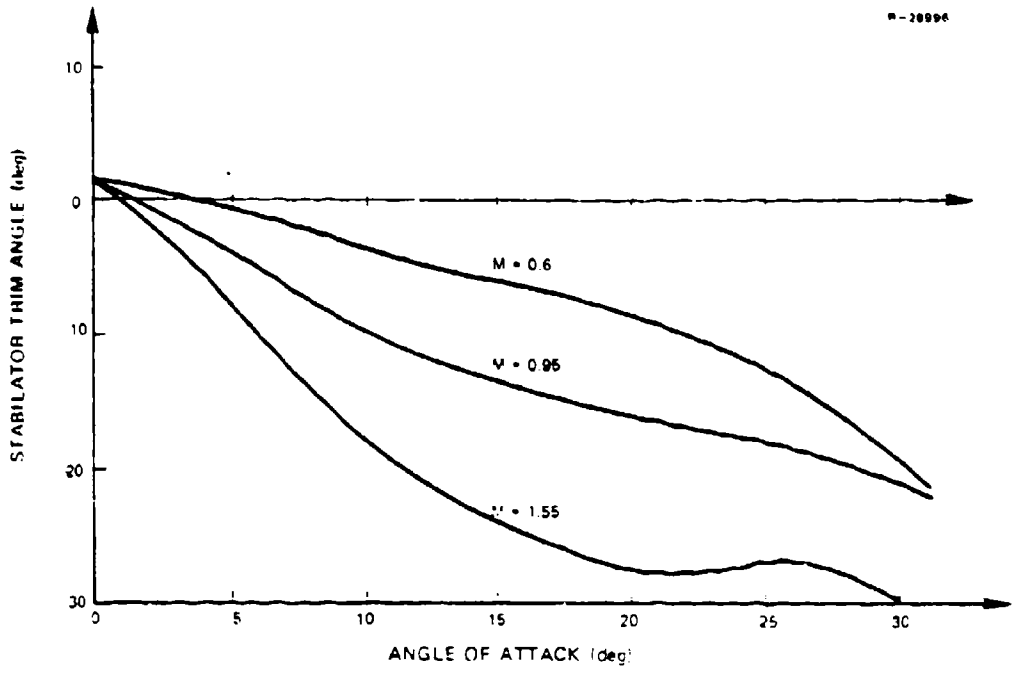

Figure 30 Trim Stabilator Deflection in Three Mach Regimes

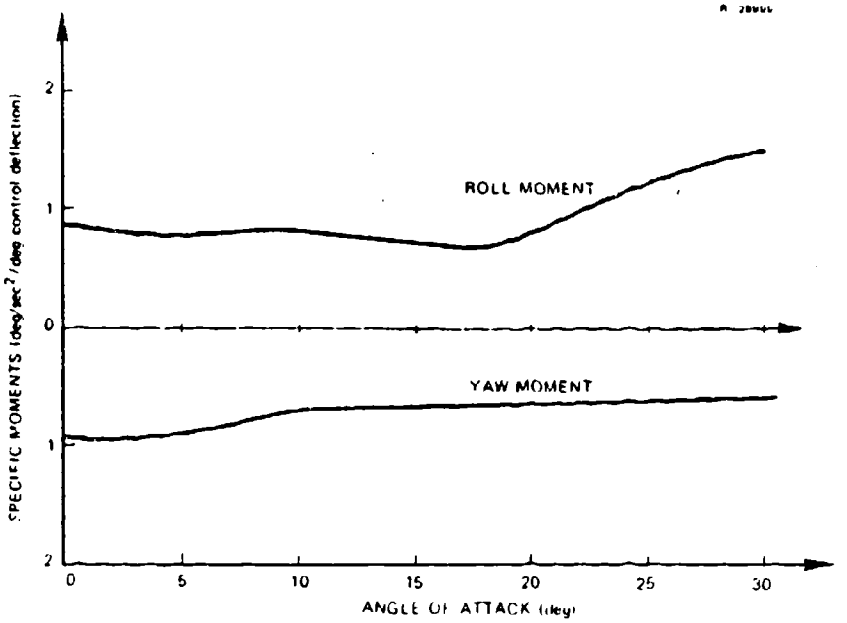

Figure 31 Rudder Specific Moments (M=1.55)

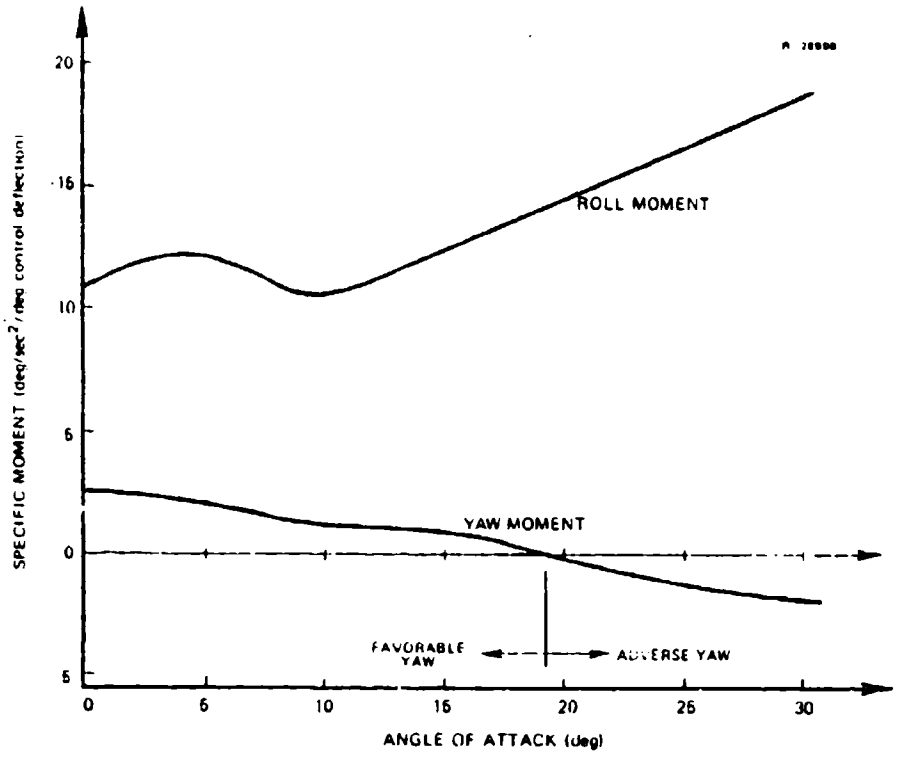

Figure 32 Differential Stabilator Specific Moments (M=1.55)

The airframe response to differential stabilator inputs changes with angle of attack, as shown in Fig. 33. The differential stabilator roll moment relative to the roll damping determines the initial slope of the roll rate response, and the effect of reduced roll damping at 15-deg α relative to 5-deg α) is apparent in the larger roll acceleration. Adverse yaw (apparent in the direction of the yaw rate response at α = 25 deg) excites the Dutch roll mode to such an extent that the net roll effect is reversed; a differential stabilator deflection that caused right-wing-up roll at low α results in net right-wing-down roll at high α.

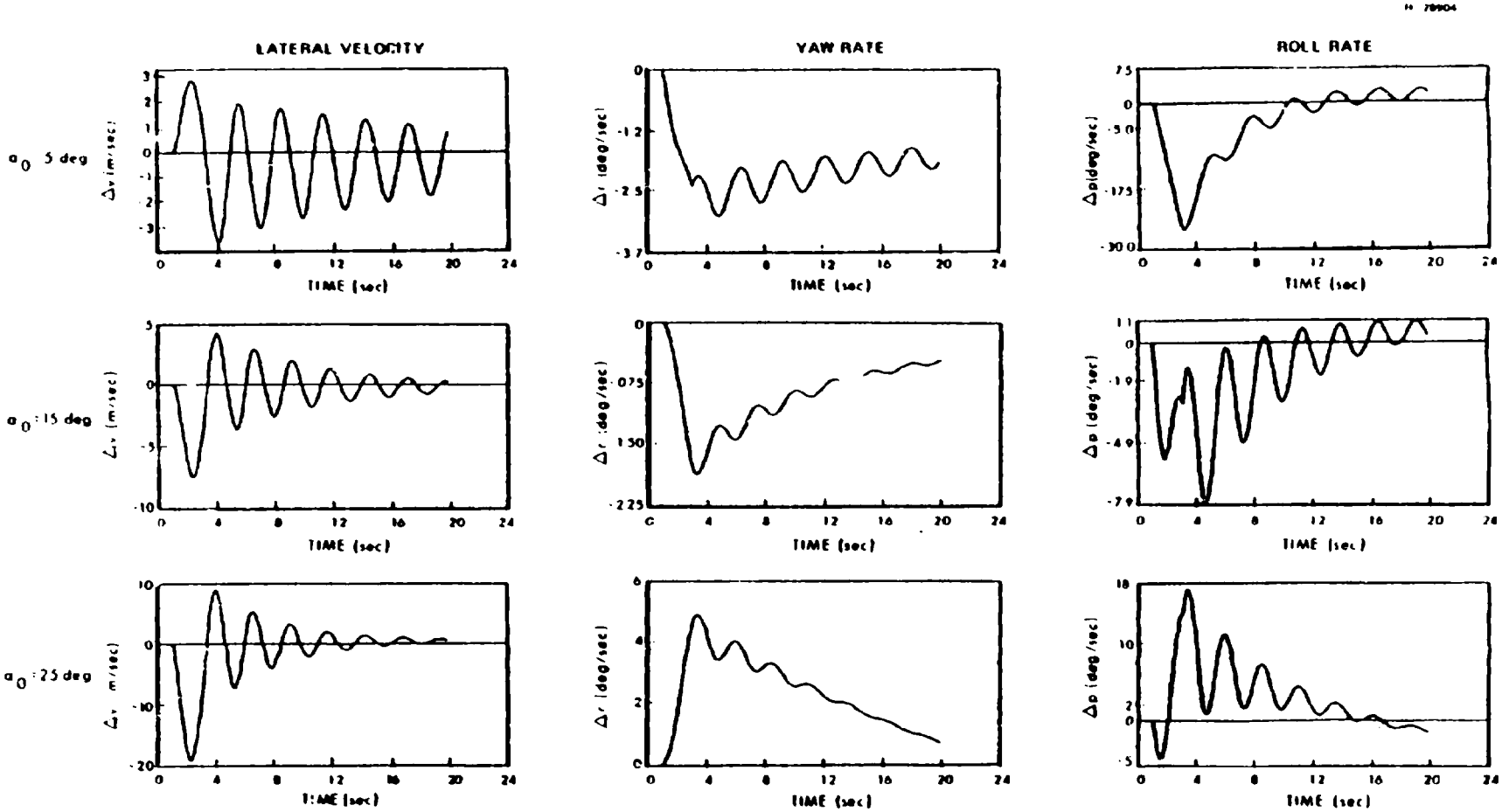

Figure 33 Differential Stabilator Response Variations at Three Angles of Attack (M=1.55, $\Delta\delta_{ds}$=1.0 deg)

The best indicator of the spiral response is the slow movement of the yaw rate remaining at the end of these 20-sec trajectories. At the two lower angles of attack, the spiral mode is real and stable, as confirmed by the approximately exponential decrease in yaw rate. At 25-deg α, the roll and spiral modes have combined into a roll-spiral (lateral phugoid) mode. This very-long-period motion appears in yaw rate as a response which will cross zero yaw-rate at about 23 seconds into this trajectory.

The Dutch roll mode dominates the sideslip (lateral-velocity) response. The sideslip response is adverse at 15-deg α, which is indicative of the adverse wind-axis yaw due to differential stabilator that appears at very low α. The large sideslip response due to differential stabilator at high α is typical of high-performance aircraft. It is this adverse sideslip which is directly tied to the roll reversal. One desirable characteristic of Dutch roll at higher angles of attack is the increased damping ratio, which improves transient response at high α.

Supersonic control power is shown in this section to be significantly reduced from that of the lower Mach numbers. In the longitudinal plane, this combines with increased static stability to result in reduced maximum trim angle of attack. The reduction in lateral control power is generally accompanied by reduced lateral mode damping, so achievable response rates remain high.

2.5 CHAPTER SUMMARY

In this study, the effects of flight condition variation (Mach number, angle of attack and sideslip, and high angular rates) on aircraft stability and control characteristics

are examined. This is achieved by forming complete linear dynamic models at a series of flight conditions and using well-developed and efficient linear analysis techniques on these models. These results depend on the validity of the nonlinear aerodynamic model used in this study (Appendix B).

The Mach effects become important in the high-subsonic regime, and they appear in the transonic area as speed and directional instabilities. In the supersonic regime, longitudinal stability is high and lateral mode damping is low. As Mach number increases, control effectiveness is reduced.

Flight at higher angles of attack (above 15 degrees) results in larger areas of transonic instability and a significant reduction in roll damping, while the Dutch roll mode damping generally improves.

High angular rates do not, in themselves, change the total amount of aircraft specific damping, but simply reapportion it. Steady pitch rate destabilizes the Dutch roll mode, especially in the supersonic regime. Steady rolling causes a transfer of damping from the short period mode to the Dutch roll mode, to the extent that an unstable α-ϕ divergence results at high roll rates. In the transonic regime, low roll rates cause the longitudinal and lateral divergences to combine into an unstable mode in some cases, and rolling can actually stabilize these modes in somewhat different flight conditions. Sideslip in either direction during a rolling maneuver destabilizes this aircraft model.

Differential stabilator produces adverse yaw at moderate to high angles of attack, which can lead to a net roll in the direction opposite to that commanded. At high angles of attack, full rudder deflection may be necessary to neutralize stability-axis yaw due to differential stabilator.

The extra controls available in subsonic flight (maneuvering flaps and spoilers) produce a significant beneficial effect on airframe control response.

3. MATHEMATICAL MODELING OF PILOTING EFFECTS IN MANEUVERING FLIGHT

The research presented in this chapter is directed at providing a better understanding of pilot-vehicle interactions in rapid maneuvers of a high-performance aircraft. Two areas addressed are the identification of adaptation strategies which experienced pilots may pursue in stabilizing the lateral-directional dynamics of an aircraft and the effect which pilot control adaptation has on aircraft tracking performance. Lateral-directional piloting tasks are particularly well-suited for studying stability and performance characteristics of the pilot-aircraft system because lateral-directional motions often are the most difficult to control (Refs. 4 and 5).

An important objective of this study is to provide insights regarding the design of future flight control systems. The control system can alleviate pilot workload by increasing aircraft stability and commanding control surfaces in response to pilot stick and pedal motions. The pilot analysis procedure presented here identifies regions of high pilot workload in a typical aircraft maneuver, thus indicating where and what type of control compensation could best aid the pilot. Furthermore, control system designs can be incorporated directly into the analysis procedure for a direct verification of their beneficial effects on pilot-aircraft stability.

The analysis of pilot-aircraft motions during maneuvers is accomplished by employing a control-theoretic pilot model, which is introduced in the first part of this chapter.

The pilot model can predict pilot behavior in realistic multi-input, multi-output aircraft tasks. The pilot model assumptions and the significance of pilot model parameters are discussed. The chapter continues by describing the construction of pilot-aircraft stability and performance diagrams, which are based upon the mathematical models of the pilot and the aircraft. These diagrams are primary tools for expressing results in this chapter.

The second part of the chapter presents these diagrams for a wind-up turn maneuver. The analysis proves to be fruitful in predicting pilot-aircraft stability regions under different control mechanization assumptions. The results tend to substantiate high-α pilot-aircraft behavior known to occur in high-performance aircraft. Such behavior includes the detrimental effects of adverse yaw caused by differential stabilators or ailerons, the stable nature of rudder control, the improved tracking performance available when both stick and pedals are used in a coordinated fashion, and the enhanced capabilities afforded by an aileron-rudder interconnect (ARI) system. The work is an extension of Ref. 2, which assumed that the pilot fixed his strategy at a single flight condition.

3.1 OPTIMAL CONTROL PILOT MODEL

This section briefly reviews the important elements of the optimal control model of the pilot. The model is linear and time-invariant, and it easily represents multi-input/multi-output control tasks, an important requirement for the aircraft application. The optimal control pilot model has been verified empirically (Refs. 6 to 11), and it has been refined for application to demanding control tasks (Refs. 12 to 14). Reference 15 presents an application to air combat maneuvering.

The basic pilot model assumptions are shown in Table 1. At a particular point along a maneuver, the aircraft dynamics are represented as a linear, time-invariant system. The n-vector, $\Delta\underline{x}(t)$, represents the perturbation aircraft states in body axes. The aircraft's stick and pedal inputs are represented by the m-vector, $\Delta\underline{u}(t)$; $\Gamma\Delta\underline{w}(t)$ models the aircraft's disturbance inputs (e.g., turbulence) as white gaussian noise.

TABLE 1 PILOT MODEL ASSUMPTIONS

T-1083

AIRCRAFT PERTURBATION STATE DYNAMICS	$\Delta\dot{\underline{x}}(t) = F\,\Delta\underline{x}(t) + G\,\Delta\underline{u}(t) + \Gamma\Delta\underline{w}(t)$
PILOT OBSERVATIONS	$\Delta\underline{y}(t) = [H \quad D]\begin{bmatrix}\Delta\underline{x}(t-\tau)\\ \Delta\underline{u}\ t-\tau)\end{bmatrix} + \Delta\underline{v}_y(t-\tau)$
PILOT COST FUNCTION	$J = E\left\{\lim_{T\to\infty}\int_0^T\left(\begin{bmatrix}\Delta\underline{x}^T\Delta\underline{u}^T\end{bmatrix} Q_C\begin{bmatrix}\Delta\underline{x}\\ \Delta\underline{u}\end{bmatrix} + \Delta\dot{\underline{u}}^T R_C\Delta\dot{\underline{u}}\right)dt\right\}$
PILOT NEUROMUSCULAR DYNAMICS	$\Delta\dot{\underline{u}}(t) = -R_L\Delta\underline{u}(t) + \Delta\underline{u}_c(t) + \Delta\underline{v}_u(t)$
PILOT NEUROMUSCULAR LAG	$R_L = \begin{bmatrix}\frac{1}{\tau_{n_1}} & 0 \ldots 0\\ 0 & \frac{1}{\tau_{n_2}} \quad \ddots\\ \vdots & \ddots \quad \frac{1}{\tau_{n_m}}\\ 0 & \ldots\end{bmatrix}$

The pilot is assumed to manipulate the aircraft controls to counteract the disturbances. The pilot's observations consist of rotational and translational perturbation positions, velocities, and accelerations, represented as a linear combination of states and controls. Perceptual observation noise,

$\Delta \underline{v}_y(t)$, is added to the observations, which are delayed by the perceptual time delay, τ. The pilot is assumed to formulate a control strategy (based on the observations) which minimizes a quadratic cost function of general form. This cost function weights combinations of perturbation state and control positions as well as control rates. Weighting the control rate causes the control solution to take the form required to model neuromuscular dynamics. The (m×m) neuromuscular dynamics matrix, R_L, is diagonal, with individual elements representing the inverse of human limb neuromotor time constants. The neuromuscular dynamics are driven by the pilot's internal control commands, $\Delta \underline{u}_c(t)$, and by neuromotor noise represented as the white gaussian m-vector, $\Delta \underline{v}_u(t)$.

The solution of the optimal control pilot model is shown in Table 2. The pilot's delayed observations are processed by a Kalman filter which generates the pilot's best estimate of the delayed states and controls. The pilot model counteracts the perception delay by predicting the current states and controls from the observations and estimates. The predicted state estimate and the feedback gain matrix, C, are used to formulate the internal control commands. The two algebraic Riccati equations shown in Table 2 must be solved to generate the pilot model gains. Each Riccati equation contains design parameters (in the form of weighting matrices) and must satisfy certain constraints. For the control Riccati equation, the state weighting matrix, Q_C, and the neuromuscular lag matrix, R_L, are known, while the control rate weighting matrix, R_C, must be adjusted to satisfy the neuromuscular constraints. For the estimator Riccati equation, the disturbance noise covariance, Q_E, is known, while the neuromotor noise covariance, V_u, and the observation noise covariance, V_y, must satisfy the requirements shown in Table 3.

TABLE 2 PILOT MODEL SOLUTION

T-1084

PILOT CONTROL	$\Delta \underline{u}_c(t) = C\, \Delta \underline{\hat{x}}_p(t)$
CONTROL GAIN MATRIX	$\begin{bmatrix} C & -R_L \end{bmatrix} = -R_c \begin{bmatrix} 0 & I \end{bmatrix} P_c$
ALGEBRAIC RICCATI EQUATION FOR OPTIMAL CONTROL LAW	$P_c \begin{bmatrix} F & G \\ 0 & 0 \end{bmatrix} + \begin{bmatrix} F^T & 0 \\ G^T & 0 \end{bmatrix} P_c + Q_c - P_c \begin{bmatrix} 0 & 0 \\ 0 & R_c^{-1} \end{bmatrix} P_c = 0$
PILOT KALMAN FILTER	$\begin{bmatrix} \Delta \dot{\underline{\hat{x}}}(t-\tau) \\ \Delta \dot{\underline{\hat{u}}}(t-\tau) \end{bmatrix} = \begin{bmatrix} F & G \\ 0 & -R_L \end{bmatrix} \begin{bmatrix} \Delta \underline{\hat{x}}(t-\tau) \\ \Delta \underline{\hat{u}}(t-\tau) \end{bmatrix} + \begin{bmatrix} 0 \\ I \end{bmatrix} C\, \Delta \underline{\hat{x}}_p(t-\tau)$ $+ K \left[\Delta \underline{y}(t) - [H \; D] \begin{bmatrix} \Delta \underline{\hat{x}}(t-\tau) \\ \Delta \underline{\hat{u}}(t-\tau) \end{bmatrix} \right]$
PILOT PREDICTOR	$\begin{bmatrix} \Delta \dot{\underline{\hat{x}}}_p(t) \\ \Delta \dot{\underline{\hat{u}}}_p(t) \end{bmatrix} = \begin{bmatrix} F & G \\ C & -R_L \end{bmatrix} \begin{bmatrix} \Delta \underline{\hat{x}}_p(t) \\ \Delta \underline{\hat{u}}_p(t) \end{bmatrix} + e^{\begin{bmatrix} F & G \\ 0 & -R_L \end{bmatrix} \tau} K \left[\Delta \underline{y}(t) - [H \; D] \begin{bmatrix} \Delta \underline{\hat{x}}(t-\tau) \\ \Delta \underline{\hat{u}}(t-\tau) \end{bmatrix} \right]$
KALMAN FILTER GAIN MATRIX	$K = P_E \begin{bmatrix} H^T \\ D^T \end{bmatrix} V_y^{-1}$
ALGEBRAIC RICCATI EQUATION FOR ESTIMATION ERROR COVARIANCE MATRIX	$P_E \begin{bmatrix} F^T & 0 \\ G^T & -R_L \end{bmatrix} + \begin{bmatrix} F & G \\ 0 & -R_L \end{bmatrix} P_E + \begin{bmatrix} Q_\xi & 0 \\ 0 & V_u \end{bmatrix} - P_E \begin{bmatrix} H^T \\ D^T \end{bmatrix} V_y^{-1} [H \; D]\, P_E = 0$

The pilot's observation noise scales with the covariance of the states and controls, while the neuromotor noise scales with the covariance of the pilot's internal control commands. The scalar, P_{y_i}, is the pilot's noise-to-signal ratio for the i^{th} observation. P_{u_i} is the pilot's noise-to-signal ratio for the i^{th} control. The scaling property has been validated for low-order systems and scalar

TABLE 3 PILOT MODEL COVARIANCE EXPRESSIONS

T-1085

PILOT OBSERVATION NOISE COVARIANCE	$E\left\{\Delta\underline{v}_y(t)\,\Delta\underline{v}_y^T(\sigma)\right\} = V_y\delta(t-\sigma)$ $(V_y)_{ii} = P_{y_i}\left([H\ D]\,X\begin{bmatrix}H^T\\D^T\end{bmatrix}\right)_{ii} \quad i = 1 \ldots \ell$
PILOT NEUROMOTOR NOISE COVARIANCE	$E\left\{\Delta\underline{v}_u(t)\,\Delta\underline{v}_u^T(\sigma)\right\} = V_u\delta(t-\sigma)$ $(V_u)_{ii} = P_{u_i}\left(R_L[C\ O]\,Y\begin{bmatrix}C^T\\O\end{bmatrix}R_L^T\right)_{ii} \quad i = 1 \ldots m$
PILOT PREDICTION ERROR COVARIANCE	$\begin{bmatrix}\Delta\tilde{\underline{x}}_p(t)\\ \Delta\tilde{\underline{u}}_p(t)\end{bmatrix} = \begin{bmatrix}\Delta\underline{x}(t) - \Delta\hat{\underline{x}}_p(t)\\ \Delta\underline{u}(t) - \Delta\hat{\underline{u}}_p(t)\end{bmatrix}$ $E\left\{\begin{bmatrix}\Delta\tilde{\underline{x}}_p(t)\\ \Delta\tilde{\underline{u}}_p(t)\end{bmatrix}\begin{bmatrix}\Delta\tilde{\underline{x}}_p^T(\sigma)\ \Delta\tilde{\underline{u}}_p^T(\sigma)\end{bmatrix}\right\} = Z\,\delta(t-\sigma)$ $Z = e^{\begin{bmatrix}F & G\\ O & -R_L\end{bmatrix}\tau}P_E e^{\begin{bmatrix}F & G\\ O & -R_L\end{bmatrix}^T\tau} + \int_0^\tau\left(e^{\begin{bmatrix}F & G\\ O & -R_L\end{bmatrix}s}\begin{bmatrix}Q_{\underline{E}} & O\\ O & V_u\end{bmatrix}e^{\begin{bmatrix}F & G\\ O & -R_L\end{bmatrix}^T s}\right)ds$
COVARIANCE OF PILOT PREDICTED STATE	$E\left\{\begin{bmatrix}\Delta\hat{\underline{x}}_p(t)\\ \Delta\hat{\underline{u}}_p(t)\end{bmatrix}\begin{bmatrix}\Delta\hat{\underline{x}}_p^T(\sigma)\ \Delta\hat{\underline{u}}_p^T(\sigma)\end{bmatrix}\right\} = Y\,\delta(t-\sigma)$ $Y = \int_0^\infty\left\{e^{\begin{bmatrix}F & G\\ C & -R_L\end{bmatrix}s}e^{\begin{bmatrix}F & G\\ O & -R_L\end{bmatrix}\tau}P_E\begin{bmatrix}H^T\\D^T\end{bmatrix}V_y^{-1}[H\ D]\,P_E\,e^{\begin{bmatrix}F & G\\ O & -R_L\end{bmatrix}^T\tau}e^{\begin{bmatrix}F & G\\ C & -R_L\end{bmatrix}^T s}\right\}ds$
COVARIANCE OF PERTURBATION STATES AND CONTROLS	$E\left\{\begin{bmatrix}\Delta\underline{x}(t)\\ \Delta\underline{u}(t)\end{bmatrix}\begin{bmatrix}\Delta\underline{x}^T(t)\ \Delta\underline{u}^T(t)\end{bmatrix}\right\} = X\,\delta(t-\tau)$ $X = Z + Y$

controls. Unfortunately, the use of the noise-to-signal ratio destroys the separability property of the estimation and control processes. If the control law is unstable, the estimator does not exist. The dependence of the estimator solution on the control solution is advantageously exploited in examining the pilot's adaptive behavior (Section 3.2.2). The closed-form expressions for covariances used in formulating and analyzing the pilot model are shown in Table 3.

A summary of key parameters of the pilot model is shown in Table 4. To construct a model for a given aircraft system, P_y, P_u, τ, R_L, H, D, and Q_C must be specified. All of these variables except Q_C have been measured experimentally, and ranges of their values can be found in the literature. The pilot model solutions obtained in the present study are not very sensitive to the choice of Q_C, and the values used here are presented in Section 3.2.2.

If the pure time delay is replaced by a first-order Padé approximation, the prediction equations in the pilot model can be eliminated (Fig. 34). The pilot's observations are degraded by noise, then passed through a lead-lag network representing the Padé approximation. The resulting signal is processed by a Kalman filter which generates a best estimate of the states, controls, and lagged observation states. The state estimates are multiplied by the feedback matrix, C, to form the pilot's internal control command. The gain matrix, C, in the pure time delay and Padé approximation pilot models are the same.

The Riccati equations shown in Table 2 for the optimal control pilot model can be solved using the closed-form covariance expressions in Table 3 and the pilot model control gain expression in Table 2. The controller Riccati equation

TABLE 4 DESCRIPTION OF THE OPTIMAL CONTROL MODEL PARAMETERS

T-1086

EQUATION PARAMETERS		RELATION TO PILOT PERFORMANCE
$\Delta\underline{x}$	Aircraft motion variables	Pilot must observe this well enough to command aircraft and to provide stability.
$\Delta\underline{u}$	Aircraft control variables	Pilot must use this to command aircraft and to provide stability. In some instances, he must be able to observe $\Delta\underline{u}$ as well.
F	Aircraft dynamics (stability derivatives and inertial coupling)	Aircraft must be stable enough for pilot to control, subject to normal human capabilities.
G	Aircraft control effects (sensitivity to control deflections)	Aircraft must respond to external commands in a way which the pilot can understand.
H	Motion variable display selection and transformation	Motion cues must be sufficient for command and stabilization.
D	Control variable display selection and transformation	Acceleration cues infer control observation.
$\left[\Delta\underline{\hat{x}}^T(t-\tau)\ \Delta\underline{\hat{u}}^T(t-\tau)\right]$	Delay motion and control variables estimated by pilot	Estimates of motion variables must be accurate enough to provide effective closed-loop control.
$\left[\Delta\underline{\hat{x}}_p^T(t), \Delta\underline{\hat{u}}_p^T(t)\right]$	Predicted motion and control variables estimated by pilot	
$\begin{bmatrix} F & G \\ 0 & -R_L \end{bmatrix}$	Dynamic model assumed (i.e., "learned") by the pilot, including neuromuscular lags	The better the pilot's knowledge of the aircraft and his own capabilities, the better he can cope with noisy measurements.
K	Estimation gains which weight the difference between the pilot's observations and his prediction of pilot-aircraft response.	Less knowledge of the aircraft as well as less noise in the pilot's observation of cues leads to higher K and more reliance on observed motions.
$\Delta\underline{y}_y(t)$	Pilot induced noise in observation	Noise in observations has direct effect on estimation performance of the pilot.
C	Control gains which transform pilot's estimates of aircraft motions to control actions	Pilot attempts to tradeoff aircraft motions with available control "power." Improper control strategy could degrade command response and destabilize the system.
R_L	Neuromuscular Lags	Neuromuscular system smooths pilot outputs and could prevent pilot from stabilizing a fast instability.
$\Delta\underline{u}_c$	Pilot internal control commands	Result of conscious effort to provide "best" control.
R_C	Weighting matrix for control output rates	R_C must be varied to match neuromotor dynamics (R_L). Value of R_C is strongly affected by aircraft control effects (G). In practice, R_L and G have a large effect on determining C.
Q_C	Weighting matrix for motion and control perturbations	Allows relative importance (to the pilot) of precise tracking of individual motions to be specified. Allows effects of limited control "throw" to be specified. In practice, has limited effect on C, due to restrictions on R_C.
Q_E	Covariance matrix of disturbance inputs (e.g., turbulence) and uncertainties in system dynamics	Large values increase importance of observations, increasing K.
V_y	Covariance matrix of observation noise	Large values decrease accuracy of observations, decreasing K
P_y	Observation noise to signal ratio	Observation noise is proportional to the covariance of $\Delta\underline{y}$
V_u	Covariance matrix of neuromotor noise	Large values indicate pilot is having difficulties controling aircraft.
P_u	Neuromotor noise to signal ratio	Neuromotor noise is proportional to the covariance of $\Delta\underline{u}_c$

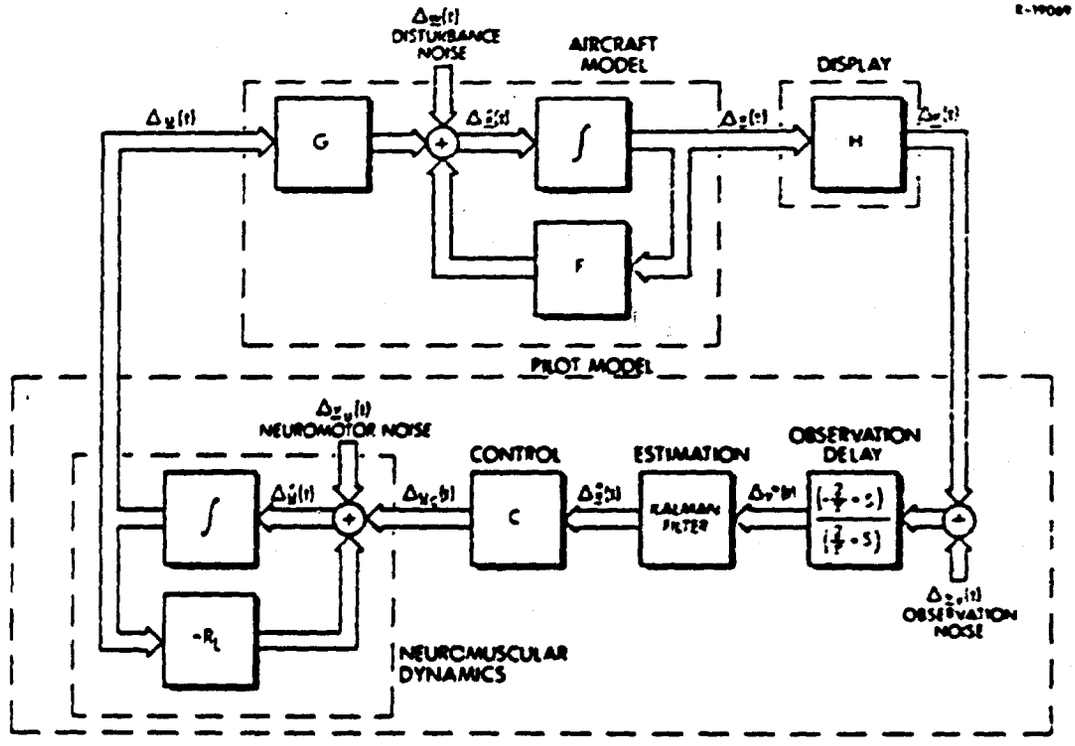

Figure 34 Block Diagram of the Pilot Model Containing the Padé Approximation to Pure Time Delay

and estimator Riccati equation algorithms were developed in the previous year's work (Ref. 2).

3.2 FUNDAMENTAL ASPECTS OF PILOT-AIRCRAFT INTERACTIONS

This section describes the procedure for analyzing pilot-aircraft interactions using the optimal control pilot model. In the first part, pilot-aircraft instabilities caused by inherent physical limitations of the pilot are compared with existence properties of the pilot model. These limitations can arise either through an inability to estimate the state properly or an inability to control the aircraft. For the cases considered, the aircraft must be unstable for

algorithm divergence to occur. The pilot also could actively destablize a stable aircraft by failing to adapt his control strategy to a changing flight condition.

3.2.1 Relationships Between the Critical Tracking Task and Existence of the Pilot Model

Divergence of tne pilot model algorithms may be an important indicator of a real pilot's ability to control his aircraft during maneuvering flight. The results which follow show that human pilots and optimal control pilot models have difficulties controlling a system in similar situations, and the pilot model parameters which cause the instability in the model are plausible reasons for human instability during actual flight. The optimal control pilot model fails to exist when the Riccati equations do not have finite, positive-definite solutions. An explicit example of Riccati equation divergence for a scalar system is discussed in Ref. 2.

As mentioned above, the pilot-model may fail to exist either because an estimation law cannot be defined or because a control law cannot be formulated. In the first case, the pilot could have inadequate information on which to base his estimate because his observation noise-to-signal ratio is too high. In the second case, the pilot cannot maintain effective control because the aircraft is unstable and his neuromuscular lag is too great.

Pilot model estimator and controller divergence is examined by using the results contained in Refs. 16 and 17 for comparison. One of the objectives in the two references is to determine at what system time constant a human subject could not control an unstable first-order system. The dynamic characteristics which cause the human subject to lose control

define the experimental critical system. In Ref. 16, changes in the experimental critical system of the human are investigated by changing the display format. In Ref. 17, the display format is not changed, but the system dynamics are made increasingly complex by placing integrators between the output of the first-order system and the display.

Some of the critical systems that have been determined experimentally (Refs. 16 and 17) are shown in Table 5. As the display format changed from aural to visual then to aural and visual combined, the unstable critical system time constant increases. Better displays make it easier for the subject to exercise control; hence, they make it possible for increasingly unstable systems to be stabilized by manual control.

TABLE 5 COMPARISON BETWEEN HUMAN AND PILOT MODEL INSTABILITIES

T-1220

OBSERVATION	CRITICAL SYSTEM	NEUROMOTOR TIME CONSTANT, τ_n (sec)	TIME DELAY, τ (sec)	CONSTANT NEUROMOTOR NOISE COVARIANCE, V_u (sec^{-2})	P_y AT ESTIMATOR ALGORITHM INSTABILITY
Aural (Ref. 16)	$\frac{1}{1-0.222s}$	0.08	0.15	0.01	0.00605 π (-22.2 dB)
Aural (Ref. 16)	$\frac{1}{1-0.222s}$	0.08	0.15	0.001	0.00605 π (-22.2 dB)
Aural (Ref. 16)	$\frac{1}{1-0.222s}$	0.08	0.15	0.0025	0.00605 π (-22.2 dB)
Aural (Ref. 16)	$\frac{1}{1-0.222s}$	0.08	0.15	0 0025	0.00382 π (-24.2 dB)
Visual (Ref. 16 and Ref. 17)	$\frac{1}{1-0.164s}$	0.08	0.15	0.0025	0.00223 π (-26.5 dB)
Visual (Ref. 17)	$\frac{1}{s(1-0.25s)}$	0.08	0.15	0.0025	0.00255 π (-26 dB)
Visual and Aural (Ref. 16)	$\frac{1}{1-0.152s}$	0.08	0.15	0.0025	(System Is Uncontrollable)

Pilot model critical systems occur when model algorithm divergence is induced. The pilot model parameters at the algorithm stability boundary can be called critical parameters. The analogy of a changing display format for the pilot is a changing observation noise-to-signal ratio, P_y, for the pilot model. The critical value of P_y at the algorithm stability boundary must decrease as the experimental critical system becomes more unstable. Furthermore, values of the critical value of P_y should be less than typical human values (-20 dB). To see how the critical value of P_y varies with the experimental critical systems, the pilot model is constructed.

For a first-order system

$$\Delta\dot{x}(t) = \frac{1}{\tau_s}\Delta x(t) + g\,\Delta u(t)$$

with the pilot model cost function

$$J = \int_0^\infty \left[q_c \Delta x^2(t) + r_c \Delta\dot{u}^2(t)\right] dt$$

the optimal control pilot model takes the following form:

$$\begin{bmatrix}\Delta\dot{x}(t)\\ \Delta\dot{u}(t)\end{bmatrix} = \begin{bmatrix}\frac{1}{\tau_s} & g\\ 0 & \frac{1}{\tau_n}\end{bmatrix}\begin{bmatrix}\Delta x(t)\\ \Delta u(t)\end{bmatrix} + \begin{bmatrix}0\\ 1\end{bmatrix}\left[-\frac{1}{2g\tau_n^2}\Delta\hat{x}_p(t) + \Delta v_u(t)\right]$$

$$\begin{bmatrix} \Delta\dot{\hat{x}}_p(t) \\ \Delta\dot{\hat{u}}_p(t) \end{bmatrix} = \begin{bmatrix} \frac{1}{\tau_s} & g \\ -\frac{1}{2g\tau_n^2} & -\frac{1}{\tau_n} \end{bmatrix} \begin{bmatrix} \Delta\hat{x}_p(t) \\ \Delta\hat{u}_p(t) \end{bmatrix}$$

$$+ e^{\begin{bmatrix} \frac{1}{\tau_s} & g \\ 0 & -\frac{1}{\tau_n} \end{bmatrix}} \begin{bmatrix} k_1 & k_2 \\ k_3 & k_4 \end{bmatrix} \left\{ \begin{bmatrix} \Delta x(t-\tau)+\Delta v_x(t-\tau) \\ \Delta\dot{x}(t-\tau)+\Delta v_{\dot{x}}(t-\tau) \end{bmatrix} - \begin{bmatrix} 1 & 0 \\ \frac{1}{\tau_s} & g \end{bmatrix} \begin{bmatrix} \Delta\hat{x}(t-\tau) \\ \Delta\hat{u}(t-\tau) \end{bmatrix} \right\}$$

$$\begin{bmatrix} \Delta\dot{\hat{x}}(t-\tau) \\ \Delta\dot{\hat{u}}(t-\tau) \end{bmatrix} = \begin{bmatrix} \frac{1}{\tau_s} & g \\ 0 & -\frac{1}{\tau_n} \end{bmatrix} \begin{bmatrix} \Delta\hat{x}(t-\tau) \\ \Delta\hat{u}(t-\tau) \end{bmatrix} + \begin{bmatrix} 0 \\ 1 \end{bmatrix} \left[-\frac{1}{2g\tau_n^2} \Delta\hat{x}_p(t-\tau) \right]$$

$$+ \begin{bmatrix} k_1 & k_2 \\ k_3 & k_4 \end{bmatrix} \left\{ \begin{bmatrix} \Delta x(t-\tau)+\Delta v_x(t-\tau) \\ \Delta\dot{x}(t-\tau)+\Delta v_{\dot{x}}(t-\tau) \end{bmatrix} - \begin{bmatrix} 1 & 0 \\ \frac{1}{\tau_s} & g \end{bmatrix} \begin{bmatrix} \Delta\hat{x}(t-\tau) \\ \Delta\hat{u}(t-\tau) \end{bmatrix} \right\}$$

The equations are based on Table 2, with the subject observing $\Delta x(t)$ and $\Delta\dot{x}(t)$. The pilot model gain of $-1/2g\tau_n^2$ (taken from Ref. 2) does not depend on the value of q_c in the cost function. In the corresponding experiments, no external disturbance noise purposely disturbed the system, so it is assumed that residual neuromotor noise, $\Delta\underline{v}_u(t)$, is the signal source in the equivalent pilot model. A <u>constant</u> value for neuromotor noise covariance, V_u, is used in the analysis.

The impact of the constant V_u assumption is shown in the first three rows of Table 5 using the aural display case. Beginning with the critical system, the observation noise-to-signal ratio, P_y, is gradually increased until estimator algorithm divergence occurs. The different values of V_u did

not change the critical value of P_y at algorithmic instability, indicating that the residual constant V_u assumption is valid. The effect of increasing the time delay in the pilot model is shown in the fourth row in Table 5. As expected, the noise-to-signal ratio must decrease, i.e., the human must perceive the signal more clearly, to produce the same critical system with an increased time delay. The effect of decreasing the critical system time constant with a visual display is shown in the fifth row of Table 5. The decrease in the value of P_y for algorithm instability is exactly the result needed to confirm the relationship between human critical systems and pilot model critical parameters. Further confirmation is shown in the sixth row, where adjoining an integrator changes the pilot's critical system time constant considerably but has little effect on the critical P_y for the pilot model, as expected. This also confirms a common optimal control pilot model assumption that P_y is relatively insensitive to plant variations.

In the first six rows of Table 5, the assumed neuromotor time constant of 0.08 sec is sufficient to control the system, and the pilot model controller Riccati equation has a solution. In the last row of Table 5, the value chosen for τ_n causes the controller algorithm to diverge. The divergence is easily understood when the eigenvalues of closed-loop pilot model matrix

$$\begin{bmatrix} F & G \\ C & -R_L \end{bmatrix} = \begin{bmatrix} \frac{1}{\tau_s} & g \\ \frac{-1}{2g\tau_n^2} & -\frac{1}{\tau_n} \end{bmatrix} \tag{1}$$

are examined. One eigenvalue is unstable for τ_s equal to -0.152 sec and τ_n equal to 0.08 sec. The last row in Table 5 represents a situation in which the human subject observation

of the signal (visual and aural combined) is so clear that the neuromuscular system instability boundary is reached before the visual instability limit.

Summary - The optimal control pilot model and pilot model algorithm largely agree with experimental and mathematical results under the extreme conditions of the critical tracking task. When the pilot model algorithm predicts an instability, the human may well have similar difficulties. What is even more important is the converse of the above statement: when the pilot model exists, then a well-trained human should be able to control the system. If the pilot model exists but the experienced pilot encounters stability problems in controlling the aircraft, then alternate reasons for pilot control difficulty must be explored. This is done in the next section.

3.2.2 Adaptive Behavior of the Pilot During Aircraft Maneuvering

This section presents an approach to analyzing pilot adaptation to varying flight conditions using the optimal control pilot model. High-performance aircraft are susceptible to degraded flying qualities during maneuvering flight, and the effect of piloting action plays a significant role in determining overall system stability. The piloting task is made difficult by the need to change control strategies if stable regulation of the aircraft is to be maintained.

Stability of the pilot-aircraft system is evaluated by eigenvalue analysis of the closed-loop system which is formed when the pilot uses aircraft outputs to regulate aircraft inputs. The pilot-aircraft system model is

$$\begin{bmatrix} \Delta\dot{\underline{x}}(t) \\ \Delta\dot{\underline{u}}(t)_{pilot} \end{bmatrix} = \begin{bmatrix} F & G \\ 0 & -R_L \end{bmatrix} \begin{bmatrix} \Delta\underline{x}(t) \\ \Delta\underline{u}(t)_{pilot} \end{bmatrix} + \begin{bmatrix} 0 \\ I \end{bmatrix} \left[C\Delta\underline{\hat{x}}_p(t) + \Delta\underline{v}_u(t) \right] + \begin{bmatrix} \Delta\underline{w}(t) \\ 0 \end{bmatrix}$$

where $\Delta\underline{\hat{x}}_p(t)$ is the pilot's predicted state estimate as shown in Tables 1 and 2. The adaptation point of the pilot specifies the pilot gain matrix, C, while the flight condition of the aircraft specifies F and G. The eigenvalues of the closed-loop regulator system are the roots of the determinant

$$\det\left(\lambda I - \begin{bmatrix} F & G \\ C & -R_L \end{bmatrix}\right) = 0 \qquad (2)$$

Equation 2 is easily restructured to incorporate alternate modes of the aircraft's control system. If the stability augmentation system (SAS) is on, F is changed by feedback. If lateral stick centering logic is employed, the column in G corresponding to lateral stick deflections and the pilot lateral stick feedback gains are eliminated. If the ARI is on, G is modified by the interconnects. If a command augmentation system (CAS) is on, both F and G are changed appropriately.

In the work of the previous year, the pilot gain matrix, C, was fixed for adaptation at α_0 = 10 deg, β_0 = 0 deg, and the aircraft's angle of attack and sideslip were varied with airspeed held constant (Ref. 2). It was shown that the instability regions in the $\alpha_0 - \beta_0$ plane are formed primarily in the lateral-directional axis, and these regions were not particularly affected by the sideslip angle. Building on this work, the current analysis assumes zero sideslip conditions (uncoupled dynamics), and the effects of the pilot fixing his control strategy at various angles of attack are determined.

The constant-altitude wind-up turn presented in Table 6 is an example of a maneuver which causes angle of attack to increase.* The flight condition sweep starts at straight-and-level flight; the aircraft rolls into a turn and maneuvers to a constant pitch rate with increasing angle of attack as the velocity drops. The effects of changes in roll angle, pitch angle, and height are neglected in constructing F and G. The assumed constant height is 6,096 m (20,000 ft) at zero flight path angle. The closed-loop pilot-aircraft eigenvalues are determined at the points shown in Fig. 35 and Table 6. The eigenvalue data is cross plotted to obtain stability regions. Once a diagram is formed, any adaptation strategy can be chosen, from perfect adaptation to no adaptation, and the effects on pilot-aircraft stability can be observed. If a wind-up turn time history is available, key points can be transferred to the diagram for validation and comparison.

The optimal control pilot model gain matrix is determined at each point in the wind-up turn. The Q_C weighting matrix used in these calculations performs a tradeoff between the following state perturbations:

- Roll Angle 5 deg
- Yaw Angle 1.4 deg
- Body Roll Rate 6 deg/sec
- Body Yaw Rate 2 deg/sec
- Lateral Velocity 0.914 m/s (3 fps)
- Lateral Acceleration 1.83 m/s^2 (0.167 g)

*The constant-altitude wind-up turn should be distinguished from the constant-velocity wind-up turn for a thrust-limited flight condition. In the latter, the aircraft must descend, trading potential energy for kinetic energy to maintain speed.

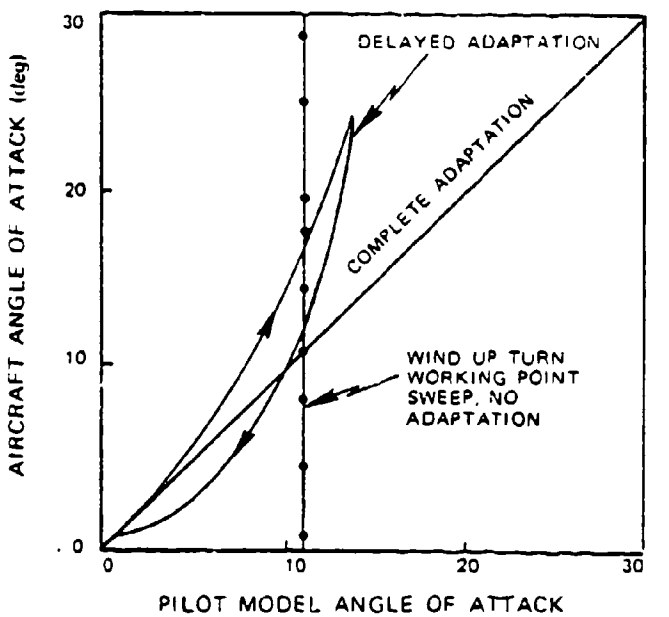

Figure 35 Pilot Model Diagram Construction for Wind-Up Turn Trajectory

The weighting coefficient for each variable is the inverse of the square of these values. Allowable control deflections are large enough to effectively eliminate them from this weighting matrix tradeoff.

Eigenvalues for the pilot-aircraft system (ARI off, SAS off) using lateral stick alone for control are shown in Table 7. As illustrated by the table, the pilot model predicts that the pilot can maintain tight control throughout the maneuver, although the Dutch roll natural frequency becomes low at the higher angles of attack.

TABLE 6 WIND-UP TURN WORKING POINTS

T-1089

POWER SETTING, δ_T, %	VELOCITY V_o, m/s (fps)	ANGLE OF ATTACK, α_o, deg	NORMAL ACCELERATION, a_n, m/s^2 (g's)	PITCH RATE, q_o, deg/sec
40(Mil)*	244 (800)	1.02	0.0 (0.00)	0.0
30(A/B)**	244 (800)	5.97	21.3 (2.17)	5.0
100(A/B)	244 (800)	8.72	31.9 (3.25)	7.5
100(A/B)	213 (700)	11.1	27.6 (2.81)	7.5
100(A/B)	183 (600)	15.4	22.9 (2.33)	7.5
100(A/B)	168 (550)	17.4	20.5 (2.09)	7.5
100(A/B)	152 (500)	19.8	18.2 (1.85)	7.5
100(A/B)	137 (450)	24.6	15.1 (1.54)	7.5
100(A/B)	130 (425)	27.8	13.1 (1.34)	7.5
100(A/B)	122 (400)	34.1	10.1 (1.03)	7.5

*Military Thrust

**Afterburner

The nonadapting pilot model (introduced in Ref. 2) is an example of mismatched internal model representation, as also addressed in Ref. 18. The system dynamics which the pilot model algorithms use to calculate the control gains,

TABLE 7 PILOT-AIRCRAFT EIGENVALUES IN THE WIND-UP TURN (LATERAL STICK ALONE, ARI OFF, SAS OFF)

T-1090

MANEUVER CONDITION			PILOT LATERAL STICK/SPIRAL		DUTCH ROLL		ROLL	YAW
V_o, m/s	α_o, deg	q_o, deg/sec	ω_n, rad/sec	ζ, –	ω_n, rad/sec	ζ, –	τ, sec	τ, sec
244	1.02	0.0	7.38	0.740	2.40	0.468	0.892	6.9
244	5.97	5.0	7.42	0.726	2.12	0.426	0.849	2.23
244	8.72	7.5	7.00	0.679	1.62	0.614	0.781	1.72
213	11.1	7.5	6.69	0.655	1.11	0.683	0.642	1.84
183	15.4	7.5	6.48	0.635	0.296	0.775	0.535	1.19
152	19.8	7.5	6.11	0.642	0.486	0.861	0.521	2.39
137	24.6	7.5	6.09	0.614	0.266	0.722	0.532	0.855

i.e., the pilot's internal model, are different from the actual aircraft's dynamics. There are good reasons for examining the effects of fixed piloting strategy in maneuvering flight, even though the pilot is capable of adaptation. If the pilot can get similar tracking performance without changing his strategy, his conscious workload is reduced. If the pilot does not know the aircraft's dynamics will change in the future, his best approach may be to continue using a fixed strategy; in any case, true pilot adaptation is likely to lag the aircraft's actual state.

There is some evidence that pilot model adaptation is more directly related to changing control effects than changing stability characteristics of the aircraft. A simple example is based on the first-order system discussed in Section 3.2 for the critical tracking task. The pilot model gain, $-1/2g\tau_n^2$, in Eq. 1 is independent of the system time constant, τ_s, and adapts only to changes in g. This result

implies that modifications which affect G (such as an ARI) have the most potential for altering pilot workload and affecting piloting style, while modifications which affect F (such as a SAS) may have less direct effect on piloting strategy.

3.2.3 Tracking Error Analysis of the Pilot-Aircraft System

This section describes a procedure for examining the effects of fixed piloting strategy on the net tracking effectiveness of the pilot-aircraft system, as well as on the control effort required of the pilot. The approach is based on the computation of steady-state covariances which accompany the generation of the pilot model estimation law. The steady-state covariance matrix, X, is shown in Table 3. Its diagonal elements are the mean-square values of the tracking errors and the control commands issued by the pilot model.

For analysis purposes, the pilot model control law is fixed at an assumed adaptation point, but the pilot model estimation law is adapted to the aircraft's flight condition. This approach is justified on the grounds that we are investigating the independent effects of pilot control strategies on tracking performance and that fixing the estimation law as well would not allow an easy comparison with future evaluations of independent estimation effects. Furthermore, the assumption simplifies the computation of system covariances, allowing direct use to be made of the Kalman filter computations, as mentioned above. The covariance matrix, X, of system state and control variables is

$$E\begin{bmatrix}\Delta\underline{x}(t)\\ \Delta\underline{u}(t)\end{bmatrix}\begin{bmatrix}\Delta\underline{x}^T(t) & \Delta\underline{u}^T(t)\end{bmatrix} = X = P_E + \int_0^T \Phi_E(t)\, P_v \Phi_E^T(t)\, dt + Y \qquad (3)$$

where τ is the pilot's perceptual time delay, and

$$Y = \int_0^\infty \Phi_C(t)\ \Phi_E(\tau)\ P_V \Phi_E^T(\tau)\ \Phi_C^T(t)\ dt$$

$$\Phi_E(t) = e^{\begin{bmatrix} F & G \\ 0 & -R_L \end{bmatrix} t}$$

$$\Phi_C(t) = e^{\begin{bmatrix} F & G \\ C(\text{unadapted}) & -R_L \end{bmatrix} t} \qquad (4)$$

$$P_V = P_E \begin{bmatrix} H^T \\ D^T \end{bmatrix} V_y^{-1} [H\ D]\ P_E$$

Equation 3 can be derived from the expression for X in Table 3 when the control law is adapted. The only change that occurs when the control law is not adapted is in Eq. 4. If the nonadapted C causes an instability, the adapted steady state tracking error does not exist (i.e., the tracking error goes to infinity).

The assumed parameters for the human pilot are the same as those used in the previous year's work (Ref. 2). The pilot observes the perturbation angles and angular rates, the human time delay is assumed to be 0.2 sec, and the longitudinal

and lateral states are assumed to be scanned with equal attention. The corresponding visual noise-to-signal ratio, P_y, is 0.025π, assuming attention allocation to the task of flying the lateral-directional dynamics of the aircraft is 40 percent. The neuromotor noise-to-signal ratio, P_u, is set at the nominal value of 0.003π for all controls.

The aircraft is assumed to be disturbed by atmospheric turbulence. This is modeled as an exponentially-correlated, gauss-markov process

$$\Delta v_w(t) = -\frac{1}{\tau_y}\Delta v_w + \Delta w_y(t)$$

along the body y-axis for the lateral-directional dynamics. The value of the time constant, τ_y, is taken to be 0.314 rad/sec, and the variance of the gust is 1.52 m/s (5 fps).

The pilot model estimator is determined at the wind-up turn working points. For each pilot model solution, the state and control variances are determined by the diagonal elements of the covariance matrix, X. By cross plotting the variances, contours of system performance can be obtained. The contours never cross the stability boundaries, which represent contours of infinite variance.

3.3 PREDICTION OF PILOT-AIRCRAFT STABILITY AND PERFORMANCE

This section presents stability regions and state and control variance contours for the F-14A aircraft in a wind-up turn maneuver. The results concentrate on the lateral-directional uncoupled dynamics of the aircraft, and they illustrate the effect of an ARI feature on pilot-aircraft interactions.

3.3.1 Stability Contours for the Pilot-Aircraft System at High Angles of Attack

Stability contours for the pilot-aircraft system demonstrate the effect of pilot adaptation point (represented by angle of attack, α_p) during the wind-up turn. In all cases, if the pilot is properly adapted to the actual flight condition (represented by α_A), the closed-loop system is stable; however, if the pilot chooses a control strategy which is optimal for a different point on the wind-up turn, he may destabilize the overall system. (As mentioned earlier, his adaptation could lag the actual flight condition, or he could purposely choose a sub-optimal policy.) If the stability of the pilot-aircraft system is evaluated at a number of points representing matched and mismatched pilot adaptation, the stability boundaries can be defined by interpolating between stable and unstable points, producing results such as those shown in Figs. 36 and 37.

Each of the figures has a band of stability in the region of the line of perfect adaptation. In Fig. 36a, the most striking feature is the stability "neck" which occurs when α_A equals 15° to 20°. The pilot must be very careful about choosing his control strategy in this region, as an unstable spiral mode region is easily entered if the strategy is not nearly optimal. The instability would be characterized by a "departure" with increasing heading and roll angles.

If the pilot uses both lateral stick and pedals, the stable regions are expanded, and the onset of the nonadapted unstable spiral mode region occurs at higher α_A, as shown in Fig. 36b. The instability region for α_p greater than α_A is eliminated, and active use of the rudder is seen to have a stabilizing effect. If the pilot model controls with foot pedals alone (not shown in the figure), there are no regions of instability in the $\alpha_A - \alpha_p$ plane, a result which is consistent with flight experience.

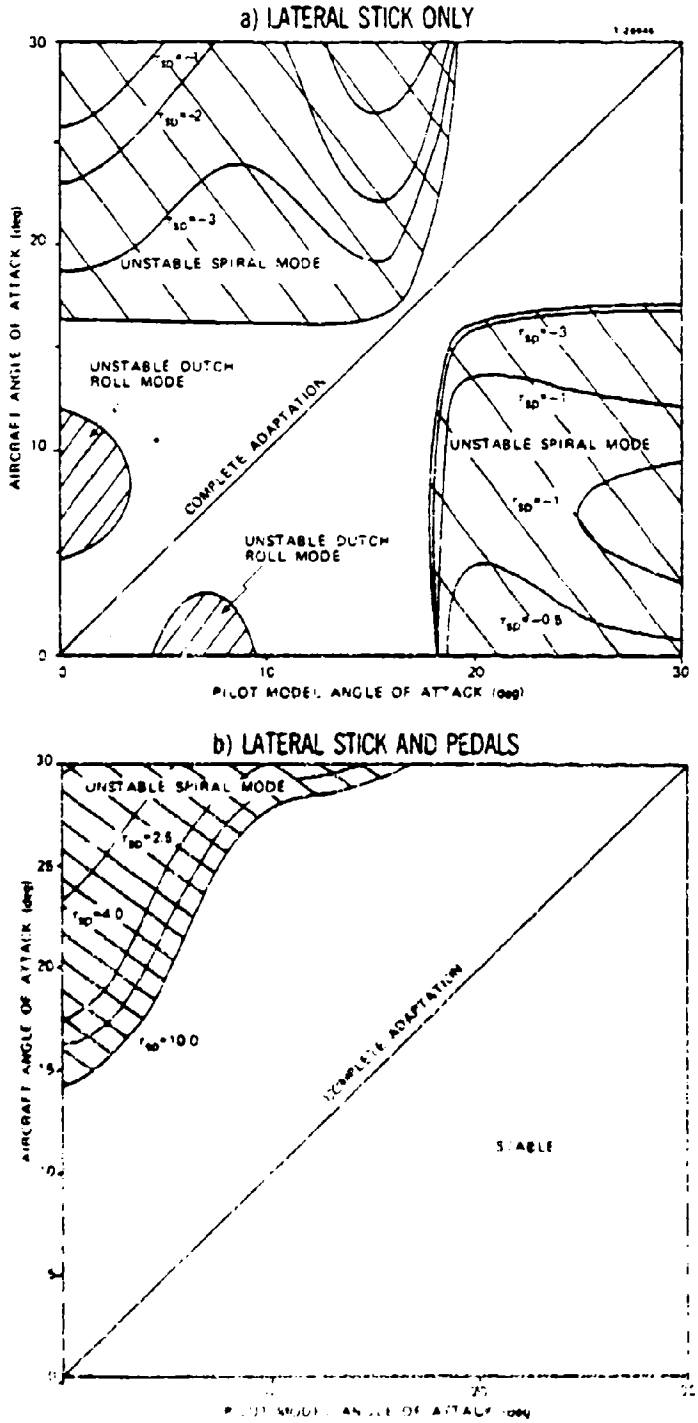

Figure 38 Effects of Pilot Model Adaptation on Maneuvering Flight Stability (ARI Off)

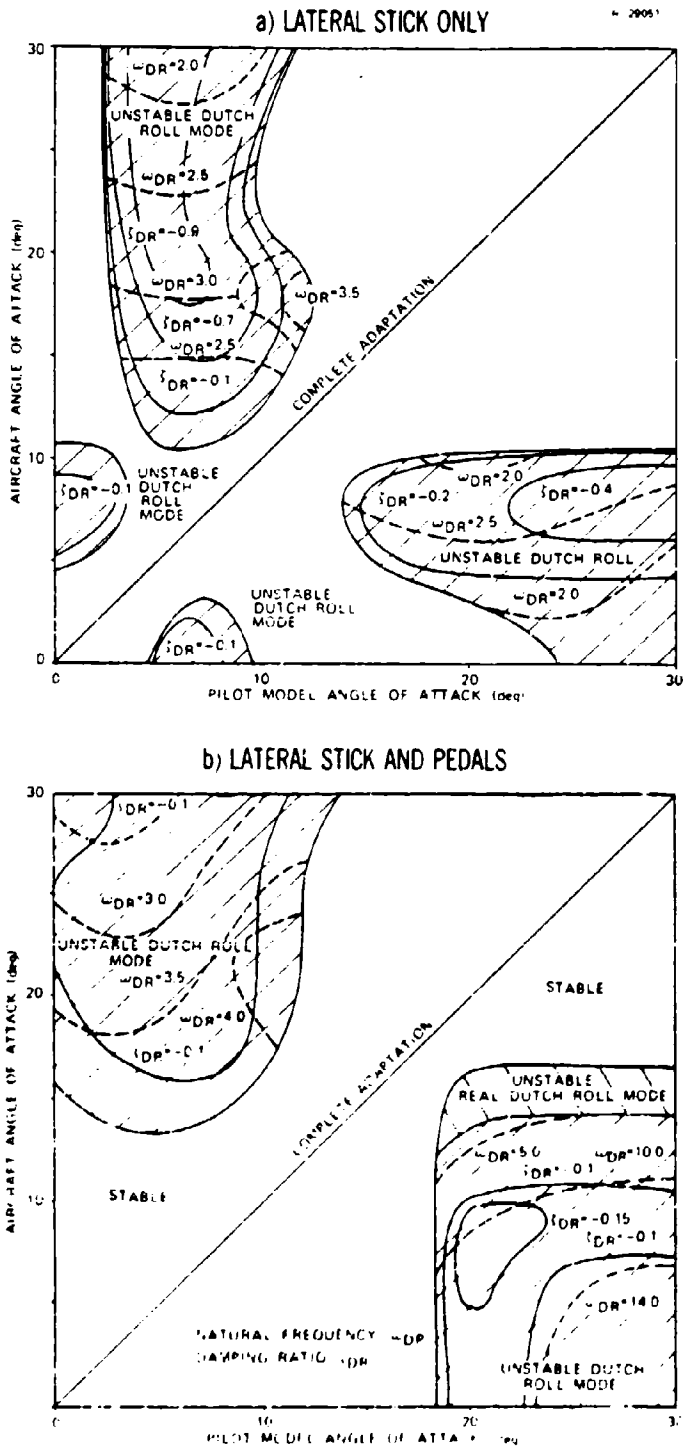

Figure 37 Effects of Pilot Model Adaptation on Maneuvering Flight Stability (ARI On)

The regions of instability in the pilot-aircraft diagrams can be linked with gain sign changes in the pilot model feedback gain matrix, C. Tables 8 to 10 show optimal pilot model gains with the ARI off. The sign changes on roll, yaw, and yaw rate in Table 8 are considered to be the cause of the spiral instability with lateral stick. The lack of sign changes in Table 9 indicates the desirable characteristic of rudder control, which produces no instabilities in the pilot-aircraft diagrams. Rudder control uniformity carries over to the dual-control pilot model gains in Table 10 where the roll, yaw, and yaw rate gains for lateral stick do not change sign up to 24.6-deg α_0.

The effect of the ARI design discussed in Ref. 2 is shown in Fig. 37. For control with the lateral stick alone, the unstable spiral regions are eliminated, but regions of Dutch roll instability occur instead. Failure of the pilot model to adapt leads to "wing rock" tendencies, which could result in divergent oscillations. As the aircraft angle of attack further penetrates the region of Dutch roll instability (with $\alpha_P<\alpha_A$), the rocking decreases in frequency and the amplitude of the oscillation increases rapidly. If the pilot overadapts ($\alpha_P>\alpha_A$) where α_A is below 10 deg, the other Dutch roll instability region is entered. Above 10-deg α_A, the pilot can overadapt significantly without encountering instabilities.

If the pilot uses both lateral stick and pedals with the ARI on, the stability contours are presented by Fig. 36b. If the pilot does not adapt, a high frequency, lightly damped, instability region is entered. The instability stays lightly damped as the aircraft angle of attack increases, causing the aircraft to rock with a moderately increasing amplitude. If the pilot overadapts significantly before 15-deg α_A, the other very high frequency, lightly damped unstable region is entered.

TABLE 8 PILOT MODEL LATERAL-STICK GAINS (SAS OFF, ARI OFF)

AIRCRAFT ANGLE OF ATTACK, deg	SIDE VELOCITY, $\partial\delta/\partial v$	YAW RATE, $\partial\delta/\partial r$	ROLL RATE, $\partial\delta/\partial p$	ROLL ANGLE, $\partial\delta/\partial\phi$	YAW ANGLE, $\partial\delta/\partial\psi$
1.02	+0.522	-4.93	-0.123	-0.345	-1.68
8.72	-0.509	+1.74	-0.619	-0.582	-1.23
11.1	-0.544	+1.43	-1.02	-0.827	-1.62
15.4	-0.433	-2.98	-3.52	-3.40	-3.72
19.8	-0.417	+18.8	-3.26	+2.89	+3.74
24.6	-1.50	+18.07	-3.66	+1.80	+4.12

TABLE 9 PILOT MODEL PEDAL GAINS (SAS OFF, ARI OFF)

AIRCRAFT ANGLE OF ATTACK, deg	SIDE VELOCITY, $\partial\delta/\partial v$	YAW RATE, $\partial\delta/\partial r$	ROLL RATE, $\partial\delta/\partial p$	ROLL ANGLE, $\partial\delta/\partial\phi$	YAW ANGLE, $\partial\delta/\partial\psi$
1.02	+0.0276	-1.049	-0.0281	-0.1618	-0.339
8.72	+0.0574	-1.097	+0.0327	-0.181	-0.324
11.1	+0.127	-1.449	+0.0526	-0.218	-0.440
15.4	+0.276	-2.01	+0.126	-0.269	-0.625
19.8	+0.503	-2.96	+0.294	-0.403	-0.987
24.6	+0.772	-4.33	+0.373	-0.729	-1.74

TABLE 10 PILOT MODEL DUAL CONTROL GAINS (SAS OFF, ARI OFF)

T-1219

CONTROL	AIRCRAFT ANGLE OF ATTACK, deg	SIDE VELOCITY $\partial\delta/\partial v$	YAW RATE $\partial\delta/\partial r$	ROLL RATE $\partial\delta/\partial p$	ROLL ANGLE $\partial\delta/\partial\phi$	YAW ANGLE $\partial\delta/\partial\psi$
Lateral-Stick	1.02	-0.645	-0.367	-0.386	-0.764	-2.08
	8.72	-0.0299	-0.0260	-0.559	-0.853	-2.19
	11.1	+0.0302	-0.420	-0.947	-1.22	-3.29
	15.4	+0.548	-2.84	-2.84	-2.98	-8.78
	19.8	+0.884	-4.34	-3.31	-3.00	-9.16
	24.6	+0.160	-3.88	-4.44	-3.48	-10.56
Pedals	1.02	+0.0342	-0.995	+0.0572	+0.109	+0.101
	8.72	+0.0137	-1.074	+0.0387	-0.0901	-0.397
	11.1	+0.0474	-1.48	+0.0451	-0.169	-0.721
	15.4	+0.154	-2.39	+0.073	-0.369	-1.57
	19.8	+0.339	-3.90	+0.259	-0.625	-2.82
	24.6	+0.454	-5.42	+0.119	-1.04	-4.66

The instabilities with the ARI on can also be related to pilot model gain sign changes, as shown in Table 11. Unlike results with the ARI off, the sign changes in Table 11 for lateral stick with the ARI on occur for feedback of lateral velocity and roll rate, which primarily affect stability of the Dutch roll mode, as shown in Fig. 37. The ARI does significantly reduce the magnitude of the pilot model gains at high angle of attack, implying reduced pilot control effort. Gain sign changes also occur in the dual-control pilot model with the ARI on, as shown in Table 12. Lateral velocity, yaw rate, and yaw angle gains for the pedal commands show the most change with increasing angle of attack. The ARI does not reduce gain magnitude with dual control, and it significantly increases the gains for the pedals when compared with Table 10.

TABLE 11 PILOT MODEL LATERAL-STICK GAINS (SAS OFF, ARI ON)

T-1221

AIRCRAFT ANGLE OF ATTACK, deg	SIDE VELOCITY, $\partial\delta/\partial v$	YAW RATE, $\partial\delta/\partial r$	ROLL RATE, $\partial\delta/\partial r$	ROLL ANGLE, $\partial\delta/\partial\phi$	YAW ANGLE, $\partial\delta/\partial\psi$
1.02	+0.522	-4.93	-0.123	-0.345	-1.68
8.72	-0.509	+1.73	-0.620	-0.582	-1.23
11.1	-0.610	-6.16	-0.0702	-0.741	-3.08
15.4	+0.327	-2.42	+0.281	-0.178	-0.685
19.8	+0.352	-1.94	+0.284	-0.149	-0.589
24.6	+0.515	-2.74	+0.408	-0.280	-0.991

TABLE 12 PILOT MODEL DUAL CONTROL GAINS (SAS OFF, ARI ON)

T-1218

CONTROL	AIRCRAFT ANGLE OF ATTACK, deg	SIDE VELOCITY $\partial\delta/\partial v$	YAW RATE $\partial\delta/\partial r$	ROLL RATE $\partial\delta/\partial p$	ROLL ANGLE $\partial\delta/\partial\phi$	YAW ANGLE $\partial\delta/\partial\psi$
Lateral-Stick	1.02	-0.645	-0.367	-0.386	-0.764	-2.08
	8.72	-0.0300	-0.0260	-0.559	-0.853	-2.19
	11.1	+0.0302	-0.421	-0.947	-1.22	-3.29
	15.4	+0.581	-2.816	-2.63	-2.79	-8.16
	19.8	+0.890	-4.33	-3.27	-2.97	-9.05
	24.6	+0.816	-4.44	-4.49	-3.53	-9.44
Pedals	1.02	+0.0342	-0.995	+0.0572	+0.110	+0.201
	8.72	+0.0137	-1.074	+0.0387	-0.0901	-0.397
	11.1	+0.0418	-1.404	+0.223	+0.0589	-0.106
	15.4	-0.362	+0.153	+2.47	+2.17	+5.88
	19.8	-1.11	+3.17	+5.63	+4.24	+12.01
	24.6	-0.755	+2.48	+8.09	+5.27	+12.8

3.3.2 Effects of Nonadaptive Piloting Behavior on Tracking Performance Contours

This section uses the covariance values obtained from the pilot model to produce performance contours in the α_A - α_p plane. The technique for obtaining the contours is described in Section 3.2.3. The performance contours show the effects of adapted and nonadapted control behavior on the closed-loop motions of the aircraft which result from turbulence inputs. The important feature in the contour plots is not the actual rms values of the motions and control usage (which are disturbance-model-dependent) but the contour variations as the pilot model adaptation point is varied.

In each series of figures, the three variables shown are the variances of the lateral stick and/or pedal commands, the variance of the roll rate, and the variance of the lateral velocity. The stick and pedal variances give indications of the effort which the pilot must exert to achieve control. Roll rate is a key variable for maneuvering flight, and its variance is an important indicator of maneuvering precision. The lateral velocity variance can be associated with pointing precision, which is of obvious concern in air combat maneuvering.

The rms performance contours, using a single control, are shown in Fig. 38. The performance contours can portray improved rms values in off-diagonal regions because the optimal control pilot model is not separable, i.e., the optimal filter design depends upon the control gains. For lateral stick alone, the state rms values exhibit remarkable uniformity in performance, even very close to the stability boundary where the state rms values have infinite variance. This suggests that the pilot-aircraft stability boundary is encountered abruptly if the pilot fails to adapt.

ROLL RATE

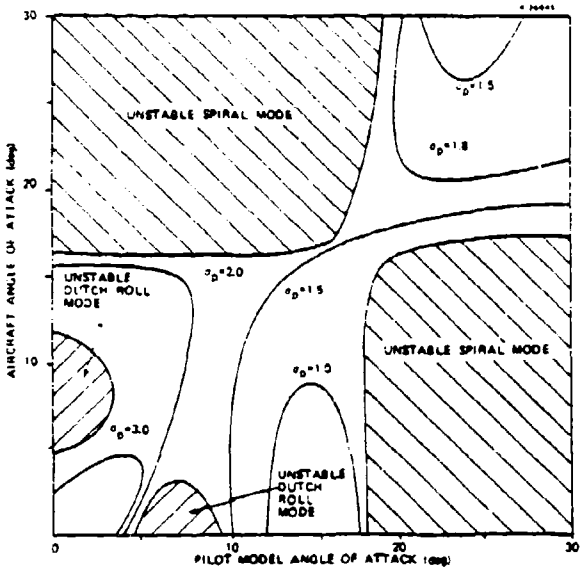

LATERAL VELOCITY

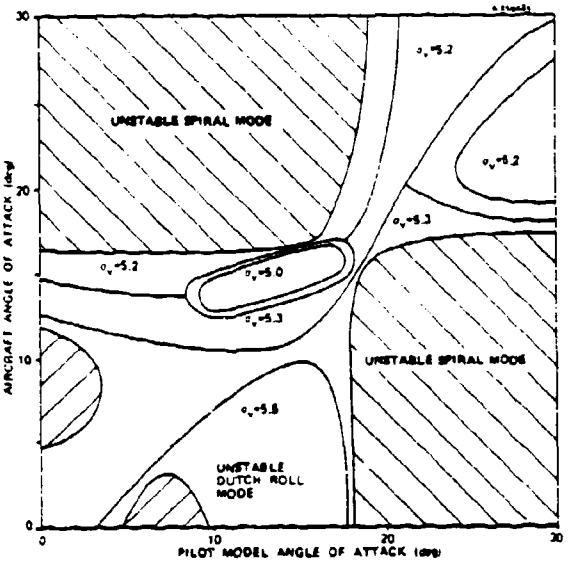

LATERAL STICK

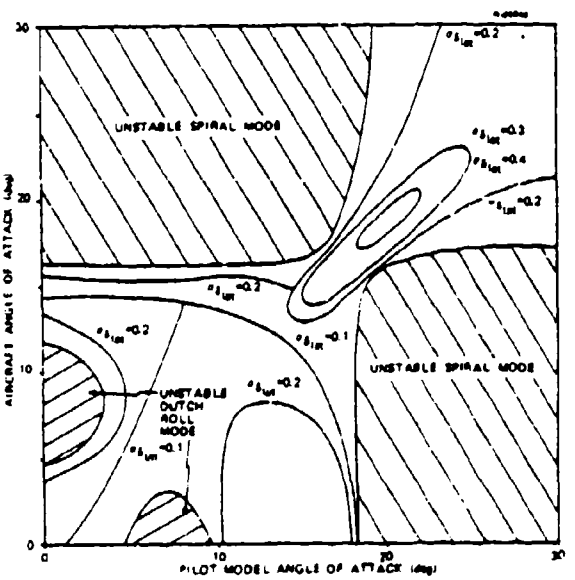

Figure 38a Performance Contours for Lateral Stick Only Control (ARI Off)

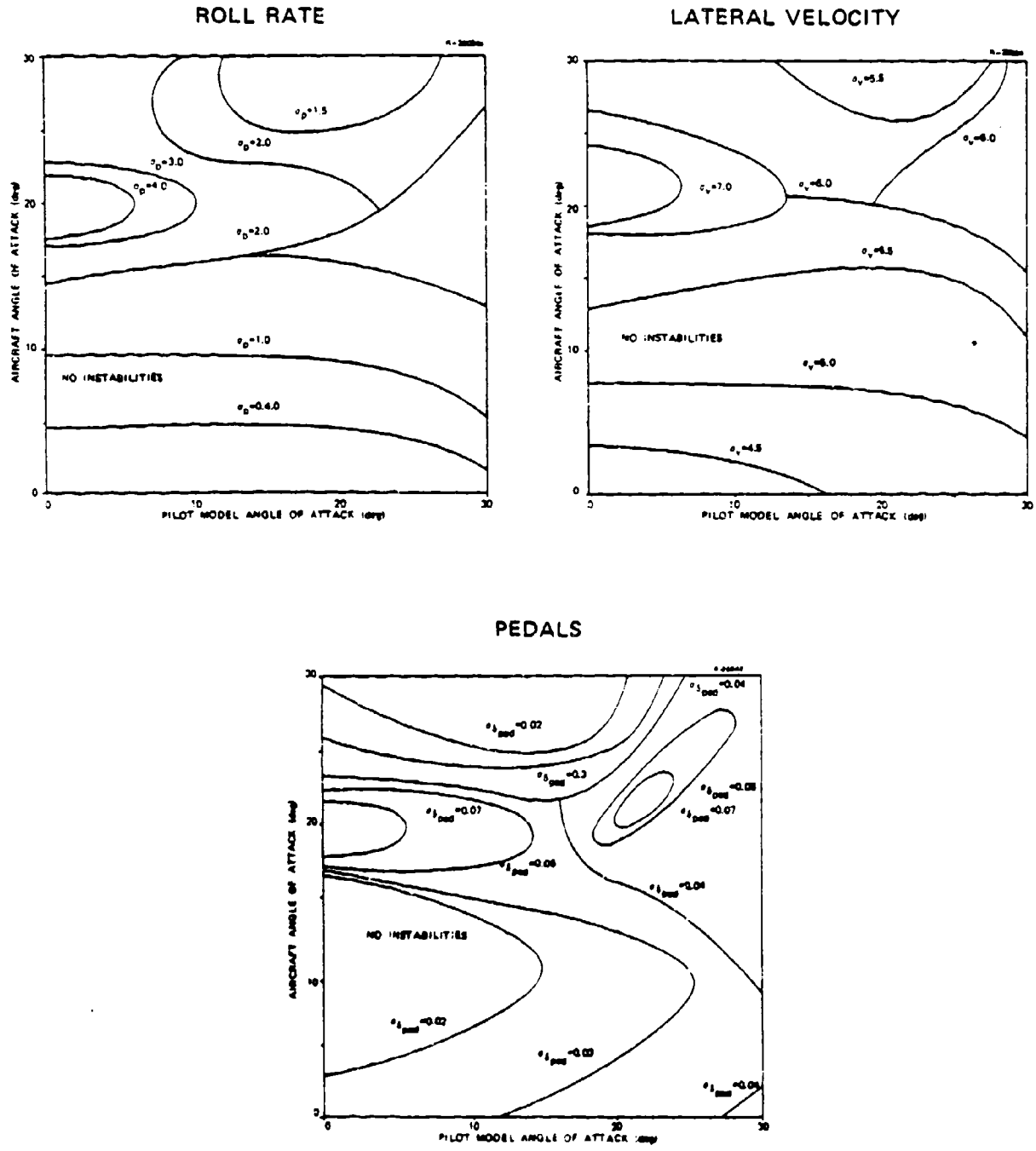

Figure 38b Performance Contours for Pedals Only Control (ARI Off)

For control with the pedals alone, the opposite tends to be true up to an aircraft angle of attack of 20 deg. If the pilot model does not adapt, tracking performance (particularly lateral velocity) deteriorates. This is a further indication that the rudder is a favorable control surface for high angle of attack regions, because motion cues aid the pilot in adapting correctly with rudder control.

When the pilot model uses both the lateral stick and pedals (with the ARI off), the tracking performance contours are shown by Fig. 39. There is an improvement in performance, as signified by the decrease in the rms values for the states and control for low α_A. Figure 39 shows that the adapting pilot model must continually increase control effort as the aircraft angle of attack increases. At the top of each diagram in Fig. 39 is a region where the pilot model estimator algorithm diverges with the chosen human parameters. The neuromuscular noise-to-signal ratio, P_u, is found to be the primary cause of the divergence, because the estimator algorithm converges to a solution if P_u is decreased sufficiently. Decreasing P_y does not stop the algorithm divergence. The divergence region does not occur when the pedals or lateral stick are used separately, as shown in Fig. 38.

As pointed out in Section 3.2.1, algorithm divergence suggests that the pilot could have control difficulties; however, it is not clear that the constant neuromotor noise-to-signal scaling is an accurate representation of human response when the signal level becomes very large, as in the region of divergence. It is at least as likely that the neuromotor noise would reach a maximum level, implicitly decreasing P_u at large signal levels. This assumption is employed to generate results shown in Fig. 40b. In the two-control (stick plus pedal) case, neuromotor noise forces estimator divergence for

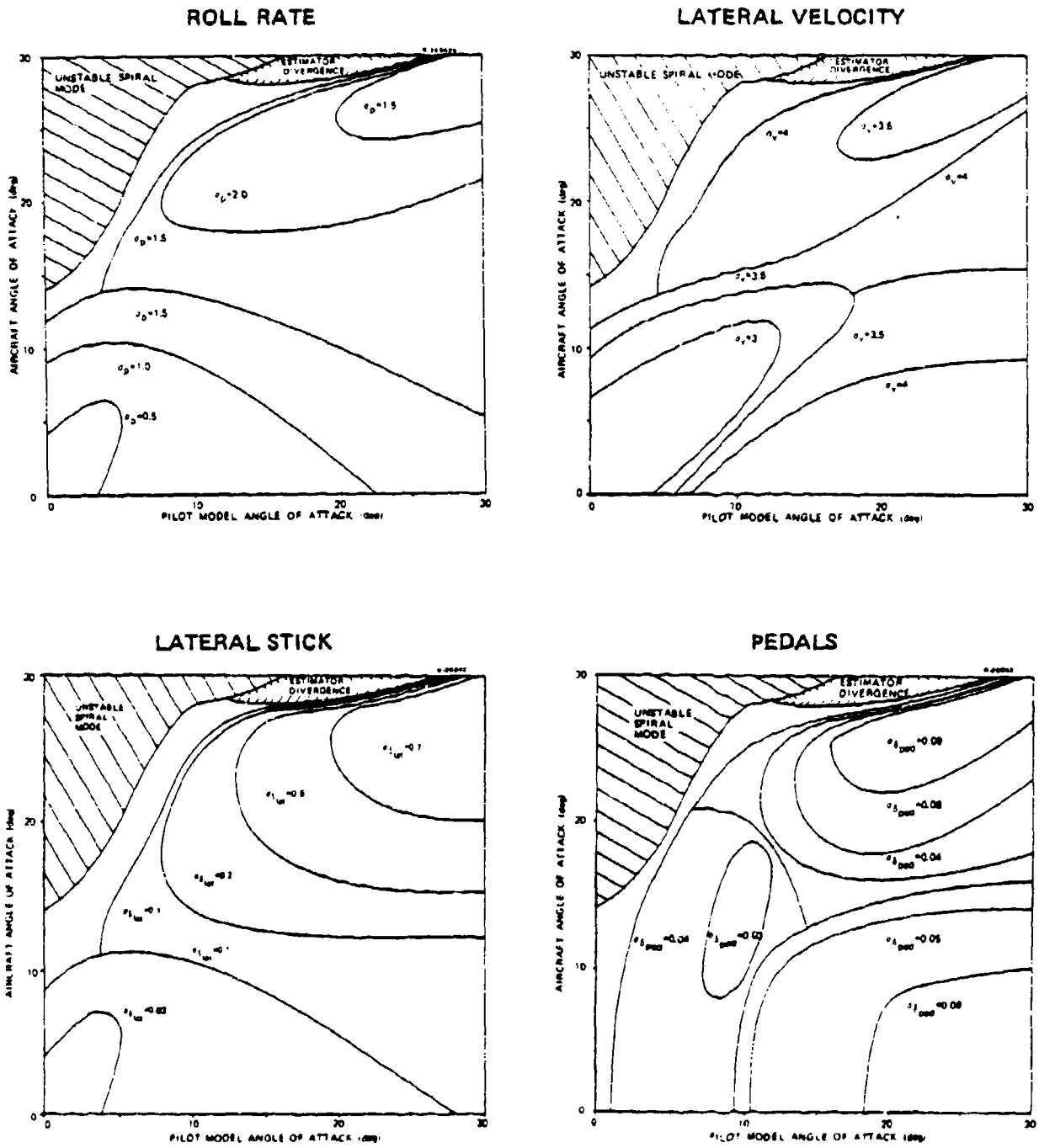

Figure 39 Performance Contours for Dual Control (ARI Off)

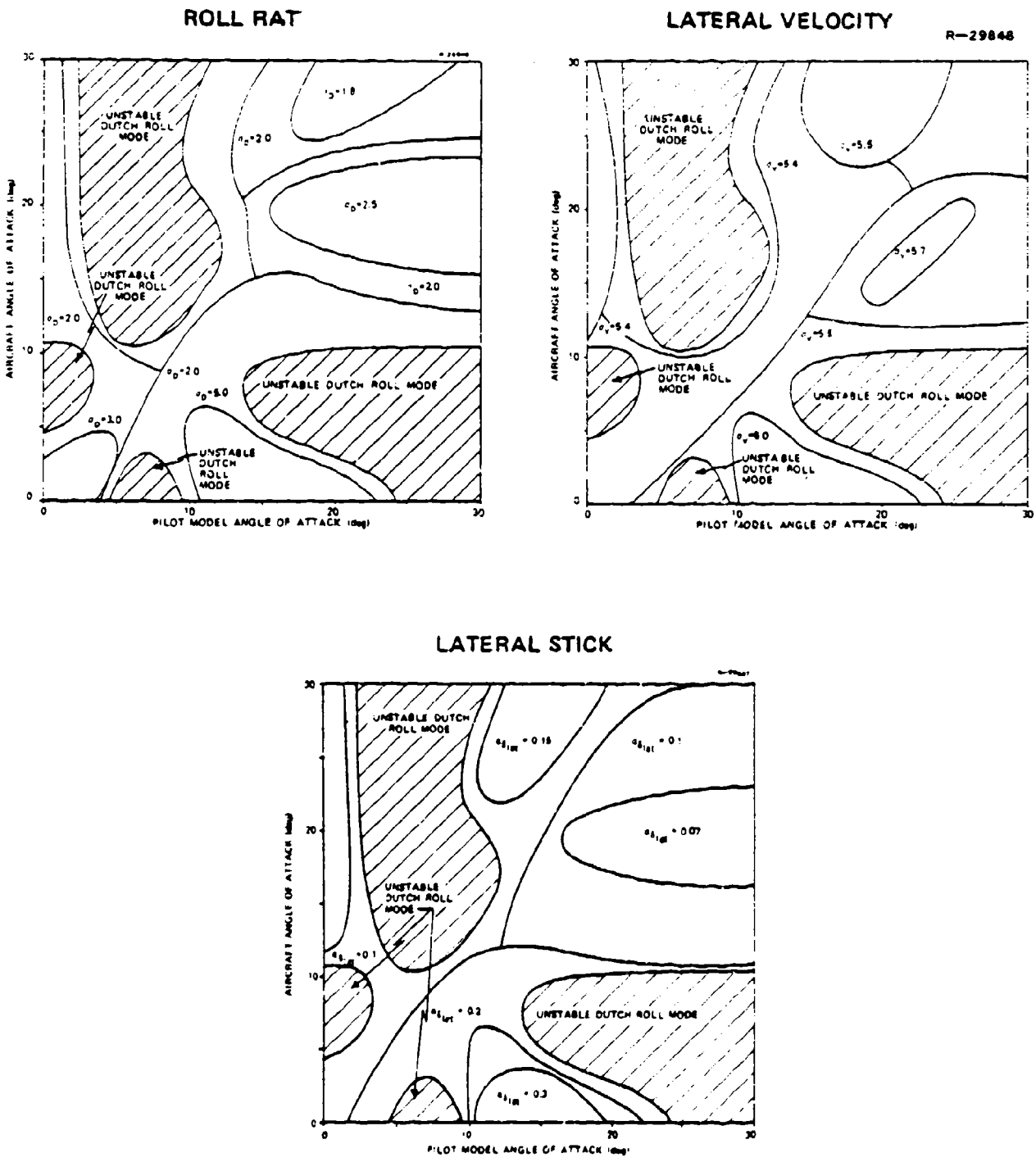

Figure 40a Performance Contours for Single and Dual Controls (ARI On)

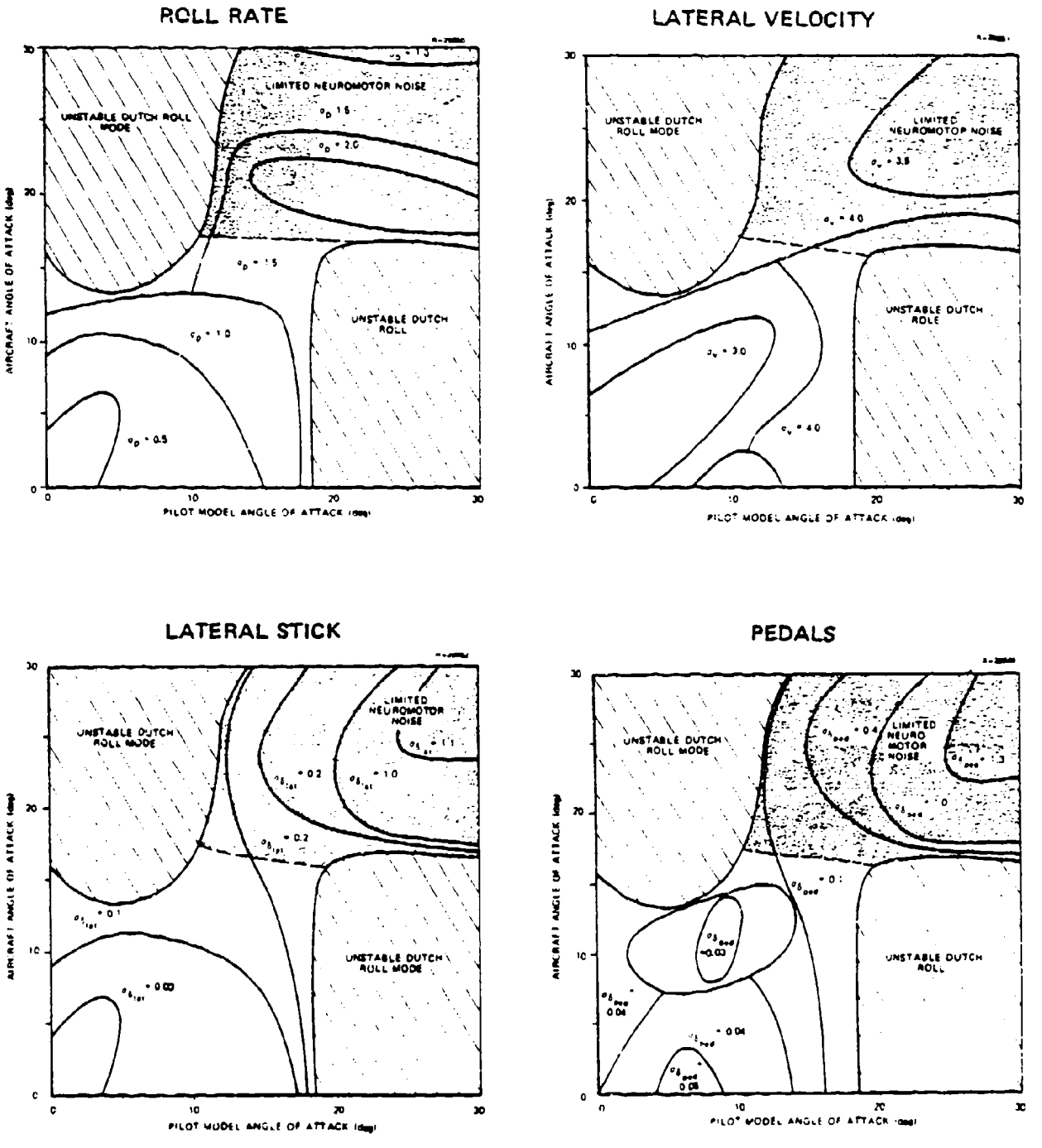

Figure 40b Performance Contours for Single and Dual Controls (ARI On) (Continued)

all values of α_A beyond about 16 deg. Consequently the two-control results are obtained with V_u frozen at its single control level. Even with fixed V_u, dual-control rms values rapidly increase with α_A.

In contrast, performance contours in Fig. 40a, with lateral stick only and the ARI on, show good results. There is a marked improvement in lateral-stick control effort with the ARI on when compared to Fig. 39a, in which the ARI is off.

The conclusion is that dual control at high α_o is difficult because the ARI logic causes both the stick and pedals to command rudder only. Improving performance with lateral stick alone, is the primary purpose of the ARI.

3.3.3 Predicted Tracking Performance in a Typical Air Combat Maneuver

An interesting observation concerning the pilot's control effort can be made using the results of the previous section. Contours of minimum control effort do not necessarily fall along the diagonal line of perfect adaptation because the pilot model is nonseparable and because the weighted sum of state and control variances does not guarantee minimum values of control variance alone. Figures 38 and 39 illustrate that minimum values of lateral stick and rudder variances frequently occur at sub-optimal adaptation points. Furthermore, as will be shown below, contours of minimum control effort often imply less control strategy adaptation than is required to maintain overall optimality. The combination of reduced control effort and reduced variation in control strategy strongly suggests the hypothesis of minimum-control-effort (MCE) pilot model adaptation, which is discussed in the remainder of this section.

MCE pilot model adaptation presents a rationale for how the pilot changes his control strategy, including the selection of his control outputs when more than one is available, as flight condition varies. Figure 41 illustrates the MCE adaptation pattern which would be followed in the wind-up turn, with the heavy line tracing out the corresponding MCE $\alpha_A - \alpha_P$ relationship. For α_A below 12 deg, there is no significant lateral control effort reduction associated with using the pedals as well as the stick (as seen with comparison of Fig. 41 with Fig. 40), and the MCE pilot model is "content" to use stick alone. The MCE strategy is slightly overadapted at low α_A, and slightly underadapted at α_A = 12 deg; hence, the net amount of adaptation is lower than that implied by fully optimal control.

As α_A continues to increase, Fig. 41 shows that the stick-alone MCE strategy is headed for a stability boundary. The pilot can avoid the boundary by adapting to a more nearly optimal stick-alone control strategy, but this requires substantially increased control effort in the vicinity of the stability neck. As alternatives, he can either blend in the use of foot pedals (coordinated adaptation) or resort to the use of pedals alone (stick-centered adaptation) for lateral-directional control. The advantage of the first approach is that relatively good maneuvering precision can be maintained with both controls without requiring counter-intuitive control style (i.e., pilot model control gains in Table 11 do not change sign at high α_A). However, the coordinated use of stick and pedals at high angle of attack is a difficult task, and the stick-centered adaptation is likely to be the preferable solution for this aircraft model with the ARI off. The resulting increases in roll rate and lateral velocity variances are modest using pedals alone for control.

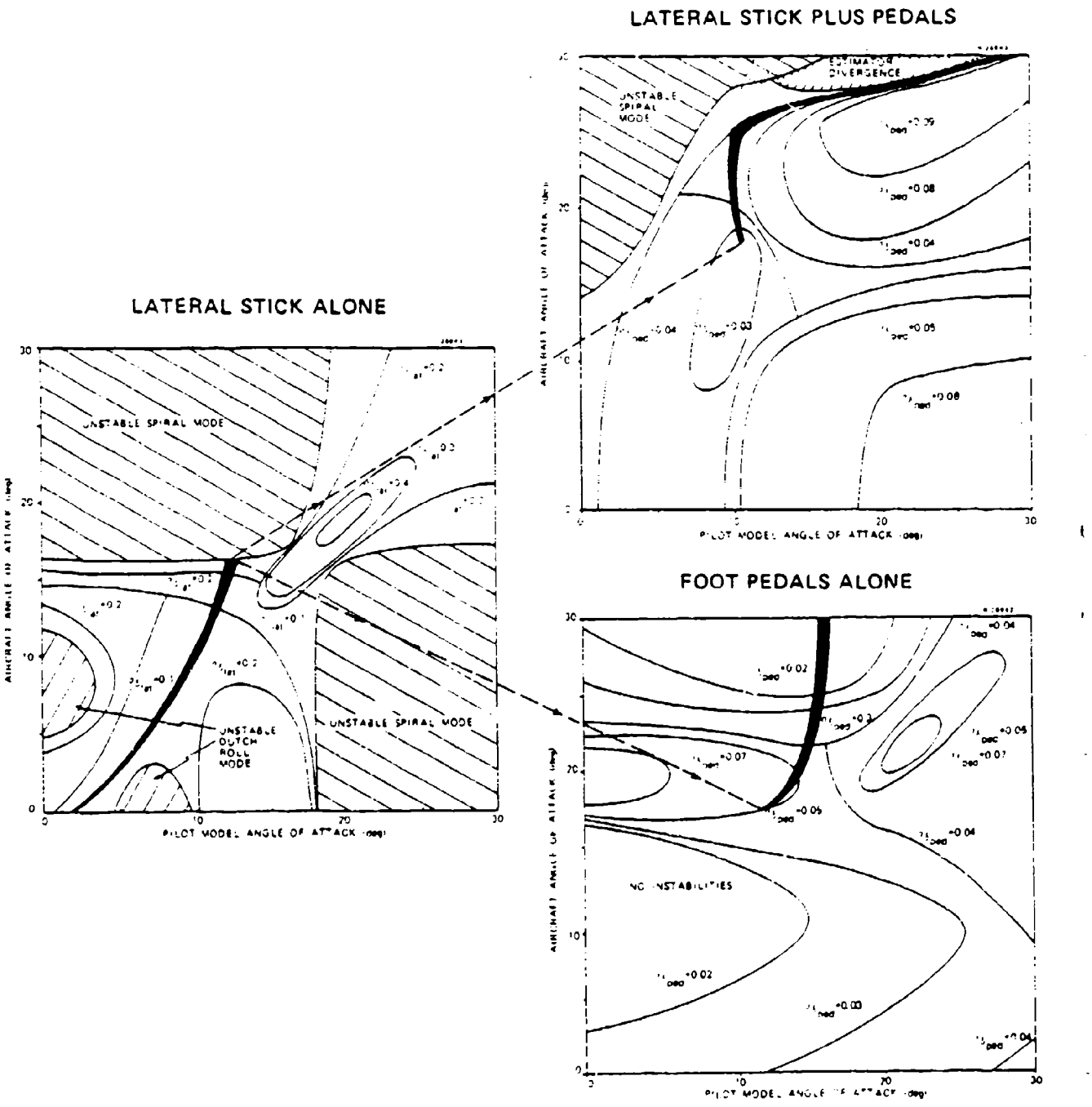

Figure 41 Prediction of Pilot Behavior at High Angle of Attack Under Minimum Control Effort (MCE) Adaptive Behavior Assumption

Experimental results indicate that the MCE pilot model hypothesis does, in fact, describe a realistic pattern of pilot adaptation. Figure 42 is a partial time history of a wind-up turn maneuver in which a trained pilot is flying a ground-based simulation of the subject aircraft. The aerodynamic model of the aircraft is the same as that used in our linear analysis, although the nonlinear, time-varying equations of motion drive the simulator. Below 18-deg angle of attack, the pilot controls with stick alone. As α_A increases beyond 10 deg, stick motions and sideslip excursions buildup. At α_A = 18 deg, the pilot begins to use the rudder pedals actively, while his use of the stick is substantially diminished. This result tends to confirm the MCE pilot model, although further validation is warranted.

The potential instability that can occur for lateral stick alone can be understood by considering the pilot model gain variations shown in Fig. 43. Near an α_A of 17 deg, the adapted roll and yaw gains change sign almost instantaneously. Figure 43 also shows that the minimum control effort pilot gains have little variation and approach the nonadapted pilot gains for α_A = 11 deg. The roll and yaw adapted pilot model gains do not change sign for lateral stick at 17-deg α_o when stick and pedals are used.

The sign change of the pilot model roll and yaw gains is a characteristic of the unusual way control rate weighting is incorporated in the pilot model and is not a characteristic of optimal regulators in general. The roll and yaw gains for a DPSAS design using the same reference aircraft are shown in Ref. 2 and do not "jump" near 17 deg α_o. The jump can be understood by using the pilot model gain for a first-order system, shown in Eq. 1. If an important element, g, in the control effect matrix, G, for the aircraft changes sign

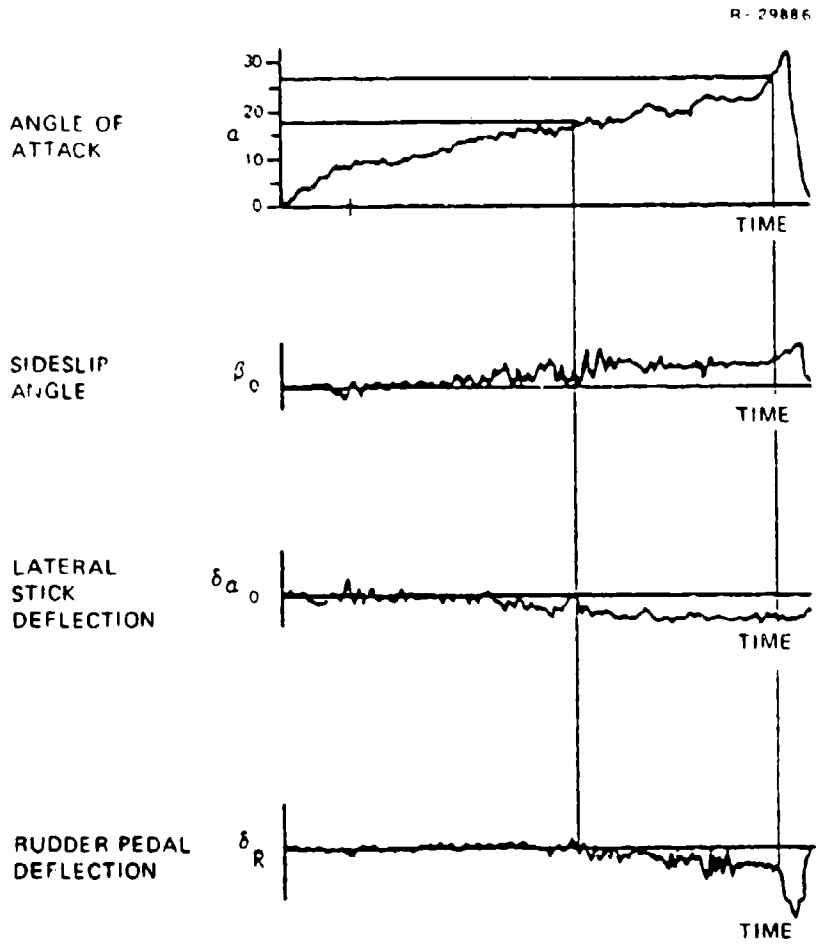

Figure 42 Results of Manned Simulation

by going through zero, the "1/g" behavior of the pilot model gain could occur. The specific control yaw moment due to differential stabilator shown in Fig. 43 has such a sign change near 17-deg α_o for the reference aircraft.

The control yaw moment is just one explanation for the stability characteristics of the pilot-aircraft system. The importance of the optimal control pilot model approach to finding potential departure boundaries is that all characteristics of the aircraft model which could cause instability

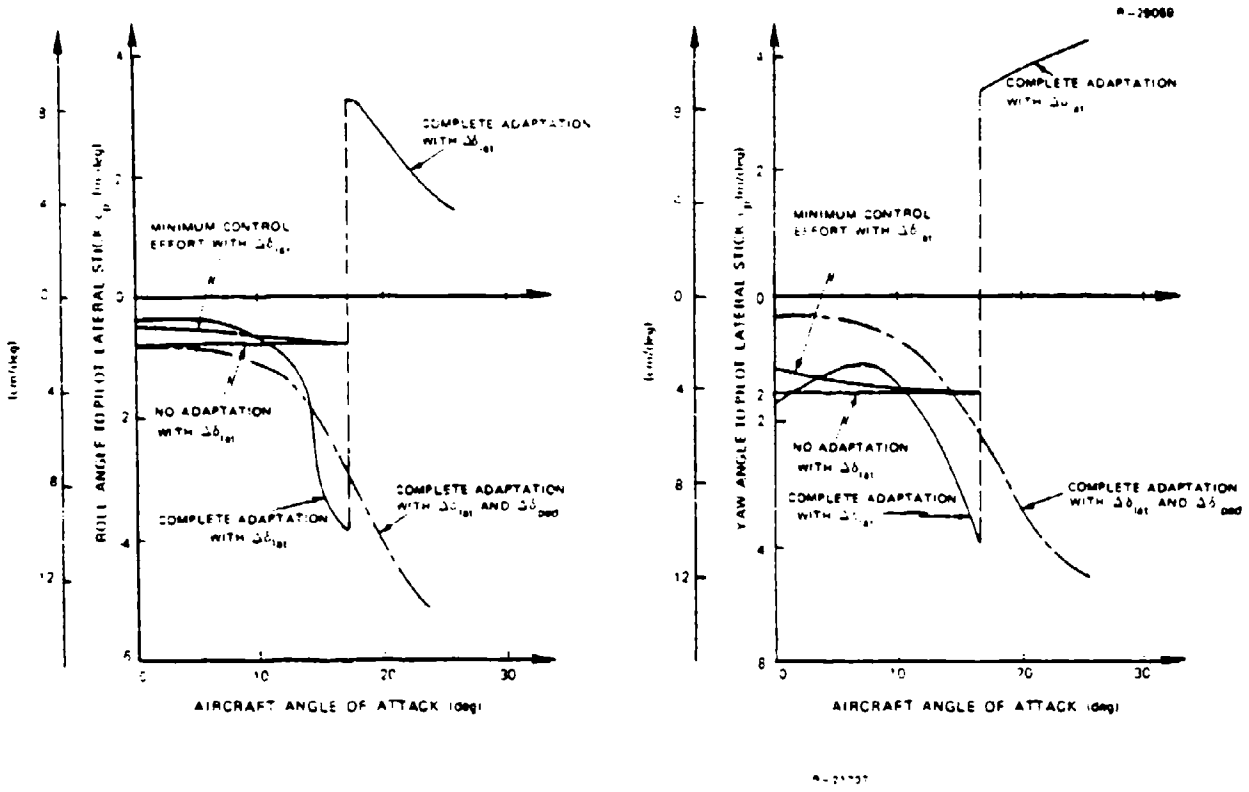

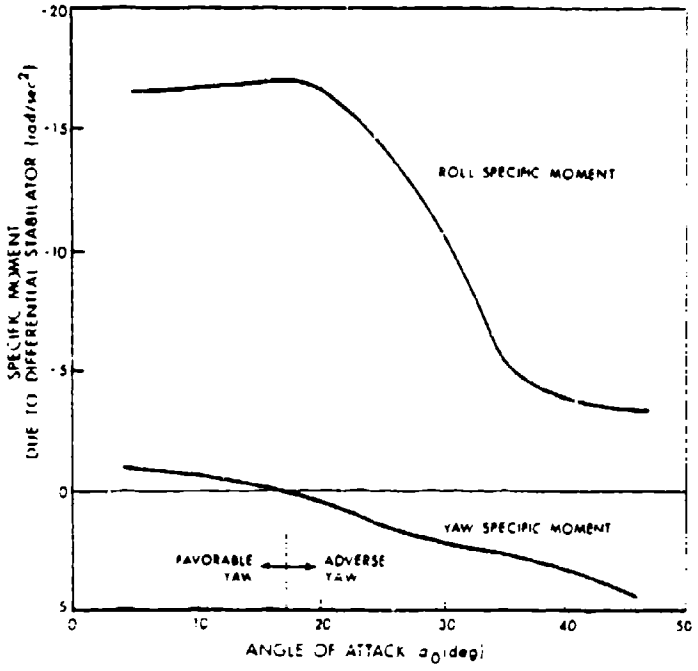

Figure 43 Pilot Model Gain Variations Under Various Adaptation Strategies (ARI Off)

are included in the analysis. The analysis is not constrained to a few parameters ($C_{n_{\beta dyn}}$, LCDP, etc.) which have shown correlation with stability boundaries in the past.

The MCE path for lateral stick control with the ARI on is shown in Fig. 44. Minimum control effort predicts stability particularly at high angles of attack. On the other hand, nonadaptive pilot model behavior fixed at α_p = 11 deg predicts an unstable Dutch roll region for α_A between 15 and 18 deg with a stable region between 20 and 29 deg.

Figure 44 constitutes a case where nonadaptation and MCE predict markedly different pilot behavior at high angles of attack. This is an indication that test results with the ARI on may have variability from pilot to pilot and even from run to run. For example, a pilot simply flying the wind-up turn trajectory will have sufficient time to monitor the MCE performance and remains reasonably adapted and stable. On the other hand, a pilot vigorously tracking an opponent who is performing a wind-up turn may not fully monitor his aircraft's flight condition. If he remains unadapted, the unstable Dutch roll region will be encountered. ARI and CAS designs other than that assumed here could eliminate the unstable Dutch roll region in Fig. 44, greatly improving the reference aircraft's capabilities.

3.4 CHAPTER SUMMARY

The optimal control pilot model is used in a technique for predicting pilot-aircraft behavior at high angles of attack. Using the pilot model algorithms developed in Ref. 2, pilot-aircraft stability diagrams are constructed by examining linear models of a fighter aircraft and pilot along

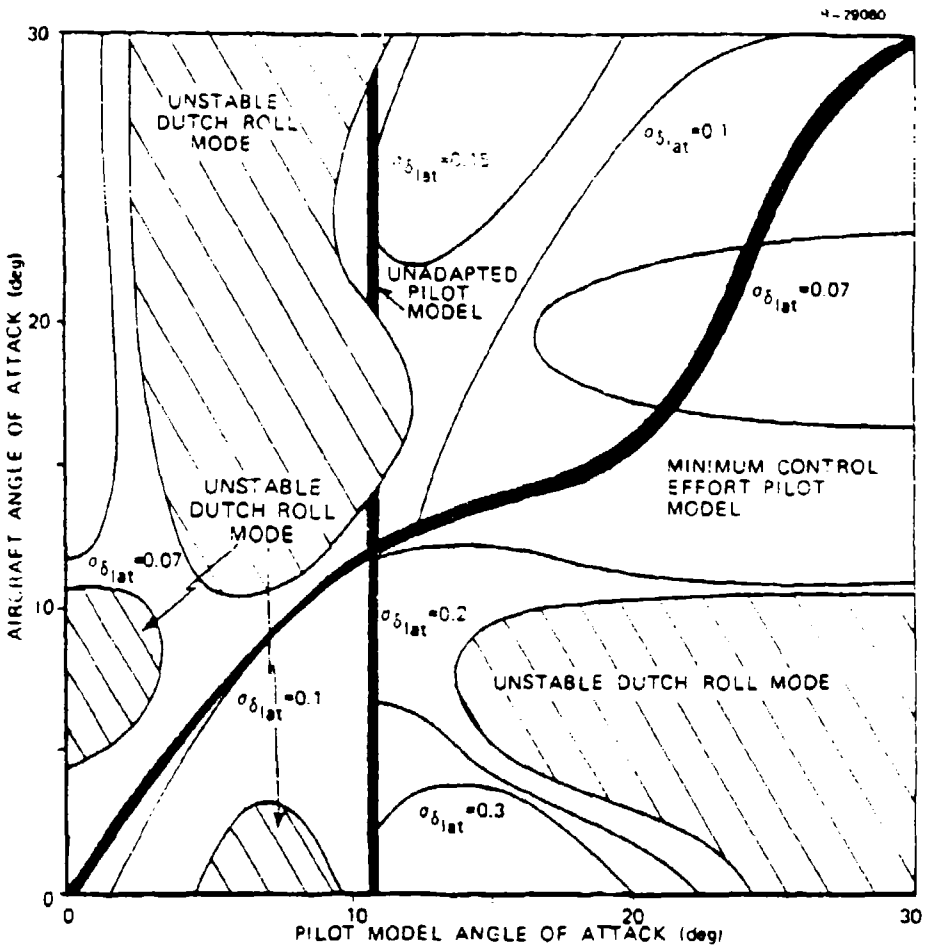

Figure 44 Prediction of Pilot Behavior at High Angle of Attack using Lateral Stick Only (ARI On)

a wind-up turn maneuver. The effects of pilot control strategies, from complete adaptation to no adaptation, can be represented and analyzed as functions of the actual flight condition and that which is assumed by the pilot in selecting his control strategy. Differing piloting strategies can result in pilot-aircraft instability. The unstable regions indicate conditions under which the aircraft could depart from controlled flight.

In the stable regions of the stability diagrams, performance contours of pilot model tracking are constructed. The performance contours show the effect of nonadapted pilot control strategy on the rms values of aircraft states and controls. The importance of the results in this chapter are:

- A new method has been determined for predicting departure boundaries of high-performance aircraft.
- The method uses all information available in a linear model of the aircraft and is not restricted to uncoupled flight conditions.
- The method incorporates pilot behavior in predicting departure boundaries through the use of the optimal control pilot model. Instabilities caused by pilot physical limitations and control strategies are included in the method.
- The effects of control implementation on departure boundaries can be included in the method. For the aircraft considered in this study, the beneficial use of an ARI is extensively studied.
- When the method indicates an instability, both the characteristics of the instability (i.e., wing rock, nose slice), as well as the relative severity, are predicted.
- When the method indicates stability, the performance of the pilot's tracking ability inside the stability region can be analyzed.

- To predict the adaptation path a pilot could take in flight, the minimum control effort (MCE) strategy can be used. An MCE strategy is shown to be the path taken by a pilot in the wind-up turn maneuver with the aircraft under study.

In summary, the optimal control pilot model shows considerable promise as a general effective approach for the prediction of pilot-aircraft behavior in maneuvering flight.

4. COMMAND AUGMENTATION SYSTEM DESIGN FOR IMPROVED MANEUVERABILITY

This chapter presents the design of a departure-prevention command augmentation system (DPCAS) for the subject aircraft. The system is designed to augment aircraft stability throughout the maneuvering envelope and to provide precise response to pilot commands. The DPCAS design employs new techniques in coordinated control mechanization and proportional-integral command system formulation.

This DPCAS design methodology is particularly useful for defining the control systems of modern aircraft, which may be expected to maneuver at high angles and with high rates, which may be equipped with redundant control surfaces, and which may be designed as control-configured vehicles (CCV). By and large, current control design practice treats each aircraft axis separately in preliminary design, using "prior art" to define control structures and "tuning" the system (including the addition of selected nonlinearities and crossfeeds) during a program of exhaustive testing. The DPCAS design approach takes the opposite approach, first defining the gain-scheduled, coupled-control structure which is required to provide "Level 1" flying qualities (Ref. 20) throughout the aircraft's maneuvering envelope and using the testing phase to simplify the controller, as appropriate. The advantage of this approach is that control system requirements are visible at an early stage of system development. Testing is required in either approach; however, DPCAS design relies less on the designer's intuition and more on quantitative measures of system performance.

This chapter's objective is to develop and demonstrate flight control design technology which can improve the performance and mission effectiveness of a fighter aircraft. Antecedents can be found in the development of departure-prevention stability augmentation systems (DPSAS) for fighter aircraft (Refs. 1 and 2) and in the design of digital-adaptive command augmentation controllers for a helicopter (Refs. 21, 22, and 23). Two versions of the DPCAS are designed using linear-optimal control theory; they are "Type 0" and "Type 1" controllers, in the parlance of control system design. The two versions yield almost identical step response characteristics for a given set of aircraft dynamics, since the Type 1 law is a linear transformation of the Type 0 law (and vice versa); however, their responses are not identical when there is measurement noise or turbulence and when the aircraft's actual characteristics do not match the characteristics used for design.

An outline of Type 0 and Type 1 DPCAS fundamentals is presented in this chapter. The aircraft motions about a reference flight path are assumed to be adequately defined by a linear model which, when combined with a quadratic cost function (to be minimized by control), leads to the DPCAS design. Using a pilot command mode discussed in Appendix C, the final part of the chapter presents control designs for a wide range of dynamic pressure, angle of attack, and roll rate. Variations in control gains caused by differing flight conditions are demonstrated graphically. A summary of results is presented at the end of the chapter, and details of Type 0/Type 1 linear-optimal control system design are described in Appendix D.

4.1 FUNDAMENTALS FOR DPCAS DESIGN

4.1.1 Type 0 and Type 1 Proportional-Integral Controllers

A Type 0 DPCAS tracks constant commands without using a pure integration in the forward loop. This means that if aircraft characteristics differ from the design model or if constant disturbances affect the aircraft (e.g., wind), the pilot must compensate to obtain the desired command response. A Type 1 DPCAS tracks constant commands with zero steady-state error using a pure integration in the forward loop. The Type 1 DPCAS performs the necessary measures needed to counteract modeling errors and disturbances. A Type 0 DPCAS has approximate trim capability, while the Type 1 DPCAS has automatic trim capability.

The design of Type 0 and Type 1 DPCAS begins with the definition of a coupled linear, time-invariant model of the aircraft,

$$\Delta\dot{\underline{x}}(t) = F\,\Delta\underline{x}(t) + G\,\Delta\underline{u}(t) \qquad (5)$$

where $\Delta\underline{u}(t)$ is the m-vector of control command perturbations, and $\Delta\underline{x}(t)$ represents the n-vector of the aircraft's dynamic states. The purpose of the control vector in a DPCAS design is to stabilize the aircraft and, at the same time, force a desired output combination of states and controls, given by

$$\Delta\underline{y}(t) = H_x\,\Delta\underline{x}(t) + H_u\,\Delta\underline{u}(t)$$

to attain an arbitrary, constant reference value, $\Delta\underline{y}_d$, of dimension ℓ; that is,

$$\lim_{t\to\infty} \Delta\underline{y}(t) = \Delta\underline{y}_d$$

where H_x and H_u are constant ($\ell \times n$) and ($\ell \times m$) matrices, respectively. The reference, $\Delta \underline{y}_d$, represents the pilot's perturbation command through the center stick, pedals, or other available control input devices.

Both the Type 0 and Type 1 DPCAS minimize the same scalar-valued cost functional of states and controls:

$$J = \int_0^\infty \left\{ \begin{bmatrix} \Delta \underline{x}^T & \Delta \underline{u}^T \end{bmatrix} \begin{bmatrix} Q_1 & M \\ M^T & Q_2 \end{bmatrix} \begin{bmatrix} \Delta \underline{x} \\ \Delta \underline{u} \end{bmatrix} + \Delta \dot{\underline{u}}^T R \, \Delta \dot{\underline{u}} \right\} dt$$

The designer's freedom rests in the choice of the matrices Q and R, which weight perturbations in state, control displacement, and control rate. The design procedure consists of the choice of Q and R, the computation of closed-loop performance, and the adjustment of Q and R, as discussed in Section 4.2.1.

The Type 0 DPCAS is shown in Fig. 45; its control command takes the following form:

$$\Delta \underline{u}(t) = \Delta \underline{u}(0) + \int_0^t \left\{ -K_1 \Delta \underline{x}(\tau) - K_2 \Delta \underline{u}(\tau) + L \Delta \underline{y}_d \right\} d\tau \qquad (6)$$

The matrix, K_1, is the state feedback gain; the matrix, K_2, is the control "low-pass filter" gain, which results from weighting $\Delta \dot{\underline{u}}$ in the cost functional; and the matrix, L, is the steady-state decoupling gain.

The Type 1 DPCAS is shown in Fig. 46, and its control command can be expressed as

$$\Delta \underline{u}(t) = -C_1 \, \Delta \underline{x}(t) - C_2 \int_0^t \left\{ \Delta \underline{y}(t) - \Delta \underline{y}_d \right\} dt - C_2 \Delta \underline{\xi}(0) \qquad (7)$$

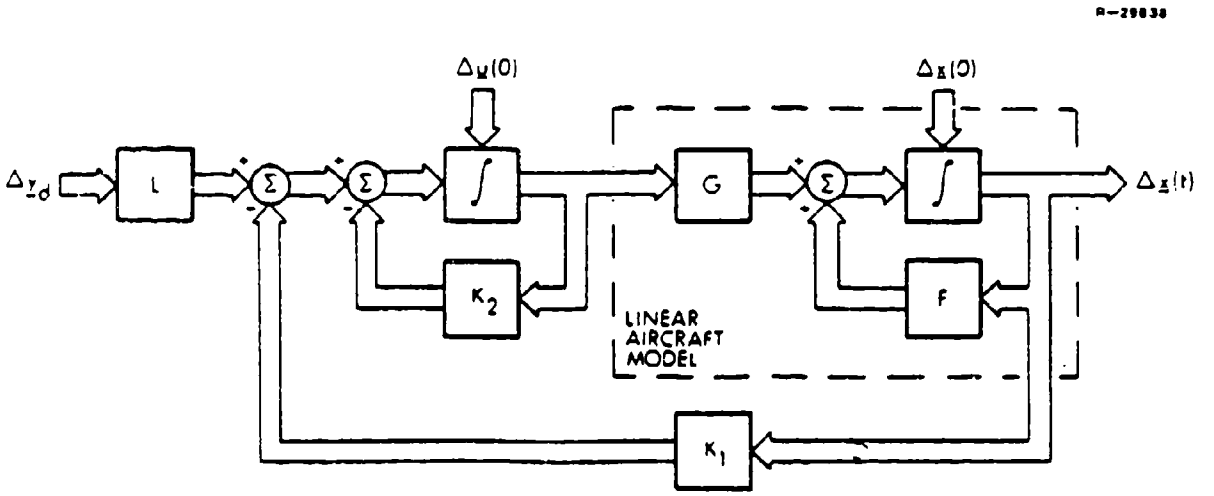

Figure 45 Type 0 DPCAS with Control-Rate Weighting

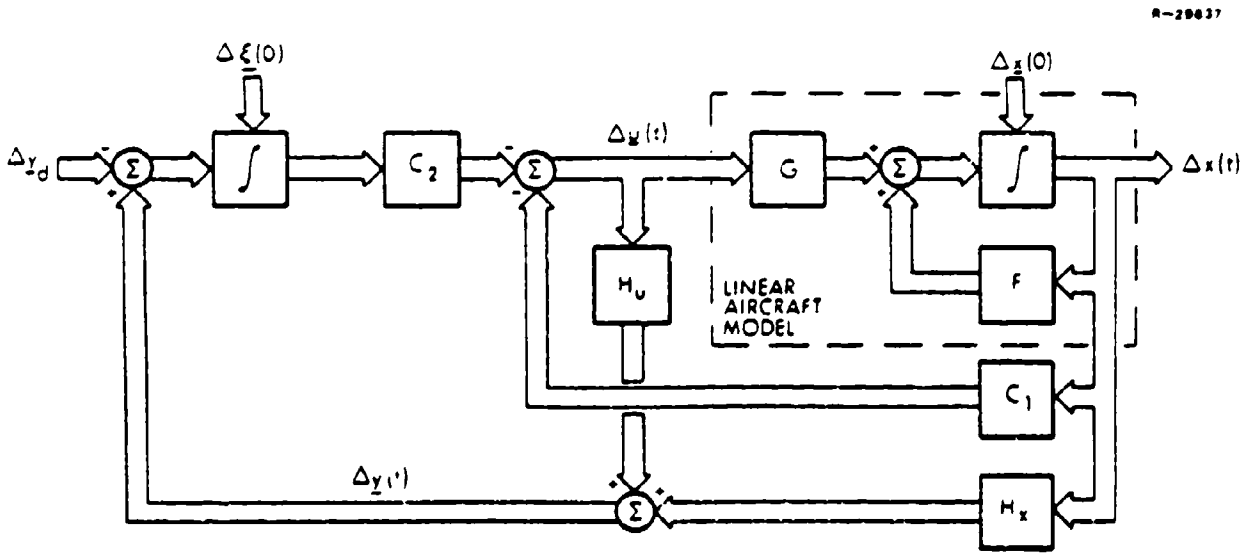

Figure 46 Type 1 DPCAS with Control-Rate Weighting

C_1 is the state feedback gain, and C_2 is the gain of the integral of the command error. The relationship between the gains in Eq. 6 and Eq. 7 is

$$\begin{bmatrix} C_1 & C_2 \end{bmatrix} \begin{bmatrix} F & G \\ H_x & H_u \end{bmatrix} \triangleq \begin{bmatrix} K_1 & K_2 \end{bmatrix} \tag{8}$$

The Type 1 control gains (C_1, C_2) and the gain L can be obtained from the Type 0 control gains (K_1 and K_2) if the composite matrix in Eq. 8 can be inverted. This requires that the matrix be square, which is not the case if the dimension of the control vector (m) and the dimension of the command vector (ℓ) are different. In such case, we can take the Penrose pseudoinverse (Ref. 24) of the $\left((n+\ell)\ (n+m)\right)$ composite matrix,

$$\begin{bmatrix} F & G \\ H_x & H_u \end{bmatrix}^{\#} = \begin{bmatrix} S_{11} & S_{12} \\ S_{21} & S_{22} \end{bmatrix} \tag{9}$$

Then, the Type 1 control gains and the gain L are readily expressed as

$$C_1 = K_1 S_{11} + K_2 S_{21}$$

$$C_2 = K_1 S_{12} + K_2 S_{22}$$

$$L = C_2$$

The derivation of these gain relationships and the "total value" version of the control laws (for implementation onboard the actual aircraft) are discussed in Appendix D.

The pseudoinverse in Eq. 9 determines a best possible alignment among the gains in Eq. 8. Different pseudoinverses obtained using a weighted-least-squares approach produce different steady-state control position values as discussed in Appendix D. When the composite matrix in Eq. 9 is square and invertible, C_1, C_2, L, and control steady-state values are unique. The reason for the nonsquare composite matrix for the DPCAS design presented here is that there are more controls than commands, as shown in the next section.

4.1.2 Command Mode Selected for Study

The study aircraft is assumed to have six controls effectors which can be commanded by the control system: throttle, $\Delta\delta_T$, stabilator, $\Delta\delta_s$, and main flap, $\Delta\delta_{mf}$ (for the longitudinal axis); spoiler, $\Delta\delta_{sp}$, differential stabilator, $\Delta\delta_{ds}$, and rudder, $\Delta\delta_r$ (for the lateral-directional axes). Appendix C discusses the candidate command modes which could be executed with this control set. Each command mode can have (at most) six independent commands. As shown in Appendix C, a perturbation command vector set which is suited to aircraft maneuvering (as distinguished from precision pointing and tracking) is: true airspeed, ΔV, normal acceleration, Δa_n, angle of attack, $\Delta\alpha$, sideslip angle, $\Delta\beta$, stability-axis roll rate, Δp_w, and lateral acceleration, Δa_y. The command vector set is similar to the direct lift/direct sideforce mode used in Ref. 3.

The total-value command vector set is related to the body-axis aircraft states as follows:

$$V = \sqrt{u^2 + v^2 + w^2}$$

$$\beta = \arctan \; v/\sqrt{u^2 + w^2}$$

$$\alpha = \arctan\,(w/u)$$

$$p_w = p \cos\alpha \cos\beta + q \sin\beta + r \sin\alpha \cos\beta$$

$$\begin{bmatrix} \dot{V} \\ a_y \\ -a_n \end{bmatrix} = H_B^W(\alpha,\beta) \left\{ \begin{bmatrix} \dot{u} \\ \dot{v} \\ \dot{w} \end{bmatrix} + \omega_{B/I} \begin{bmatrix} u \\ v \\ w \end{bmatrix} \right\} \qquad (10)$$

Only the last two rows in Eq. 10 are needed, as $\dot{V}$ is not a command variable. $H_B^W(\alpha,\beta)$ is the body-to-wind-axis transformation matrix, and $\tilde{\omega}_B^I$ is the matrix equivalent of the vector cross-product, where

$$\tilde{\omega}_B^I = \begin{bmatrix} 0 & -r & q \\ r & 0 & -p \\ -q & p & 0 \end{bmatrix}$$

By linearizing the relationships between the commands and aircraft states about the nominal flight condition, the perturbation commands can be written as

$$\Delta y_d = \left[\Delta V \;\; \Delta\alpha \;\; \Delta a_n \;\; \Delta\beta \;\; \Delta a_y \;\; \Delta B\right]^T = H_x \, \Delta\underline{x} + H_u \, \Delta\underline{u} \qquad (11)$$

where H_x and H_u are constant matrices depending on the nominal conditions. A controllability rank test of the composite matrix, Eq. 9, is presented in Appendix C; this demonstrates that the six commands can be accommodated. Unfortunately, many of the control effectors readily saturate due to control surface displacement limits for the 6-dimensional command vector. To form a more desirable control-command situation within the constraints, some commands must be eliminated. In rapid maneuvering, throttle is usually at full power; hence, ΔV can be treated as a separate control problem. A lateral acceleration command would enable the aircraft to perform a flat turn (or "side step"), but lateral acceleration is difficult to accommodate without auxiliary control surfaces (e.g., "chin fins") and is eliminated. The more common turning procedure is to bank the aircraft with Δp_w and to command normal acceleration, Δa_n, at zero sideslip angle. Keeping these three commands, Δa_n, Δp_w, and $\Delta\alpha$, angle of attack must be eliminated because main flap and stabilator have difficulty providing

direct lift with $\Delta\alpha$ held constant. Removing ΔV, $\Delta\alpha$, and Δa_y from the command vector, and $\Delta\delta_T$ from the active control vector, the perturbation commands and controls reduce to the following sets for this study:

$$\Delta\underline{y}_d = \left[\Delta a_n,\ \Delta\beta,\ \Delta p_w\right]^T$$

$$\Delta\underline{u} = \left[\Delta\delta_s,\ \Delta\delta_{mf},\ \Delta\delta_{sp},\ \Delta\delta_{ds},\ \Delta\delta_T\right]^T$$

The pilot is assumed to command normal acceleration and stability-axis roll rate with conventional center-stick motions, and sideslip angle is commanded by the foot pedals. The five control surfaces (throttle has been eliminated) receive coordinated commands from the pilot and the feedback loops. Rows and columns in H_x and H_u in Eq. 11 are eliminated as appropriate to match the reduced control-command set.

4.1.3 Flight Conditions for Point Design

The optimal control gains derived for a single flight condition would stabilize the aircraft for some range of nominal variations because linear-optimal regulators are "robust" (Ref. 25); however, changes in the aircraft dynamics would lead to less-than-optimal regulation. To understand how the control gains should change to maintain best performance during maneuvering flight, the DPCAS is redesigned at each of 25 flight conditions. As will be shown in the remainder of the chapter, it is found that many gains are relatively invariant with flight condition, some could be neglected entirely, and others must be scheduled to maintain near-optimal stability and command response.

Two separate maneuvering condition sweeps have been conducted, with the reference aircraft flying at an altitude

of 6,096 m (20,000 ft). Angle of attack and dynamic pressure are varied in the longitudinal sweep, and angle of attack and stability-axis roll rate are varied in the lateral sweep. The aircraft is trimmed at each flight condition in each sweep, because the perturbation command transformation matrix $\begin{bmatrix} H_x & H_u \end{bmatrix}$ requires knowledge of the nominal states.

A range of angles of attack and dynamic pressures is considered in the longitudinal sweep, as shown in Fig. 47a. The aircraft dynamics remain uncoupled in the longitudinal sweep. Changes in dynamic pressure, q_∞, are accomplished by changes in true airspeed, V_o,

$$q_\infty = \frac{1}{2} \rho V_o^2$$

where ρ is the air density. Changes in trim angle of attack are performed by increasing the nominal pitch rate. The solid points in Fig. 47 represent the two primary design points used to obtain the nominal DPCAS cost function weightings.

The lateral sweep, shown in Fig. 47b, varies angle of attack and stability-axis roll rate at a velocity of 144 m/s (600 fps). For non-zero roll rates, the aircraft is fully coupled about all three axes. Pitch rate is varied in the lateral sweep to maintain trim conditions.

4.2 DPCAS PERFORMANCE IN MANEUVERING FLIGHT

4.2.1 Control Design Procedure

The design procedure for the linear-optimal DPCAS design involves specifying elements in Q and R until the shapes of the step responses of the command variables and associated

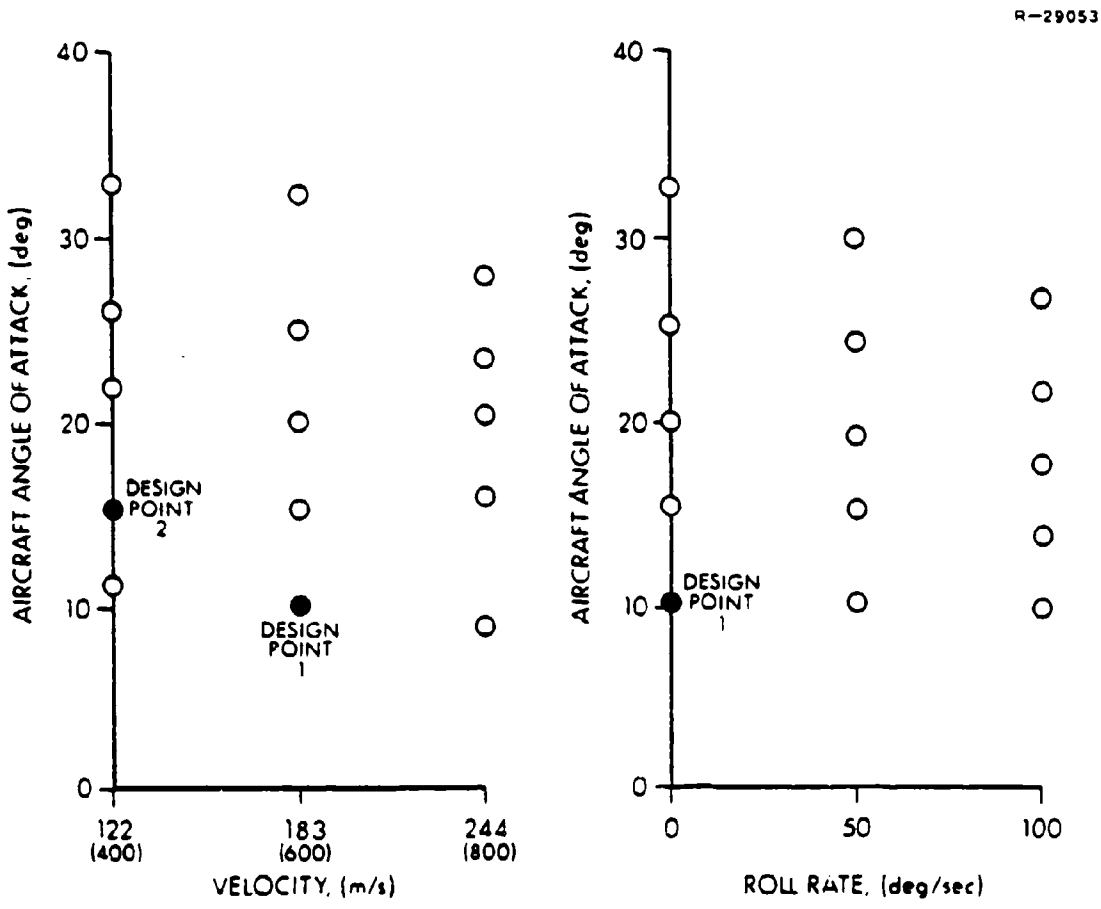

a) Longitudinal Sweep b) Lateral Sweep

Figure 47 Flight Conditions for DPCAS Point Design

control motions meet design objectives. In addition, the closed-loop eigenvalues of the system should be located in preferred regions of the left-half complex plane.

The elements in Q and R are specified as the inverses of the maximum mean-square values of the weighted variables, i.e.,

$$q_{ii} = 1/\Delta x_{i_{max}}^2$$

$$r_{ii} = 1/\Delta \dot{u}_{i_{max}}^2$$

TABLE 13 DPCAS WEIGHTS AT DESIGN POINT 1

T-1091

MATRIX	MATRIX TYPE	MATRIX ELEMENT	MAXIMUM MEAN VALUE
Q	State Position	Axial Velocity, Δu	12.2 m/s (40 fps)
		Lateral Velocity, Δv	3.05 m/s (10 fps)
		Normal Velocity, Δw	3.66 m/s (12 fps)
		Body Angular Rates	20 deg/sec
Q	State Rate	Lateral Acceleration, $\Delta \dot{v}$	3.66 m/s^2 (12 fps^2)
		Normal Acceleration, $\Delta \dot{w}$	1.53 m/s^2 (5 fps^2)
Q	Pilot Command	Stability-Axis Normal Acceleration Command, Δa_n	0.533 m/s^2 (1.75 fps^2)
		Sideslip Command, $\Delta \beta$	0.9 deg
		Stability-Axis Roll Rate Command, Δp_w	2.5 deg/sec
Q	Control Position	Stabilator Deflection, $\Delta \delta_s$	10 deg
		Main Flap Deflection, $\Delta \delta_{mf}$	5 deg
		Spoiler Deflection, $\Delta \delta_{sp}$	27 deg
		Differential Stabilator Deflection, $\Delta \delta_{ds}$	6 deg
		Rudder Deflection, $\Delta \delta_r$	15 deg
R	Control Rate	Stabilator Rate, $\Delta \dot{\delta}_s$	3 deg/sec
		Main Flap Rate, $\Delta \dot{\delta}_{mf}$	4 deg/sec
		Spoiler Rate, $\Delta \dot{\delta}_{sp}$	4 deg/sec
		Differential Stabilator Rate, $\Delta \dot{\delta}_{ds}$	3 deg/sec
		Rudder Rate, $\Delta \dot{\delta}_r$	4 deg/sec

Q is composed of weighting factors for state positions, state rates, commands, and control positions. The elements of Q combine as

$$Q = \left[\begin{array}{c|c} \frac{1}{\Delta x^2_{max}} I & 0 \\ \hline 0 & \frac{1}{\Delta u^2_{max}} I \end{array}\right] + \begin{bmatrix} F^T \\ G^T \end{bmatrix} \left[\frac{1}{\Delta \dot{x}^2_{max}} I\right] [F \; G] + \begin{bmatrix} H_x^T \\ H_u^T \end{bmatrix} \left[\frac{1}{\Delta y^2_{max}} I\right] [H_x \; H_u]$$

Q generally is full, positive definite, and has cross-weighting between state and control positions. R is diagonal and positive definite.

The Q and R elements used as the baseline design at Design Point 1 in Fig. 47 have the values shown in Table 13 for both the Type 0 and Type 1 DPCAS. The weighting on control position is chosen as one-half the maximum travel of the control surface. The weighting on control rate is chosen as one-tenth the maximum rate of the control surface actuator. The state, state rate, and command weightings are found by observing command step response time histories at the two design points in Fig. 47.

Experience has determined that five weighting elements in Q are instrumental in shaping the step response of the system:

- Increasing the lateral velocity weight (i.e., decreasing the allowable lateral velocity) decreases the sideslip rise time
- Increasing the roll rate command weight decreases the roll rate rise time
- Increasing the normal acceleration command weight decreases the normal acceleration rise time

- Increasing the lateral and normal acceleration weights reduces command overshoot and moves complex pairs to higher frequencies at higher damping ratios.

These primary weights have to be adjusted carefully, because large weights induce large gains, making the system more and more sensitive to feedback noise and increasing the possibility of limit cycles.

The DPCAS is designed to the flying qualities specification for Class IV aircraft, defined by MIL-F-8785B(ASG) (Ref. 20). Level 1 flying qualities in the Category A flight phase provide the design goal. The use of linear-optimal control theory causes the closed-loop system to meet the majority of the flying qualities specifications readily. Two criteria that require monitoring during the determination of Q and R are the short-period frequency specifications and the requirement to roll through 90 degrees in one second. The latter could not always be met at low dynamic pressure.

Table 14 shows the effect of the Type 0 and Type 1 DPCAS designs at Design Point 2 of Fig. 47. The Type 0 and Type 1 DPCAS introduce new modes, as identified in Table 14. The dynamic modes of the open-loop aircraft are classical, and they include the effects of the roll and pitch angles. As discussed in Appendix C, the roll and pitch Euler angles are not considered in the DPCAS design model. When Δa_n and Δp_w are commanded, pitch and roll angle reach unreasonable steady state values (>360 deg); hence, they become meaningless as feedback variables for regulation. Table 14 demonstrates that loop closure increases short period and Dutch roll damping and couples the roll mode with the roll command integrator state.

TABLE 14 EFFECTS OF DPCAS ON THE DYNAMIC MODE AT DESIGN POINT 2

.T-1092

DYNAMIC MODE	OPEN-LOOP CHARACTERISTICS			CLOSED-LOOP CHARACTERISTICS TYPE 0			CLOSED-LOOP CHARACTERISTICS TYPE 1		
	NATURAL FREQUENCY, rad/sec	DAMPING RATIO	TIME CONSTANT, sec	NATURAL FREQUENCY, rad/sec	DAMPING RATIO	TIME CONSTANT, sec	NATURAL FREQUENCY, rad/sec	DAMPING RATIO	TIME CONSTANT, sec
Short Period	1.28	0.423	–	3.51	0.752	–	3.54	0.753	–
Dutch Roll	1.69	0.0857	–	2.02	0.638	–	2.02	0.638	–
Roll Command				2.96	0.590	–	2.96	0.590	–
Roll	–	–	1.7						
Longitudinal Control				–	–	19.3	–	–	–
Phugoid	0.132	-0.00287	–						
Normal Acceleration Command				–	–	0.558	–	–	0.564
z-Axis Velocity				–	–	1.64	–	–	1.59
Spoiler Control				–	–	6.66	–	–	–
Spiral	–	–	14.5						
Sideslip Command				–	–	0.723			0.688

Although the number of closed-loop eigenvalues is different for the Type 0 and Type 1 systems, the DPCAS design approach provides interesting similarities between the two systems. The Type 0 closed-loop eigenvalues are given by the roots of

$$\det\left(\lambda I - \begin{bmatrix} F & G \\ -K_1 & -K_2 \end{bmatrix}\right) = 0 \tag{12}$$

while the Type 1 eigenvalues are the roots of

$$\det\left(\lambda I - \begin{bmatrix} F-GC_1 & -GC_2 \\ H_x-H_uC_1 & -H_uC_2 \end{bmatrix}\right) = 0 \tag{13}$$

The number of eigenvalues in Eq. 12 is n+m (states plus controls), while the number of eigenvalues in Eq. 13 is n+ℓ (states plus commands). If ℓ and m are equal the eigenvalues are the same in both cases. If ℓ is less than m, some eigenvalues are eliminated and others are perturbed, as shown in Table 14. In transforming from the Type 0 DPCAS to the Type 1 DPCAS, the longitudinal control and spoiler eigenvalues are eliminated.

The effect of the DPCAS design on the eigenvectors at Design Point 2 is shown in Tables 15 and 16 (only the normalized magnitudes are shown). The eigenvectors for the states change little when transforming from the Type 0 to Type 1 DPCAS. The eigenvectors for the longitudinal secondary control (main flap) actively couple into the longitudinal modes, while the lateral-directional secondary control (spoiler) is virtually separated from the other lateral-directional modes at the flight condition. This secondary control coupling behavior prevails for most of the design flight conditions considered here.

TABLE 15 EIGENVECTOR MAGNITUDES FOR THE LONGITUDINAL DYNAMICS AT DESIGN POINT 2 (V_o=122 m/s (400 fps), α_o=15.3 deg, q_o=2.5 deg/sec)

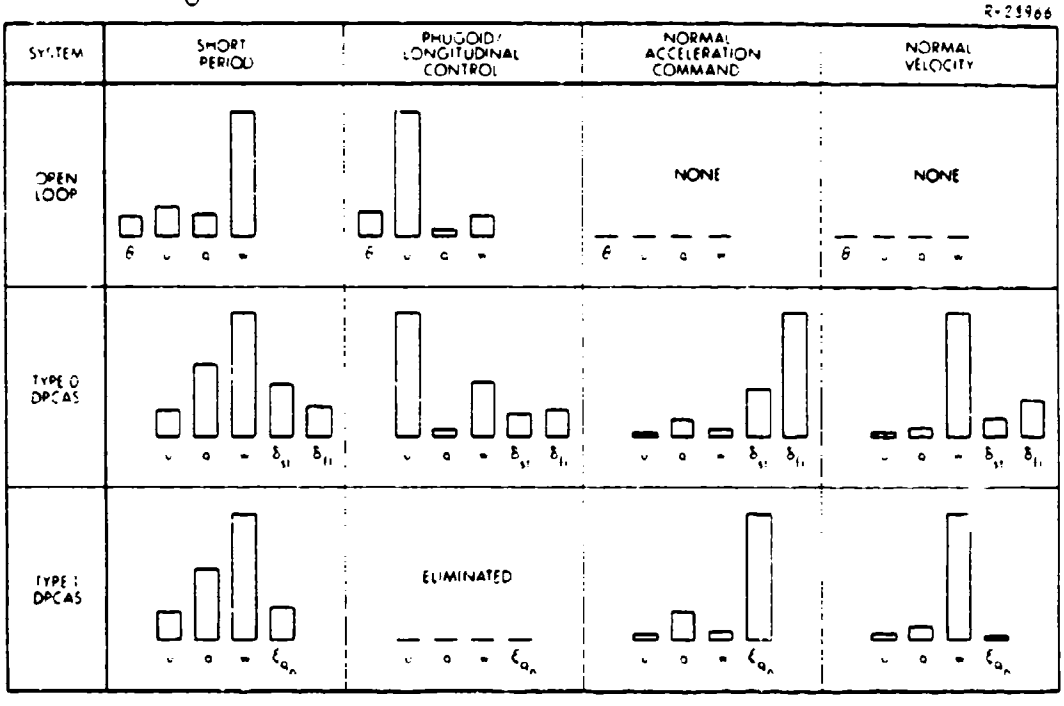

TABLE 16 EIGENVECTOR MAGNITUDES FOR THE LATERAL DYNAMICS AT DESIGN POINT 2 (V_o=122 m/s (400 fps), α_o=15.3 deg, q_o=2.5 deg/sec)

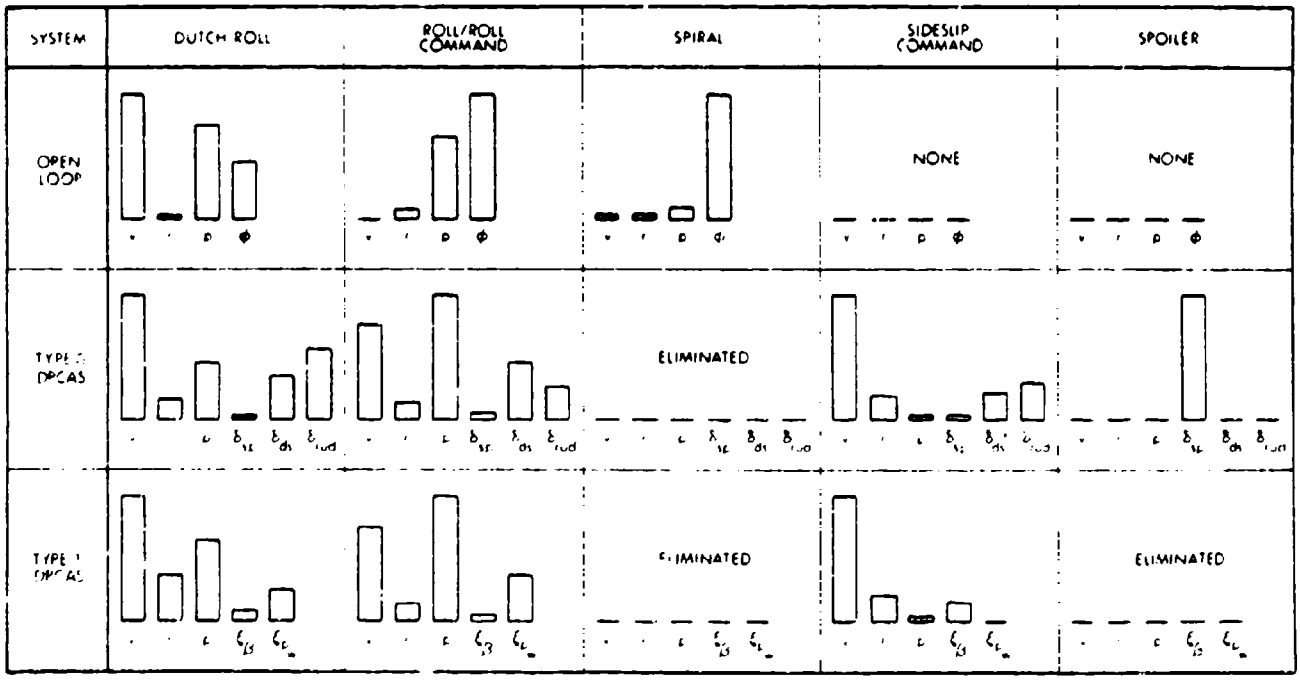

The Type 0 and Type 1 DPCAS gain matrices at Design Point 2 are shown in Tables 17 and 18. The gain matrices illustrate why damping is increased in the closed-loop system: rate feedback gains are large. The gains can be lowered by decreasing the elements of Q at the cost of possibly deteriorated (though stable) performance. Large gains for the Type 0 DPCAS may not be particularly adverse because control surface commands are passed through low-pass filters. For example, the break frequency of the low-pass filter element in Table 17 is approximately 0.58 Hz (obtained from the diagonal elements of the gain K_2). High-frequency noise effects and the potential for limit cycles are greatly reduced in the Type 0 DPCAS design.

The gains in Table 17 and 18 indicate that the stabilators and main flap equally share control requirements while rudder, particularly in the Type 1 DPCAS, is the primary controller for the lateral-directional controls. As previously noted, the spoiler has small gains and little interaction with the system states.

Command response time histories of the DPCAS design are demonstrated by separately stepping each command to unity (in English units) and simulating the control law with the linear, time-invariant aircraft model. The model is not changed as the command drives the system away from the nominal conditions. Figure 48 illustrates the smooth control movement for a normal acceleration command of 0.305 m/s^2 (1 fps^2) at Design Point 1. The steady-state main flap value indicates that the main flap will saturate for a command of 3.4 m/s^2 (0.35 g). After main flap saturates, the stabilator will accommodate the command until it saturates as well. In an operational system, provisions must be made for control saturation effects. For the Type 0 system, this could require

TABLE 17 TYPE 0 DPCAS GAINS AT DESIGN POINT 2

T-1093

CONTROLLER	FEEDBACK GAIN, K_1					
	AXIAL VELOCITY, Δu, m/sec	PITCH RATE, Δq, deg/sec	NORMAL VELOCITY, Δw, m/sec	LATERAL VELOCITY, Δv, m/sec	YAW RATE, Δr, deg/sec	ROLL RATE, Δp, deg/sec
Stabilator, $\Delta\delta_s$, deg	-0.177	-2.65	-0.466	0.0	0.0	0.0
Main Flaps, $\Delta\delta_{mf}$, deg	1.01	-1.61	1.62	0.0	0.0	0.0
Spoilers, $\Delta\delta_{sp}$, deg	0.0	0.0	0.0	-0.135	0.140	.0502
Differential Stabilator, $\Delta\delta_{ds}$, deg	0.0	0.0	0.0	1.64	-0.469	-0.939
Rudder, $\Delta\delta_r$, deg	0.0	0.0	0.0	0.994	-4.51	0.534

CONTROLLER	LOW-PASS GAIN, K_2				
	STABILATOR, $\Delta\delta_s$, deg	MAIN FLAPS, $\Delta\delta_{mf}$, deg	SPOILERS, $\Delta\delta_{sp}$, deg	DIFFERENTIAL STABILATORS, $\Delta\delta_{ds}$, deg	RUDDER, $\Delta\delta_r$, deg
Stabilator, $\Delta\delta_s$, deg	3.64	1.23	0.0	0.0	0.0
Main Flaps, $\Delta\delta_{mf}$, deg	2.18	2.99	0.0	0.0	0.0
Spoilers, $\Delta\delta_{sp}$, deg	0.0	0.0	0.158	-0.198	-0.058
Differential Stabilator, $\Delta\delta_{ds}$, deg	0.0	0.0	-0.112	3.34	-0.168
Rudder, $\Delta\delta_r$, deg	0.0	0.0	-0.058	-0.30	3.16

TABLE 18 TYPE 1 DPCAS GAINS AT DESIGN POINT 2

T-1094

CONTROLLER	FEEDBACK GAIN, C_1					
	AXIAL VELOCITY, Δu, m/sec	PITCH RATE, Δq, deg/sec	NORMAL VELOCITY, Δw, m/sec	LATERAL VELOCITY, Δv, m/sec	YAW RATE, Δr, deg/sec	ROLL RATE, Δp, deg/sec
Stabilator, $\Delta\delta_s$, deg	0.97	-1.47	-0.686	0.0	0.0	0.0
Main Flaps, $\Delta\delta_{mf}$, deg	9.64	-0.585	1.65	0.0	0.0	0.0
Spoilers, $\Delta\delta_{sp}$, deg	0.0	0.0	0.0	-0.0531	0.0624	0.0342
Differential Stabilator, $\Delta\delta_{ds}$, deg	0.0	0.0	0.0	-0.0653	0.0273	-0.580
Rudder, $\Delta\delta_r$, deg	0.0	0.0	0.0	2.43	-2.82	0.109

CONTROLLER	INTEGRATOR GAIN, C_2		
	NORMAL ACCELERATION COMMAND INTEGRATOR, $\Delta\xi_{a_n}$, m/sec	SIDESLIP COMMAND INTEGRATOR, $\Delta\xi_\beta$, deg/sec	ROLL RATE COMMAND INTEGRATOR, $\Delta\xi_{p_w}$, deg
Stabilator, $\Delta\delta_s$, deg	-3.74	0.0	0.0
Main Flaps, $\Delta\delta_{mf}$, deg	4.92	0.0	0.0
Spoilers, $\Delta\delta_{sp}$, deg	0.0	-0.00734	0.109
Differential Stabilator, $\Delta\delta_{ds}$, deg	0.0	-1.88	-1.33
Rudder, $\Delta\delta_r$, deg	0.0	4.72	-0.931

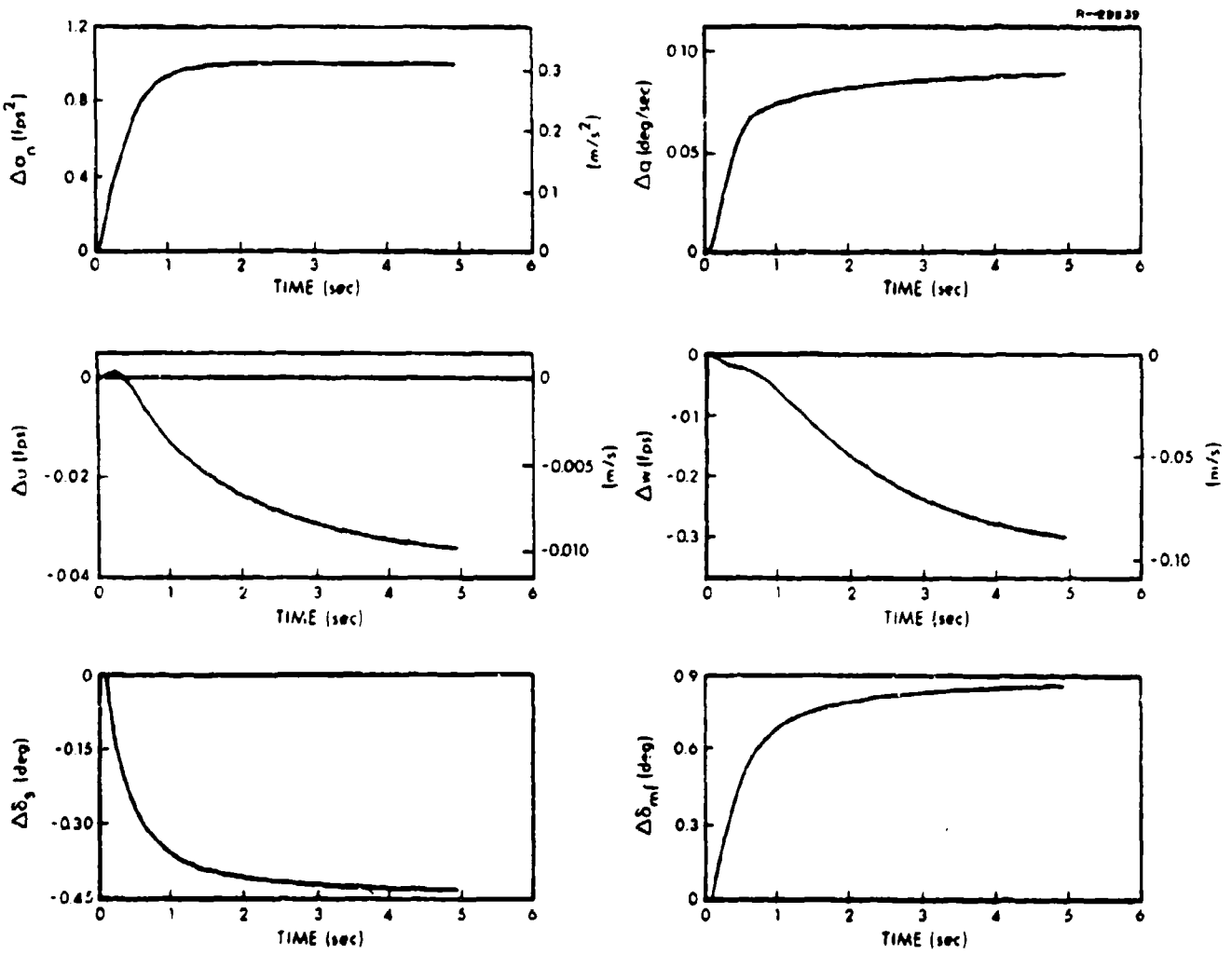

Figure 48* Normal Acceleration Command Step Response at Design Point 1 (V_o=183 m/s (600 fps), α_o=9.8 deg, q_o=5 deg/sec)

a gain shift at flap saturation and acceptance of the "g" limit associated with stabilator saturation. For the Type 1 system, "integrator runaway" (Ref. 26) also is a concern; this must be handled by "anti-windup" measures, as in Ref. 27.

The sideslip step response and stability-axis roll rate step response at Design Point 1 using the Type 1 DPCAS are shown in Figs. 49 and 50, respectively. The sideslip

*All simulations for DPCAS in this report start at 0.1 sec into the simulation.

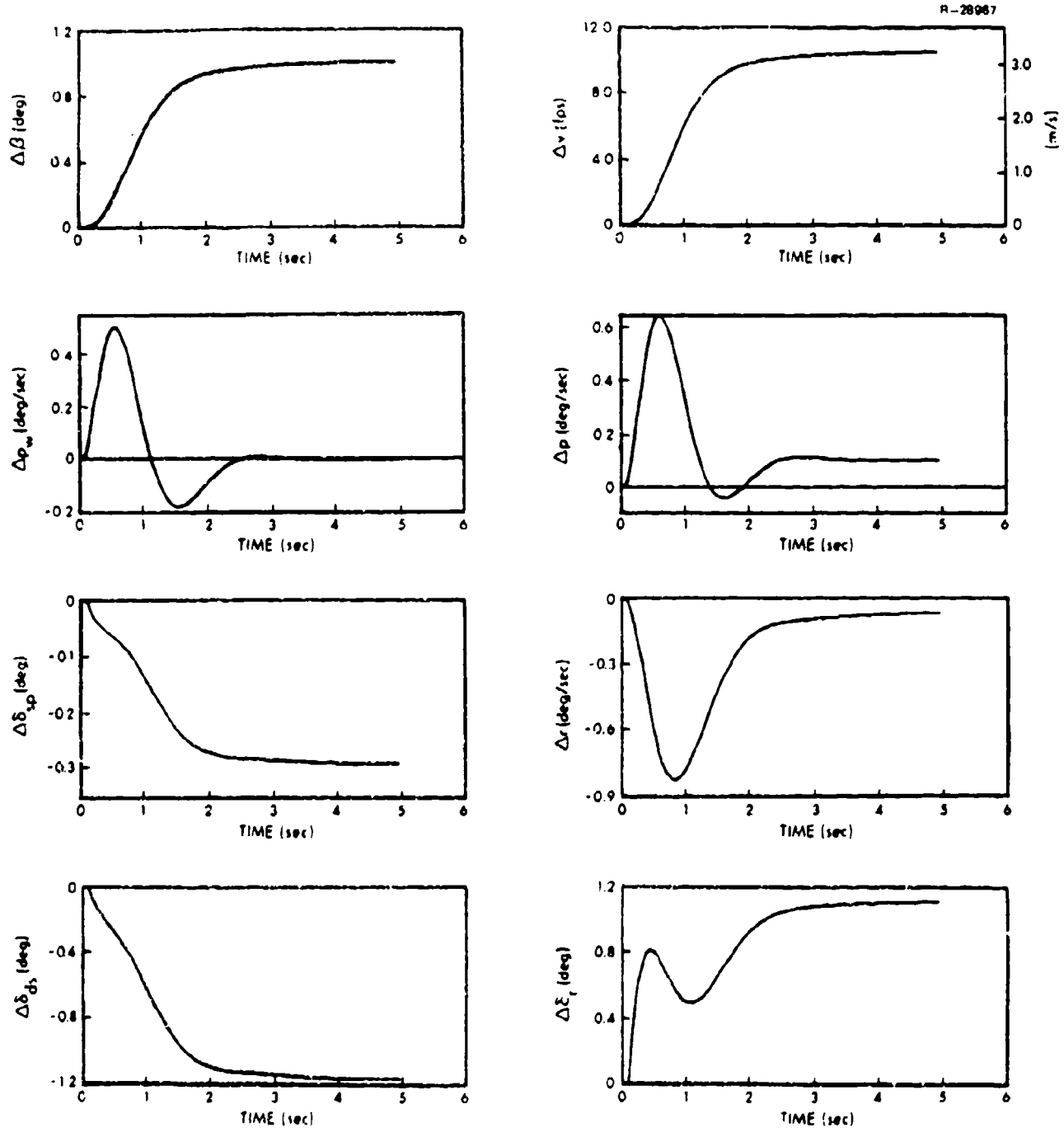

Figure 49 Sideslip Angle Command Step Response at Design Point 1 (V_o=183 m/s (600 fps), α_o=9.8 deg, q_o=5 deg/sec)

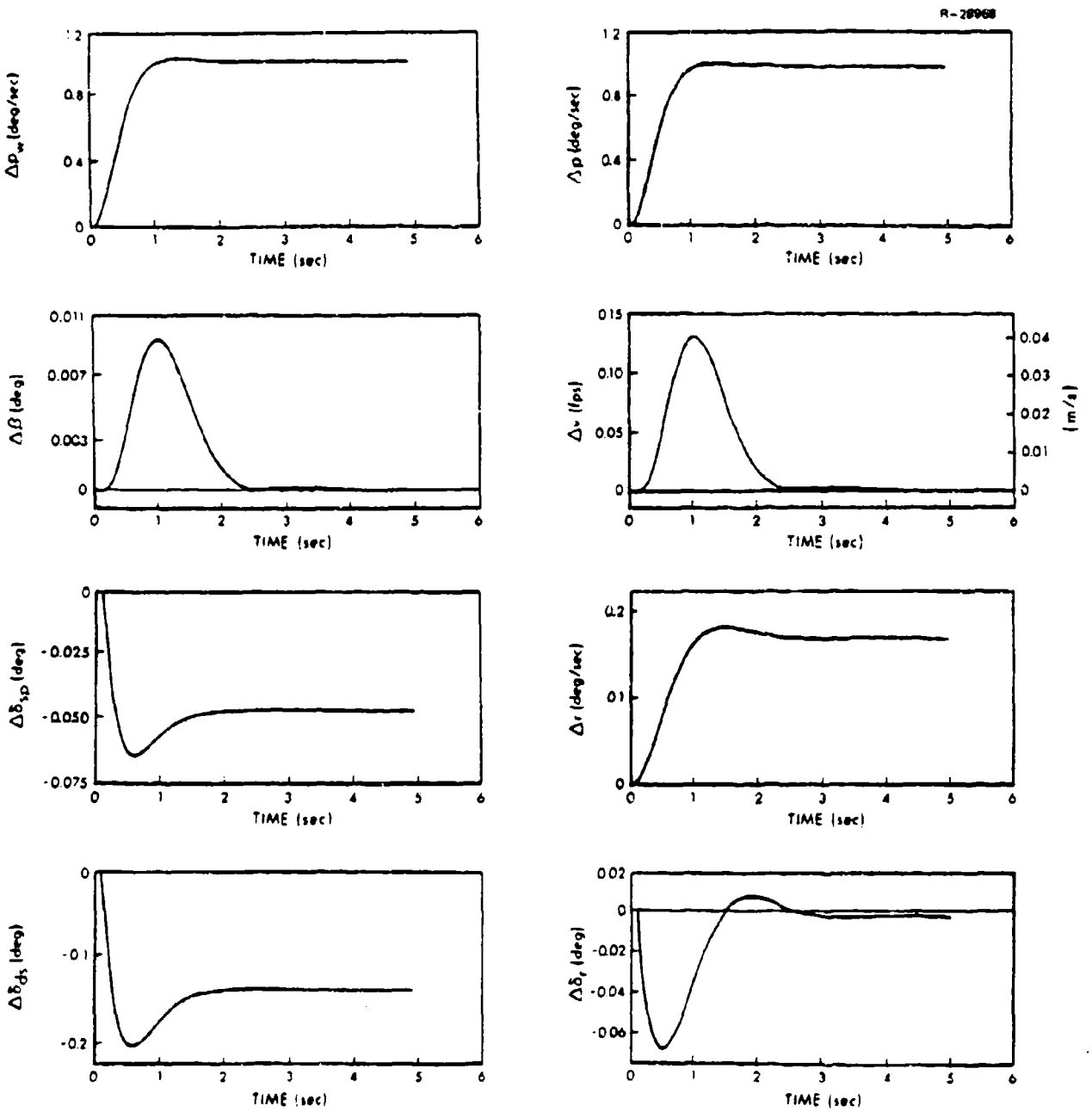

Figure 50 Stability-Axis Roll Rate Command Step Response at Design Point 1 (V_o = 183 m/s (600 fps), α_o = 9.8 deg, q_o = 5 deg/sec)

response has no overshoot, spoiler and differential stabilator smoothly reach negative values to cause zero stability-axis roll rate, and rudder oscillates to dampen the Dutch roll mode while accommodating the nonzero sideslip command. The stability-axis roll rate response is obtained from rapid differential stabilator and spoiler motions to their required steady-state values, while sideslip excursions are damped by rudder. The step responses in Figs. 48 to 50 and all remaining simulations in this chapter are computed using the Type 1 DPCAS. As indicated by the eigenvalues and eigenvectors shown in Tables 14 to 16, the state (and, therefore, the control) time histories are nearly identical for the Type 0 and Type 1 DPCAS.

4.2.2 Combined Effects of Dynamic Pressure and Angle of Attack

This section presents the effects of angle of attack and dynamic pressure on closed-loop eigenvalues, DPCAS control gains, and aircraft response. The fifteen flight points used in the sweep are shown in Fig. 47. The sweep covers much of the normal angle of attack, pitch rate, and dynamic pressure (represented as changes in velocity) range for the aircraft.

As pointed out in the previous section, there are a few key weighting elements in the cost function which apparently can be used to modify the step response of the command variables as desired. This feature is advantageously used as the angle of attack is varied to maintain approximate system uniformity. Exact system uniformity, such as might be available through pole placement algorithms, is not necessarily desirable from the pilot's point of view, because system variability can provide the pilot with useful information regarding flight condition.

The four weighting elements that are changed with flight condition are shown in Table 19. The general trend is to increase the weight by decreasing the maximum mean value as the angle of attack increases. Increasing the weights generally offsets the loss in rise time encountered as the angle of attack increases.

The effects of the weighting matrices on the response characteristics are shown in Table 20. Table 20 lists the rise time, overshoot, and settling time for each command at each flight condition. The rise time is the time it takes the response to reach 90 percent of the commanded value. The overshoot is the maximum peak of the response expressed as a percentage of the command. The settling time is the time required for the response to settle within 5 percent of the commanded value. The step response characteristics in Table 20 show little overshoot and acceptable rise times. The roll rate and sideslip results show gradual increases in rise time as the angle of attack increases. The rise time increases occur because the rudder and differential stabilator are less effective at the higher angles of attack.

Closed-loop stability at the 15 flight conditions for the longitudinal sweep are shown in Tables 21 and 22 for the Type 0 DPCAS and Type 1 DPCAS, respectively. There is little eigenvalue variation among those modes that remain in transforming from the Type 0 to Type 1 DPCAS. The most variation occurs for the normal velocity mode, which becomes faster (i.e., more stable). The three complex roots have increased natural frequency with dynamic pressure, and the damping ratios remain fairly constant under all variations. The increase in short period natural frequency is a requirement of MIL-F-8785B (Ref. 20), since the incremental change in

TABLE 19 WEIGHTING MATRIX ELEMENT VARIATIONS FOR THE LONGITUDINAL SWEEP

T-1095

MANEUVER CONDITIONS				MAXIMUM MEAN VALUE WEIGHTING MATRIX ELEMENTS			
V_o m/s (fps)	p_{w_o} deg/sec	α_o deg	q_o deg/sec	BODY-AXIS NORMAL ACCELERATION m/s^2 (fps^2)	STABILITY-AXIS NORMAL ACCELERATION m/s^2 (fps^2)	BODY-AXIS LATERAL VELOCITY m/s (fps)	STABILITY-AXIS ROLL RATE deg/sec
122 (400)	0.0	11.3	1.25	2.45 (8.0)	0.61 (2.0)	3.05 (10.0)	2.0
		15.3	2.50	1.98 (6.5)	0.61 (2.0)	3.05 (10.0)	2.0
		22.0	5.0	1.98 (6.5)	0.53 (1.75)	2.29 (7.5)	1.6
		26.7	6.25	1.98 (6.5)	0.457 (1.5)	2.13 (7.0)	1.2
		34.1	7.5	1.98 (6.5)	0.396 (1.3)	2.13 (7.0)	1.0
183 (600)	0.0	9.8	5.0	1.52 (5.0)	0.53 (1.75)	3.05 (10.0)	2.5
		15.4	7.5	1.52 (5.0)	0.53 (1.75)	2.74 (9.0)	2.1
		19.4	10.0	1.52 (5.0)	0.61 (2.0)	2.44 (8.0)	1.8
		25.0	12.5	1.52 (5.0)	0.61 (2.0)	1.98 (6.5)	1.4
		33.4	15.0	1.52 (5.0)	0.61 (2.0)	1.52 (5.0)	1.0
244 (800)	0.0	8.73	7.5	2.44 (8.0)	0.61 (2.0)	3.05 (10.0)	3.0
		16.4	12.5	1.83 (6.0)	0.914 (3.0)	3.05 (10.0)	2.5
		19.3	15.0	1.83 (6.0)	0.914 (3.0)	2.74 (9.0)	2.5
		23.4	17.5	1.83 (6.0)	1.22 (4.0)	3.05 (10.0)	2.5
		28.1	20.0	1.83 (6.0)	1.22 (4.0)	2.44 (8.0)	2.0

TABLE 20 STEP RESPONSE CHARACTERISTICS FOR THE LONGITUDINAL SWEEP

T-1096

MANEUVER CONDITIONS			STABILITY-AXIS NORMAL ACCELERATION COMMAND			SIDESLIP COMMAND			STABILITY-AXIS ROLL RATE COMMAND		
V_o m/s (fps)	a_o deg	q_o deg/sec	RISE TIME, sec	OVER-SHOOT, percent	SETTLING TIME, sec	RISE TIME, sec	OVER-SHOOT, percent	SETTLING TIME, sec	RISE TIME, sec	OVER-SHOOT, percent	SETTLING TIME, sec
122 (400)	11.3	1.25	1.90	–	2.60	1.90	1.70	2.05	1.00	2.0	1.10
	15.3	2.50	1.55	–	2.05	2.00	–	2.40	1.10	1.8	1.25
	22.0	5.00	1.45	–	1.80	2.10	–	2.55	1.2	1.6	1.35
	26.7	6.25	1.3	–	1.65	2.25	–	2.70	1.30	1.6	1.55
	34.1	7.50	1.25	2.5	1.45	5.00	–	>5.00	1.50	2.6	1.65
183 (600)	9.80	5.0	0.85	–	1.10	1.75	–	2.25	0.75	2.0	0.85
	15.4	7.5	0.65	–	0.80	1.75	–	2.20	0.75	1.4	0.85
	19.4	10.0	0.70	–	0.85	1.80	–	2.20	0.80	1.6	0.90
	25.0	12.5	0.75	–	0.90	1.75	–	2.15	0.90	1.7	1.00
	33.4	15.0	0.80	–	0.95	3.00	–	3.90	1.00	1.0	1.10
244 (800)	8.73	7.5	0.60	–	0.80	1.85	–	2.35	0.65	2.1	0.70
	16.4	12.5	0.55	–	0.70	1.90	–	2.40	0.65	2.2	0.70
	19.3	15.0	0.55	–	0.70	1.85	–	2.30	0.70	2.2	0.80
	23.4	17.5	0.75	–	0.95	2.00	–	2.55	0.85	2.0	0.95
	28.3	20.0	0.80	–	1.00	1.90	–	2.30	0.95	2.0	1.05

TABLE 21 TYPE 0 DPCAS CLOSED-LOOP EIGENVALUES FOR THE LONGITUDINAL SWEEP

T-1097

MANEUVER CONDITIONS			SHORT PERIOD		NORMAL ACCEL-ERATION COMMAND	NORMAL VELOCITY	LONGI-TUDINAL CONTROL	ROLL COMMAND		DUTCH ROLL		SIDESLIP COMMAND	SPOILER
V_o m/s (fps)	α_o deg	q_o deg/sec	ω_n rad/sec	ζ –	τ sec	τ sec	τ sec	ω_n rad/sec	ζ –	ω_n rad/sec	ζ –	τ sec	τ sec
122 (400)	11.3	1.25	3.36	0.674	0.674	1.43	26.1	2.10	0.518	2.91	0.733	0.718	4.78
	15.3	2.50	3.51	0.752	0.558	1.64	19.3	2.96	0.590	2.02	0.638	0.723	6.66
	22.0	5.00	2.89	0.747	0.442	1.83	9.22	3.35	0.523	1.77	0.765	0.649	6.74
	26.7	6.25	2.67	0.694	0.338	1.93	6.77	3.38	0.567	1.57	0.790	0.583	6.28
	34.1	7.50	2.69	0.394	0.279	2.00	6.84	2.94	0.480	1.93	0.958	4.95	2.28
183 (600)	9.8	5.0	7.13	0.747	0.351	1.92	23.2	3.78	0.651	3.38	0.657	0.692	5.42
	15.4	7.5	6.89	0.814	0.221	2.23	10.9	4.57	0.584	3.05	0.692	0.667	6.67
	19.4	10.0	6.86	0.808	0.247	2.29	7.16	5.05	0.532	2.91	0.741	0.651	6.72
	25.0	12.5	5.64	0.782	0.563	2.61	6.82	5.27	0.549	2.61	0.798	0.564	6.82
	33.4	15.0	5.26	0.664	0.160	0.341*	0.979*	4.58	0.533	2.73	0.952	1.16	6.92
244 (800)	8.73	7.5	9.07	0.756	0.245	1.44	18.2	5.23	0.618	4.40	0.745	0.710	5.05
	16.4	12.5	9.71	0.776	0.214	1.98	6.97	6.32	0.568	3.92	0.736	0.727	6.71
	19.3	15.0	9.62	0.786	0.208	2.03	6.78	6.70	0.532	3.63	0.764	0.700	5.21
	23.4	17.5	8.76	0.743	0.286	2.14	6.83	6.75	0.552	3.20	0.795	0.759	4.18
	28.1	20.0	8.59	0.715	0.316	0.385*	0.999*	6.51	0.637	2.86	0.821	0.658	6.90

*Complex Pair

TABLE 22 TYPE 1 DPCAS CLOSED-LOOP EIGENVALUES FOR THE LONGITUDINAL SWEEP

T-1098

MANEUVER CONDITIONS			SHORT PERIOD		NORMAL ACCEL-ERATION COMMAND	NORMAL VELOCITY	ROLL COMMAND		DUTCH ROLL		SIDESLIP COMMAND
V_o m/s (fps)	α_o deg	q_o deg/sec	ω_n rad/sec	ζ	τ sec	τ sec	ω_n rad/sec	ζ	ω_n rad/sec	ζ	τ sec
122 (400)	11.3	1.25	3.38	0.673	0.673	1.73	2.10	0.518	2.41	0.733	0.718
	15.3	2.50	3.54	0.753	0.564	1.59	2.96	0.590	2.02	0.638	0.722
	22.0	5.00	2.96	0.748	0.443	1.92	3.35	0.522	1.77	0.765	0.649
	26.7	6.25	2.77	0.701	0.514	2.11	3.38	0.567	1.57	0.790	0.582
	34.1	7.50	2.78	0.438	0.281	2.00	2.94	0.480	1.93	0.958	4.93
183 (600)	9.8	5.0	7.13	0.747	0.351	1.75	3.78	0.651	3.38	0.657	0.692
	15.4	7.5	6.91	0.814	0.221	1.98	4.57	0.584	3.05	0.691	0.666
	19.4	10.0	6.89	0.808	0.247	1.90	5.05	0.531	2.91	0.741	0.651
	25.0	12.5	5.71	0.782	0.562	2.02	5.27	0.549	2.61	0.798	0.564
	33.4	15.0	5.41	0.674	0.162	2.87	4.58	0.534	2.73	0.952	1.16
244 (800)	8.73	7.5	9.07	0.756	0.245	1.34	5.23	0.618	4.40	0.745	0.710
	16.4	12.5	9.74	0.776	0.212	1.66	6.32	0.568	3.92	0.736	0.727
	19.3	15.0	9.65	0.785	0.206	1.59	6.70	0.532	3.63	0.764	0.700
	23.4	17.5	8.83	0.744	0.286	1.63	6.75	0.552	3.20	0.795	0.759
	28.1	20.0	8.66	0.716	0.316	1.56	6.51	0.637	2.86	0.821	0.658

normal acceleration divided by the incremental change in angle of attack increases with dynamic pressure.

The effects of varying dynamic pressure on the step response of the commanded variables are shown in Figs. 51 to 53. The main flap and stabilator controls have decreased steady-state values as the rise in dynamic pressure increases control effectiveness, as shown in Fig. 51. The rudder, differential stabilator, and spoiler controls have approximately the same steady-state requirements for sideslip and roll rate responses in Figs. 52 and 53, with more rudder movement needed at the lower velocities to dampen the Dutch roll mode.

As indicated in Table 20, the step response time histories for the commanded variables do not change significantly from Figs. 51 to 53 as the angle of attack increases. On the other hand, the necessary control motions, particularly for the lateral-directional dynamics, can have significant changes at higher angles of attack, as shown in Fig. 54. To satisfy a one-deg/sec roll rate command at α_o = 32.4 deg, spoiler motion changes sign, differential stabilator initially moves in a positive direction to counteract the adverse yaw effect at high α_o, and a considerable amount of rudder is needed to return a slow sideslip mode back to zero.

There are 36 non-trivial Type 0 DPCAS gains and 23 non-trivial Type 1 DPCAS generated for the angle of attack-dynamic pressure sweep. Plotting some of these gains as functions of the flight condition brings out the basic relationships that could be used to form a gain schedule.

Longitudinal Gains - The gains in Figs. 55 to 58 show a fairly orderly progression with velocity, and the variation with α_o shows a distinct change at 20-deg α_o. As the

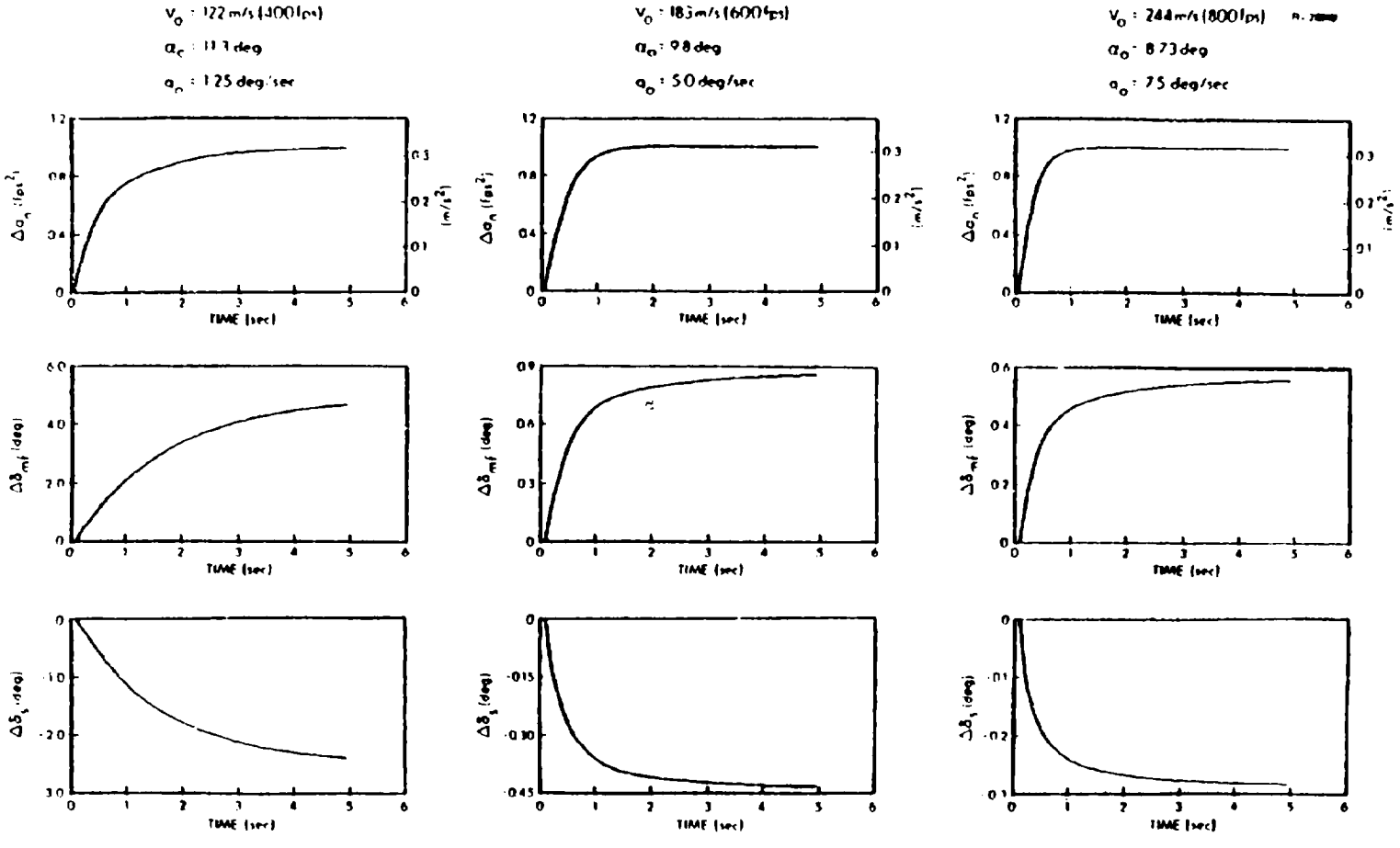

Figure 51 Normal Acceleration Step Responses for Varying Dynamic Pressure, $\Delta a_{n_d} = 0.305$ m/s^2 (1.0 fps^2)

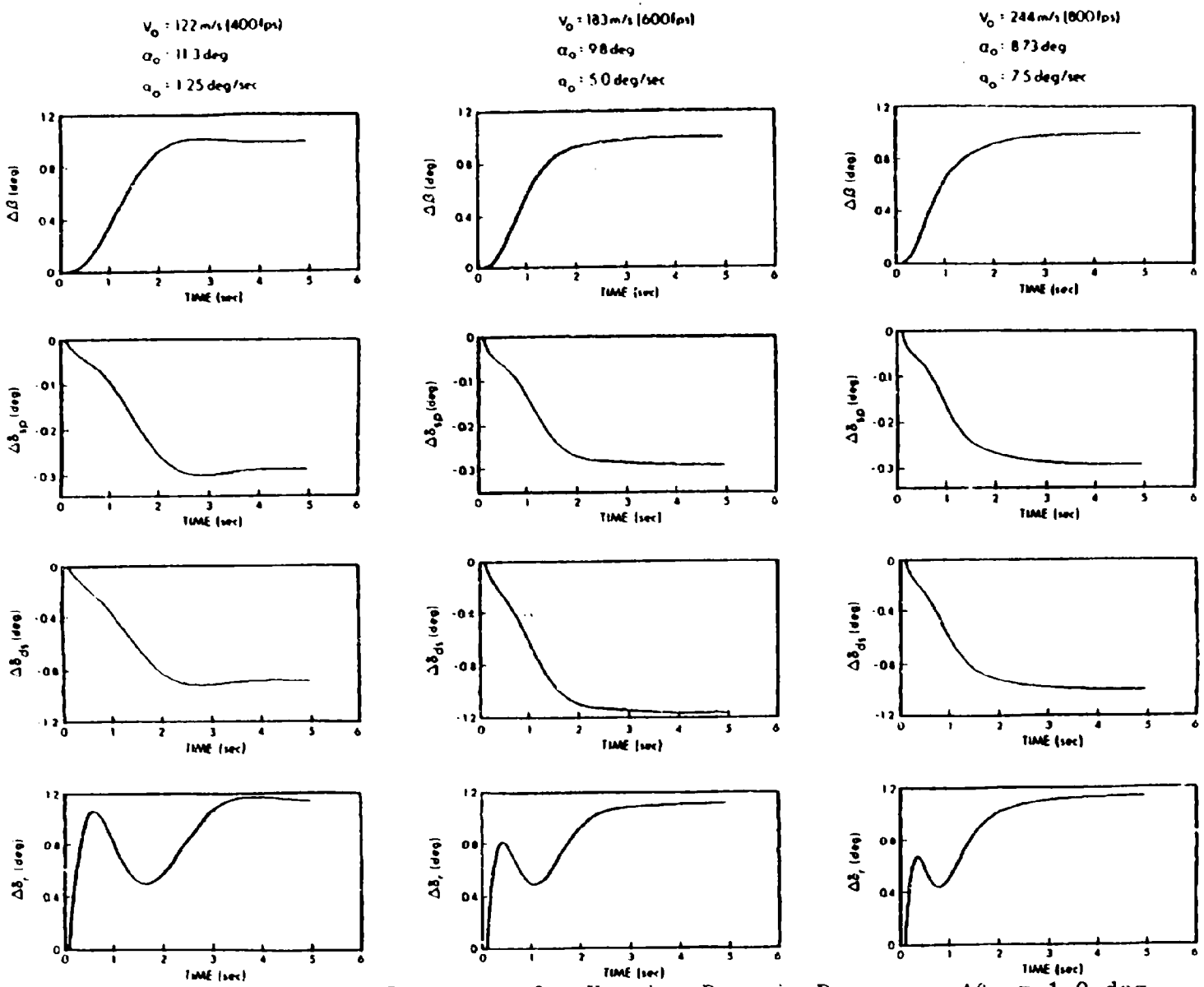

Figure 52 Sideslip Step Responses for Varying Dynamic Pressure, $\Delta\beta_d$ = 1.0 deg

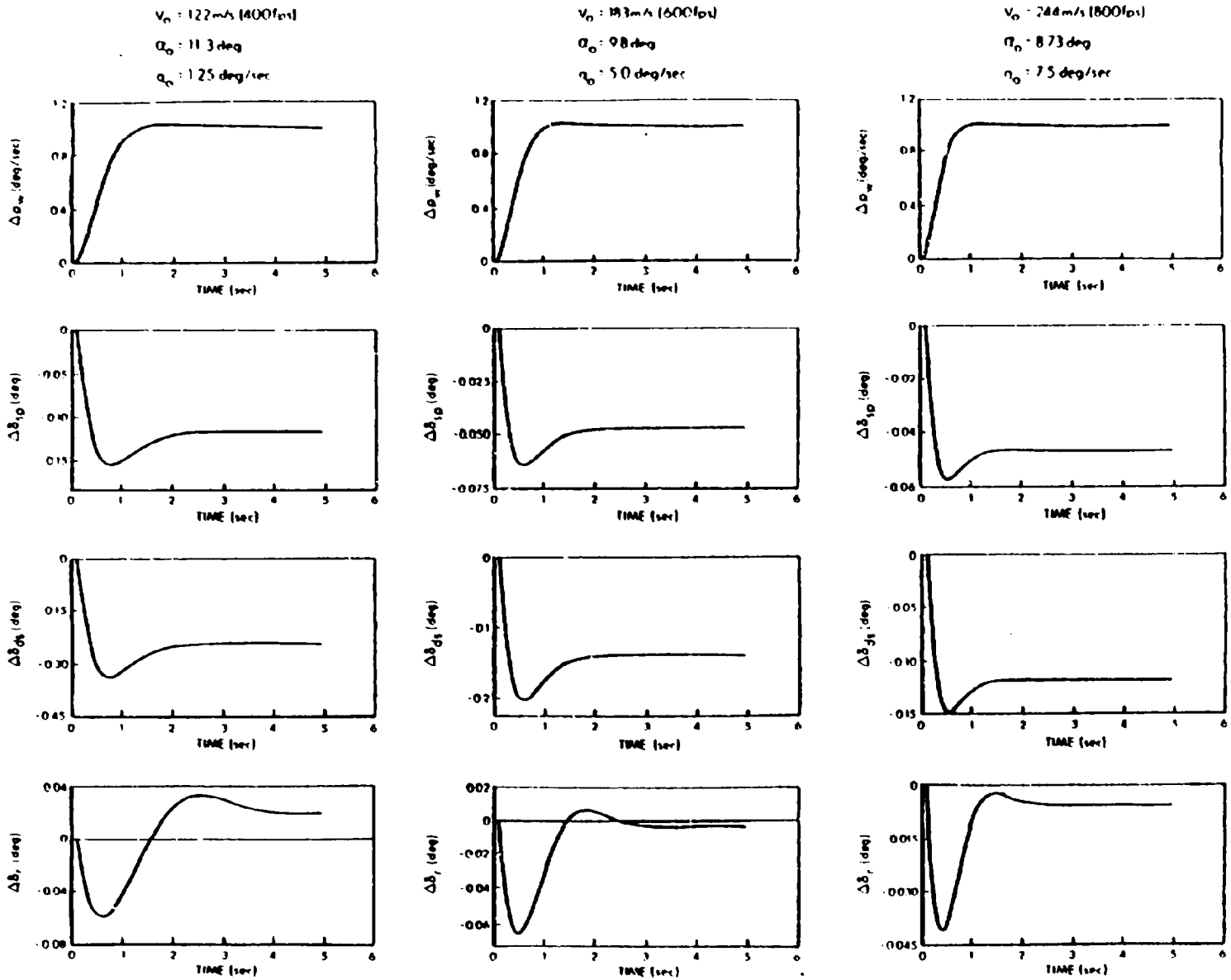

Figure 53 Stability-Axis Roll Rate Step Responses for Varying Dynamic Pressure, Δp_{w_d} = 1.0 deg/sec

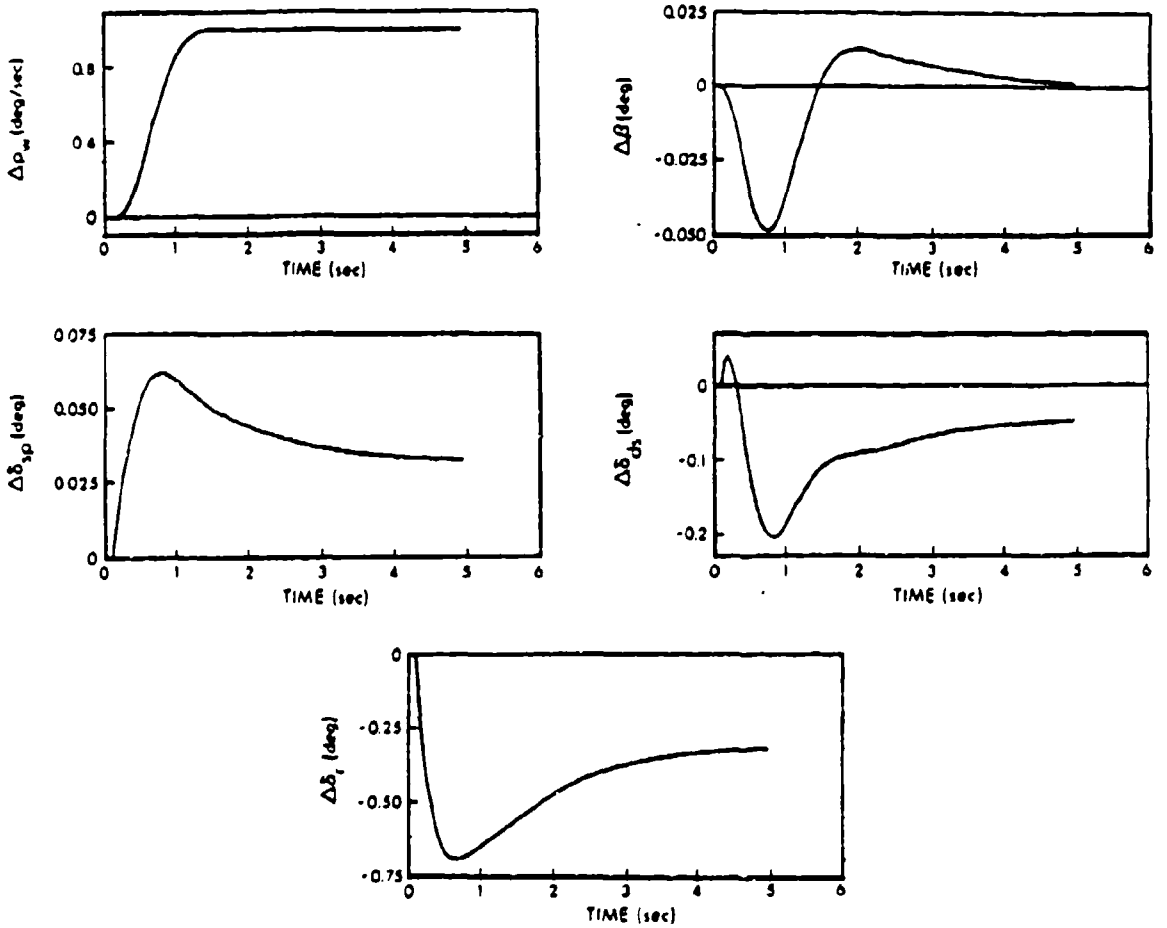

Figure 54 Stability-Axis Roll Rate Step Response at V_o=183 m/s (600 fps), α_o=33.4 deg, q_o=15 deg/sec, Δp_{w_d}=1 deg/sec

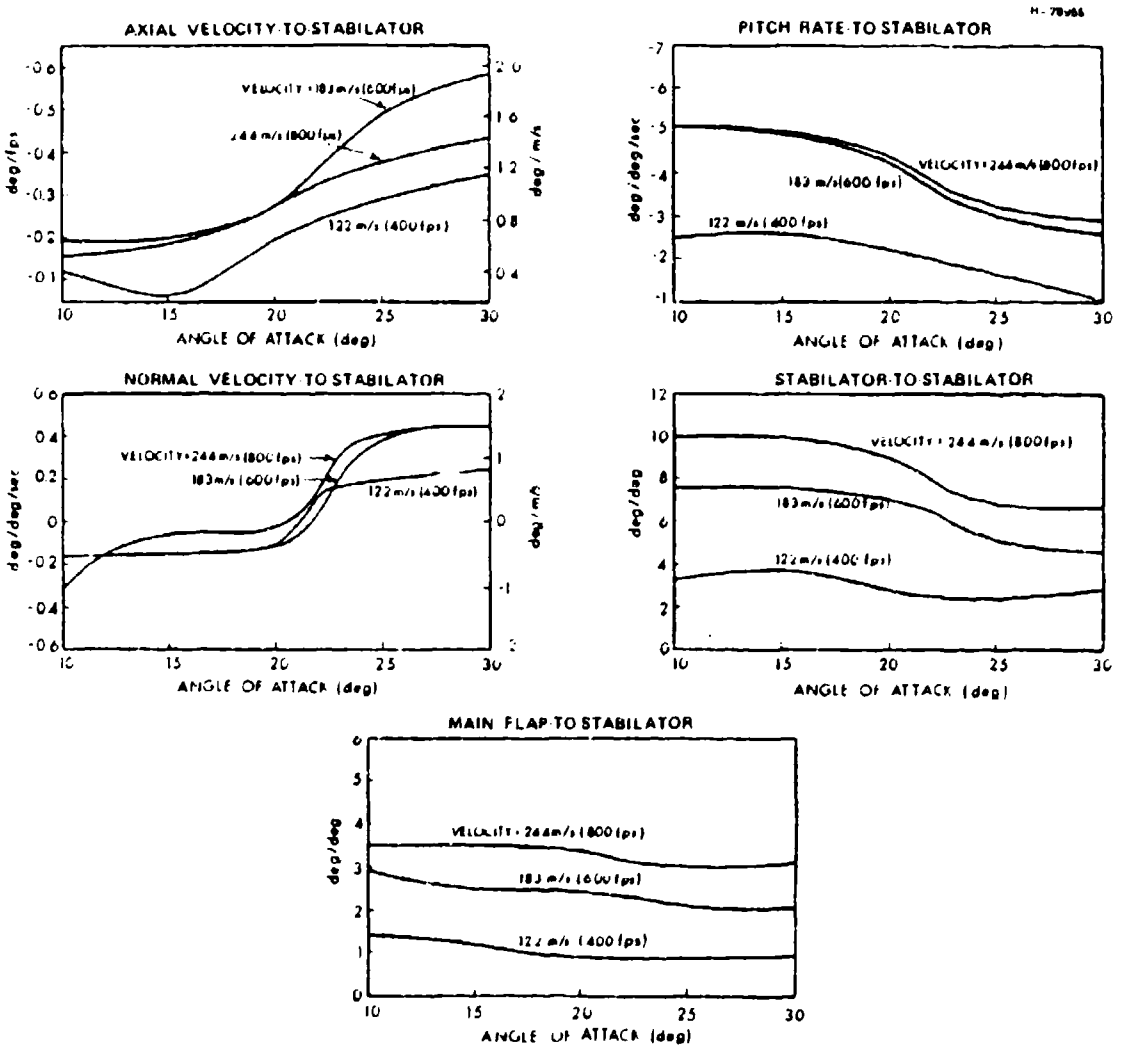

Figure 55 Angle of Attack-Dynamic Pressure Sweep -- Stabilator Type 0 DPCAS Gains

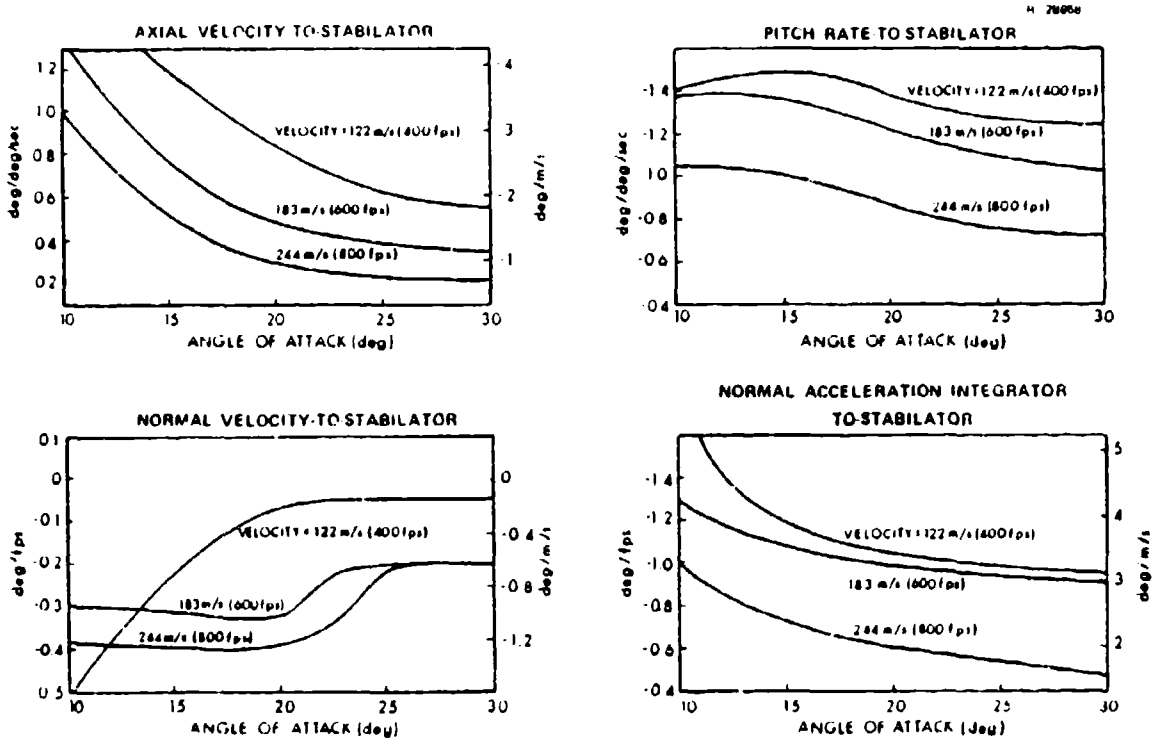

Figure 56 Angle of Attack-Dynamic Pressure Sweep -- Stabilator Type 1 DPCAS Gains

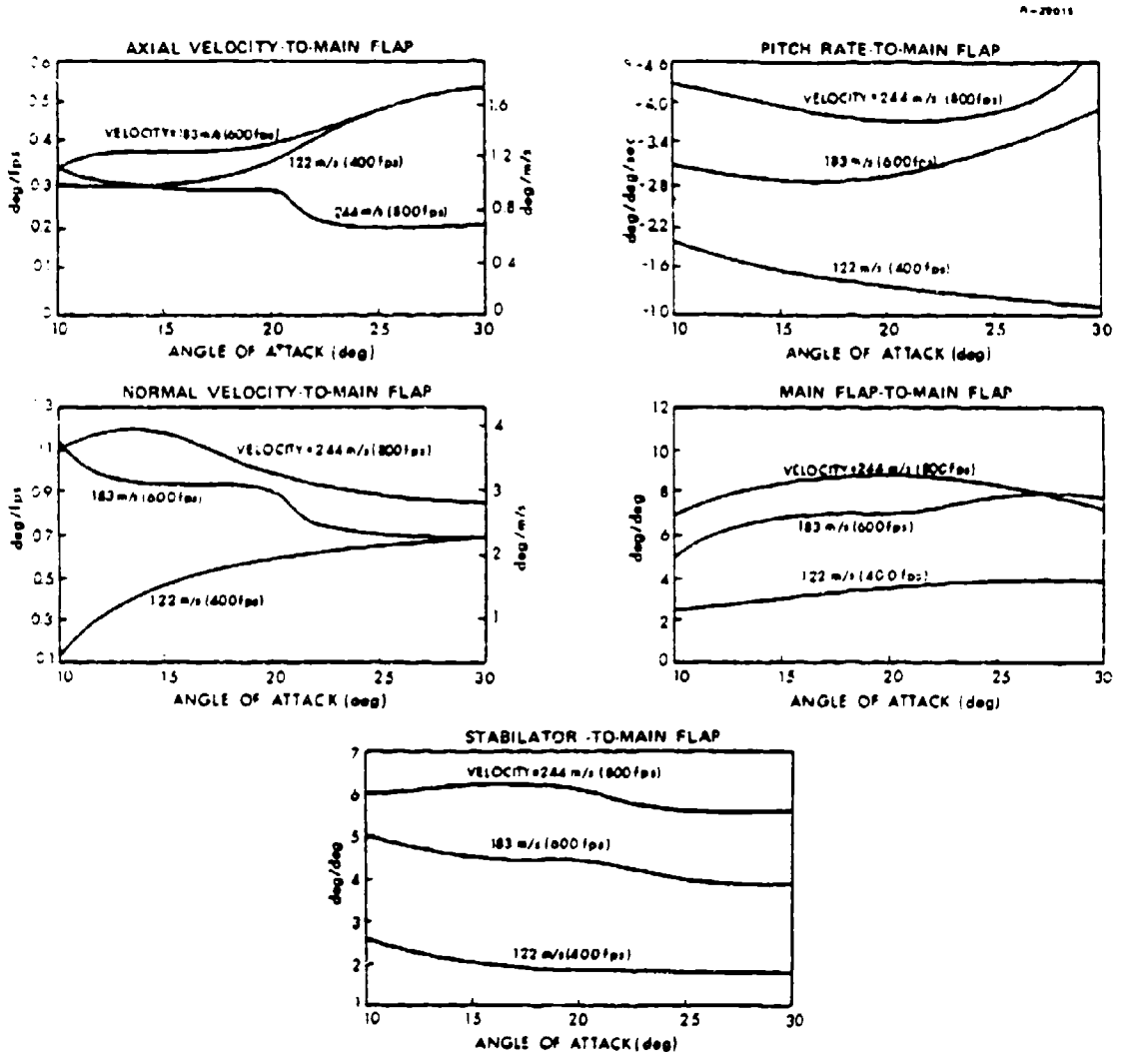

Figure 57 Angle of Attack-Dynamic Pressure Sweep - Main Flap Type 0 DPCAS Gains

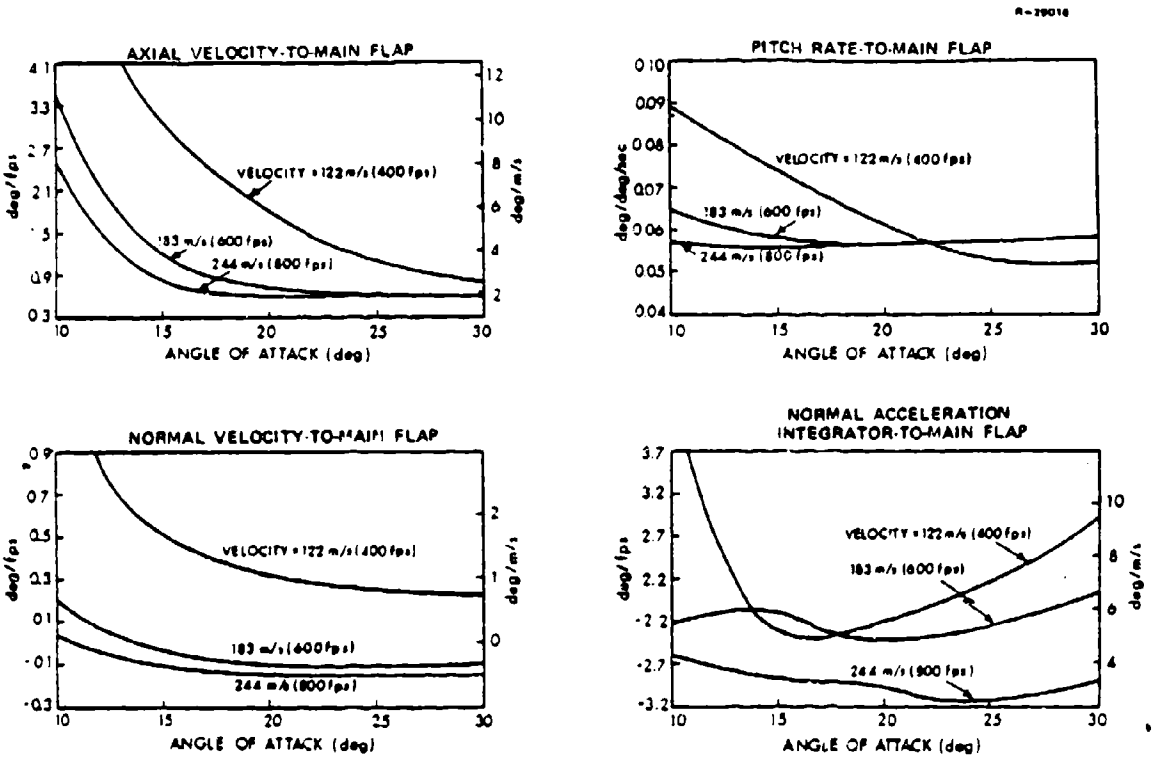

Figure 58 Angle of Attack-Dynamic Pressure Sweep - Main Flap Type 1 DPCAS Gains

velocity increases, the $\Delta\delta_s$-to-$\Delta\delta_s$ gains in Fig. 55 and $\Delta\delta_{mf}$-to-$\Delta\delta_{mf}$ gains in Fig. 57 increase to enlarge the bandwidth of the low-pass filter for the Type 0 DPCAS. The velocity feedback gains for the Type 1 DPCAS (Figs. 56 and 58) tend to be large at low angles of attack. Some reduction in normal acceleration command performance at low α_o would be required to reduce the velocity gains.

Lateral Gains - Spoiler gains show a general trend of approaching zero as the angle of attack increases (Figs. 59 and 60). Changes with velocity in spoiler and differential stabilator gains are evident in Figs. 59 to 62, primarily at low angles of attack. Many of the spoiler and differential stabilator gains show sign changes just before α_o = 15 deg. In the transformation from Type 0 DPCAS to Type 1 DPCAS, the state feedback gains undergo a reduction in magnitude. The reduction compensates for the fact that the Type 1 DPCAS feeds back all frequency components in the state equally without the low-pass filter effect. Increased yaw moment effectiveness of the differential stabilator relative to the rudder is apparent in the increase in yaw rate and sideslip integrator gains as the angle of attack increases (Figs. 61 and 62).

Directional Gains - The rudder gains shown in Figs. 63 and 64 reflect variations with increasing α_o as the fuselage blocks the flow over the aircraft tail. The rudder decreases its sideslip control and increases its roll rate control as the angle of attack increases. This is demonstrated by the integrator gains in Fig. 64. The gain variations for rudder reflect the aerodynamic changes that occur after α_o = 20 deg. The rudder gains show a fairly orderly progression as the dynamic pressure increases. The most

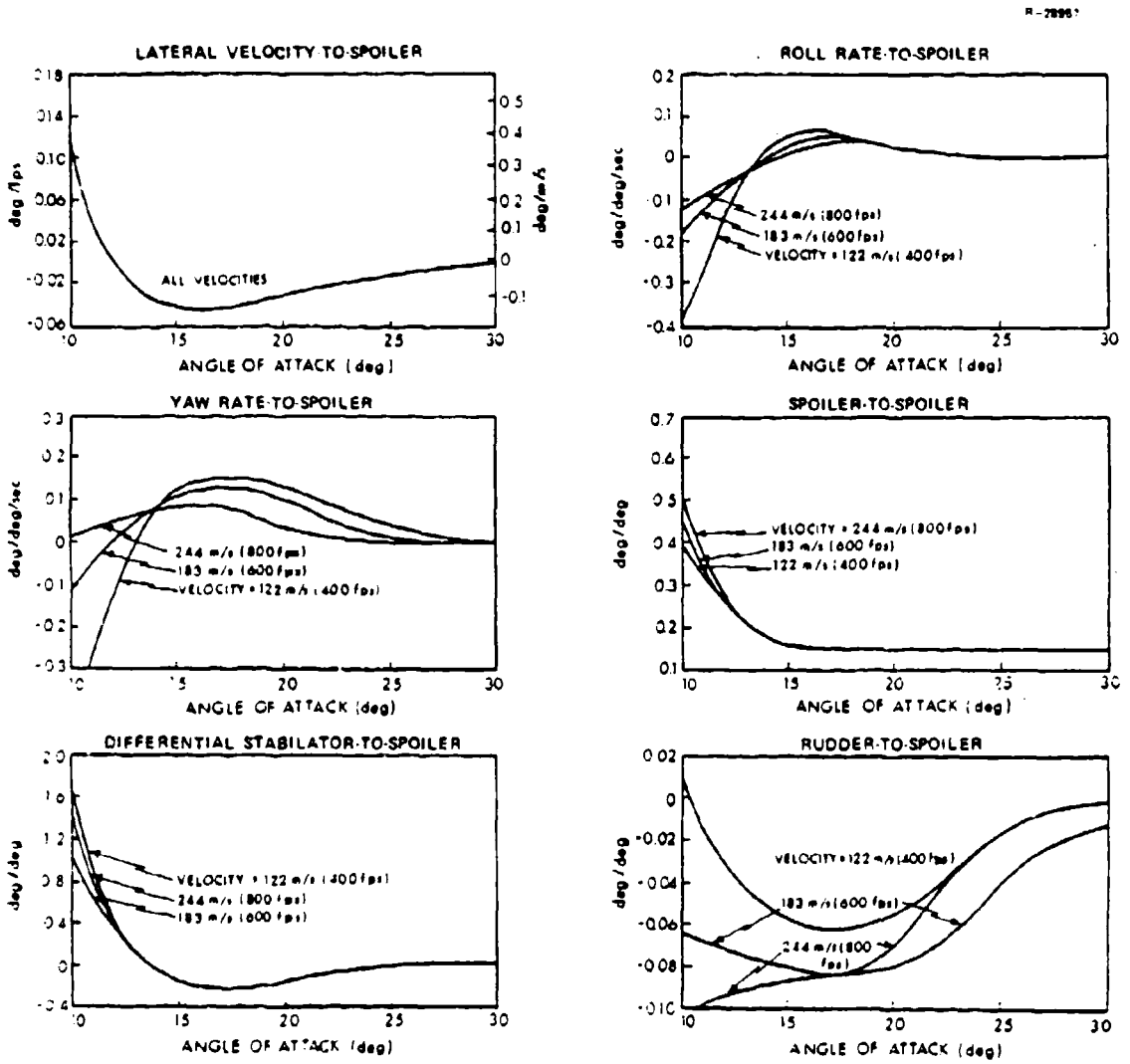

Figure 59 Angle of Attack-Dynamic Pressure Sweep -- Spoiler Type 0 DPCAS Gains

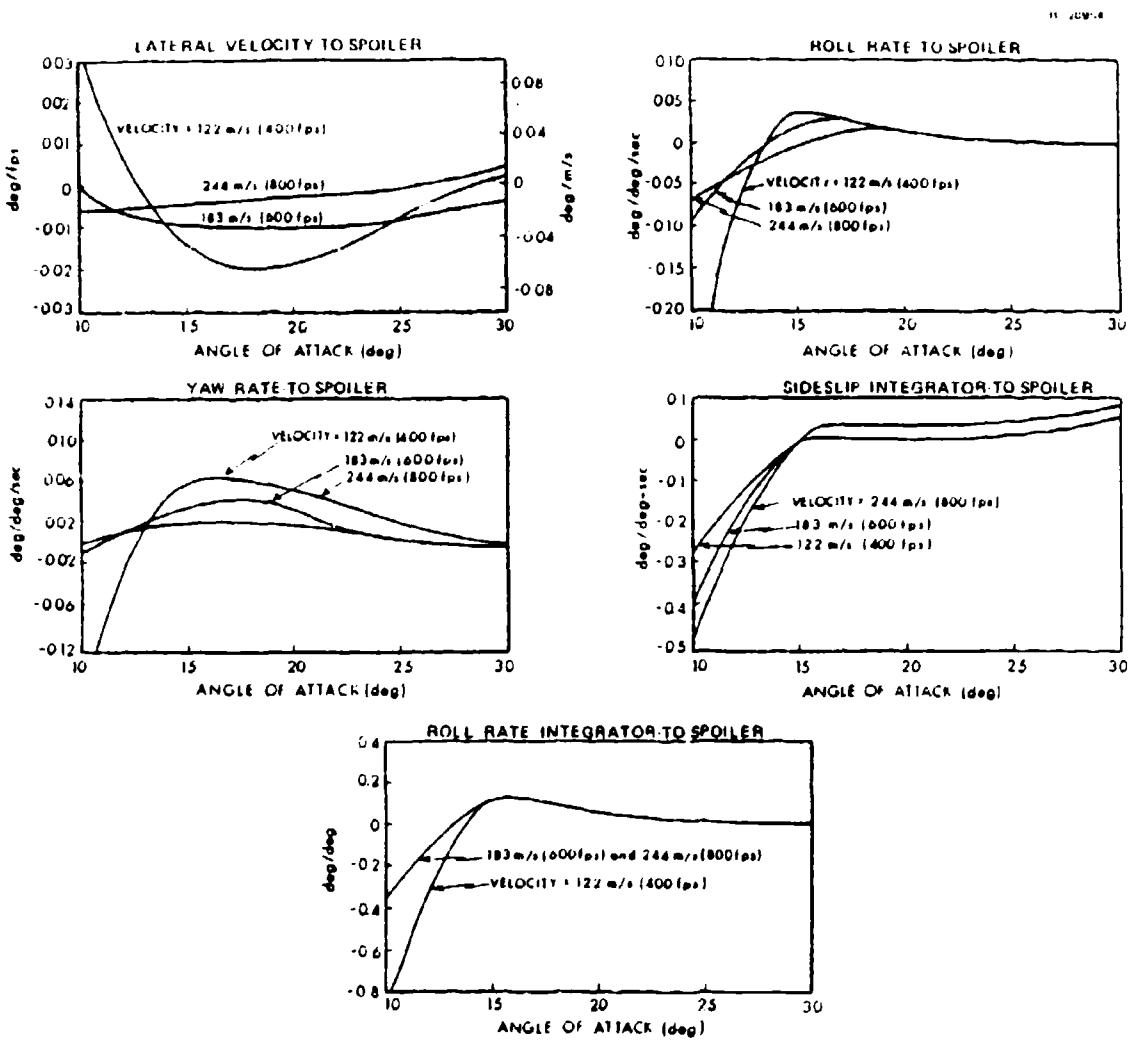

Figure 60 Angle of Attack-Dynamic Pressure Sweep -- Spoiler Type 1 DPCAS Gains

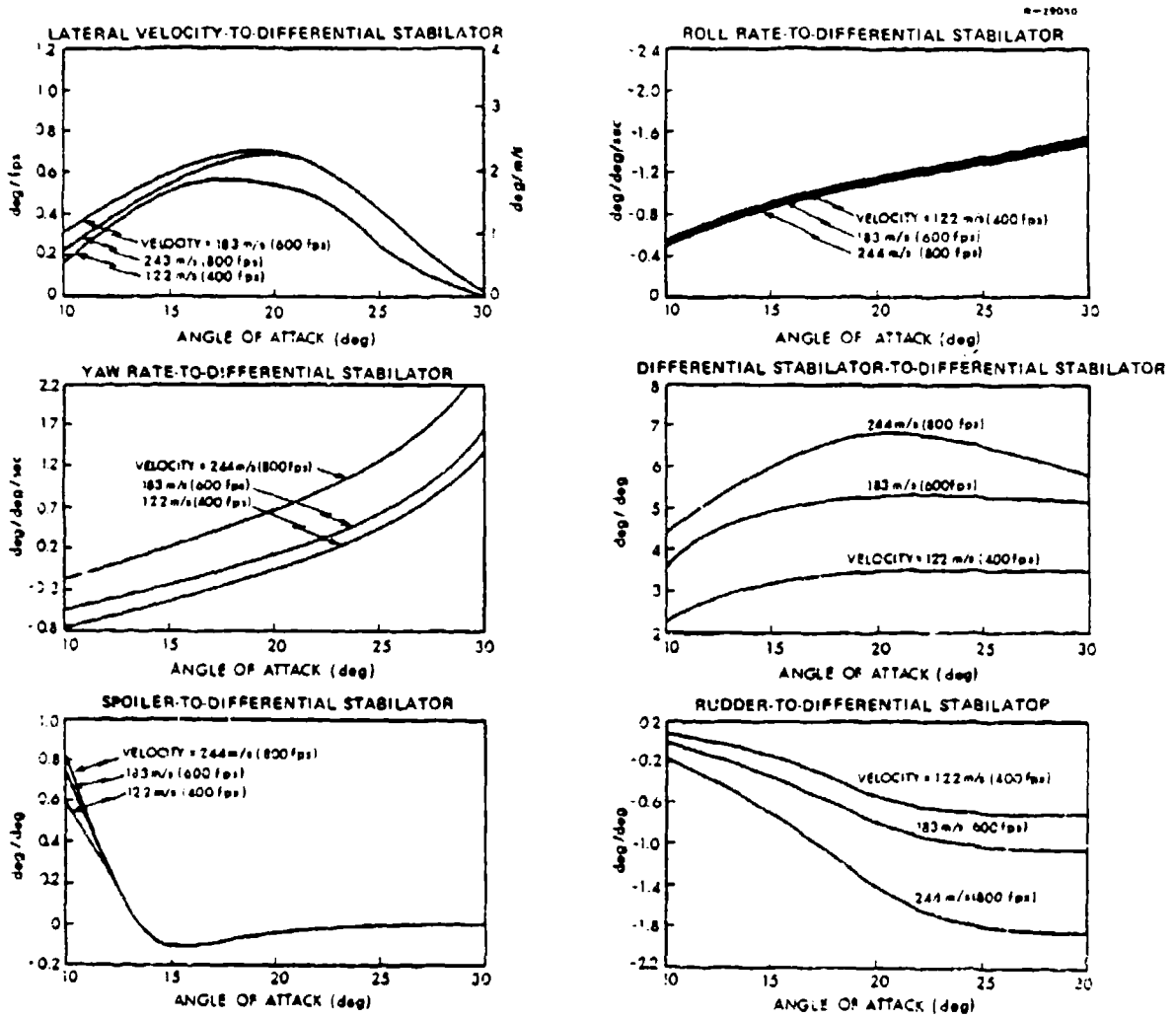

Figure 61 Angle of Attack-Dynamic Pressure Sweep -- Differential Stabilator Type 0 DPCAS Gains

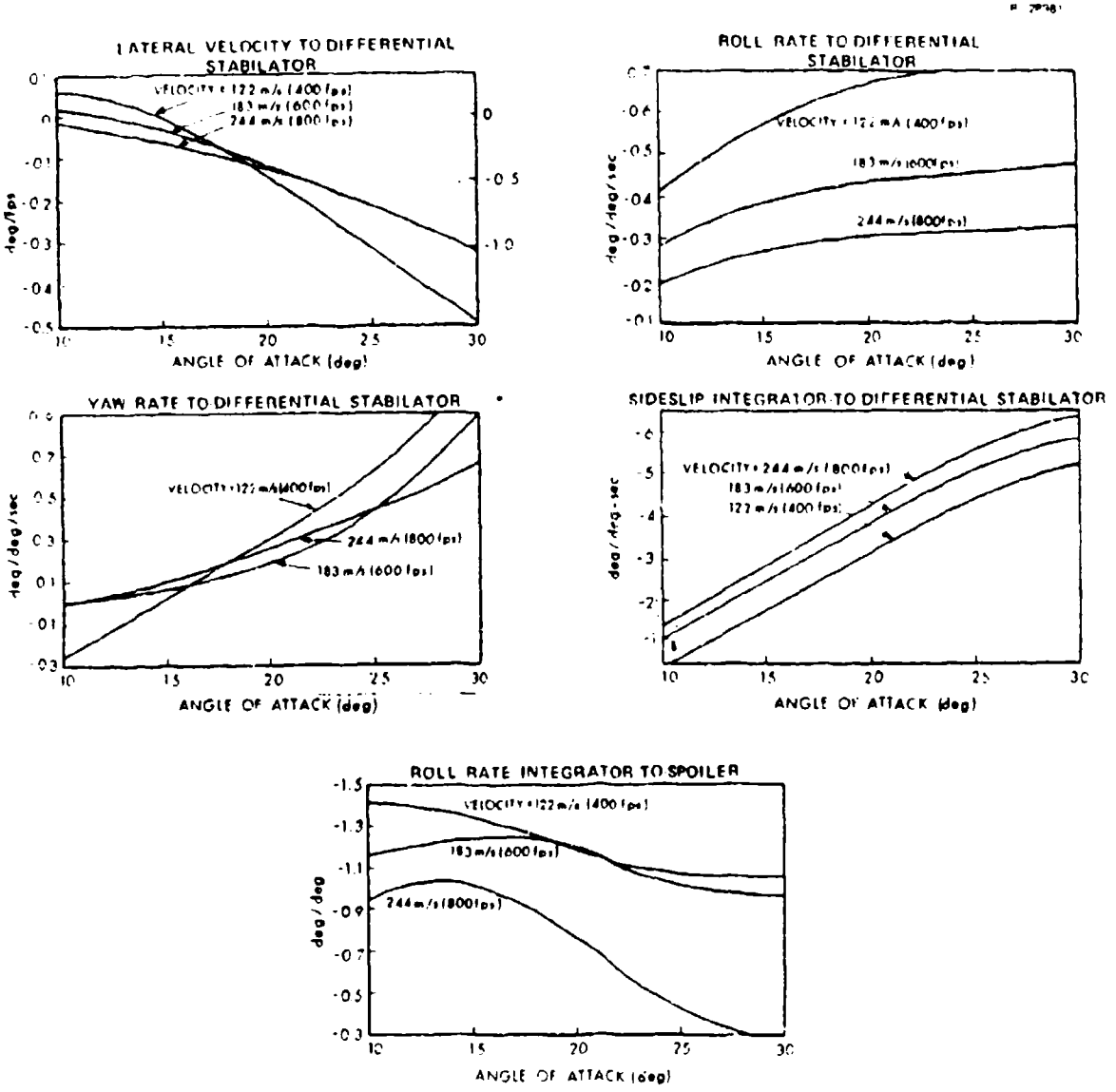

Figure 62 Angle of Attack-Dynamic Pressure Sweep -- Differential Stabilator Type 1 DPCAS Gains

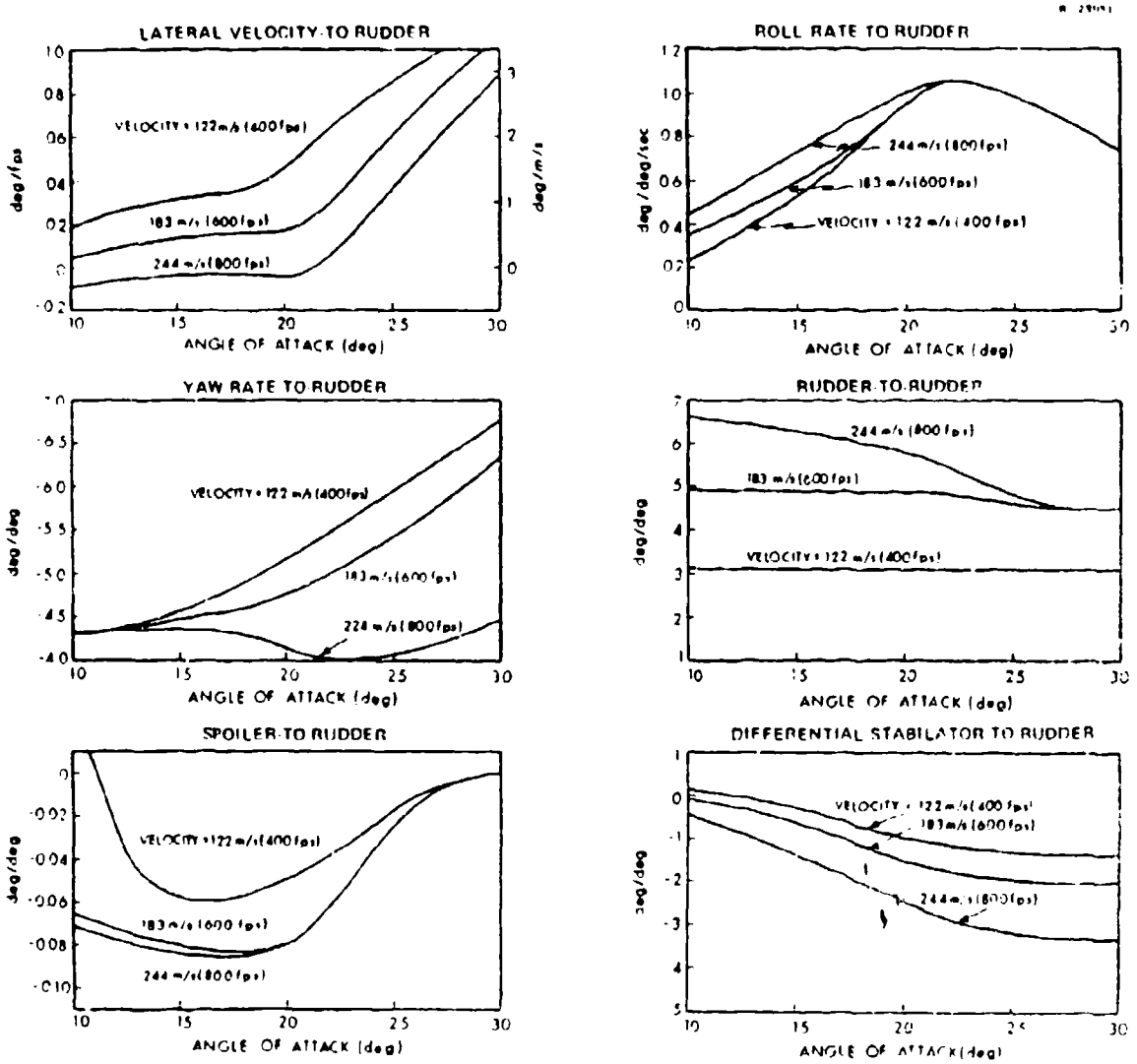

Figure 63 Angle of Attack-Dynamic Pressure Sweep -- Rudder Type 0 DPCAS Gains

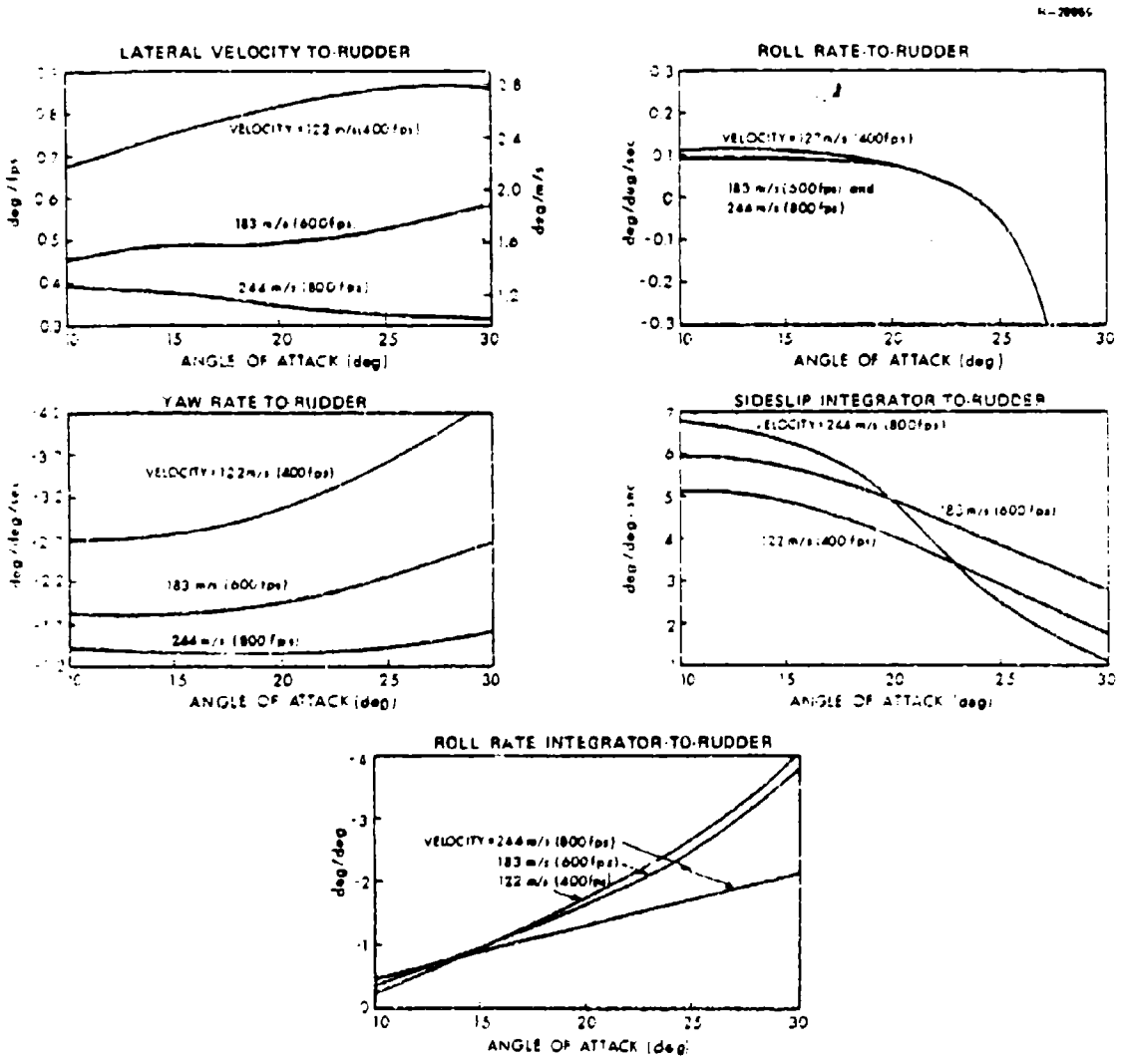

Figure 64 Angle of Attack-Dynamic Pressure Sweep -- Rudder Type 1 DPCAS Gains

significant change is in the sideslip integrator gain, which drops considerably for high dynamic pressure and increasing angle of attack.

4.2.3 Combined Effects of Roll Rate and Angle of Attack

This section presents the effect of varying stability-axis roll rate and angle of attack on Type 0 and Type 1 DPCAS closed-loop eigenvalues, control gains, and aircraft response. The velocity is held at 183 m/s (600 fps), and the aircraft is trimmed using increasing pitch rate at roll rates of 0 deg/sec, 50 deg/sec, and 100 deg/sec, as shown in Fig. 47 for a constant altitude of 6,096 m (20,000 ft).

Table 23 shows the variations for the four primary weighting matrix elements in Q. The weighting element variations are kept to a minimum and are similar to values in Table 19. The step response characteristics are shown in Table 24. Even though the aircraft has significantly coupled modes, the step response characteristics are only slightly changed from Table 20 (where the aircraft is uncoupled) because of the nonzero crossfeed gains. The same can be said for the closed-loop eigenvalues, shown in Tables 25 and 26. The one noticeable change is that the longitudinal normal velocity mode forms a complex pair with the lateral spoiler mode at the extreme conditions (pw_0 = 100 deg/sec, α_0 = 26.6 deg) for the Type 0 DPCAS in Table 25. The spoiler mode is eliminated in the Type 1 DPCAS. There is a propensity for complex pair formation at the high angles of attack, as evidenced by the conditions p_{W_0} = 50 deg/sec, α_0 = 30.9 deg in Tables 25 and 26.

TABLE 23 WEIGHTING MATRIX ELEMENT VARIATIONS FOR THE LATERAL SWEEP (V_o=183 m/s (600 fps))

T-1099

MANEUVER CONDITIONS			MAXIMUM MEAN VALUE WEIGHTING MATRIX ELEMENTS			
p_{w_o} deg/sec	α_o deg	q_o deg/sec	BODY-AXIS NORMAL ACCELERATION m/s (fps)	STABILITY-AXIS NORMAL ACCELERATION m/s (fps)	BODY-AXIS LATERAL VELOCITY m/s (fps)	STABILITY-AXIS ROLL RATE deg/sec
50.0	10.4	5.0	1.52 (5.0)	0.53 (1.75)	3.05 (10.0)	2.0
	15.2	7.5	1.52 (5.0)	0.53 (1.75)	3.05 (10.0)	2.0
	19.0	10.0	1.52 (5.0)	0.61 (2.0)	3.05 (10.0)	2.0
	24.4	12.5	1.52 (5.0)	0.53 (1.75)	2.44 (8.0)	1.8
	30.9	15.0	1.22 (4.0)	0.914 (3.0)	1.83 (6.0)	2.0
100.0	9.6	5.0	1.52 (5.0)	0.53 (1.75)	3.05 (10.0)	2.5
	13.9	7.5	1.52 (5.0)	0.53 (1.75)	3.05 (10.0)	2.5
	17.6	10.0	1.52 (5.0)	0.61 (2.0)	3.05 (10.0)	2.0
	21.3	12.5	1.22 (4.0)	0.914 (3.0)	3.05 (10.0)	2.0
	26.6	15.0	1.22 (4.0)	0.914 (3.0)	3.05 (10.0)	2.0

TABLE 24 STEP RESPONSE CHARACTERISTICS FOR THE LATERAL SWEEP (V_o=183 m/s (600 fps))

T-1100

MANEUVER CONDITIONS			STABILITY-AXIS NORMAL ACCELERATION COMMAND			SIDESLIP COMMAND			STABILITY-AXIS ROLL RATE COMMAND		
r_{w_o} deg/sec	α_o deg	q_o deg/sec	RISE TIME, sec	OVER-SHOOT, percent	SETTLING TIME, sec	RISE TIME, sec	OVER-SHOOT, percent	SETTLING TIME, sec	RISE TIME, sec	OVER-SHOOT, percent	SETTLING TIME, sec
50.0	10.4	5.0	0.85	–	1.05	1.90	–	2.50	0.75	1.6	0.85
	15.2	7.5	0.65	–	0.80	1.90	–	2.35	0.80	1.6	0.85
	19.0	10.0	0.80	–	1.00	1.90	–	2.30	0.85	1.5	0.95
	24.4	12.5	0.65	–	0.75	1.90	–	2.30	0.95	1.4	1.1
	30.9	15.0	1.15	–	1.45	2.15	–	2.70	1.4	1.2	1.55
100.0	9.6	5.0	0.80	–	1.05	1.85	–	2.30	0.75	0.6	0.90
	13.9	7.5	0.65	–	0.75	1.90	–	2.40	0.75	0.6	0.90
	17.6	10.0	0.60	–	0.80	2.00	–	2.40	0.75	0.5	0.85
	21.3	12.5	1.00	–	1.2	2.05	–	2.55	0.90	0.6	1.05
	26.6	15.0	1.05	–	1.35	2.15	–	2.65	1.15	0.5	1.35

TABLE 25 TYPE 0 DPCAS CLOSED-LOOP EIGENVALUES FOR THE LATERAL SWEEP (V_o=183 m/s (600 fps))

T-1101

MANEUVER CONDITIONS			SHORT PERIOD		NORMAL ACCEL-ERATION COMMAND	NORMAL VELOCITY	LONGI-TUDINAL CONTROL	ROLL COMMAND		DUTCH ROLL		SIDESLIP COMMAND	SPOILER
P_{w_o} deg/sec	α_o deg	q_o deg/sec	ω_n rad/sec	ζ –	τ sec	τ sec	τ sec	ω_n rad/sec	ζ –	ω_n rad/sec	ζ –	τ sec	τ sec
50.0	10.4	5.0	6.82	0.736	0.353	2.06	13.7	4.29	0.629	3.25	0.690	0.683	6.06
	15.2	7.5	6.77	0.802	0.224	2.22	10.6	4.13	0.562	2.98	0.736	0.692	6.67
	19.0	10.0	6.77	0.796	0.251	2.29	6.98	4.95	0.522	2.91	0.758	0.717	6.72
	24.4	12.5	5.21	0.782	0.163	2.54	6.81	5.13	0.525	2.48	0.819	0.626	4.70
	30.9	15.0	6.69	0.652	1.56*	0.909*	6.85	4.20	0.642	2.35	0.982	0.323*	0.952*
100.0	9.6	5.0	7.12	0.676	0.428	1.82	26.5	4.30	0.658	3.49	0.754	0.629	5.84
	13.9	7.5	6.49	0.711	0.254	2.24	10.1	4.43	0.587	3.09	0.849	0.667	6.74
	17.6	10.0	6.60	0.742	0.277	2.29	7.56	5.00	0.559	3.13	0.879	0.659	6.71
	21.3	12.5	7.42	0.703	0.415	3.46	6.77	5.08	0.521	2.76	0.857	0.698	4.80
	22.6	15.0	6.96	0.687	0.506	0.293*	6.84	4.87	0.558	2.34	0.905	0.654	0.954*

*Complex Pair

TABLE 26 TYPE 1 DPCAS CLOSED-LOOP EIGENVALUES FOR THE LATERAL SWEEP (V_o=183 m/s (600 fps))

T-1102

MANEUVER CONDITIONS			SHORT PERIOD		NORMAL ACCEL-ERATION COMMAND	NORMAL VELOCITY	ROLL COMMAND		DUTCH ROLL		SIDESLIP COMMAND
p_{w_o} deg/sec	α_o deg	q_o deg/sec	ω_n rad/sec	ζ –	τ sec	τ sec	ω_n rad/sec	ζ –	ω_n rad/sec	ζ –	τ sec
50.0	10.4	5.0	6.83	0.737	0.356	1.95	4.29	0.629	3.25	0.689	0.662
	15.2	7.5	6.79	0.802	0.224	2.00	4.43	0.562	2.98	0.735	0.688
	19.0	10.0	6.79	0.796	0.251	1.89	4.95	0.522	2.91	0.757	0.714
	24.4	12.5	5.26	0.784	0.163	1.96	5.13	0.526	2.48	0.817	0.623
	30.9	15.0	6.78	0.656	1.56*	0.906*	4.20	0.641	2.35	0.982	2.48
100.0	9.6	5.0	7.13	0.676	0.428	1.80	4.30	0.658	3.49	0.753	0.632
	13.9	7.5	6.50	0.711	0.254	1.93	4.43	0.587	3.09	0.848	0.667
	17.6	10.0	6.62	0.743	0.277	1.89	5.00	0.559	3.13	0.879	0.661
	21.3	12.5	7.46	0.704	0.415	2.29	5.08	0.521	2.76	0.857	0.695
	26.6	15.0	7.00	0.688	0.502	2.16	4.87	0.557	2.34	0.904	0.654

*Complex Pair

In contrast to the similarities between the eigenvalues of the roll rate sweep and the dynamic pressure sweep, the control motions necessary to produce the command step responses are strikingly different. The sideslip command response at α_o = 19.0 deg and α_o = 30.9 deg for p_{w_o} = 50 deg/sec are shown in Fig. 65, along with control movement. There is a large amount of coupling between the longitudinal controls and the sideslip dynamics, as shown in Fig. 65. The high frequency normal acceleration response is excited and returned to zero primarily by the main flap. The steady-state requirement for the rudder has shifted sign from the low angle-of-attack conditions in Fig. 52. The large amounts of rudder needed at the high angle of attack are indicative of the loss in rudder effectiveness that occurs between 20- and 30-deg angle of attack.

Examples of the Type 1 DPCAS crossfeed gain variations with roll rate and angle of attack are plotted in Figs. 66 and 67. There is a large amount of gain variation with angle of attack and numerous changes of sign, particularly for the differential stabilator. The large sideslip integrator gains for the longitudinal controls indicate that a significant amount of cross-axis control motion is needed to maintain zero sideslip in rolling situations. All of the gains shown in Figs. 66 and 67 are zero at zero sideslip angle and roll rate.

4.3 CHAPTER SUMMARY

This chapter uses a new design approach for obtaining a Departure Prevention Command Augmentation System (DPCAS); the DPCAS uses Type 0 and Type 1 proportional-integral control obtained from quadratic synthesis and linear-optimal regulator methods. The Type 0 and Type 1 DPCAS offer

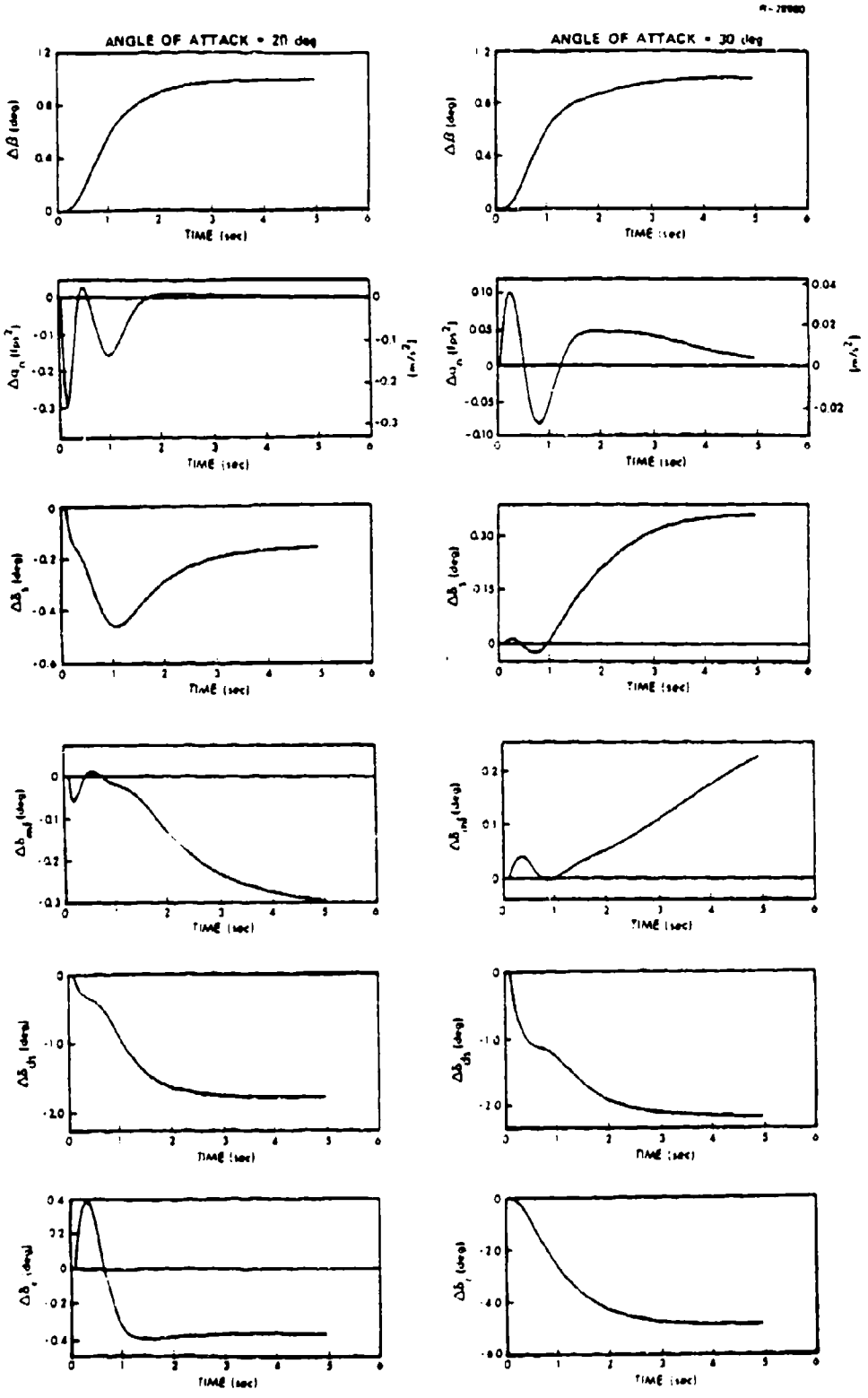

Figure 65 Sideslip Step Responses for Varying Angle of Attack at Constant Roll Rate and Velocity, $\Delta\beta_d = 1.0$ deg/sec, $p_{w_o} = 50$ deg/sec, $V_o = 183$ m/s

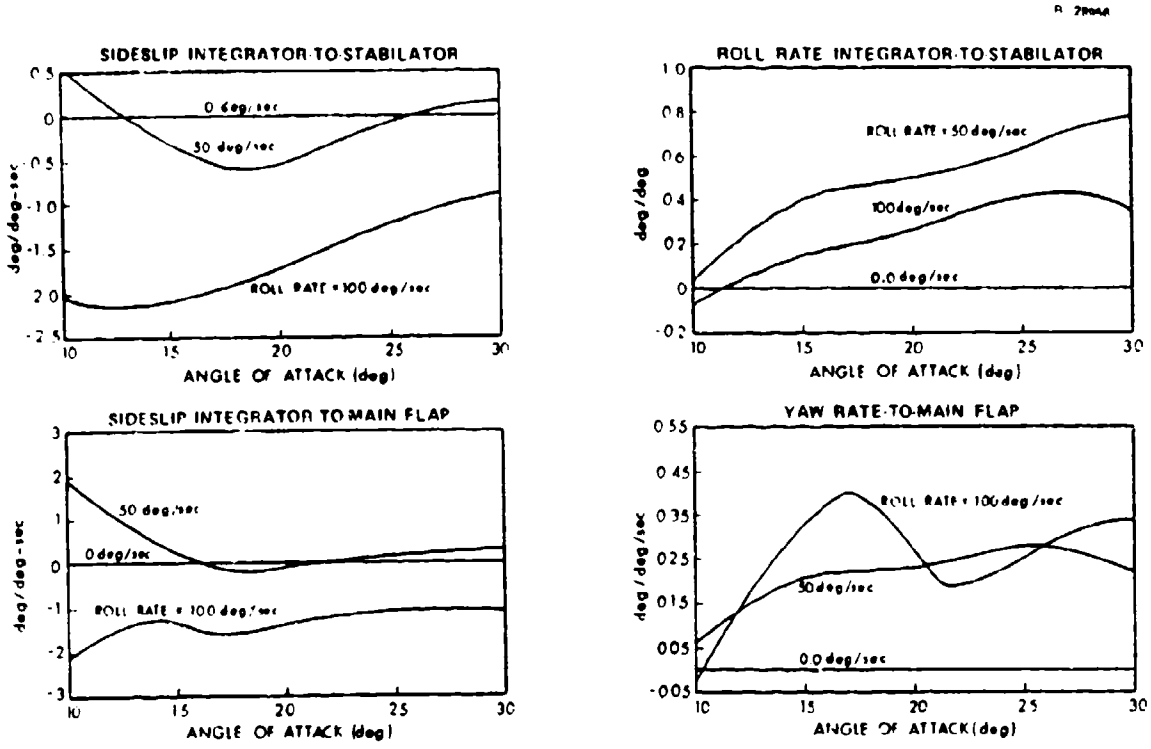

Figure 66 Selected Longitudinal Crossfeed Gains for the Lateral Sweep

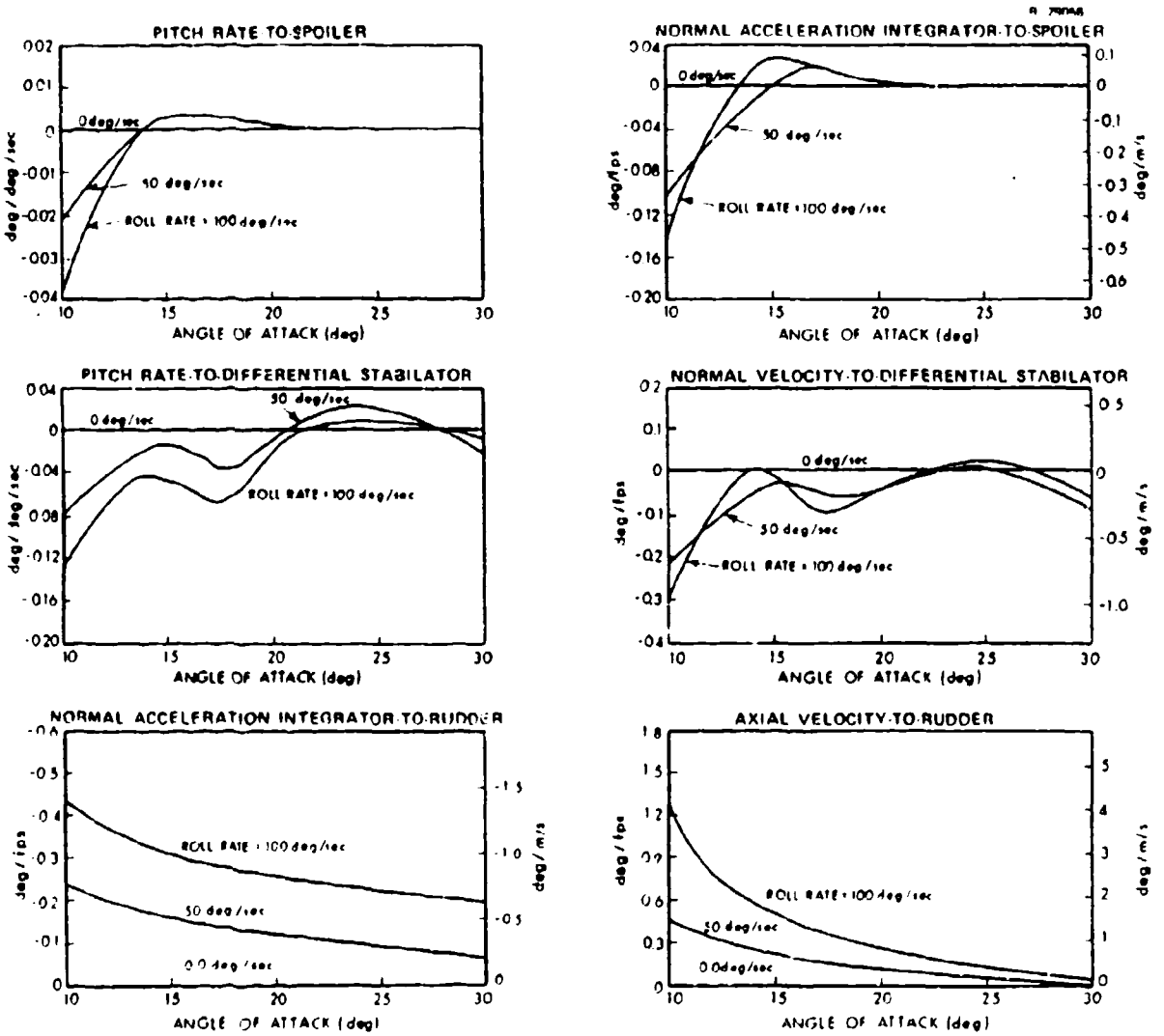

Figure 67 Selected Lateral-Directional Crossfeed Gains for the Lateral Sweep

interesting alternatives for control system implementation. The Type 0 DPCAS has a low-pass filter between pilot inputs and control outputs. The pilot must compensate for disturbances and off-nominal conditions in the Type 0 DPCAS, and this provides the pilot with indirect indications of changes in flight condition. The Type 1 DPCAS is easily implemented, and it has fewer gains than the Type 0 DPCAS. Integrator compensation in the Type 1 DPCAS relieves pilot workload allowing the pilot to concentrate on other tasks, but the system must be protected against control saturation effects.

The commands for the DPCAS design consist of normal acceleration, sideslip angle, and stability-axis roll rate. The three commands affect five of the available control effectors, taking advantage of most of the aircraft's capabilities through optimal blending of control surface motions.

The gain calculation method is based on tradeoffs between perturbation states, accelerations, commands, and the control motions and rates used to achieve desirable step response characteristics. The majority of the cost function tradeoffs (represented as weighting elements in the cost function) are held constant during the flight condition sweeps. The sweeps indicate that the DPCAS stabilizes the aircraft and exhibits uniform step response characteristics over the entire investigated flight envelope.

In summary, a scheduled-gain DPCAS can be designed to Level 1 flying qualities specifications for maneuvering flight. The DPCAS design methodology uses modern control theory to satisfy practical stability and response objectives for high-performance aircraft.

5. LIMIT-CYCLE ANALYSIS FOR NONLINEAR AIRCRAFT MODELS

5.1 INTRODUCTION

In a realistic system model that represents the dynamics of a high-performance aircraft at moderate and high angle of attack, the analyst is confronted with a large number of nonlinearities. These nonlinearities arise in the characterization of both the empirical aerodynamic data for the specific aircraft (aerodynamic coefficients and stability derivatives), and dynamic and kinematic effects. The combined nonlinear equations for the aircraft motion (Appendix B) can be written as shown in Eq. 14 if the very small off-diagonal moment-of-inertia terms and non-axial thrust components are neglected.

$$\dot{\underline{x}} \triangleq \begin{bmatrix} \dot{\theta} \\ \dot{u} \\ \dot{q} \\ \dot{w} \\ \dot{v} \\ \dot{r} \\ \dot{p} \\ \dot{\phi} \end{bmatrix} = \begin{bmatrix} q\cos\phi - r\sin\phi \\ (X+T)/m + rv - qw - g\sin\theta \\ \left((I_z - I_x)pr + M\right)/I_y \\ Z/m + qu - pv + g\cos\phi\cos\theta \\ Y/m + pw - ru + g\sin\phi\cos\theta \\ \left((I_x - I_y)pq + N\right)/I_z \\ \left((I_y - I_z)qr + L\right)/I_x \\ p + q\sin\phi\tan\theta + r\cos\phi\tan\theta \end{bmatrix} \qquad (14)$$

Most of the dynamic and kinematic nonlinearities are expressed explicitly in Eq. 14, with terms that include products of states, states times trigonometric functions of states, and

products of trigonometric functions of states. The aircraft data and response characteristics are associated with the force and moment components, X, Y, Z, L, M, N; these contributions are expressed in terms of non-dimensional aerodynamic force and moment coefficients as

$$
\begin{aligned}
X &= \tfrac{1}{2}\rho V^2 S C_{X_T} \\
Y &= \tfrac{1}{2}\rho V^2 S C_{Y_T} \\
Z &= \tfrac{1}{2}\rho V^2 S C_{Z_T} \\
L &= \tfrac{1}{2}\rho V^2 S b C_{\ell_T} \\
M &= \tfrac{1}{2}\rho V^2 S \bar{c} C_{m_T} \\
N &= \tfrac{1}{2}\rho V^2 S b C_{n_T}
\end{aligned}
\qquad (15)
$$

A realistic formulation of these highly nonlinear terms in the state-vector differential equation, Eq. 14, is provided in Appendix B of Ref. 2 (Eqs. B-1 through B-6).

The classical Taylor series or "small-signal" linearization technique can be used to good advantage in studying the perturbed response characteristics of a complicated nonlinear system model such as that given in Eq. 14. However, such analyses capture only a part of the overall aircraft flying qualities. This is especially true in flight conditions near the small-signal linear system stability boundaries, e.g., for α_0 near 20 and 30 deg, as shown in Section 4.3.1 of Ref. 2. When the small-signal eigenvalues are neutrally stable, the response properties (stability or

instability) are completely determined by the higher-order terms in the Taylor series expansion, which are truncated. For this reason, it is of considerable importance that nonlinear effects be investigated for flight conditions corresponding to angle of attack in the range 20 to 30 deg for the aircraft under consideration.

A nonlinear phenomenon that can have significant impact on aircraft handling qualities is the existence of limit cycle conditions. A number of different limit cycle effects are possible. The simplest case is illustrated in Fig. 68 where a hypothetical single limit cycle exists. Two possibilities are shown. The limit cycle is stable, in an orbital sense, if trajectories that start near the limit cycle converge toward the limit cycle, or unstable if near-by trajectories diverge from it. The region inside an unstable limit cycle is a region of stability, since trajectories in this area converge to the reference flight condition. Observe that if α_0 and β_0 correspond to the "trim" or reference flight condition without oscillation determined by a reference control setting, $\underline{u}_0$, then for fixed controls the center of the limit cycle, denoted $(\bar{\alpha}, \bar{\beta})$ in Fig. 68, may be displaced from (α_0, β_0) due to rectification effects inherent in a nonlinear system.

The amplitude and stability properties of a limit cycle are both important factors in assessing its impact on aircraft performance. A small, stable limit cycle may be permissible, while a larger stable limit cycle would be unacceptable. An unstable limit cycle, on the other hand, should be large if it is not to be adverse, since such a limit cycle is the boundary of a region of stability. Perturbations that force the aircraft trajectory outside the unstable limit cycle result in trajectory divergence.

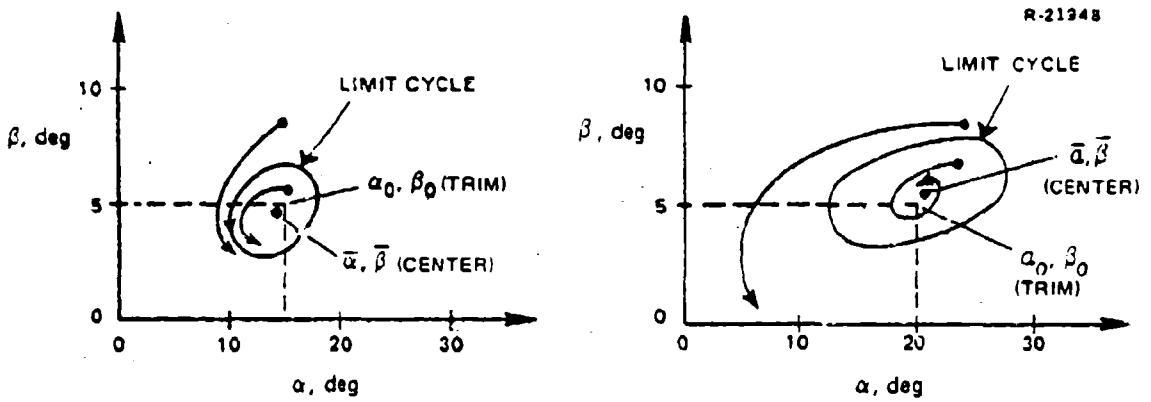

(a) Stable Limit Cycle (b) Unstable Limit Cycle

Figure 68 Single Limit Cycles

The above comments establish the importance of nonlinear effects, especially limit cycle phenomena, in the study of aircraft performance. The remainder of this chapter deals with quasi-linear or describing function techniques for analyzing systems of the complexity illustrated in Eq. 14 which may exhibit limit cycles in their response. Of particular importance is a new methodology, called the MUltivariable Limit Cycle Analysis Technique (MULCAT) which was originated at TASC during the first year of the current contract

5.2 A NEW APPROACH TO LIMIT CYCLE ANALYSIS

A new describing function (DF) technique has been devised for problems of the complexity exhibited in Eq. 14. The need for a fresh approach was discussed in Ref. 2; in summary, the existing or "classical" DF methodology based on frequency domain considerations cannot handle system models which realistically represent aerodynamic effects, having a

number of multiple-input nonlinearities. The remainder of this section outlines the MULCAT methodology of limit cycle analysis.

5.2.1 Background

The context for the discussion that follows is the problem of analyzing high angle-of-attack flight characteristics, although a more general mathematical formulation is used. It is assumed that the problem is open loop, in the sense that the control vector (rudder, spoiler, differential stabilator deflection, etc.) is fixed ($\underline{u}(t) \equiv \underline{u}_0$).

In a preliminary investigation of aircraft stability for a given flight regime, the small-signal linearization technique described in Section 3.1 of Ref. 2 is useful. As a first step, consistent input data is specified such that an iterative technique may be used to obtain the complete equilibrium or trim condition. (Assume, for example, that this input data includes a steady-state value of α, denoted α_0.) The values of $\underline{x}_0$ and $\underline{u}_0$ that satisfy $\dot{\underline{x}}(\underline{x}_0, \underline{u}_0) = \underline{0}$ then are determined, according to the fully nonlinear state-vector differential equation given by Eq. 14. Based on the trim condition, the ($n \times n$) matrix, F_0, defined by

$$F_0 \triangleq \left[f_{ij} = \frac{\partial \dot{x}_i}{\partial x_j} \right]_{\underline{x}=\underline{x}_0,\ \underline{u}=\underline{u}_0} \tag{16}$$

determines the dynamic properties of the perturbation equation corresponding to Eq. 14. The small-signal eigenvalues, or solutions $\lambda_{0,k}$, $k = 1,2,\ldots,n$, to the small-signal characteristic equation

$$\det(\lambda_0 I - F_0) = 0 \tag{17}$$

govern the transient response of the aircraft to small perturbations. A typical concern in studying the high angle-of-attack flight characteristics of an aircraft using the above analysis is to determine the value of α_0, denoted $\bar{\alpha}$, such that all small-signal eigenvalues are in the open left-half plane (LHP) for $0 \leq \alpha_0 < \bar{\alpha}$; for $\alpha_0 = \bar{\alpha}$, some pair of eigenvalues is on the imaginary axis. Stability boundaries can be established in the state-space, with results like those illustrated in Section 4.3.1 of Ref. 2.

For small α, the eigenvalues given by small-signal linearization (defined in Eq. 16) are generally moderately well damped, and nonlinear effects may not be important. As α approaches or exceeds $\bar{\alpha}$, however, the nonlinear effects become critical in determining the behavior of the aircraft. The MULCAT methodology presented in this chapter provides a general approach for analyzing the effect of nonlinearity -- as typified by the possible existence of stable or unstable limit cycles -- on aircraft handling qualities. The next section treats this new methodology in some depth.

5.2.2 Outline of the Multivariable Limit Cycle Analysis Technique

As in all describing function analyses for limit cycle conditions, the first step is to assume that an oscillation exists in the system. For the present problem, it may be natural to assume that the steady-state angle-of-attack satisfies

$$\alpha = \alpha_0(1 + \kappa \sin \delta t) \tag{18}$$

where α_0 is large (near $\bar{\alpha}$, as determined by small-signal linearization) and κ is generally less than unity*. The assumed frequency, ω, is initially the imaginary part of the most lightly damped eigenvalue given by small-signal linearization; ω will be adjusted in the subsequent iterations. The goal of the limit cycle investigation is to determine either that some κ (or several values of κ) exists such that Eq. 18 is a valid assumption (limit cycles probably are present), or that no value of κ can be found for which Eq. 18 is consistent with the quasi-linear system dynamic equations (limit cycles probably are not present). The describing function analysis technique developed for such a determination is iterative, and includes the following steps, which are portrayed in Fig. 69:

Step 1: Choose an initial trial value of κ, e.g., $\kappa = 0.1$.

Step 2: Based on the assumed oscillation, Eq. 18, and the current quasi-linear system dynamics matrix, F_i, determine the amplitudes of oscillation throughout the system model by finding $\underline{a}_i$ and $\underline{b}_i$ in the steady-state solution

$$\underline{x} = \underline{x}_i + \underline{a}_i \sin(\omega_i t) + \underline{b}_i \cos(\omega_i t) \qquad (19)$$

Determining $\underline{a}_i$ and $\underline{b}_i$ in Eq. 19 is an important step, since quasi-linear models of nonlinearities require knowing the nonlinearity input amplitudes, as is demonstrated in the next section, and it is desired to be able to treat any nonlinearity which is a function of any state variable(s).

Step 3: Using the quasi-linear system model, determine the adjusted trim (denoted $\underline{x}_{i+1}(\kappa)$ to stress its dependence on κ and to indicate that it is the result of i+1 iterations), which reflects the change in trim caused by the postulated sinusoidal component of

*Choosing the sinusoidal component amplitude to be $\kappa\alpha_0$ often leads to a convenient normalization. For limit cycle analysis about a zero center value, it would not be appropriate.

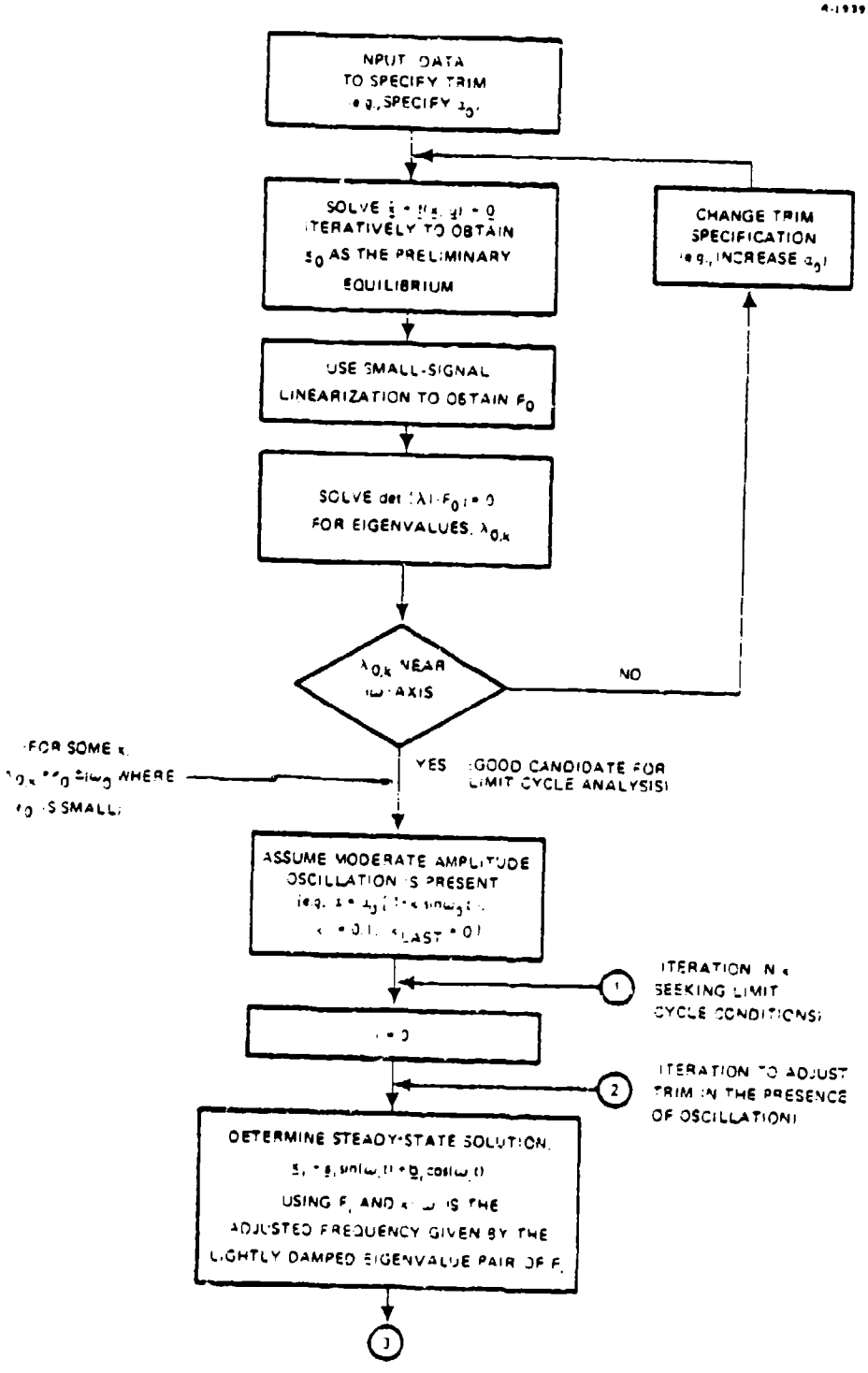

Figure 69 Iterative Search Technique for Limit Cycles -- The Multivariable Limit Cycle Analysis Technique (Sheet 1 of 2)

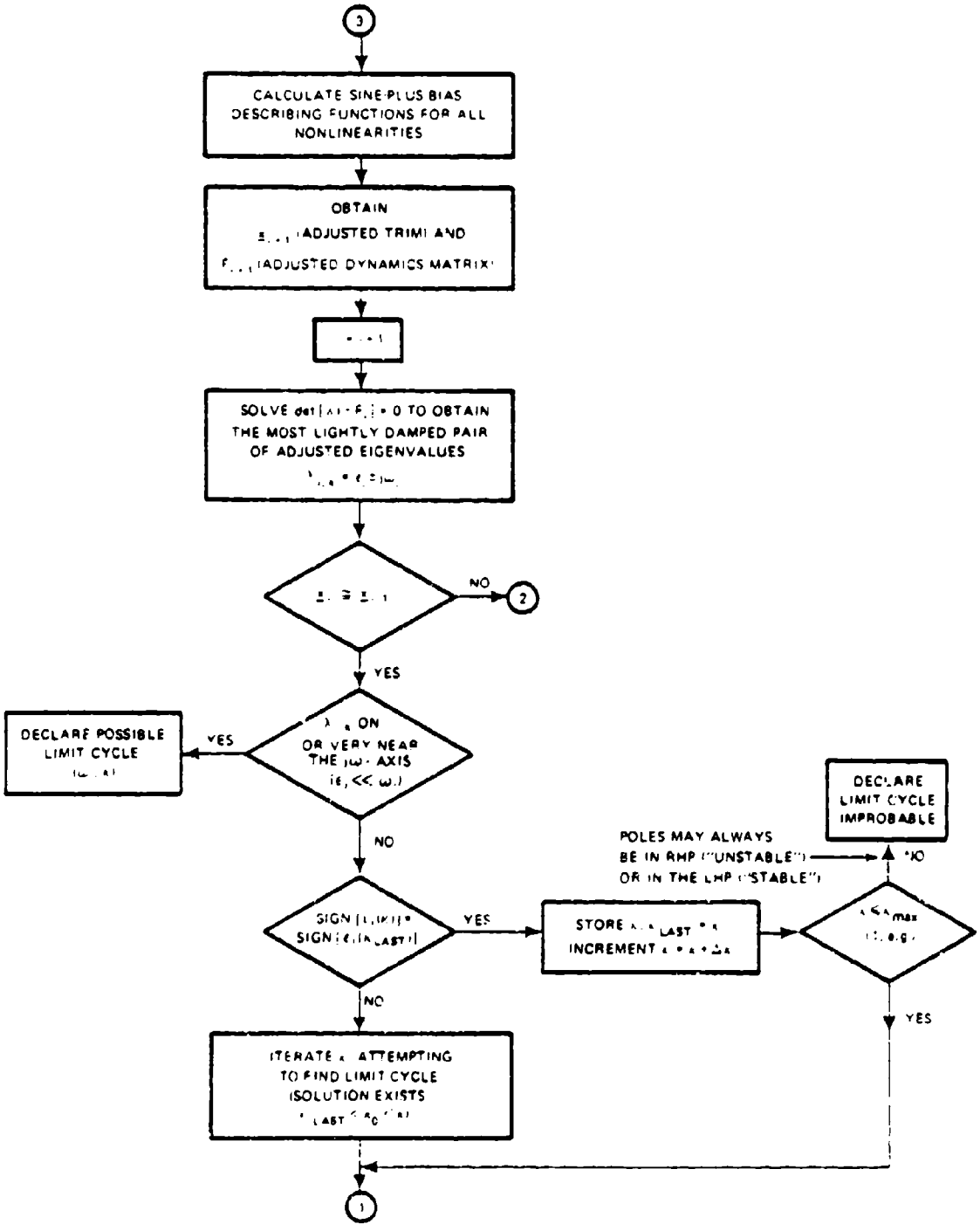

Figure 69 Iterative Search Technique for Limit Cycles -- The Multivariable Limit Cycle Analysis Technique (Sheet 2 of 2)

the state vector. In the same procedure, one obtains the adjusted quasi-linear system dynamics matrix $F_{i+1}(\kappa)$, which contains the sinusoidal-component describing function gains for all nonlinearities. Reset i = i+1.

Step 4: Calculate the adjusted frequency, ω_i, which is the imaginary part of the most lightly damped of the adjusted quasi-linear eigenvalues, $\lambda_{i,k}(\kappa)$, k = 1,2,...,n, that satisfy

$$\det(\lambda I - F_i(\kappa)) = 0 \qquad (20)$$

Step 5: Check to see if the iterative trim-determination procedure has converged;* if not, return to Step 2; if so, continue to Step 6.

Step 6: Compare $\lambda_{i,k}(\kappa)$ with the eigenvalues obtained for the previous value of κ, denoted κ_{LAST} (in the first trial $\kappa_{LAST} = 0$, i.e., the eigenvalues are as obtained by small-signal linearization -- see Eq. 17):

- If the pair of eigenvalues near the imaginary axis has crossed the axis, then some value of κ exists in the range (κ_{LAST}, κ) such that one pair of the adjusted quasi-linear eigenvalues $\lambda_{i,k}(\kappa)$ are on the imaginary axis -- a limit cycle probably exists. The value of κ, denoted κ_0, can be found by iteration on κ.

- If the pair of eigenvalues near the imaginary axis remains on the same side of the axis, increment κ (for example, by adding $\Delta\kappa$=0.1) and repeat Steps 1 to 6.

*Steps 2 to 5 represent an iterative solution of the steady-state conditions for the bias component or "center" (Fig. 68) in the presence of an assumed oscillation.

If for a representative set of values of κ (such as, κ = 0, 0.1, 0.2, ..., 1.0) the lightly damped eigenvalue pair obtained by solving Eq. 20 does not cross the imaginary axis, then it is probable that limit cycles cannot exist for the particular fixed control setting specified by the original input data (including the value of α_0 under consideration). Otherwise, the above procedure will iterate to find the value or values of κ which are probable limit cycle amplitudes. The procedures involved in the MULCAT approach, especially Step 2, are discussed in some detail in Ref. 2.

5.3 NONLINEAR MODEL FOR AIRCRAFT LIMIT CYCLE STUDIES

The nonlinearities in Eq. 14 which have been singled out in the first application of MULCAT are given as follows (identified by the state differential equation in which they occur):

pitch:	$-r \sin \phi$	
pitch rate:	$(I_z-I_x)pr/I_y$	
z-axis velocity:	Z/m	(21)
yaw rate:	N/I_z	
roll rate:	L/I_x	

These five nonlinear terms are potentially of importance in studying lateral-mode oscillations, including possible "wing rock" mechanisms, so they have been chosen for describing function treatment; the remaining terms in Eq. 14 continue to be handled by small-signal linearization. Combining Eqs. 14, 15 and B-1 through B-6 of Ref. 2 leads to the general formulation

$$\frac{Z}{m} = \frac{1}{2m}\rho V^2 S\left\{C_Z(\alpha,\beta) + \Delta C_{Z,sp}(\alpha)\frac{|\delta_{sp}|}{55} + \Delta C_{Z_{\delta_s}}(\alpha,\beta,\delta_s) + \frac{\bar{c}q}{2V}C_{Z_q}(\alpha)\right\}$$

$$\frac{N}{I_z} = \frac{1}{2I_z}\rho V^2 Sb\left\{C_n(\alpha,\beta,\delta_s) - \frac{\bar{c}}{b}C_{Y_T}x_{cg} + C_{n_{\delta_{ds}}}(\alpha,\beta)\delta_{ds} + C_{n_{\delta_{sp}}}(\alpha)\delta_{sp} + C_{n_{\delta_r}}(\alpha,\beta)\delta_r + \frac{b}{2V}\left[C_{n_r}(\alpha)r + C_{n_p}(\alpha)p\right]\right\} \quad (22)$$

$$\frac{L}{I_x} = \frac{1}{2I_x}\rho V^2 Sb\left\{C_\ell(\alpha,\beta) + C_{\ell_{\delta_{ds}}}(\alpha,\beta)\delta_{ds} + C_{\ell_{\delta_{sp}}}(\alpha)n_{sp}(M)\delta_{sp} + C_{\ell_{\delta_r}}(\alpha,\beta)\delta_r + \frac{b}{2V}\left[C_{\ell_r}(\alpha)r + C_{\ell_p}(\alpha)p\right]\right\}$$

The nonlinearities given in Eq. 22 are supplied in the form of empirically determined values of the aerodynamic coefficients and stability derivatives at various flight conditions. Based on this information, the following representations have been developed by curve fitting:

$$\begin{aligned} C_Z &\cong -k_1\alpha(1-k_2\alpha^2) \\ \Delta C_{Z,sp} &\cong k_3(1-k_4\alpha^2) \\ \Delta C_{Z_{\delta_s}} &\cong -k_5(1+k_6\alpha)\delta_s \\ C_{Z_q} &\cong -k_7\alpha \end{aligned} \quad (23)$$

$$
\begin{aligned}
C_n &\cong k_8(1-k_9\alpha)\beta \\
x_{cg} &\cong 0 \\
C_{n_{\delta_{ds}}} &\cong -k_{10}(1-k_{11}\alpha^2) \\
C_{n_{\delta_{sp}}} &\cong k_{12}(1-k_{13}\alpha) \qquad (24) \\
C_{n_{\delta_r}} &\cong -k_{14}(1-k_{15}\alpha) \\
C_{n_r} &\cong -k_{16}(1+k_{17}\alpha) \\
C_{n_p} &\cong -k_{18}(1+k_{19}\alpha+k_{20}\alpha^2)
\end{aligned}
$$

$$
\begin{aligned}
C_\ell &\cong -k_{21}(1+k_{22}\alpha+k_{23}\alpha^2)\beta \\
C_{\ell_{\delta_{ds}}} &\cong -k_{24}(1+k_{25}\alpha+k_{26}\alpha^2) \\
C_{\ell_{\delta_{sp}}} &\cong -k_{27}(1+k_{28}\alpha+k_{29}\alpha^2) \\
\eta_{sp(M)} &\cong 1 \qquad (25) \\
C_{\ell_{\delta_r}} &\cong k_{30}(1-k_{31}\alpha) \\
C_{\ell_r} &\cong -k_{32}(1-k_{33}\alpha) \\
C_{\ell_p} &\cong -k_{34}(1+k_{35}\alpha+k_{36}\alpha^2)
\end{aligned}
$$

To complete the nonlinear state-vector differential equation given in Eq. 14, the approximations

$$
\begin{aligned}
V &= \sqrt{u^2+v^2+w^2} \cong u \\
\alpha &= \tan^{-1}(w/u) \cong w/u \qquad (26) \\
\beta &= \sin^{-1}(v/V) \cong v/u
\end{aligned}
$$

are used in most instances. The resulting model still retains the highly nonlinear nature of the aircraft dynamics, and for k_i suitably evaluated, is realistic for the aircraft considered in this report at angles of attack between 15 and 30 deg.

The nonlinearities defined by Eqs. 21 through 26 required the derivation of the following new describing function representations*:

$$x_1 \sin x_2 \cong \left[x_{1,i} \sin x_{2,i} + \frac{1}{2} r_{12} \cos x_{2,i}\right] + x_{1,i} \cos x_{2,i}(a_{2,i} \sin\omega_i t + b_{2,i} \cos\omega_i t) + \sin x_{2,i}(a_{1,i} \sin\omega_i t + b_{1,i} \cos\omega_i t) \quad (27)$$

$$x_1 x_2 \cong \left[x_{1,i}x_{2,i} + \frac{1}{2} r_{12}\right] + x_{1,i}(a_{2,i} \sin\omega_i t + b_{2,i} \cos\omega_i t) + x_{2,i}(a_{1,i}\sin\omega_i t + b_{1,i} \cos\omega_i t) \quad (28)$$

$$x_1^3 \cong \left[x_{1,i}^3 + \frac{3}{2} x_{1,i} r_{11}\right] + \left[3x_{1,i}^2 + \frac{3}{4} r_{11}\right]\cdot\left(a_{1,i} \sin \omega_i t + b_{1,i} \cos \omega_i t\right) \quad (29)$$

*The state variable numbering is arbitrary. The general format is: $f \cong f_0(\underline{x}_i, \underline{a}_i, \underline{b}_i) + \sum_{j=1}^{n} n_i(\underline{x}_i, \underline{a}_i, \underline{b}_i)\cdot(a_{j,i}\sin\omega_i t + b_{j,i}\cos\omega_i t)$ where f_0 and n_i, i=1,n are the describing function gains.

$$x_1 x_2^3 \cong \left[x_{1,i} x_{2,i}^3 + \frac{3}{2} x_{2,i}\left(x_{1,i} r_{22} + x_{2,i} r_{12}\right) + \frac{3}{8} r_{12} r_{22}\right]$$

$$+ \left[x_{2,i}^3 + \frac{3}{4} x_{2,i} r_{22}\right] \cdot \left(a_{1,i} \sin \omega_i t + b_{1,i} \cos \omega_i t\right)$$

$$+ \left[3 x_{1,i} x_{2,i}^2 + \frac{3}{4} x_{1,i} r_{22} + \frac{3}{2} x_{2,i} r_{12}\right]$$

$$\cdot \left(a_{2,i} \sin \omega_i t + b_{2,i} \cos \omega_i t\right) \qquad (30)$$

$$\frac{x_1 x_2^2}{x_3} \cong \frac{1}{x_{3,i}^2} \left\{ x_{3,i}\left[x_{1,i}\left(x_{2,i}^2 + \frac{1}{2} r_{22}\right) + x_{2,i} r_{12}\right] \right.$$

$$- x_{2,i}\left(x_{1,i} r_{23} + \frac{1}{2} x_{2,i} r_{13}\right) - \frac{1}{8}\left(r_{22} r_{13} + 2 r_{12} r_{23}\right)$$

$$+ \left[x_{3,i}\left(x_{2,i}^2 + \frac{1}{4} r_{22}\right) - \frac{1}{2} x_{2,i} r_{23}\right]$$

$$\cdot \left(a_{1,i} \sin \omega_i t + b_{1,i} \cos \omega_i t\right)$$

$$+ \left[2 x_{3,i}\left(x_{1,i} x_{2,i} + \frac{1}{4} r_{12}\right) - \frac{1}{2} x_{1,i} r_{23} - \frac{1}{2} x_{2,i} r_{13}\right]$$

$$\cdot \left(a_{2,i} \sin \omega_i t + b_{2,i} \cos \omega_i t\right)$$

$$- \left[x_{1,i} x_{2,i}^2 + \frac{1}{4} r_{22} + \frac{1}{2} x_{2,i} r_{12}\right]$$

$$\left. \cdot \left(a_{3,i} \sin \omega_i t + b_{3,i} \cos \omega_i t\right) \right\} \qquad (31)$$

where

$$r_{jk} \triangleq a_{j,i}\, a_{k,i} + b_{j,i} b_{k,i} \; ; \quad j,k = 1,2,3$$

Results for x_1^2 and x_1^3/x_3 can be obtained from Eqs. 28 and 31, respectively, by setting $x_1 = x_2$.

The result given in Eq. 29 is from Ref. 28; the others are original with this effort. To the best of our knowledge, multi-state nonlinearities such as those in Eqs. 27, 28, 30, and 31 have never been dealt with using sinusoid-plus-bias describing functions.

The aerodynamic data curve fits obtained by adjusting the coefficients k_1 through k_{36} in Eqs. 23 to 25 were tested by plotting the Dutch roll eigenvalue real part, obtained by small-signal linearization, versus the trim value of angle of attack. The curve, shown in Fig. 70, quite faithfully reflects the observation that the Dutch roll mode stability boundary is very close to 20 deg ($\bar{\alpha} \doteq 19.6$ deg). To achieve this degree of agreement, the number of terms used in Eqs. 23 to 25 was increased from the previous effort (26 coefficients in Ref. 2 versus 36 coefficients here).

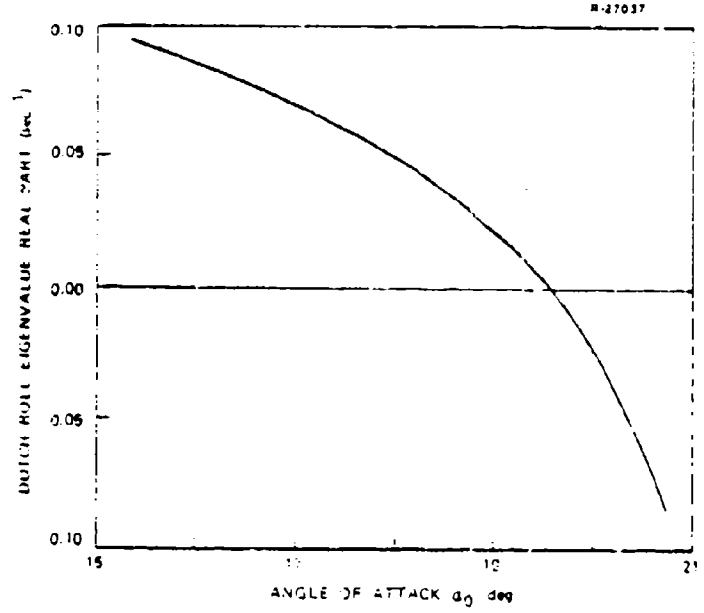

Figure 70 Dutch Roll Eigenvalue Real Part as Determined by Trim Angle of Attack

5.4 LIMIT CYCLE ANALYSIS RESULTS AND VERIFICATION

The nonlinear model described in the previous section provided the basis for the first application of MULCAT. The value of trim angle of attack chosen for study, α_0, is 19.6 deg. The corresponding eigenvalues associated with the Dutch roll mode are

$$\lambda_{DR} = 0.0366 \pm 1.52j$$

which for small perturbations predicts an unstable response. It should be observed that there is a much slower unstable lateral mode ("lateral phugoid"), with eigenvalues

$$\lambda_{LP} = 0.0187 \pm 0.131j$$

In most instances, a mode which is as slow as the lateral phugoid in the present case is not a concern, so attention is generally restricted hereafter to the behavior of the Dutch roll mode. The values of the state variables at trim are given in Table 27.

TABLE 27. INITIAL TRIM CONDITION IN THE ABSENCE OF OSCILLATION

STATE VARIABLE (ELEMENT OF $\underline{x}_0$)	VALUE
θ_0	17.46 deg
u_0	81.7 m/sec
q_0	0.296 deg/sec
w_0	29.1 m/sec
v_0	6.04 m/sec
r_0	-0.033 deg/sec
p_0	-0.011 deg/sec
ϕ_0	-5.303 deg

The first search for possible limit cycles was conducted by assuming that the velocity along the body y-axis is given by

$$v = v_o\left[1 + \kappa \sin(\omega_{DR}t)\right]$$

where ω_{DR} is the imaginary part of the lightly damped Dutch roll mode. The parameter κ was varied from 0 to 3 in steps of 0.5; the resulting change in $\lambda_{DR}(\kappa)$ given by MULCAT is shown in Fig. 71. Based on these results, limit cycles for κ between 1 and 1.5 and for κ between 2.5 and 3.0 are predicted.

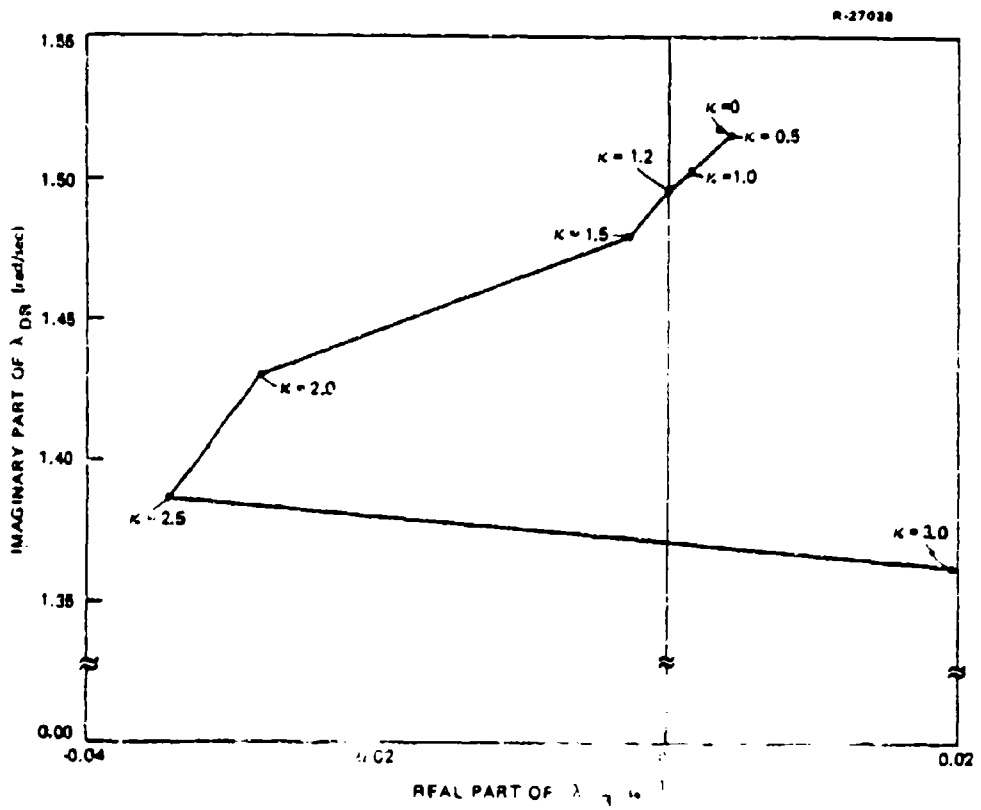

Figure 71 Variation of the Dutch roll [illegible] with Assumed Oscillation Amplitude

The MULCAT program was then permitted to iterate to find the exact limit cycle condition. It was found that λ_{DR} is virtually on the imaginary axis,

$$\lambda_{DR} = 4\times10^{-5} \pm 1.4954j$$

for κ equal to 1.20. Corresponding to this value of κ, the "center" value, $\underline{x}_i$, and oscillation components, $\underline{a}_i$ and $\underline{b}_i$, for the state vector are given in Table 28. Since decreasing κ moves λ_{DR} into the right half plane, and increasing κ moves λ_{DR} into the left half plane, the predicted limit cycle for κ = 1.2 should be stable.

TABLE 28 TRIM CONDITION AND PREDICTED LIMIT CYCLE AMPLITUDE FOR THE STABLE LIMIT CYCLE

STATE VARIABLE CENTER (ELEMENT OF $\underline{x}_i$)	$\underline{a}_i$	$\underline{b}_i$	UNITS
θ_i	18.35	0.259	-0.234	deg
u_i	80.25	-0.177	0.165	m/sec
q_i	0.174	0.219	0.182	deg/sec
w_i	28.80	-0.810	-0.718	m/sec
v_i	6.14	7.38	0.0	m/sec
r_i	0.792	-1.79	-1.89	deg/sec
p_i	-0.310	-7.35	14.90	deg/sec
ϕ_i	8.55	9.55	5.295	deg

A verification of the limit cycle prediction requires that nonlinear simulations of the dynamics specified in Eqs. 14, 22, and 23 to 25 be performed. To do this, the original state equation, Eq. 14, is formulated as

$$\dot{\underline{x}} = F_1\underline{x} + \begin{bmatrix} -r \sin \phi \\ 0 \\ (I_z - I_x)pr/I_y \\ Z/m \\ 0 \\ N/I_z \\ L/I_x \\ 0 \end{bmatrix} + G_1\underline{u}$$

$$\triangleq F_1\underline{x} + \underline{f}_1(\underline{x},\underline{u}) + G_1\underline{u} \qquad (32)$$

where F_1 and G_1 are constant matrices which capture effects other than those chosen for study via quasi-linearization, and $\underline{f}_1(\underline{x},\underline{u})$ is the vector of nonlinearities selected for treatment using MULCAT. Equation 32 can then be directly integrated to yield the desired time histories.

Choice of the initial condition for this procedure is critical. This is due to the presence of an unstable mode, a slow spiral mode which for $\kappa = 1.2$ is governed by

$$\lambda_S = 0.0618$$

If this mode is excited appreciably, its growth will completely obscure the fast limit cycle that is sought. One of the benefits of MULCAT is that the eigenvector for the predicted limit cycle is proportional to $\underline{a}_i + j\underline{b}_i$, in the standard phasor notation; therefore, if we choose the initial value of $\underline{x}$ by

$$\underline{x}(0) = \underline{a}_i$$

only the limit cycle in the Dutch roll mode should be excited.

The stable limit cycle prediction shown in Table 28 was verified by choosing $\underline{x}(0) = 0.8\underline{a}_i$. The resulting time histories of pitch angle, θ, y body-axis velocity, v, and z body-axis velocity, w, are portrayed in Fig. 72*. The plot of θ shows that the solutions do very slowly diverge, due to a small unavoidable excitation of the spiral mode. The time histories of v and w show that the dominant Dutch roll mode is very slowly growing for the first 25 sec of the simulation, as would be expected for an initial condition that is slightly interior to the predicted stable limit cycle. The predicted center value of v is nearly exact, while that for w is in error by about -0.5 m/sec, or about -1.4 percent. Finally, the predicted limit cycle frequency is 1.495 rad/sec, while the observed frequency is 1.497 rad/sec; the agreement is excellent. After 25 sec of simulation, the slow divergence begins to alter the limit cycle shown to have developed in the first part of the simulation.

Further analysis of the simulation results was undertaken to attempt to separate out the effect of the slow divergence. The time history depicted in Fig. 72b was processed to determine the exponential growth component ($c_1 e^{c_2 t}$); then the predicted limit cycle envelope is given by the relation

$$e_{LC} = c_1 e^{c_2 t} \pm a_5$$

where a_5 is the amplitude of the predicted limit cycle in u (state 5). This envelope is portrayed in Fig. 72b; within the limits of the simulation accuracy, convergence of the time history to the envelope is shown.

---

*The plots show the perturbation of each variable about the predicted center value, $\underline{x}_1$; i.e., $\Delta\underline{x} \triangleq \underline{x} - \underline{x}_1$ is the abscissa in Fig. 72.

The effort to verify MULCAT limit cycle conditions by direct simulation has pointed up the difficulty of using the latter technique as an exploratory tool to locate limit cycles, without recourse to describing function analysis. Realistic aerodynamic models such as those used here often have slow modes that are unstable or that are very lightly damped. Direct simulation initial conditions must be chosen very carefully to avoid exciting these modes. In a linear system, it is not difficult to use eigenvector information to obtain initial conditions that selectively excite a desired mode. However, eigenvectors are not rigorously defined for nonlinear systems.

A concept which can be used with some success may be called the quasi-linear eigenvector; in essence, the complex vector $\underline{a}^*$, given by $\underline{a}_1 + j\underline{b}_1$ as in Table 28, is in a sense an amplitude-dependent eigenvector, which specifies an initial condition that excites the assumed oscillation. The fact that the quasi-linear eigenvector $\underline{a}^*$ is amplitude-dependent is illustrated in Fig. 73, which shows $\underline{a}^*$ for various values of κ, corresponding to the study depicted in Figs. 71 and 72†. For κ = 1.0 and 1.5, the eigenvector components for θ and q are too small to be shown; the differences between the remaining components (which are normalized to make the length of the v component equal in each plot) are rather small. For κ = 2.5 and 3.0, the changes in $\underline{a}^*$ are quite substantial. For example, the θ and q components of $\underline{a}^*$ are much larger than for small κ, and can be seen to rotate nearly 45 deg for κ increased from 2.5 to 3.0.

---

†The eigenvectors correspond to the variables θ, u, q, w, v/10, r, p/5, ϕ/5; this scaling was performed to permit all components of $\underline{a}^*$ to be shown on the plots for κ=2.5 and 3.0.

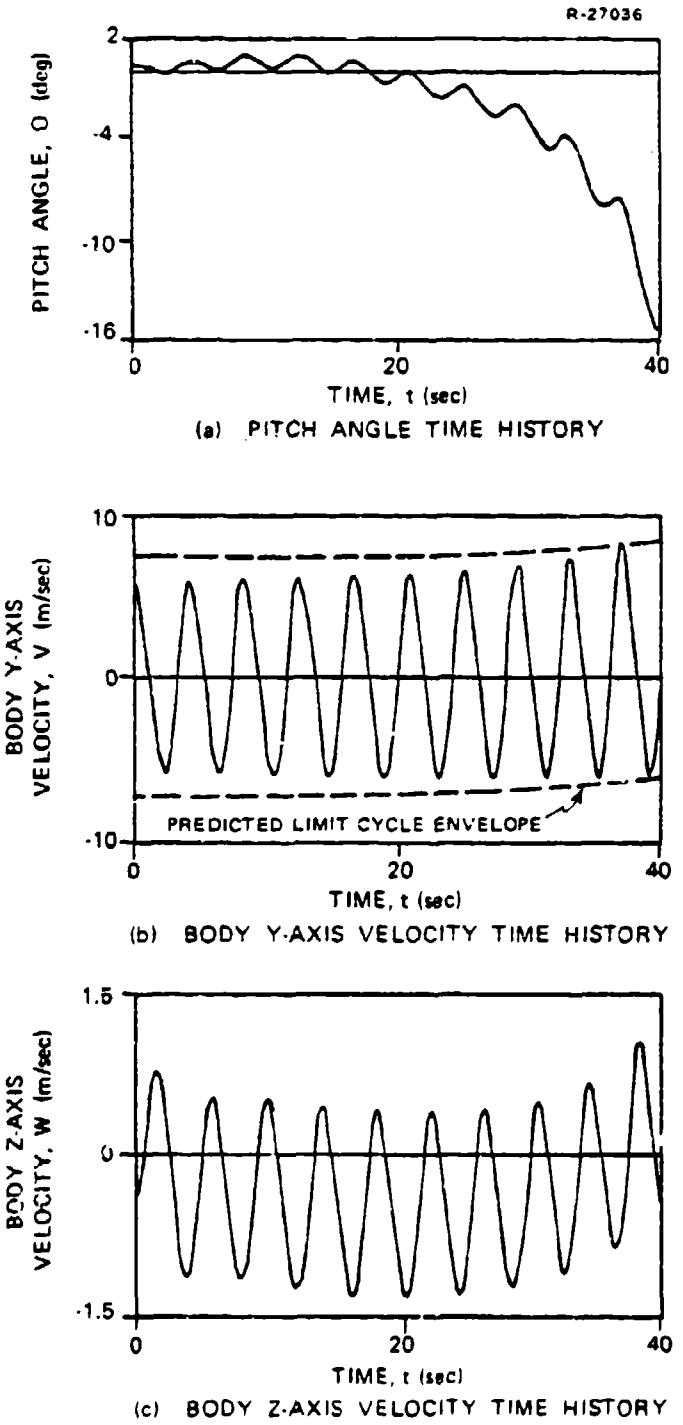

Figure 72 Verification of the MULCAT Limit Cycle Prediction

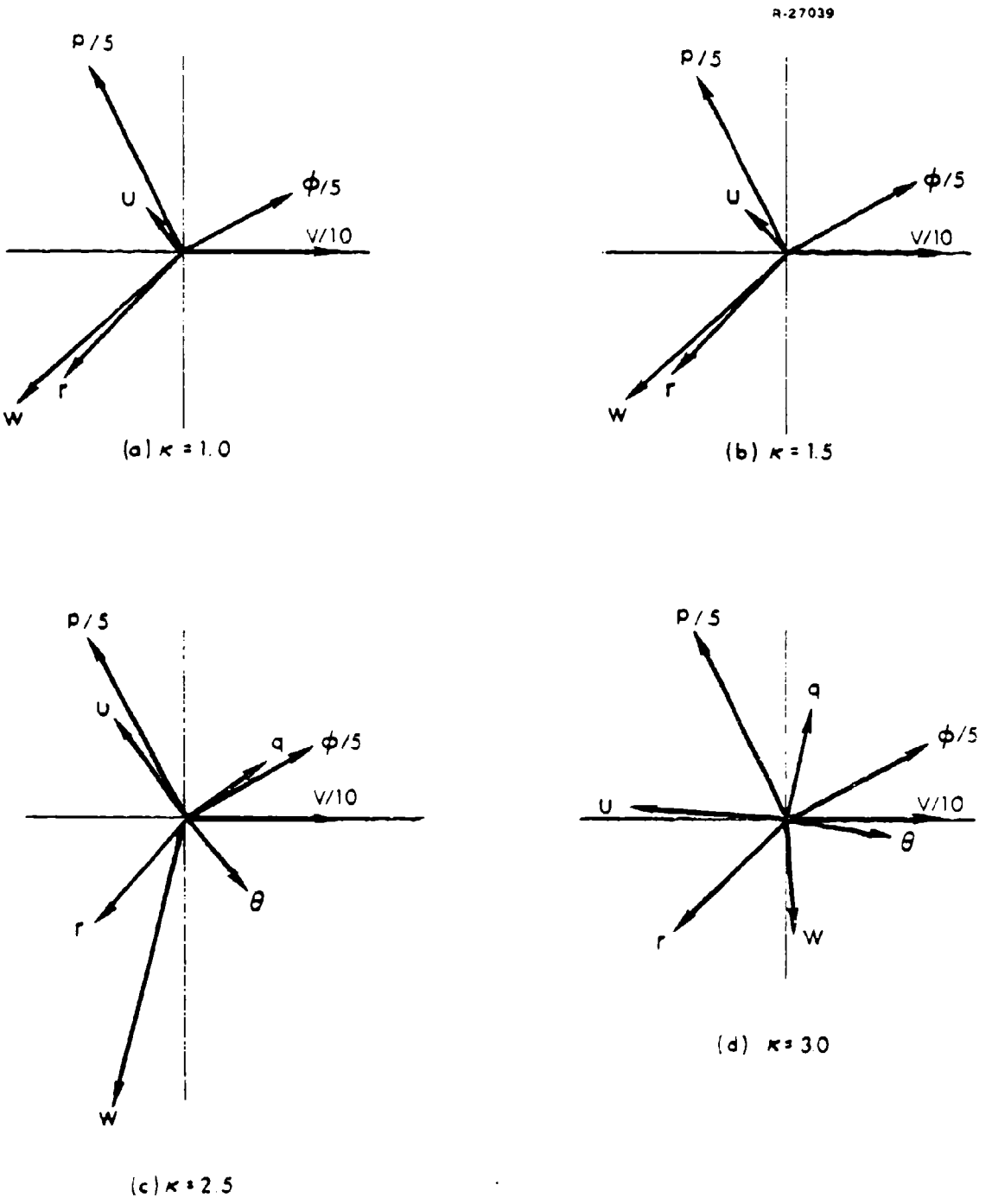

Figure 73 Amplitude Dependence of Quasi-Linear Eigenvectors Obtained by MULCAT

Finally, validity of the quasi-linear eigenvector can be bolstered by comparing Fig. 73a with Fig. 74. The latter is the eigenvector for Dutch roll, obtained from the more conventional eigenvalue/eigenvector analysis used in other sections of the report. The agreement is quite good, especially considering that Fig. 74 is based on the empirical aerodynamic data, rather than the analytic nonlinearity approximations shown in Eqs. 23 to 25.

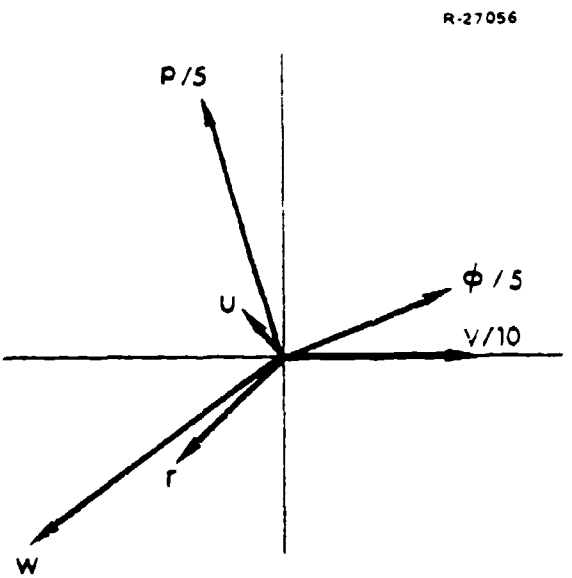

Figure 74. Exact Dutch Roll Eigenvector Diagram Corresponding to Empirical Aerodynamic Data

5.5 CHAPTER SUMMARY AND OBSERVATIONS

The Multivariable Limit Cycle Analysis Technique is fully developed in conceptual terms, as outlined in Section 5.2; it is discussed in more detail in Ref. 2. The analytic and quasi-linear models for the subject aircraft are similar to those developed in the first phase of the study (Ref. 2);

a number of terms were added, and coefficients were recalculated to achieve a better match between the analytic model and the empirical aerodynamic data used in other investigations described in this report. The limit cycle analysis procedures involved in MULCAT are incorporated in ALPHA-2, the general high-α study program developed under this contract.

The benefits of this technique are

- An iterative algorithmic approach to limit cycle analysis is much more suitable for mechanization on a digital computer than classical frequency-domain techniques, which are typically graphical in nature;
- Any number of nonlinear effects can be investigated, singly or in any combination, without continually manipulating the system model into the appropriate "linear plant with nonlinear feedback" formulation required in the frequency-domain approach (Ref. 2);
- The amount of computer time required to determine the existence of limit cycles by a MULCAT analysis is significantly less than the computer time expenditure that would be needed using direct simulation alone.

The last observation is based on the difficulty of choosing the direct simulation initial condition correctly to excite only the desired nearly oscillatory mode, as discussed in the preceding section.

The study presented in Section 5.4 illustrates the effectiveness of MULCAT in limit cycle prediction. The limit cycle frequency and "center" value (Fig. 68) given by MULCAT are in good agreement with the simulation results; the accuracy of the amplitude prediction is more difficult to

assess quantitatively due to the simulation problems mentioned previously (see Fig. 72b). In general, these results bolster the expectation that the MULCAT iterative technique will be found to converge to locate limit cycle conditions, provided that

- The input trim condition specification leads to a pair of small-signal linear eigenvalues that are lightly damped,
- The nonlinearities are well-behaved (e.g., realistically modeled by low-order power series expansions or products thereof); and
- Limit cycles indeed exist (as verified by simulating solutions to the original nonlinear state-vector differential equation, with suitable initial conditions).

Considerable further research could be performed in conclusively proving the power and accuracy of MULCAT. As a first step, it would be valuable to exercise MULCAT upon a simpler model (fewer states and nonlinearities), particularly one that does not contain system variables that are slowly divergent. The existence of unstable modes, or even of modes that are slowly decaying oscillations, makes limit cycle verification by direct simulation very difficult, since it is impossible not to excite them in the simulation.

An area of MULCAT application that would be of great interest is the study of limit cycle conditions when a human pilot model is incorporated to "close the loop" in the aircraft dynamic model. While it may be useful to examine fixed control settings that give rise to limit cycles, as in the present study, the ability of the pilot to correct the problem -- or to create limit cycle conditions when they do

not exist for fixed controls -- would be a subject of considerable significance. Such an analysis using MULCAT presents no foreseeable difficulties.

6. CONCLUSIONS AND RECOMMENDATIONS

New methodologies and results in the study of aircraft stability and control, including detailed consideration of piloting effects, have been presented. These lead to the conclusions and recommendations given below.

6.1 CONCLUSIONS

- Aircraft Dynamic Models - This report has demonstrated that the first-order effects of aerodynamic and inertial coupling can be considered in linear, time-invariant dynamic models for maneuvering flight and that such analysis can be extended into the transonic and supersonic flight regimes. Two data sets are used during the study, and their differences in an overlapping region (subsonic flight, with wings swept forward) highlight the importance of basing stability and control analyses of actual aircraft on the best, most consistent data available.

- Mach-Dependent Effects - The general trends in aircraft stability which arise at subsonic speed for asymmetric flight conditions (e.g., the transfer of damping from one axis to another, the appearance of longitudinal variables in characteristically lateral-directional modes, and so on) also occur at higher Mach numbers. Previously understood potential problem areas, including low control power in transonic flight and the need to maintain small sideslip angle in unaugmented supersonic flight, are evidenced in the present analysis. The aircraft dynamic model studied here is relatively stable throughout the Mach range in low-α, straight-and-level flight. Maneuvering at high α with high angular rates can lead to a requirement for stability augmentation.

- Pilot-Aircraft Interactions - Whether or not a pilot experiences difficulties in maneuvering flight depends upon how he adapts his control strategy to changing flight conditions. Stability boundaries plotted as functions of the aircraft's actual α and the α assumed by the pilot in forming his control strategy illustrate that the pilot's adaptation must be very nearly optimal to maintain stability in certain flight conditions. Consideration of statistical tracking error and control usage within stable boundaries leads to the concept of minimum-control-effort (MCE) adaptation in the pilot model. The MCE model provides a rationale for non-optimal adaptation which accounts for fundamental changes in the control modes selected by the pilot, such as the decision to use stick and pedals in a coordinated fashion rather than stick alone.

- Departure-Prevention Command Augmentation System (DPCAS) - Precision response to pilot commands (normal acceleration, stability-axis roll rate, and sideslip angle) is afforded by using modern control theory in flight control system design. Proportional-integral compensation provides "Level 1" flying qualities throughout an expanded maneuvering envelope in two candidate implementations of the DPCAS: a "Type 0" version, which is especially insensitive to disturbance inputs and feedback measurement noise, and a "Type 1" version, which assures proper steady-state command response for wide variations in the aircraft's parameters. The two versions have virtually identical step response when the design model and the actual aircraft are matched. Although the DPCAS design methodology is illustrated with an advanced (but conventional) 3-axis command vector, it can be applied to "CCV" control modes with equal facility.

- Nonlinear Wing Rock Analysis - The possible existence of limit cycles in nonlinear dynamic models of the aircraft can be investigated using the multivariable limit cycle analysis technique (MULCAT) originated and developed in this study. Dual-input describing functions which reflect the scaling changes and trim shifts

in the presence of oscillation that occur in nonlinear terms of the equations are combined with eigenvalue analysis to predict the amplitude and frequency of limit cycle oscillations. The MULCAT algorithm converged to limit cycle predictions in several cases involving the subject aircraft, and direct simulation of the dynamic equations confirmed the existence of persistent oscillations. Because the initial conditions also forced divergent modes of motion (in addition to the limit cycle modes), the numerical simulations did not conclusively show the "locked-in" nature that is normally associated with limit cycles, so it is felt that MULCAT should be investigated further using simpler nonlinear dynamic models.

6.2 RECOMMENDATIONS

It is recommended that the following studies be undertaken to extend and demonstrate the utility of the work described in this report.

- Evaluate the DPCAS Using Nonlinear Aircraft Simulation

  After a digitally implemented DPCAS is synthesized, including both controller and gain adaptation logic, the study would then evaluate type 0 and type 1 structures by numerical simulation.

- Compare Pilot Model Predictions with Flight Test Records

  This study would evaluate pilot modelling -- as supported by nonlinear simulation, actual flight test, and hypothesis testing methods -- as an aid to understanding and defining air combat maneuver requirements.

- Evaluate the Sensitivity of Controller Gain Schedules to the Aircraft Model

  This study would evaluate the robustness of the gain schedule with respect to aircraft parameter or trajectory variations. Type 0

and Type 1 DPCAS control laws should be further compared with respect to their sensitivity properties.

- Investigate the Effectiveness and Generality of MULCAT

  Confidence in the use of the MULCAT approach should be developed in the context of simpler nonlinear dynamic models.

- Investigate the Effects of Partial State Feedback

  The sensor suite and associated noise and estimator required to recover the unmeasured states all play an important role in the overall aircraft performance. This important function should be addressed before DPCAS is evaluated on an actual aircraft.

REFERENCES

1. Stengel, R.F. and Berry, P.W., "Stability and Control of Maneuvering High-Performance Aircraft," NASA CR-2788, April 1977.

2. Stengel, R.F., Taylor, J.H., Broussard, J.R., and Berry, P.W., "High Angle of Attack Stability and Control," ONR-CR215-237-1, April 1976.

3. Merkel, P.A., and Whitmayer, R.A., "Development and Evaluation of Precision Control Modes for Fighter Aircraft," Proceedings of the AIAA Guidance and Control Conference, San Diego, California, 1976.

4. Weissman, R., "Preliminary Criteria for Predicting Departure Characteristics/Spin Susceptibility of Fighter-Type Aircraft," Journal of Aircraft, Vol. 10, No. 4, April 1973, pp. 214-218.

5. McRuer, D.T. and Johnston, D.E., "Flight Control Systems Properties and Problems, Vol. I," NASA CR-2500, Washington, February 1975.

6. Kleinman, D.L., Baron, S., and Levison, W.H., "A Control Theoretic Approach to Manned-Vehicle Systems Analysis," IEEE Trans. on Automatic Control, Vol. AC-16, No. 6, December 1971.

7. Kleinman, D.L. and Baron, S., "Manned Vehicle Systems Analysis by Means of Modern Control Theory," Bolt Beranek and Newman, Inc., Cambridge, Mass., BBN Rep. 1967, June 1970.

8. Kleinman, D.L., Baron, S., and Levison, W.H., "An Optimal Control Model of Human Response, Part 1 and Part 2," Automatica, Vol. 6, May 1970.

9. Kleinman, D.L. and Perkins, T.R., "Modeling Human Performance in a Time-Varying Anti-Aircraft Tracking Loop," IEEE Trans. on Automatic Control, Vol. AC-19, No. 6, August 1974.

10. Baron, S. and Levison, W.H., "An Optimal Control Methodology for Analyzing the Effects of Display Parameters on Performance and Workload in Manual Flight Control, IEEE Trans. on Systems, Man, and Cybernetics, Vol. SMC-5, No. 4, July 1975.

REFERENCES (Continued)

11. Baron S., et. al., "Application of Optimal Control Theory to the Prediction of Human Performance in a Complex Task," AFFDL-TR-69-81, March 1970.

12. Levison, W.H., "Use of Motion Cues in Steady-State Tracking," Proceedings of the Twelfth Annual Conference on Manual Control, Urbana-Champaign, Illinois, May 25-27, 1976.

13. Curry, R.E., Hoffman, W.C., and Young, L.R., "Pilot Modeling for Manned Simulation," AFFDL-TR-76-124, Vol. I, December, 1976.

14. Phatak, A.V., "Formulation and Validation of Optimal Control Theoretic Models for the Human Operator," Man-Machine Systems Review, Vol. 2, No. 2, June 1976.

15. Harvey, T.R. and Pillow, J.D., "Fly and Fight: Predicting Piloted Performance in Air-to-Air Combat," Proceedings of the Tenth Annual Conference on Manual Control, Wright-Patterson AFB, April 9-11, 1974.

16. Pitkin, E.T. and Vinje, E.W., "Evaluation of Human Operator Aural and Visual Delays with the Critical Tracking Task," Proceedings of the Eighth Annual Conference on Manual Control, May 17-19, 1972.

17. Jex, H.R. and Allen, R.W., "Research on a New Human Dynamic Response Test Battery," Proceedings of the Sixth Annual Conference on Manual Control, Wright Patterson AFB, Ohio, April 7-9, 1970, pp. 743 to 777.

18. Baron, S. and Berliner, J.E., "The Effects of Deviate Internal Representations in the Optimal Model of the Human Operator," Proceedings of the IEEE Conference on Decision and Control, Clearwater Beach, Florida, December 1-3, 1976, pp. 1055 to 1057.

19. Baron, S. and Levison, W.H., "A Display Evaluation Methodology Applied to Vertical Situation Displays," Proceedings of the Ninth Annual Conference on Manual Control, Cambridge, Mass., May 23-25, 1973.

20. Anon. "Flying Qualities of Piloted Airplanes," MIL-F-8785B(ASG), U.S. Air Force, August, 1969.

21. Stengel, R.F., Broussard, J.R., and Berry, P.W., "The Design of Digital Adaptive Controllers for VTOL Aircraft," NASA CR-144912, March 1976.

REFERENCES (Continued)

22. Stengel, R.F., Broussard, J.R., and Berry, P.W., "Digital Controllers for VTOL Aircraft," Proceedings of the 1976 IEEE Conference on Decision and Control, Clearwater, Dec. 1976, pp. 1009-1016.

23. Stengel, R.F., Broussard, J.R., and Berry, P.W., "Digital Flight Control Design for a Tandem-Rotor Helicopter," 33rd Annual National Forum of the American Helicopter Society, Washington, May 1977.

24. Ben-Israel, A. and Greville, T.N.E., Generalized Inverses: Theory and Applications, Wiley-Interscience, 1974.

25. Safonov, M.G. and Athans, M., "Gain and Phase Margin for Multiloop LQG Regulators," Proceedings of the 1976 IEEE Conference on Decision and Control, Clearwater, December, 1976, pp. 361-368.

26. Anon., "Tactical Aircraft Guidance System Advanced Development Program Flight Test Phase Report," Vols. I and II, USAAMRDL TR-73-89A,B, Ft. Eustis, VA, (prepared by CAE Electronics Ltd., Boeing Vertol Co., and IBM Federal Systems Division), April 1974.

27. DeHoff, R.L. and Hall, W.E., "Design of a Multivariable Controller for an Advanced Turbofan Engine," Proceedings of the 1976 IEEE Conference on Decision and Control, Clearwater, December 1976, pp. 1002-1008.

28. Gelb, A. and Vander Velde, W.E., Multiple-Input Describing Functions and Nonlinear System Design, McGraw-Hill, New York, 1968.

29. Sandell, Nils R., "Optimal Linear Tracking Systems," MIT Electronics Systems Laboratory, ESL-R-456 (Masters Thesis), September, 1971.

30. Anderson, B.D.O. and Moore, J.B., Linear Optimal Control, Prentic Hall, New Jersey, 1971.

31. Young, P.C. and Willems, J.C., "An Approach to the Linear Multivariate Servomechanism Problem," International Journal of Control, Vol. 15, No. 5, May 1972.

32. Kwakernaak, H. and Sivan, R., Linear Optimal Control Systems, Wiley-Interscience, New York, 1972.

REFERENCES (Continued)

33. Communications with M. Athans.

34. Davison, E.J., "The Feedforward Control of Linear Multivariable Time-Invariant Systems," Automatica, Vol. 9, 1973, pp. 561-573.

35. Davison, E.J. and Goldenberg, A., "Robust Control of a General Servomechanism Problem: The Servo Compensator," Automatica, Vol. 11, 1975, pp. 461-471.

APPENDIX A
LIST OF SYMBOLS

In general, matrices are represented by capital letters and vectors are underscored; exceptions to these rules are only made when they are contradicted by standard aerodynamic notation. Capital script letters are used to denote scalars in some cases.

Variable	Description
$\underline{a}$	In-phase component of state-vector limit cycle amplitude
$\underline{a}^*$	Total state-vector limit cycle amplitude in phasor notation ($\underline{a}^* = \underline{a} + j\underline{b}$)
a_n	Normal acceleration
a_y	Lateral acceleration
b	Wing span
$\underline{b}$	Quadrature component of state-vector limit cycle amplitude
C	Pilot control-strategy feedback matrix Type 1 DPCAS gain
C_{1_2}	Partial derivative of the nondimensional coefficient of force or moment 1 with respect to the nondimensional variable 2 (scalar)
$C_{n_\beta}{}_{dyn}$	Stability-axis derivative, corrected to principal axes
$\bar{c}$	Mean aerodynamic chord
D	Pilot control-observation matrix
e	Natural logarithm base (2.7183 ...)
F	System dynamics matrix

LIST OF SYMBOLS (Continued)

Variable	Description
$\underline{f}$	Vector-valued nonlinear function
G	Control input allocation matrix
g	Magnitude of gravitational acceleration vector Control effect scalar
H	Pilot aircraft-state observation matrix Command variable transformation matrix
H_1^2	Euler angle transformation from Frame 1 axes to Frame 2 axes
h	Altitude
I	Identity matrix
i	Index integer
J	Cost functional
j	$\sqrt{-1}$
K	Gain matrix Type 0 DPCAS gain matrix Pilot Kalman-filter gain matrix
k	Scalar gain
L	Type 0 DPCAS perturbation command gain (matrix) Aerodynamic moment about the x-axis (scalar)
ℓ	Number of pilot observations Number of commands
l_t	Tail center of pressure location
M	Aerodynamic moment about the y-axis (scalar) Cross weighting matrix between states and controls Mach number (scalar)
m	Mass of the vehicle Number of controls Meters
N	Aerodynamic moment about the z-axis (scalar) Newtons (kg m sec^{-2})

LIST OF SYMBOLS (Continued)

Variable	Description
n	Number of states
P	Riccati matrix in the optimal regulator problem
P_C	Pilot model regulator Riccati matrix
P_E	Estimation error covariance matrix of system states and pilot controls
P_u	Pilot noise-to-signal ratio for neuromotor noise
P_v	Covariance matrix in Riccati Equation
P_y	Pilot noise-to-signal ratio for observation noise
p	Rotational rate about the body x-axis
p_W	Stability-axis roll rate
Q_C	State weighting matrix
Q_E	Disturbance noise covariance matrix
q	Rotational rate about the body y-axis Weighting matrix element
q_∞	Free stream dynamic pressure ($=\frac{1}{2}\rho V_o^2$)
R_C	Control or control-rate weighting matrix
R_E	Measurement noise covariance matrix
R_L	Matrix with diagonal elements consisting of the inverse of human neuromuscular time constants
r	Rotational rate about the body z-axis Control weighting element
S	Reference area (usually wing area) Steady-state matrix inverse Control rate weighting matrix
t	Time
u	Body x-axis velocity component

LIST OF SYMBOLS (Continued)

Variable	Description
$\underline{u}$	Control vector
$\underline{u}_c$	Pilot model control command
V	Inertial velocity magnitude
V_u	Pilot neuromotor noise covariance matrix
V_x	Aircraft state covariance matrix
V_y	Pilot observation noise covariance matrix
v	Body y-axis velocity component
v_w	Wind velocity y-component
$\underline{v}_u$	Pilot neuromotor noise vector
$\underline{v}_y$	Pilot observation noise vector
w	Body z-axis velocity component
$\underline{w}$	Aircraft disturbance vector
w_y	Wind gust noise
X	Aerodynamic force along the x-axis (scalar)
	Covariance matrix of system states and pilot controls
x	Position along the x-axis
$\underline{x}$	State vector
x_{cg}	Normalized longitudinal distance between actual c.g. location and point used for aerodynamic moment measurements expressed in body axes)
$\underline{x}_I$	Inertial position vector
Y	Aerodynamic force along the y-axis (scalar)
	Covariance matrix of predicted system states and pilot controls

LIST OF SYMBOLS (Continued)

Variable	Description
y	Position along the y-axis
$\underline{y}$	Delayed pilot observation vector
$\underline{y}_d$	Command vector
Z	Aerodynamic force along the z-axis (scalar) Pilot predicted error covariance matrix of system states and controls
z	Position along the z-axis

Variable (Greek)	Description
α	Wind-body pitch Euler angle (angle of attack)
α_A	Angle of attack of aircraft
α_P	Angle of attack perceived by pilot
β	Negative of wind-body yaw Euler angle (sideslip angle)
Γ	Noise effect matrix
δ	Control variable
$\delta(t)$	Delta function
δ_{ds}	Differential stabilator deflection
δ_{mf}	Maneuvering flap deflection
δ_{ped}	Rudder pedal deflection
δ_r	Rudder delection
δ_s	Symmetric or collective stabilator deflection
δ_{sp}	Spoiler deflection
δ_T	Thrust command
ζ	Damping ratio
θ	Inertial-body pitch Euler angle

LIST OF SYMBOLS (Continued)

Variable (Greek)	Description
Λ	Wing sweep angle
λ	Eigenvalue
ξ	Integrator state
ρ	Air density Correlation coefficient
σ	Real part of an eigenvalue in sec^{-1} Alternate time variable
τ	Human time delay
τ_{n_i}	Human neuromuscular time constant
τ_y	Wind gust time constant
ϕ	Inertial-body axis roll Euler angle
ψ	Inertial-body axis yaw Euler angle
ω	Frequency in sec^{-1}; imaginary part of an eigenvalue
$\underline{\omega}_1^2$	Rotational rate vector of Reference Frame 2 with respect to Reference Frame 1 and expressed in Frame 1 coordinates. ($\underline{\omega}_1^2 = H_2^1 \underline{\omega}_2^1$ so $\underline{\omega}_2^1$ is left-handed. Thus, Frame 1 and Frame 2 are <u>not</u> interchangeable.)

Variable (Subscript or Superscript)	Description
B	Body axes
I	Inertial axes
IC	Interconnect gain Initial condition

LIST OF SYMBOLS (Continued)

Variable (Subscript or Superscript)	Description
ℓ	Aerodynamic moment about the x-axis
m	Aerodynamic moment about the y-axis
max	Maximum value
n	Aerodynamic moment about the z-axis
p	Predicted value
S	Stability axes
s	Scalar system
u	Control vector
W	Wind axes (same as stability axes for $\dot{\varepsilon}_0=\dot{\alpha}_0=0$)
X	Aerodynamic force along the x-axis
Y	Aerodynamic force along the y-axis
Z	Aerodynamic force along the z-axis
x	State vector

Operator	Definition
$(\dot{})$	Time derivative
$(\tilde{})$	Matrix equivalent to vector cross product. Specifically, if $\underline{x}$ is the three-dimensional vector

$$\underline{x} = \begin{bmatrix} x \\ y \\ z \end{bmatrix}, \text{ then } \tilde{x} = \begin{bmatrix} 0 & -z & y \\ z & 0 & -x \\ -y & x & 0 \end{bmatrix}$$

and the cross product of $\underline{x}$ and $\underline{f}$ is equal to the product of the matrix $\tilde{x}$ and the vector $\underline{f}$,

$$\underline{x} \times \underline{f} = \tilde{x}\underline{f}$$

LIST OF SYMBOLS (Continued)

Operator	Definition
$( )^T$	Transpose of a vector or matrix
$( )^{-1}$	Inverse of a matrix
$( )^*$	Steady state value
$( )_0$	Reference or nominal value of a variable
$\Delta( )$	Perturbation about the nominal value of a variable
E( )	Expected value of
det( )	Determinant of a matrix
$( )_{max}$	Maximum value, usually due to displacement limit of an actuator.
$( )_{TOT}$	Total value, usually of an aerodynamic coefficient

Acronym	Corresponding Phrase
ACM	Air Combat Maneuvering
ARI	Aileron-Rudder Interconnect
CAS	Command Augmentation System
c.g.	Center of Gravity
c.p.	Center of Pressure
DPCAS	Departure Prevention CAS
DPSAS	Departure Prevention SAS
DR	Dutch Roll
dB	Decibels
IAS	Indicated Air Speed
LCDP	Lateral control departure parameter

LIST OF SYMBOLS (Continued)

Acronym	Corresponding Phrase
LP	Lateral Phugoid
MCE	Minimum-control-effort
PIO	Pilot-Induced Oscillation
S	Spiral
SAS	Stability Augmentation System

APPENDIX B

AIRCRAFT AERODYNAMIC MODEL

The reference aircraft is a supersonic fighter designed for air superiority missions. Mass, dimensional, and inertial characteristics are listed in Table B-1.

TABLE B-1. CHARACTERISTICS OF THE REFERENCE AIRCRAFT

Mass, m	1512.7 slugs	22076 kg
Reference Area, S	565.0 ft^2	55.28 m^2
Mean Aerodynamic Chord, $\bar{c}$	9.8 ft	3.0 m
Wing Span, b	64.1 ft	19.5 m
Length	62.0 ft	18.9 m
Center of Gravity Location, x_{cg}	0.09	

The control variables are symmetric stabilator (δ_s), maneuvering flaps (δ_{mf}), differential stabilator (δ_{ds}), spoiler (δ_{sp}), and rudder (δ_r). The ranges of these variables are listed in Table B-2.

TABLE B-2. CONTROL VARIABLE RANGES

δ_s	+10 to -33 deg
δ_{mf}	+10 to 0 deg
δ_{ds}	+12 to -12 deg
δ_{sp}	+55 to -55 deg
δ_r	+30 to -30 deg

Two aerodynamic models are used in this study. One of them (the subsonic model) includes very few Mach number effects and assumes a fixed wing sweep of 22 deg. The effects of sideslip on the static forces and moments are given by tabular data, and the maximum stored angle of attack is fairly high (55 deg). This model is described in Appendix B of Ref. 2, and it will not be discussed further here.

The second model used in this study includes very complete Mach number effects and is referred to as the Mach-dependent model. Wing sweep is programmed as a function of Mach number up to the full flight sweep angle (68 deg). This model includes only linear sideslip effects, and it has a lower maximum angle of attack (30 deg).

The Mach-dependent model also differs from the subsonic model in that it expresses the angular rates and the forces and moments in stability axes. (The stability axis x-z plane lies in the body x-z plane, but with the x-stability axis along the x-z plane projection of the velocity vector.) The velocity relations are given in Eq. B-1, and the angular rates in Eq. B-2.

$$\begin{bmatrix} V \\ \beta \\ \alpha \end{bmatrix} = \begin{bmatrix} \sqrt{u^2+v^2+w^2} \\ \arctan \quad v/\sqrt{u^2+w^2} \\ \arctan\,(w/u) \end{bmatrix} \tag{B-1}$$

$$\begin{bmatrix} p_S \\ q_S \\ r_S \end{bmatrix} = \begin{bmatrix} \cos\alpha & 0 & \sin\alpha \\ 0 & 1 & 0 \\ -\sin\alpha & 0 & \cos\alpha \end{bmatrix} \begin{bmatrix} p_B \\ q_B \\ r_B \end{bmatrix} \tag{B-2}$$

The equations for the force and moment coefficients (in stability axes) are given in Eqs. B-3 to B-17. The independent variables, besides those listed above, are Mach number (M), altitude (h) and angle of attack rate ($\dot{\alpha}$).

$$\Delta C_{L_{\delta_s}} = \begin{cases} \eta_{L_{\delta_s}}(M, h)\, C_{L_{\delta_{s_1}}}(M, \alpha)\, \delta_s & 10 \geq \delta_s > -15 \\ \eta_{L_{\delta_s}}(M, h)\left[C_{L_{\delta_{s_1}}}(M, \alpha)(-15) + C_{L_{\delta_{s_2}}}(M, \alpha)(\delta_s + 15)\right] & -15 \geq \delta_s > -33 \end{cases} \tag{B-3}$$

$$\Delta C_{m_{\delta_s}} = \begin{cases} \eta_{m_{\delta_s}}(M, h)\, C_{m_{\delta_{s_1}}}(M, \alpha)\, \delta_s & 10 \geq \delta_s > -15 \\ \eta_{m_{\delta_s}}(M, h)\left[C_{m_{\delta_{s_1}}}(M, \alpha)(-15) + C_{m_{\delta_{s_2}}}(M, \alpha)(\delta_s + 15)\right] & -15 \geq \delta_s > -33 \end{cases} \tag{B-4}$$

$$C_{m_{\delta_{ds}}} = \eta_{m_{\delta_s}}(M, h)\, \Delta C_{m_{\delta_{ds}}}(M, \alpha, \delta_s) \tag{B-5}$$

$$C_{L_{\delta_{ds}}} = -\eta_{L_{\delta_s}}(M, h)\, \Delta C_{m_{\delta_{ds}}}(M, \alpha, \delta_s) \Big/ \left[\frac{\ell_t}{\bar{c}}(M) - \left[x_{cg} - 0.162\right]\right] \tag{B-6}$$

$$C_{L_{sp}} = \eta_{L_{sp}}(M, h)\, \Delta C_{L_{sp}}(M, \alpha) \tag{B-7}$$

$$C_{m_{sp}} = \eta_{m_{sp}}(M, h)\, \Delta C_{m_{sp}}(M, \alpha) \tag{B-8}$$

$$C_{A_{sp}} = \eta_{A_{sp}}(M, h)\, \Delta C_{A_{sp}}(M, \alpha) \tag{B-9}$$

$$C_{L_{mf}} = {}^{n}L_{mf}(M, h)\ \Delta C_{L_{mf}}(M, \alpha) \tag{B-10}$$

$$C_{m_{mf}} = {}^{n}m_{mf}(M, h)\ \Delta C_{m_{mf}}(M, \alpha) \tag{B-11}$$

$$C_{L_{TOT}} = C_{L_{BASIC}}(M, h, \alpha) + C_{L_{mf}}(\delta_{mf}/\delta_{mf_{MAX}}) + C_{L_{sp}}\left|\delta_{sp}/\delta_{sp_{MAX}}\right| + C_{L_{\delta_{ds}}}\left|\delta_{ds}/\delta_{ds_{REF}}\right| + \Delta C_{L_{\delta_s}} + (\bar{c}/2V)\left[C_{L_q}(M, \alpha)\ q_b + C_{L_{\dot{\alpha}}}(M, \alpha)\ \dot{\alpha}\right] \tag{B-12}$$

$$C_{Y_{TOT}} = C_{Y_\beta}(M, h, \alpha)\ \beta + C_{Y_{sp}}(M, \alpha)(\delta_{sp}/\delta_{sp_{MAX}}) + \left[C_{Y_{\delta_{ds}}}(M, \alpha) + C_{Y_{\delta_{ds}\delta_s}}(M, \alpha)\ \delta_s + C_{Y_{\delta_{ds}\delta_{ds}}}(M, \alpha)\left|\delta\right|\right]\delta_{ds} + C_{Y_{\delta_r}}(M, \alpha)\ \delta_r + (b/2V)\left[C_{Y_p}(M, \alpha)\ p_s + C_{Y_r}(M, \alpha)\ r_s\right] \tag{B-13}$$

$$C_{D_{TOT}} = C_{D_{BASIC}}(M, C_{L_{BASIC}}) + \Delta C_{D_{mf}}(M, \alpha)(\delta_{mf}/\delta_{mf_{MAX}}) + \Delta C_{D_{sp}}(M, \alpha)\left|\delta_{sp}/\delta_{sp_{MAX}}\right| \tag{B-14}$$

$$C_{l_{TOT_S}} = \left[C_{l_\beta}(M, h, \alpha) + \Delta C_{l_{\beta_s}}(M, \alpha) + \Delta C_{l_{\beta_{mf}}}(M, \alpha)(\delta_{mf}/\delta_{mf_{max}})\right]\beta + C_{l_{sp}}(\delta_{sp}/\delta_{sp_{max}}) + \left[C_{l_{\delta_{ds}}}(M, h, \alpha) + C_{l_{\delta_{ds}\delta_s}}(M, h, \alpha)\ \delta_s\right]\delta_{ds} + C_{l_{\delta_r}}(M, h, \alpha)\ \delta_r + (b/2V)\left[C_{l_p}(M, \alpha)\ p_s + C_{l_r}(M, \alpha)\ r_s\right] \tag{B-15}$$

$$C_{m_{TOT_S}} = C_{m_{BASIC}}(M, h, \alpha) + \Delta C_{m_{mf}}(\ell_{mf}/\ell_{mf_{MAX}}) + C_{m_{sp}}(\ell_{sp}/\ell_{sp_{MAX}})$$

$$+ C_{m_{\ell_{ds_i}}}(\ell_{ds}/\ell_{ds_{REF}}) + \Delta C_{m_{\ell_s}} + (\bar{c}/2V)\left[C_{m_q}(M, \alpha)\, q_b + C_{m_{\dot{\alpha}}}(M, \alpha)\, \dot{\alpha}\right]$$

$$+ C_{L_{TOT}}\left[\alpha_{act} - 0.162\right] \qquad \text{(B-16)}$$

$$C_{n_{TOT_S}} = \left[C_{n_\beta}(M, h, \alpha) + \Delta C_{n_{\beta_{\ell_s}}}(M, \alpha)\,\ell_s + \Delta C_{n_{\beta_{MF}}}(M, \alpha)(\ell_{mf}/\ell_{mf_{MAX}})\right]\beta$$

$$+ \Delta C_{n_{sp}}(M, \alpha)(\ell_{sp}/\ell_{sp_{MAX}}) + \left[C_{n_{\ell_{ds}}}(M, h, \alpha) + C_{n_{\ell_{ds}\ell_s}}(M, \alpha)\,\ell_s\right.$$

$$\left. + C_{n_{\ell_{ds}\ell_{ds}}}(M, \alpha)\,\ell_{ds_i}\right]\ell_{ds}$$

$$+ (b/2V)\left[C_{n_p}(M, \alpha)\, p_s + C_{n_r}(M, \alpha)\, r_s\right] \qquad \text{(B-17)}$$

The resulting stability-axis force and moment coefficients are transformed into body-axis force and moment coefficients by Eqs. B-18 and B-19.

$$\begin{bmatrix} C_{X_{TOT}} \\ C_{Y_{TOT}} \\ C_{Z_{TOT}} \end{bmatrix} = \begin{bmatrix} -\cos\alpha_o & 0 & \sin\alpha_o \\ 0 & 1 & 0 \\ -\sin\alpha_o & 0 & -\cos\alpha_o \end{bmatrix} \begin{bmatrix} C_{D_{TOT}} \\ C_{Y_{TOT}} \\ C_{L_{TOT}} \end{bmatrix} \qquad \text{(B-18)}$$

$$\begin{bmatrix} C_{l_{TOT_B}} \\ C_{m_{TOT_B}} \\ C_{n_{TOT_B}} \end{bmatrix} = \begin{bmatrix} \cos \alpha_o & 0 & -\sin \alpha_o \\ 0 & 1 & 0 \\ \sin \alpha_o & 0 & \cos \alpha_o \end{bmatrix} \begin{bmatrix} C_{l_{TOT_S}} \\ C_{m_{TOT_S}} \\ C_{n_{TOT_S}} \end{bmatrix} \qquad \text{(B-19)}$$

The total force and moment coefficients can be used directly to calculate the forces and moments on the aircraft for trim analysis or for nonlinear time history generation. However, a linear analysis requires the partial derivatives of the six coefficients with respect to all of the independent variables. For example, the derivative of the x-axis force coefficient ($C_{X_{TOT}}$) with respect to non-dimensional x-axis velocity (u/V_o) is given in Eq. B-20.

$$\begin{aligned} C_{X_u} = \frac{\partial C_{X_{TOT}}}{\partial (u/V_o)} = & \left[-C_{Z_{TOT}} - \cos \alpha_o \frac{\partial C_{D_{TOT}}}{\partial \alpha} + \sin \alpha_o \frac{\partial C_{L_{TOT}}}{\partial \alpha} \right] \left[\frac{\partial \alpha}{\partial (u/V_o)} \right] \\ & + \left[- \frac{\bar{c} q_o}{2V_o} C_{X_q} (M_o, \alpha_o) - \frac{\bar{c} \dot{\alpha}_o}{2V_o} C_{X_{\dot{\alpha}}} (M_o, \alpha_o) + \frac{\partial C_{X_{TOT}}}{\partial M} \frac{\partial M}{V/V_o} \right] \left[\frac{\partial (V/V_o)}{\partial (u/V_o)} \right] \\ & + \left[\frac{\partial C_{X_{TOT}}}{\partial \beta} \right] \left[\frac{\partial \beta}{\partial (u/V_o)} \right] \end{aligned} \qquad \text{(B-20)}$$

A partial derivative with respect to an angular rate is illustrated in Eq. B-21.

$$\begin{aligned} C_{l_r} = \frac{\partial C_{l_{TOT_B}}}{\partial r_B} \left(\frac{2V_o}{b} \right) = & \left\{ \cos \alpha_o \left[\frac{\partial C_{l_{TOT_S}}}{\partial p_S} \right] \left[\frac{\partial p_S}{\partial r_B} \right] + \cos \alpha_o \left[\frac{\partial C_{l_{TOT_S}}}{\partial r_S} \right] \left[\frac{\partial r_S}{\partial r_B} \right] \right. \\ & \left. - \sin \alpha_o \left[\frac{\partial C_{n_{TOT_S}}}{\partial r_S} \right] \left[\frac{\partial r_S}{\partial r_B} \right] - \sin \alpha_o \left[\frac{\partial C_{n_{TOT_S}}}{\partial p_S} \right] \left[\frac{\partial p_S}{\partial r_B} \right] \right\} \left(\frac{2V_o}{b} \right) \end{aligned} \qquad \text{(B-21)}$$

Many of these derivatives contain the partial derivatives of the nondimensional wind-axis translational velocities (V/V_0, β, α) with respect to the nondimensional body-axis translational velocities (u/V_0, v/V_0, w/V_0). This matrix of derivatives, evaluated at the nominal flight condition, is

$$\left.\frac{\partial(V/V_0,\ \beta,\ \alpha)^T}{\partial(u/V_0),\ v/V_0,\ w/V_0)^T}\right|_{V_0,\ \alpha_0,\ \beta_0} = \begin{bmatrix} \cos\alpha_0\cos\beta_0 & \sin\beta_0 & \sin\alpha_0\cos\beta_0 \\ -\cos\alpha_0\sin\beta_0 & \cos\beta_0 & -\sin\alpha_0\sin\beta_0 \\ -\sin\alpha_0/\cos\beta_0 & 0 & \cos\alpha_0/\cos\beta_0 \end{bmatrix}$$

Dimensional stability derivatives are formed by taking the derivatives of the dimensional aerodynamic forces and moments with respect to the dimensional state variables. These dimensional derivatives contain the nondimensional derivatives; $\frac{\partial X}{\partial u}$ and $\frac{\partial L}{\partial r}$ are examples of these derivatives:

$$\frac{\partial X}{\partial u} = \frac{\partial}{\partial u}\left[\tfrac{1}{2}\rho V^2 S\ C_{X_T}\right]$$

$$= \rho_0\ u\ S\ C_{X_T}\left[M_0, h_0, \alpha_0, \dot{\alpha}_0, \delta_{s_0}, \delta_{mf_0}, \delta_{sp_0}, \delta_{ds_0}, \frac{q_0\bar{c}}{2V_0}\right]$$

$$+ \tfrac{1}{2}\rho_0 V_0^2 S\ C_{X_u}\ V_0^{-1}$$

$$\frac{\partial L}{\partial r} = \frac{\partial}{\partial r}\left[\tfrac{1}{2}\rho V^2 S\ C_{l_{TOT}}\right]$$

$$= \tfrac{1}{2}\rho_0 V_0^2 S\ C_{l_r}\ \frac{b}{2V_0}$$

The complete dimensional stability derivative matrices are essentially as presented in Ref. 2.

APPENDIX C

COMMAND AUGMENTATION MODES

The primary control channels in most present-day aircraft consist of direct connections between the pilot's controls and the main control surface actuators. Additional control channels, often computer implemented, provide limited control surface movement by augmentation actuators. This appendix examines the command-to-control connections that are desirable in advanced command augmentation systems.

The first section illustrates an aileron-rudder interconnect (ARI) design method that can provide invariant steady-state response to control deflections over a range of flight conditions. The tradeoffs between various command modes are discussed, and the specific linearized command mode equations are derived for use in Chapter 4. A steady-state analysis of this command vector concludes the appendix.

C.1 AILERON-RUDDER INTERCONNECT DESIGN

The steady-state (algebraic trim) design of a control interconnect system is discussed in the context of ARI system design. The new technique is general, creating invariant steady-state response to pilot control surface commands over a wide range of angles of attack.

The steady-state solution of the linear dynamic model

$$\Delta\dot{\underline{x}}(t) = F\,\Delta\underline{x}(t) + G\,\Delta\underline{u}(t)$$

is

$$\underline{0} = F\,\Delta\underline{x}^* + G\,\Delta\underline{u}^*$$

Thus, desired values of $\Delta\underline{x}^*$ specify values of $\Delta\underline{u}^*$. For direct connections between pilot commands, $\Delta\underline{\delta}$, and control surface commands, $\Delta\underline{u}$ ($\Delta\underline{\delta} \triangleq \Delta\underline{u}$), the steady-state control setting which provides a given $\Delta\underline{x}^*$ changes as the dynamics and control effectiveness matrices change. The adjustments required for $\Delta\underline{u}^*$ become complicated at high angles of attack and can even be counter-intuitive. The aileron-rudder interconnect (ARI) used in many aircraft provides one solution to this particular problem. The ARI phases out the lateral stick-to-aileron channel and phases in a lateral stick-to-rudder channel as α_o increases, minimizing the adverse yaw effects of lateral control surfaces. The relationship between pilot and control surface commands is $K_{IC}\Delta\underline{\delta} \triangleq \Delta\underline{u}$, where K_{IC} is an interconnect "gain" matrix.

The interconnect design problem can be generalized as follows: find the interconnect matrix, K_{IC}, which compensates for dynamic variations such that the relationship between $\Delta\underline{\delta}^*$ and $\Delta\underline{x}^*$ is invariant in the steady-state solution,

$$\underline{0} = F\Delta\underline{x}^* + GK_{IC}\Delta\underline{\delta}^* \qquad \text{(C-1)}$$

K_{IC} is assumed to vary with flight condition, i.e., $K_{IC} = K_{IC}(\underline{x}_o)$. The solution is discussed using the reduced state vector

$$\Delta\underline{x} = [\Delta u\ \Delta q\ \Delta w\ \Delta v\ \Delta r\ \Delta p]^T \qquad \text{(C-2)}$$

which preserves the aircraft's essential dynamic characteristics, and F and G are defined accordingly.

Assuming that the steady-state relationship between $\Delta\underline{x}^*$ and $\Delta\underline{\delta}^*$ is acceptable at some nominal flight condition (e.g., low-α_o, straight-and-level flight), no interconnect is needed (i.e., $K_{IC}=I$), and, from Eq. C-1,

$$\Delta\underline{x}^* = -F_1^{-1}G_1\Delta\underline{\delta}^*$$

To preserve the same $\underline{x}^*$-$\Delta\underline{\delta}^*$ relationship at a different flight condition, the interconnect must be used:

$$\Delta\underline{x}^* = -F_2^{-1}G_2K_{IC}\Delta\underline{\delta}^*$$

These two equations define the interconnect matrix as

$$K_{IC} = G_2^{\#}F_2F_1^{-1}G_1 \qquad \text{(C-3)}$$

where the pseudoinverse of G_2 is taken (since G_2 is, in general, not square) and F_1 is assumed invertible (virtually always the case when the state variable is defined by Eq. C-2). K_{IC} must change with flight condition, and it can be scheduled accordingly (as in Chapter 4).

As an example, consider the pseudoinverse ARI design for a reference flight condition specified by trimmed flight at a velocity of 244 m/s (800 fps) and an altitude of 6,096 m (20,000 ft). Two pilot controls (lateral stick and pedals) command two control surfaces (differential stabilator and rudders). The four control interconnect gains obtained from Eq. C-3 vary with α_o as shown by the solid lines in Fig. C-1. The existing ARI characteristics are illustrated by the dashed lines for comparative purposes. The lateral stick-to-differential stabilator gain is close to unity in Fig. C-1 until the design angle of attack is reached (denoted by ◔), then rapidly drops. The reduction in the lateral stick to

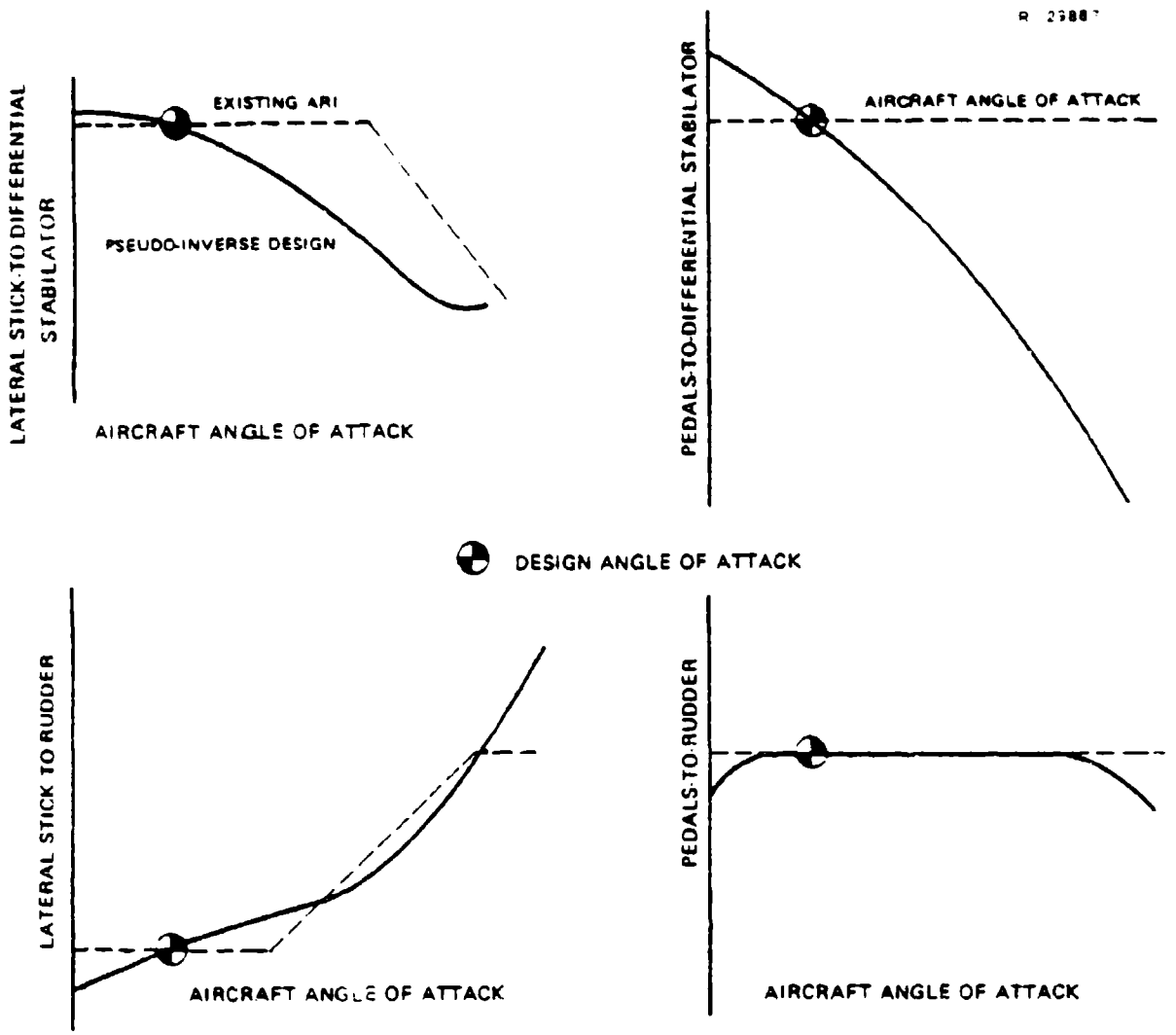

Figure C-1 Comparison of Pseudoinverse ARI Design with Existing ARI Characteristics

differential stabilator interconnect with increasing angle of attack is typical in ARI designs, as the existing ARI (the dotted curves in Fig. C-1) illustrates. The pedal-to-rudder gain remains close to unity throughout the angle of attack range studied, with some dropoff at low angles of attack because of increased rudder effectiveness. The lateral stick-to-rudder gain remains near zero for low angles of attack and rapidly increases as the lateral stick-to-differential stabilator gain decreases.

The general agreement between the control interconnect gains calculated according to Eq. C-3 and the interconnect gains actually implemented lends credence to the algebraic design procedure presented here, while suggesting possible modifications for study in the present ARI.

One difference between the pseudoinverse ARI design presented here and the actual ARI is in the pedals-to-differential stabilator gain; it is not insignificant and in fact increases in magnitude rapidly with angle of attack. Judging from the smooth behavior of the pedals-to-differential stabilator term, the use of such an interconnect gain would enable the differential stabilator to be used to improve maneuverability in high angle-of-attack flight.

C.2 AIRCRAFT COMMAND VECTOR ALTERNATIVES

The pilot command vector need not consist of the aircraft states alone; it can be formed from any reasonable combination of aircraft states and controls. This section discusses some command vector elements that are desirable from a piloting point of view, and the mathematical state-to-command transformations are derived. Linearized versions of these transformations are used in Appendix D and Chapter 4 to construct a command augmentation system.

The form of the command transformation is given by

$$\underline{y}_d = h(\underline{x}, \underline{u})$$

where $\underline{y}_d$ is the command vector, and $\underline{h}$ is a vector-valued nonlinear transformation of the states, $\underline{x}$, and the controls, $\underline{u}$. In general, the command vector can only contain as many degrees of freedom as the number of independent controls, which is, at most, six.

The four basic commanded motions are longitudinal, lateral, normal, and directional motions. Longitudinal motion results in a velocity magnitude change and can be commanded by V or $\dot{V}$. Lateral (rolling) motion is used to orient the maneuver plane and can be commanded by p, p_w, or ϕ. Normal and directional plane motions are two degree-of-freedom motions, and, in general, require two commands. In the normal plane, acceleration (a_n or q) and/or attitudes (θ, α, or γ) can be commanded, with the two-element directional command vector chosen in an analogous way. All of these commands are desirable in one situation or another. In ground attack, both flight path control (γ) and independent fuselage pointing (α) might be desirable. In air combat maneuvering, normal acceleration (a_n) is certainly a useful command, as is stability-axis roll rate (p_w).

Complete six-element command vectors are assembled next. The first example command vector is the attitude command vector,

$$\underline{y}_d = [V, \gamma, \theta, \psi, \xi, \phi]^T$$

This vector obtains flight-path control from the flight path angle, γ, and the velocity vector heading, ξ. Independent fuselage pointing is available from body pitch angle, θ; body

yaw angle, ψ, is available for crosswind correction or gun aiming. For a fighter pilot requiring rapid sustained orientation changes, an acceleration-oriented maneuvering set,

$$y_d = \left[V,\ a_n,\ \alpha,\ \beta,\ a_y,\ p_W\right]^T$$

could be useful. The maneuvering set gives the pilot direct control over normal acceleration, a_n, and roll rate about the velocity vector, p_W. Independent fuselage pointing is provided about the velocity vector using angle of attack, α, and sideslip, β, commands. The air-relative velocity magnitude, V, is commanded, and the aircraft can be directed to make a flat turn (no bank angle) with the lateral acceleration, a_y, command.

The nonlinear relations between the elements of the maneuvering command vector and the aircraft body states are given next. Some of the maneuvering commands are used in the DPCAS design in Chapter 4 and could be determined in flight using the nonlinear relations. The aircraft velocity in wind axes is

$$\begin{bmatrix} V \\ \beta \\ \alpha \end{bmatrix} = \begin{bmatrix} \sqrt{u^2 + v^2 + w^2} \\ \tan^{-1}\left(v/\sqrt{u^2 + w^2}\right) \\ \tan^{-1}\left(w/u\right) \end{bmatrix}$$

The accelerations are the second and third components of the earth-relative acceleration expressed in wind axes:

$$\begin{bmatrix} \dot{V} \\ a_y \\ a_n \end{bmatrix} = H_I^W \ddot{\underline{x}}_I = H_B^W(\alpha,\beta)\left[\dot{\underline{v}}_B + \tilde{\omega}_B^I \underline{v}_B\right]$$

where

$$H_B^W(\alpha,\beta) = \begin{bmatrix} \cos\alpha\cos\beta & \sin\beta & \sin\alpha\cos\beta \\ -\cos\alpha\sin\beta & \cos\beta & -\sin\alpha\sin\beta \\ -\sin\alpha & 0 & \cos\alpha \end{bmatrix}$$

The wind-axis roll rate is the first component of the body angular velocity expressed in wind axes, which is

$$\begin{bmatrix} p_W \\ q_W \\ r_W \end{bmatrix} = H_B^W(\alpha,\beta)\ \underline{\omega}_B^I$$

These nonlinear equations serve to relate the maneuvering command vector to the state and state rates involved in the actual aircraft dynamics, and they represent the <u>total</u> command values which drive the nonlinear model of the aircraft. Their linearized equivalents must be defined for control system design, as presented in the following section.

C.3 LINEARIZED MANEUVERING COMMAND VECTOR

The command augmentation system design methods of Chapter 4 require linearized versions of the maneuvering command vector equations given in Section C.2. The command vector is a function of both aircraft states and controls, so the following perturbation command vector equation results:

$$\Delta \underline{y}_d = H_x(\underline{x}_o, \underline{u}_o)\ \Delta \underline{x} + H_u(\underline{x}_o, \underline{u}_o)\ \Delta \underline{u}$$

The individual rows of H_x and H_u depend on the chosen elements of the command vector, and the following equations are used to derive the linear maneuvering command vector. The perturbation wind-axis velocity vector is related to the perturbation body-axis velocity vector as

$$\begin{bmatrix} \Delta V \\ \Delta \beta \\ \Delta \alpha \end{bmatrix} = J_W^{-1}(V_o, \beta_o)\ H_B^W(\alpha_o, \beta_o)\ \Delta \underline{v}_B \qquad \text{(C-4)}$$

J_W is a diagonal matrix which has elements 1, V_o, and $V_o \cos \beta_o$.

The perturbation wind-axis roll rate depends on both the perturbation body-axis angular rate and on the perturbation body-axis velocity, which affects the body-to-wind-axis transformation matrix. The desired result is the first row of the vector equation,

$$\begin{bmatrix} \Delta p_W \\ \Delta q_W \\ \Delta r_W \end{bmatrix} = H_B^W(\alpha_o, \beta_o)\Delta \underline{\omega}_B^I - H_B^W(\alpha_o, \beta_o)\tilde{\omega}_{B_o}^I L_W(\alpha_o)\ J_W^{-1}(V_o, \beta_o)\ H_B^W(\alpha_o, \beta_o)\ \Delta \underline{v}_B \qquad \text{(C-5)}$$

where

$$L_W(\alpha_o) = \begin{bmatrix} 0 & \sin\alpha & 0 \\ 0 & 0 & 1 \\ 0 & -\cos\alpha & 0 \end{bmatrix}$$

Equations C-4 and C-5 are easily evaluated using general computer routines that have been developed for this type of analysis.

The third necessary vector equation gives the relationship between the body-axis state variables and the perturbation wind-axis accelerations:

$$\begin{bmatrix} \Delta\dot{V} \\ \Delta a_y \\ \Delta a_n \end{bmatrix} = H_B^W(\alpha_o, \beta_o) \left\{ \Delta\dot{\underline{v}}_B + \tilde{\omega}^I_{B_o} \Delta\underline{v}_B - \tilde{\underline{v}}_{B_o} \Delta\underline{\omega}^I_B \right.$$
$$\left. - \left[\dot{\underline{v}}_{B_o} + \tilde{\omega}^I_{B_o} \underline{v}_{B_o} \right] L_W(\alpha_o) J_W^{-1}(V_o, \beta_o) H_B^W(\alpha_o, \beta_o) \Delta\underline{v}_B \right\} \qquad \text{(C-6)}$$

This equation requires both the nominal and perturbation body-axis velocity derivatives, $\dot{\underline{v}}_{B_o}$ and $\Delta\dot{\underline{v}}_B$. $\dot{\underline{v}}_{B_o}$ is part of the nominal flight condition specification, while $\Delta\dot{\underline{v}}_B$ consists of three rows of the linear system differential equation. Introducing these three rows causes the accelerations to be functions of the perturbation Euler angles, body-axis translational and angular rates, and the perturbation control deflections. Evaluation of Eq. C-6 is straightforward using available computer subroutines.

The perturbation maneuvering command vector is related to the perturbation states and controls by assembling the T_x and T_u matrices as indicated by Table C-1.

TABLE C-1

PERTURBATION MANEUVERING COMMAND VECTOR

COMMAND VECTOR ELEMENT	TRANSFORMATION EQUATION
ΔV	1^{st} row of Eq. C-4
Δa_n	3^{rd} row of Eq. C-6
$\Delta\alpha$	3^{rd} row of Eq. C-4
$\Delta\beta$	2^{nd} row of Eq. C-4
Δa_y	2^{nd} row of Eq. C-6
Δp_w	1^{st} row of Eq. C-5

C.4 STEADY-STATE ANALYSIS OF THE MANEUVERING COMMAND VECTOR

The maneuvering command vector contains six command variables tc be accommodated by six aircraft controls. It must be determined whether or not this command vector has practical significance for the subject aircraft -- is the system controllable, and does the aircraft possess sufficient control power to execute all six commands? These questions are easily answered using the theory contained in Appendix D.

The question of controllability can be answered by rank tests of two compound matrices:

$$\text{rank}\left[F,\ F^2G,\ \ldots\ F^{n-1}G\right] = n \qquad \text{(C-7)}$$

$$\text{rank}\begin{bmatrix} F & G \\ H_x & H_u \end{bmatrix} = n + \ell \qquad \text{(C-8)}$$

Equation C-7 is the familiar definition of controllability for a linear system, and Eq. C-8 determines whether or not the commands can be accommodated by the available controls (see Eq. D-32). Using a typical flight condition (α_o = 8 deg, V_o = 122 m/s (400 fps), h = 6,096 m (20,000 ft), q_o = 1.25 deg/sec) and computing the transformation matrix $[H_x, H_u]$ from Eq. C-6, both rank tests are satisfied, i.e., the system is controllable if the controls are allowed to have unlimited movement.

As shown in Appendix D, steady-state values of the system are obtained by taking the inverse (or pseudoinverse) of the composite matrix,

$$\begin{bmatrix} F & G \\ H_x & H_u \end{bmatrix}^{-1} = \begin{bmatrix} S_{11} & S_{12} \\ S_{21} & S_{22} \end{bmatrix}$$

and using the inverse partitions as follows:

$$\Delta \underline{x}^* = S_{12}\, \Delta \underline{y}_d^*$$

$$\Delta \underline{u}^* = S_{22}\, \Delta \underline{y}_d^*$$

Elements in S_{12} and S_{22} indicate how controls and states change positions as the commands are varied. Large values in S_{22} indicate that the controls may reach their limits before the command is accommodated. Values for S_{12} and S_{22} obtained from the rank test at the flight condition chosen are shown in Eqs. C-9 and C-10. The units of the states and commands in Eq. C-9 remain the same for the rest of this section. Control output is in degrees.

$$\begin{bmatrix} \Delta\theta \text{ deg/sec} \\ \Delta u \text{ fps} \\ \Delta q \text{ deg/sec} \\ \Delta w \text{ fps} \\ \Delta v \text{ fps} \\ \Delta r \text{ deg/sec} \\ \Delta p \text{ deg/sec} \\ \Delta\phi \text{ deg/sec} \end{bmatrix}^{\bullet} = \begin{bmatrix} -0.0675 & 10^6 & -2.45 & 0.0 & 0.0 & 0.0 \\ 0.990 & -0.0861 & -0.983 & 0.0 & 0.0 & 0.0 \\ 0.0 & 0.139 & 0.0 & 0.0 & 0.0 & 0.0 \\ 0.141 & 0.877 & 6.91 & 0.0 & 0.0 & 0.0 \\ 0.0 & 0.0 & 0.0 & 6.98 & 3.34 & 0.0 \\ 0.0 & 0.0 & 0.0 & 0.0 & -0.281 & 0.142 \\ 0.0 & 0.0 & 0.0 & 0.0 & -0.048 & -0.0202 \\ 0.0 & 0.0 & 0.0 & 0.700 & 10^5 & 1.82 \end{bmatrix} \begin{bmatrix} \\ \Delta V \text{ fps} \\ \Delta a_n \text{ fps}^2 \\ \Delta\alpha \text{ deg} \\ \Delta\beta \text{ deg} \\ \Delta p_W \text{ deg/sec} \\ \Delta a_y \text{ fps}^2 \end{bmatrix}^{\bullet} \tag{C-9}$$

$$\begin{bmatrix} \Delta\delta_T \\ \Delta\delta_s \\ \Delta\delta_{mf} \\ \Delta\delta_{sp} \\ \Delta\delta_{ds} \\ \Delta\delta_r \end{bmatrix}^{\bullet} = \begin{bmatrix} -0.00582 & -1.23(10^4) & -0.185 & 0.0 & 0.0 & 0.0 \\ 0.167 & -3.01(10^4) & 2.29 & 0.0 & 0.0 & 0.0 \\ -0.301 & 3.19(10^4) & -5.47 & 0.0 & 0.0 & 0.0 \\ 0.0 & 0.0 & 0.0 & 2.08 & 10^6 & 1.26 \\ 0.0 & 0.0 & 0.0 & -1.48 & 10^6 & -0.296 \\ 0.0 & 0.0 & 0.0 & 1.16 & 10^5 & -0.0106 \end{bmatrix} \begin{bmatrix} \Delta V \\ \Delta a_n \\ \Delta\alpha \\ \Delta\beta \\ \Delta p_W \\ \Delta a_y \end{bmatrix}^{\bullet} \tag{C-10}$$

The pitch and roll Euler angles are included in F and G and, as expected, exhibit very large values when either Δa_n or Δp_W is commanded. The large (though finite) values for $\Delta\theta$ and $\Delta\phi$ also cause the controls to saturate. The Euler angles are almost pure integrations (they couple into the other states because of the gravity vector) and have meaningless steady-state interpretations when Δa_n or Δp_W is commanded. The Euler angles are removed from F and G, and the composite matrix is inverted again producing the steady-state matrices shown next.

$$\begin{bmatrix} \Delta u \\ \Delta q \\ \Delta w \\ \Delta v \\ \Delta r \\ \Delta p \end{bmatrix}^{\bullet} = \begin{bmatrix} 0.990 & 0.0 & -0.983 & 0.0 & 0.0 & 0.0 \\ 0.0 & 0.143 & 0.0 & 0.0 & 0.0 & 0.0 \\ 0.141 & 0.0 & 6.91 & 0.0 & 0.0 & 0.0 \\ 0.0 & 0.0 & 0.0 & 6.98 & 0.0 & 0.0 \\ 0.0 & 0.0 & 0.0 & 0.0 & 0.141 & 0.142 \\ 0.0 & 0.0 & 0.0 & 0.0 & 0.990 & -0.020 \end{bmatrix} \begin{bmatrix} \Delta V \\ \Delta a_n \\ \Delta\alpha \\ \Delta\beta \\ \Delta p_W \\ \Delta a_y \end{bmatrix}^{\bullet}$$

$$\begin{bmatrix} \Delta\delta_T \\ \Delta\delta_s \\ \Delta\delta_{mf} \\ \Delta\delta_{sp} \\ \Delta\delta_{ds} \\ \Delta\delta_r \end{bmatrix}^* = \begin{bmatrix} -0.0002 & 0.0089 & 0.018 & 0.0 & 0.0 & 0.0 \\ 0.181 & -1.15 & 2.79 & 0.0 & 0.0 & 0.0 \\ -1.316 & 4.95 & -6.00 & 0.0 & 0.0 & 0.0 \\ 0.0 & 0.0 & 0.0 & -34.8 & -0.063 & -94.78 \\ 0.0 & 0.0 & 0.0 & 7.60 & -0.258 & 23.35 \\ 0.0 & 0.0 & 0.0 & 0.827 & 0.020 & -0.867 \end{bmatrix} \begin{bmatrix} \Delta V \\ \Delta a_n \\ \Delta\alpha \\ \Delta\beta \\ \Delta p_w \\ \Delta a_y \end{bmatrix}^*$$

The steady-state values are meaningful but indicate that any significant Δa_y command causes the lateral controls to reach their control limits. The lateral controls have poor lateral acceleration command power, requiring Δa_y to be eliminated as a command. Throttle is considered to be a fixed control, and $\Delta\delta_T$ and ΔV are removed from F and G.

To continue the steady-state analysis, the steady-state matrices are obtained using the pseudoinverse (Eq. D-9) of the composite matrix, since the number of controls now exceed the commands. The rank test given by Eq. C-8 is still satisfied, producing

$$\begin{bmatrix} \Delta u \\ \Delta q \\ \Delta w \\ \Delta v \\ \Delta r \\ \Delta p \end{bmatrix}^* = \begin{bmatrix} 42.15 & 85.4 & 0.0 & 0.0 \\ 0.143 & 0.0 & 0.0 & 0.0 \\ 5.99 & 19.2 & 0.0 & 0.0 \\ 0.0 & 0.0 & 6.98 & 0.0 \\ 0.0 & 0.0 & -0.052 & 0.142 \\ 0.0 & 0.0 & 0.0074 & 0.99 \end{bmatrix} \begin{bmatrix} \Delta a_n \\ \Delta\alpha \\ \Delta\beta \\ \Delta p_w \end{bmatrix}^*$$

$$\begin{bmatrix} \Delta\delta_s \\ \Delta\delta_{mf} \\ \Delta\delta_{sp} \\ \Delta\delta_{ds} \\ \Delta\delta_r \end{bmatrix}^* = \begin{bmatrix} 6.54 & 18.5 & 0.0 & 0.0 \\ -11.48 & -33.5 & 0.0 & 0.0 \\ 0.0 & 0.0 & -0.313 & -0.116 \\ 0.0 & 0.0 & -0.914 & -0.258 \\ 0.0 & 0.0 & 1.14 & 0.020 \end{bmatrix} \begin{bmatrix} \Delta a_n \\ \Delta\alpha \\ \Delta\beta \\ \Delta p_w \end{bmatrix}^*$$

A sideslip command produces reasonable settings of three lateral-directional controls, and a roll rate command primarily affects the lateral controls. In the longitudinal states, problems still exist because of the large changes in velocity and the large longitudinal control values needed to accommodate both Δa_n and $\Delta\alpha$ commands. Using Δa_n as the more desirable longitudinal command and eliminating $\Delta\alpha$, the steady-state values reduce to

$$\begin{bmatrix} \Delta u \\ \Delta q \\ \Delta w \\ \Delta v \\ \Delta r \\ \Delta p \end{bmatrix}^* = \begin{bmatrix} 2.67 & 0.0 & 0.0 \\ 0.143 & 0.0 & 0.0 \\ -2.88 & 0.0 & 0.0 \\ 0.0 & 6.98 & 0.0 \\ 0.0 & -0.052 & 0.142 \\ 0.0 & 0.0074 & 0.99 \end{bmatrix} \begin{bmatrix} \Delta a_n \\ \\ \Delta\beta \\ \\ \\ \Delta p_w \end{bmatrix}^*$$

$$\begin{bmatrix} \Delta\delta_s \\ \Delta\delta_{mf} \\ \Delta\delta_{sp} \\ \Delta\delta_{ds} \\ \Delta\delta_r \end{bmatrix}^* = \begin{bmatrix} -2.41 & 0.0 & 0.0 \\ 4.66 & 0.0 & 0.0 \\ 0.0 & -0.313 & -0.116 \\ 0.0 & -0.914 & -0.258 \\ 0.0 & 1.14 & 0.020 \end{bmatrix} \begin{bmatrix} \Delta a_n \\ \\ \Delta\beta \\ \\ \Delta p_w \end{bmatrix}^*$$

The results are reasonable, and the controls and commands in Eq. C-11 represent a controllable situation.

In summary, this appendix has investigated command vector sets ranging from direct pilot-to-control surface linkage to aircraft state-oriented maneuvering command sets. A lateral-directional control interconnect design procedure which results in invariant aircraft steady-state response to the pilot's stick and pedal deflections is developed. The

pseudoinverse interconnect design is similar to conventional ARI design philosophy, and a comparison demonstrates they produce remarkably similar gain variations.

Pilot-oriented command vector sets are discussed, and the necessary mathematical transformations are derived. The maneuvering command vector set is subjected to controllability and steady-state tests at a typical flight condition, taking into account control power and command practicality. The controls and state commands are subsequently reduced until reasonable results are obtained. The resulting control vector

$$\Delta \underline{u} = \left[\Delta\delta_s \;\; \Delta\delta_{mf} \;\; \Delta\delta_{sp} \;\; \Delta\delta_{ds} \;\; \Delta\delta_r \right]^T$$

and command vector

$$\Delta \underline{y}_d = \left[\Delta a_n \;\; \Delta\beta \;\; \Delta p_w \right]^T$$

are employed in the DPCAS designs in Chapter 4.

APPENDIX D

DESIGN OF PROPORTIONAL-INTEGRAL CONTROLLERS BY LINEAR-OPTIMAL CONTROL THEORY

Extending the results in Ref. 2, a continuous-time linear-optimal regulator combined with forward-loop dynamic compensation is applied to the design of a Departure-Prevention Command Augmentation System (DPCAS). This appendix summarizes DPCAS theory and design principles and expands on Type 1 control results reported in Refs. 29 and 22.

A command system attempts to stabilize a dynamical system and drive the states and controls to desired nonzero steady-state values. Steady-state analysis of a dynamical system plays a major role in DPCAS design and is discussed in the following section. The rest of the appendix presents Type 0 and Type 1 control laws. The Type 0 and Type 1 controllers with control-rate-weighting are the DPCAS mechanizations used in this report.

D.1 STEADY-STATE ANALYSIS

A linear, time-invariant system, given by

$$\Delta\dot{\underline{x}}(t) = F\,\Delta\underline{x}(t) + G\,\Delta u(t)$$

where $\Delta\underline{x}(t)$ is an $(n\times 1)$ state vector and $\Delta\underline{u}(t)$ is an $(m\times 1)$ control vector, is in steady state when the state rates, $\Delta\dot{\underline{x}}(t)$, are zero. In steady state, the states and controls reach the equilibrium points $\Delta\underline{x}^*$ and $\Delta\underline{u}^*$, which must satisfy

$$0 = F\ \Delta\underline{x}^* + G\ \Delta\underline{u}^* \qquad \text{(D-1)}$$

If the (n×n) system matrix, F, is invertible, then the equilibrium state values for fixed controls are:

$$\Delta\underline{x}^* = -F^{-1}\ G\ \Delta\underline{u} \qquad \text{(D-2)}$$

Consider the situation where combinations of states and controls must reach values specified by the (ℓ×1) vector, $\Delta\underline{y}_d$, which is a linear function of the states and controls:

$$\Delta\underline{y}_d = H_x\Delta\underline{x}^* + H_u\Delta\underline{u}^* = \begin{bmatrix} H_x & H_u \end{bmatrix}\begin{bmatrix} \Delta\underline{x}^* \\ \Delta\underline{u}^* \end{bmatrix} \qquad \text{(D-3)}$$

H_x and H_u are constant (ℓ×n) and (ℓ×m) matrices, respectively. Equation D-3 can be combined with Eq. D-1 to produce the simultaneous set of equations,

$$\begin{bmatrix} F & G \\ H_x & H_u \end{bmatrix}\begin{bmatrix} \Delta\underline{x}^* \\ \Delta\underline{u}^* \end{bmatrix} = \begin{bmatrix} 0 \\ I \end{bmatrix}\Delta\underline{y}_d$$

If the number of desired values, ℓ, and the number of controls, m, are equal, and if the composite matrix is invertible,

$$\begin{bmatrix} F & G \\ H_x & H_u \end{bmatrix}^{-1} = \begin{bmatrix} S_{11} & S_{12} \\ S_{21} & S_{22} \end{bmatrix} \qquad \text{(D-4)}$$

then $\Delta\underline{x}^*$ and $\Delta\underline{u}^*$ are uniquely given by

$$\Delta\underline{x}^* = S_{12}\Delta\underline{y}_d \qquad \text{(D-5)}$$

$$\Delta \underline{u}^* = S_{22} \Delta \underline{y}_d \qquad \text{(D-6)}$$

Equation D-4 is the most general method for obtaining the steady-state matrices, S_{12} and S_{22}, when the commands and controls are equal. If F is invertible, then the solution for these matrices can be expressed directly. Substituting for $\Delta \underline{x}^*$ in Eq. D-3 using Eq. D-2 and solving for $\Delta \underline{u}^*$ leads to

$$\Delta \underline{u}^* = \left(-H_x F^{-1} G + H_u \right)^{-1} \Delta \underline{y}_d \qquad \text{(D-7)}$$

With this result, Eq. D-2 can be rewritten

$$\Delta \underline{x}^* = -F^{-1} G \left(-H_x F^{-1} G + H_u \right)^{-1} \Delta \underline{y}_d \qquad \text{(D-8)}$$

Comparing Eqs. D-5 and D-6 with Eqs. D-7 and D-8 we obtain,

$$S_{22} = \left(-H_x F^{-1} G + H_u \right)^{-1}$$

$$S_{12} = -F^{-1} G \left(-H_x F^{-1} G + H_u \right)^{-1}$$

Difficulty arises when the composite matrix in Eq. D-4 can not be inverted. There are two reasons why the composite matrix may not be invertible. The first reason is that it is singular, i.e., that it contains linearly dependent (or null) rows or columns. The second possible reason is that the composite matrix is not square. This is <u>always</u> the case when the dimensions of $\Delta \underline{y}_d$ and $\Delta \underline{u}$ are not equal. All of these cases can arise in the aircraft control problem and are discussed below.

Consider first the case of the <u>singular composite matrix</u>. This could occur, for example, if $\Delta \underline{y}_d$ contains body-axis yaw rate, Δr_d, and the aircraft's dynamic model includes

the yaw Euler angle, $\Delta\psi$. In this case, F and H_x contain the same zero column (since $\Delta\psi$ has no direct dynamic effect), and the composite matrix is singular. The physical meaning of this result is that the yaw angle is continually changing as the aircraft turns and does not reach a steady-state constant value, i.e., elements in S_{12} are infinite. In Chapter 4, $\Delta\psi$ is eliminated from the state vector to avoid a singular composite matrix ($\Delta\phi$ and $\Delta\theta$ can introduce singularity for certain non-straight-and-level flight conditions and also are eliminated from $\Delta\underline{x}$; see Eq. C-9).

The second case can occur when there are more controls than commands, i.e., the steady-state problem is underconstrained. There are many steady-state control positions, $\Delta\underline{u}^*$, (actually, an infinite number) which correspond to the desired final value, $\Delta\underline{y}_d$. In practice, the deflection limits on control effector motions restrict the allowable $\Delta\underline{u}^*$, and this information can be put to good use in control system design. The DPCAS is an underconstrained system, because five control effectors are used to achieve desired steady-state values of three commands.

There are at least three techniques for defining $\Delta\underline{u}^*$ in the underconstrained case. The first approach is to make commands to the "extra" control effectors linear combinations of the commands to the primary control effectors, essentially making ℓ and m equal. For example, spoiler commands can be proportional to aileron (or differential stabilator) commands, and flap commands can be keyed to elevator (or symmetric stabilator) commands:

$$\delta_{sp} = k_1\delta_a$$

$$\delta_{mf} = k_2\delta_e$$

k_1 and k_2 can be specified by requiring that the two related controls reach their respective deflection limits at the same time. (The scale factors can vary with flight condition, blending controls in and out, as appropriate.)

The second method for handling the underconstrained case is to increase the number of desired values until ℓ and m are equal. For example, some control deflections may have desired values (e.g., flap setting during landing approach); then Eq. D-3 can be written as

$$\begin{bmatrix} \Delta \underline{y}_{d_1} \\ \hline \Delta \underline{y}_{d_2} \end{bmatrix} = \begin{bmatrix} H_x \\ \hline 0 \end{bmatrix} \Delta \underline{x}^* + \left[\begin{array}{c|c} H_{u_1} & H_{u_2} \\ \hline 0 & I \end{array}\right] \begin{bmatrix} \Delta \underline{u}^*_1 \\ \hline \Delta \underline{u}^*_2 \end{bmatrix}$$

Using this technique, the ($\ell \times 1$) vector, $\Delta \underline{u}^*_1$ accommodates $\Delta \underline{y}_{d_1}$ and compensates for $\Delta \underline{u}^*_2$; $\Delta \underline{u}^*_2$ can be placed at any position desired.

The third technique, and the one used in the DPCAS design, makes use of the pseudoinverse (Ref. 24) to invert a non-square matrix. In the underconstrained case, the pseudoinverse matrix is defined as

$$\begin{bmatrix} F & G \\ H_x & H_u \end{bmatrix}^{\#} \triangleq \begin{bmatrix} F & G \\ H_x & H_u \end{bmatrix}^T \left\{ \begin{bmatrix} F & G \\ H_x & H_u \end{bmatrix} \begin{bmatrix} F & G \\ H_x & H_u \end{bmatrix}^T \right\}^{-1}$$

Steady-state values of $\Delta \underline{x}$ and $\Delta \underline{u}$ are computed as

$$\begin{bmatrix} \Delta \underline{x}^* \\ \Delta \underline{u}^* \end{bmatrix} = \begin{bmatrix} F & G \\ H_x & H_u \end{bmatrix}^{\#} \begin{bmatrix} 0 \\ I \end{bmatrix} \Delta \underline{y}_d \qquad \text{(D-9)}$$

where the pseudoinverse composite matrix is of dimension $(n+m) \times (n+\ell)$. As in Eq. D-4, there are four partitions in the pseudoinverse composite matrix:

$$\begin{bmatrix} F & G \\ H_x & H_u \end{bmatrix}^{\#} = \begin{bmatrix} S_{11} & S_{12} \\ S_{21} & S_{22} \end{bmatrix} \qquad \text{(D-10)}$$

The physical interpretation is that the matrices S_{12} and S_{22} provide a least-squares solution of minimum length for $\Delta\underline{u}^*$, given $\Delta\underline{y}_d$. This property of the pseudoinverse is appealing because it allows $\Delta\underline{y}_d$ to be accommodated using minimum changes in the control positions.

Steady-state analysis indicates the trim state of the aircraft. For nonlinear dynamic models, the trim condition is defined by functional minimization, as in Ref. 1. For linear dynamic models, the trim condition is specified by Eq. D-9. If the linear system actually is an approximation to a nonlinear system (<u>always</u> the case for aircraft models), S_{12} and S_{22} represent the sensitivity of the nonlinear trim condition to small perturbations in the desired states and controls. Consider a system obtained by linearizing the aircraft's nonlinear dynamic model about some nominal trajectory. The desired command value is a nonlinear function of the nominal states and controls,

$$\underline{y}_{d_o} = h\ (\underline{x}_o^*, \underline{u}_o^*) \qquad \text{(D-11)}$$

as shown in Appendix C. For changes in $\underline{y}_{d_o}$, represented as $\Delta\underline{y}_d$, Eq. D-11 becomes

$$\underline{y}_d = \underline{y}_{d_o} + \Delta\underline{y}_d \cong h(\underline{x}_o^*, \underline{u}_o^*) + H_x\ \Delta\underline{x}^* + H_u\ \Delta\underline{u}^*$$

and the new trim values are approximately given by

$$\underline{x}^* \cong \underline{x}_o^* + \Delta\underline{x}^* = \underline{x}_o^* + S_{12}\Delta\underline{y}_d \qquad \text{(D-12)}$$

$$\underline{u}^* \cong \underline{u}_o^* + \Delta\underline{u}^* = \underline{u}_o^* + S_{22}\Delta\underline{y}_d \qquad \text{(D-13)}$$

A graphical depiction of Eqs. D-12 and D-13 is shown in Fig. D-1. Combining trim and linear steady-state values in a control law is shown in Section D.5.

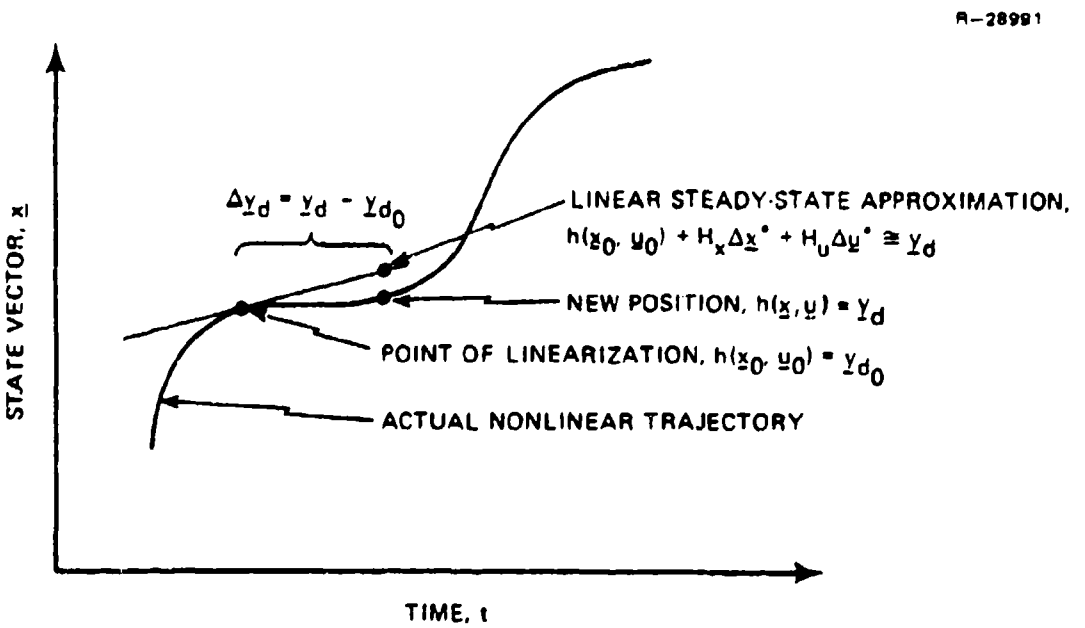

Figure D-1 Linear Projection of Steady-State Values

Steady-state analysis shows how to instantaneously change the controls to achieve the desired command. The next task is to maneuver from one steady-state condition to another using a smooth, stable, state trajectory and modest control motions. The maneuvering can be accomplished by combining steady-state analysis with optimal control design techniques to develop a control law which drives the command error to zero as time increases:

$$\lim_{t \to 0} (\Delta \underline{y}(t) - \Delta \underline{y}_d) = 0$$

where $\Delta \underline{y}(t)$ is the system output,

$$\Delta \underline{y}(t) = H_x \Delta \underline{x}(t) + H_u \Delta \underline{u}(t)$$

The two control structures used in this report to drive the command error to zero -- the Type 0 DPCAS and the Type 1 DPCAS -- are derived in the following sections.

D.2 TYPE 0 DPCAS WITH CONTROL-RATE WEIGHTING

A Type 0 controller is a feedback regulator which asymptotically stabilizes a system and drives the command error to zero without using pure integral compensation. A multi-input/multi-output Type 0 controller which implicitly limits commanded control rates can be designed using linear-optimal control theory, as in Ref. 30. The Type 0 DPCAS presented in Chapter 4 is designed using this approach, and its derivation is summarized below.

A linear-optimal regulator for the system

$$\Delta \dot{\underline{x}}(t) = F \Delta \underline{x}(t) + G \Delta \underline{u}(t) \qquad \text{(D-14)}$$

takes the form

$$\Delta \underline{u}(t) = -K \Delta \underline{x}(t) \qquad \text{(D-15)}$$

where the gain matrix, K, minimizes the quadratic cost function

$$J = \int_0^\infty \begin{bmatrix} \Delta \underline{x}^T & \Delta \underline{u}^T \end{bmatrix} \begin{bmatrix} Q & M \\ M^T & R \end{bmatrix} \begin{bmatrix} \Delta \underline{x} \\ \Delta \underline{u} \end{bmatrix} dt \qquad \text{(D-16)}$$

The state-weighting matrix, Q, is required to be non-negative definite and symmetric, while the control-weighting matrix, R, must be positive definite and symmetric. The cross-weighting matrix, M, arises when limitations on state rates are to be considered in the cost function. The design parameters for the linear-optimal regulator are contained in Q, R, and M.

The gain matrix in Eq. D-15 is defined by

$$K = R^{-1}(G^T P + M^T)$$

where P is a symmetric, positive semi-definite matrix and is the steady-state solution of a matrix Riccati equation:

$$\dot{P} = -PF - F^T P - Q + (PG+M)R^{-1}(PG+M)^T$$

Given the initial conditions on the state, P has the interesting property that value of the minimum cost is given by

$$J = \Delta\underline{x}^T(0)P\Delta\underline{x}(0) \qquad \text{(D-17)}$$

The linear-optimal regulator can be modified for non-zero command regulation by shifting the coordinates of the system to the desired steady-state values. Using the steady-state variables defined in Eqs. D-5 and D-6, the shifted variables are

$$\Delta\tilde{\underline{x}}(t) = \Delta\underline{x}(t) - \Delta\underline{x}^*$$

$$\Delta\tilde{\underline{u}}(t) = \Delta\underline{u}(t) - \Delta\underline{u}^*$$

Modifying the system dynamics to include coordinate shifting and the weighting of $\Delta\dot{\underline{u}}(t)$ in the quadratic cost functional, Eq. D-12 becomes

$$\begin{bmatrix} \Delta\dot{\underline{x}}(t) \\ \Delta\dot{\underline{u}}(t) \end{bmatrix} = \begin{bmatrix} F & G \\ 0 & 0 \end{bmatrix} \begin{bmatrix} \Delta\underline{x}(t) \\ \Delta\underline{u}(t) \end{bmatrix} + \begin{bmatrix} 0 \\ I \end{bmatrix} \Delta\underline{v}(t)$$

The (m×1) vector, $\Delta\underline{v}(t)$ is the new control variable, and it is equivalent to the control rate, $\Delta\dot{\underline{u}}(t)$.

Weighting the shifted variables and the control rate leads to the cost function

$$J = \int_0^\infty \left\{ \begin{bmatrix} \Delta\underline{x}^T(t) & \Delta\underline{u}^T(t) \end{bmatrix} \begin{bmatrix} Q_1 & M \\ M^T & Q_2 \end{bmatrix} \begin{bmatrix} \Delta\underline{x}(t) \\ \Delta\underline{u}(t) \end{bmatrix} + \Delta\underline{v}^T(t) R \Delta\underline{v}(t) \right\} dt \qquad \text{(D-18)}$$

Using the results for the linear-optimal regulator, the control law which minimizes the cost function is

$$\Delta\dot{\underline{u}}(t) = -K_1 \Delta\underline{x}(t) - K_2 \Delta\underline{u}(t) \qquad \text{(D-19)}$$

This control law is similar to the basic optimal regulator, except that control rate is commanded, $K_2\Delta\underline{u}$ introduces a low-pass filtering effect, and the feedback law operates on the shifted variables. The control gains are computed from the Riccati equation solution by

$$\begin{bmatrix} K_1 & K_2 \end{bmatrix} = R^{-1} \begin{bmatrix} 0 & I \end{bmatrix} \begin{bmatrix} P_{11} & P_{12} \\ P_{21} & P_{22} \end{bmatrix}$$

where the algebraic Riccati equation is

$$\begin{bmatrix} P_{11} & P_{12} \\ P_{21} & P_{22} \end{bmatrix} \begin{bmatrix} F & G \\ 0 & 0 \end{bmatrix} + \begin{bmatrix} F^T & 0 \\ G^T & 0 \end{bmatrix} \begin{bmatrix} P_{11} & P_{12} \\ P_{21} & P_{22} \end{bmatrix} + \begin{bmatrix} Q_1 & M \\ M^T & Q_2 \end{bmatrix} - \begin{bmatrix} P_{11} & P_{12} \\ P_{21} & P_{22} \end{bmatrix} \begin{bmatrix} 0 & 0 \\ 0 & R^{-1} \end{bmatrix} \begin{bmatrix} P_{11} & P_{12} \\ P_{21} & P_{22} \end{bmatrix} = 0$$

The control law given by Eq. D-19 can be expressed in terms of the unshifted variables by using Eqs. D-5 and D-6:

$$\Delta\dot{\underline{u}}(t) = -K_1\,\Delta\underline{x}(t) - K_2\,\Delta\underline{u}(t) + L\,\Delta\underline{y}_d$$

where

$$L = K_1 S_{12} + K_2 S_{22}$$

The control law is implemented by integrating $\Delta\dot{\underline{u}}(t)$ to provide a signal which is compatible with the linear dynamic system, as shown in Fig. 45. Thus, the control command takes the form

$$\Delta\underline{u}(t) = \Delta\underline{u}(0) + \int_0^t \left[-K_1\Delta\underline{x}(\tau) - K_2\Delta\underline{u}(\tau) + L\Delta\underline{y}_d(\tau)\right]d\tau \quad \text{(D-20)}$$

which can be rewritten as

$$\Delta\underline{u}(t) = e^{-K_2 t}\,\Delta\underline{u}(0) + \int_0^t e^{-K_2(t-\tau)}\left[-K_1\Delta\underline{x}(\tau) + L\Delta\underline{y}_d(\tau)\right]d\tau$$

The Type 0 control law follows the command for the linear system given by Eq. D-14 as long as S_{12} and S_{22} faithfully represent steady-state conditions for the system matrices (F and G) and there are no biases in the control loop. The initial value of control, $\Delta\underline{u}(0)$, still must be found; Section D-4 illustrates how an optimal value can be determined.

If it is desirable to track the command, $\Delta\underline{y}_d$, with zero steady-state error, allowing for variations in F and G as well as biases, then a Type 1 controller may be preferable. There are at least two procedures for obtaining a Type 1 control law using linear optimal control theory -- integrator-

state weighting (Refs. 31 and 32) or transformation of a control-rate weighting structure; the latter is used in the Type 1 DPCAS design and is described below.

D.3 A TYPE 1 DPCAS WITH CONTROL-RATE WEIGHTING

This section presents the derivation of the Type 1 DPCAS. The Type 1 linear-optimal controller with control-rate weighting has been derived in Ref. 29 for the case in which the controls and commands are equal. In this section, we present a derivation which does not require equal commands and controls and illustrate how the proper choice of $\Delta\underline{u}(0)$ eliminates the possibility of a feedforward element in the Type 1 DPCAS structure.

When m and ℓ are equal, the derivation proceeds as in Section D.2 up to Eq. D-19, which presents the Type 0 controller with control-rate commands using the shifted variables. Our objective is to convert this result to a Type 1 control law with shifted variables, i.e., one without the "low-pass" feedback of $\Delta\underline{u}$. The desired form of the control law is,

$$\Delta\tilde{\underline{u}}(t) = -C_1\Delta\tilde{\underline{x}}(t) - C_2\Delta\tilde{\underline{\xi}}(t) \qquad \text{(D-21)}$$

$$\Delta\tilde{\underline{\xi}}(t) = \int_0^t \left\{H_x\Delta\tilde{\underline{x}}(\tau) + H_u\Delta\tilde{\underline{u}}(\tau)\right\}d\tau \qquad \text{(D-22)}$$

The variable, $\Delta\tilde{\underline{\xi}}(t)$, is the shifted integrator state that provides the Type 1 property. Comparing Eq. D-21 with Eq. D-19, we have $m(n+\ell)$ unknowns in C_1 and C_2 and $m(n+m)$ knowns in K_1 and K_2. Since ℓ and m are equal, we have as many knowns as unknowns, and the problem should have a unique solution.

The derivation proceeds by performing mathematical and algebraic operations on Eq. D-21 until we obtain a form similar to the Type 0 DPCAS. Taking the derivatives of Eqs. D-21 and D-22, we have,

$$\Delta\dot{\underline{u}}(t) = -C_1\Delta\dot{\underline{x}}(t) - C_2\,\Delta\dot{\underline{\xi}}(t) \tag{D-23}$$

$$\Delta\dot{\underline{\xi}}(t) = H_x\Delta\dot{\underline{x}}(t) + H_u\Delta\dot{\underline{u}}(t) \tag{D-24}$$

The shifted system dynamics,

$$\Delta\dot{\underline{x}}(t) = F\Delta\underline{x}(t) + G\Delta\underline{u}(t)$$

and integrator state dynamics (Eq. D-25) are substituted into Eq. D-23, producing,

$$\Delta\dot{\underline{u}}(t) = -C_1\left[F\Delta\underline{x}(t) + G\Delta\underline{u}(t)\right] - C_2\left[H_x\Delta\underline{x}(t) + H_u\Delta\underline{u}(t)\right]$$

The components are regrouped as follows:

$$\Delta\dot{\underline{u}}(t) = -\begin{bmatrix}C_1 & C_2\end{bmatrix}\begin{bmatrix}F & G\\ H_x & H_u\end{bmatrix}\begin{bmatrix}\Delta\underline{x}(t)\\ \Delta\underline{u}(t)\end{bmatrix} \tag{D-25}$$

Comparing Eq. D-25 with the shifted Type 0 DPCAS, Eq. D-19, we observe that they are equivalent if the following relationship holds between the two gain sets:

$$\begin{bmatrix}C_1 & C_2\end{bmatrix}\begin{bmatrix}F & G\\ H_x & H_u\end{bmatrix} = \begin{bmatrix}K_1 & K_2\end{bmatrix} \tag{D-26}$$

The composite matrix in Eq. D-26 is the one used in steady-state analysis (Eq. D-4); when m and ℓ are equal, the composite

matrix is invertible. Post-multiplying both sides of Eq. D-26 by the composite matrix inverse produces,

$$\begin{bmatrix} C_1 & C_2 \end{bmatrix} = \begin{bmatrix} K_1 & K_2 \end{bmatrix} \begin{bmatrix} F & G \\ H_x & H_u \end{bmatrix}^{-1} \qquad \text{(D-27)}$$

Given the Type 0 DPCAS gains from the Riccati equation solution and the composite matrix, the Type 1 DPCAS gains can be expressed as

$$C_1 = K_1 S_{11} + K_2 S_{21}$$

$$C_2 = K_1 S_{12} + K_2 S_{22}$$

Substituting C_1 and C_2 into Eq. D-22 produces the Type 1 DPCAS with control-rate restraint. Rewriting the Type 1 DPCAS in terms of the original coordinates yields

$$\Delta \underline{u}(t) = -C_1 \Delta \underline{x}(t) - C_2(\Delta \underline{\xi}(t) - \Delta \underline{\xi}^*) + \left(C_1 S_{12} + S_{22}\right) \Delta \underline{y}_d$$

$$\Delta \dot{\underline{\xi}}(t) = \Delta \underline{y}(t) - \Delta \underline{y}_d$$

where the equilibrium value of the integrator state, $\Delta \underline{\xi}^*$ remains to be specified.

The steady-state value of the integrator state specifies the required value of $\Delta \underline{u}(0)$. To find $\Delta \underline{\xi}^*$, we assume that the system is in steady state prior to t=0 for some $\Delta \underline{y}_d(-)$. At t=0, $\Delta \underline{y}_d$ changes instantaneously and remains constant thereafter:

$$\Delta\underline{u}(0^-) = -C_1\Delta\underline{x}(0^-) - C_2\Delta\underline{\xi}(0^-) + \left(C_1S_{12}+S_{22}\right)\Delta\underline{y}_d(0^-) + C_2\Delta\underline{\xi}^*(0^-)$$

$$\Delta\underline{u}(0^+) = -C_1\Delta\underline{x}(0^+) - C_2\Delta\underline{\xi}(0^+) + \left(C_1S_{12}+S_{22}\right)\Delta\underline{y}_d(0^+) + C_2\Delta\underline{\xi}^*(0^+)$$

(D-28)

The values for $\Delta\underline{x}$ and $\Delta\underline{\xi}$ cannot change in going from 0^- to 0^+,

$$\Delta\underline{x}(0^+) = \Delta\underline{x}(0^-) = S_{12}\Delta\underline{y}_d(0^-)$$

$$\Delta\underline{\xi}(0^+) = \Delta\underline{\xi}(0^-) = \Delta\underline{\xi}^*(0^-)$$

but their steady-state values do change:

$$\Delta\underline{x}^*(0^-) \neq \Delta\underline{x}^*(0^+) = S_{12}\Delta\underline{y}_d(0^+)$$

$$\Delta\underline{u}^*(0^-) \neq \Delta\underline{u}^*(0^+) = S_{22}\Delta\underline{y}_d(0^+)$$

The question to be answered is whether or not $\Delta\underline{u}(0)$ can change instantaneously at t=0.

The answer is "no," because if $\Delta\underline{u}(0)$ changes instantaneously, then $\Delta\dot{\underline{u}}(0)$ is a delta function. The cost function (Eq. D-18) contains the integral of the <u>square</u> of $\Delta\dot{\underline{u}}$, i.e., (in this case) the integral of a delta function-squared. Although the integral of a delta function is unity, the integral of a delta function-squared is infinite (Ref. 33); therefore, an instantaneous change in $\Delta\dot{\underline{u}}$ is not admissible as an optimizing control. Since $\Delta\underline{u}(0^+)$ cannot be different from $\Delta\underline{u}(0^-)$, the value of $\Delta\underline{\xi}^*$ must be chosen to enforce this constraint on $\Delta\underline{u}$, i.e., $\Delta\underline{\xi}^*$ must satisfy,

$$\Delta\underline{\xi}^*(0^-) = -C_2^{-1}\left[C_1S_{12} + S_{22}\right]\Delta\underline{y}_d(0^-)$$

$$\Delta\underline{\xi}^*(0^+) = -C_2^{-1}\left[C_1S_{12} + S_{22}\right]\Delta\underline{y}_d(0^+) \qquad \text{(D-29)}$$

for any change in $\Delta\underline{y}_d$. Substituting Eq. D-29 into Eq. D-28 demonstrates the Type 1 DPCAS with control-rate restraint does not have a feedforward of the command and takes the following form:

$$\Delta\underline{u}(t) = -C_1\Delta\underline{x}(t) - C_2\int_0^t\left\{\Delta\underline{y}(\tau) - \Delta\underline{y}_d\right\}d\tau - C_2\Delta\underline{\xi}(0)$$

A block diagram of the control law is shown in Fig. 46. The low-pass filtering effect of the gain K_2, which destroys the integrating property in the Type 0 DPCAS, is eliminated when the Type 1 structure is used.

It can be shown that $\Delta\underline{u}(0)$ should be the same for the Type 0 and Type 1 structures; hence $\Delta\underline{u}(0^+)$ cannot be different than $\Delta\underline{u}(0^-)$ in either case. Another way of interpreting this result is that when the control law is initialized, the starting value of the control command must be equal to the current positions of the control actuators, independent of what the initial commanded value may be. Then, the control law will transfer the system from the current steady-state condition to the next desired steady-state condition in an optimal fashion.

For the case in which there are fewer commands than controls, the Type 1 derivation must be altered, beginning at Eq. D-26. Equation D-26 cannot be written because the number of unknowns in C_1 and C_2 is less than the number of knowns in

K_1 and K_2. The standard approach for obtaining reasonable values in this underconstrained case is to use the pseudo-inverse:

$$\begin{bmatrix} C_1 & C_2 \end{bmatrix} = \begin{bmatrix} K_1 & K_2 \end{bmatrix} \begin{bmatrix} F & G \\ H_x & H_u \end{bmatrix}^{\#}$$

The gains C_1 and C_2 have the best possible alignment in a least squares sense. For the pseudoinverse to exist, we require that,

$$\text{rank} \begin{bmatrix} F & G \\ H_x & H_u \end{bmatrix} = n+\ell \qquad \text{(D-30)}$$

which is the same controllability condition derived in Refs. 34 and 35 but is more general than results in Ref. 31, which require H_u to be zero.

To determine the Type 1 DPCAS for ℓ less than m, C_1 and C_2 are calculated using the Riccati equation solution, K_1 and K_2, and the composite matrix pseudoinverse. The steady-state value for $\Delta\xi^*(0^+)$ in Eq. D-29 is solved using the pseudoinverse of C_2. Eigenvalue and eigenvector analysis (Tables 15 to 18) demonstrate that the time history differences between the Type 1 and Type 0 DPCAS for ℓ less than m are small.

D.5 IMPLEMENTATION OF THE DPCAS IN THE AIRCRAFT

Care must be exercised in controlling an actual aircraft, whose dynamics are described by a nonlinear model,

with control laws that are based upon a linear model of the aircraft. The subject of how big the "small perturbations" (which are assumed in control system development) are allowed to become always is a potential problem. A related problem is accounting for the nominal states and controls which have been assumed in the control design process. The steady-state analysis presented in Section D.1 introduces this topic in the context of trimming the linear dynamic model, but trimming the nonlinear model is the problem which must be solved in actual implementation.

The problem is to define values of $\underline{x}^*$ and u^* which correspond to the command, $\underline{y}_d$. There is a nonlinear relationship of the form

$$\underline{y}_d = \underline{h}(\underline{x}^*, \underline{u}^*) \qquad \text{(D-31)}$$

which can be expanded (using Taylor series) to become

$$\underline{y}_{d_o} + \Delta\underline{y}_d = \underline{h}_o(\underline{x}^*_o, \underline{u}^*_o) + H_x\Delta\underline{x}^* + H_u\Delta\underline{u}^*$$

It is assumed that the nominal (nonlinear) and perturbation (linear) parts of the equation can be satisfied independently, giving

$$\underline{y}_{d_o} = \underline{h}_o(\underline{x}^*_o, \underline{u}^*_o)$$

and

$$\Delta\underline{y}_d = H_x\Delta\underline{x}^* + H_u\Delta\underline{u}^*$$

The former must be "inverted" (loosely speaking) to provide an operation of the form

$$\begin{bmatrix} \underline{x}^*_o \\ \underline{u}^*_o \end{bmatrix} = \underline{h}_o^{-1}(\underline{y}_{d_o}) \qquad \text{(D-32)}$$

while the latter can be expressed as

$$\begin{bmatrix} \Delta\underline{x}^* \\ \Delta\underline{u}^* \end{bmatrix} = \begin{bmatrix} S_{12} \\ S_{22} \end{bmatrix} \Delta\underline{y}_d$$

Then the total values of the states and controls which correspond to the total command, $\underline{y}_d$, can be approximated as

$$\begin{bmatrix} \underline{x}^* \\ \underline{u}^* \end{bmatrix} = \begin{bmatrix} \underline{x}^*_o \\ \underline{u}^*_o \end{bmatrix} + \begin{bmatrix} \Delta\underline{x}^* \\ \Delta\underline{u}^* \end{bmatrix} \qquad \text{(D-33)}$$

Conceptually, $\underline{y}_{d_o}$ represents the pilot's "trim button" (or thumbwheel) output, and $\underline{x}^*_o$ and $\underline{u}^*_o$ are derived as nonlinear functions of the pilot's input. These functions can be written explicitly or they can be realized as curves fitted to flight condition. The values of S_{12} and S_{22} essentially appear as gain matrices, which are either scheduled along with the other gains or are derived from the partial derivatives of $\underline{h}(\underline{x},\underline{u})$.

The total-value Type 0 control law can be expressed as

$$\underline{u}(t) = \underline{u}_I + \int_0^t \left\{ -K_1\left[\underline{x}(\tau) - \underline{x}^*(\tau)\right] - K_2\left[\underline{u}(\tau) - \underline{u}^*(\tau)\right] \right\} d\tau$$

where $\underline{x}^*(\tau)$ and $\underline{u}^*(\tau)$ are defined either by Eq. D-32 or D-33, and the integrator initial condition, $\underline{u}_I$, is set to current actuator positions (when this DPCAS control mode is switched "on") to eliminate the possibility of mode-switching transients. The total-value Type 0 DPCAS is illustrated by Fig. D-2, depicting the proper adjustment of trim settings provided by $\underline{u}^*_o$ and $\underline{x}^*_o$, the command "shaping" provided by S_{12}, and the feedforward of control set point provided by S_{22}.

Similarly, the total-value Type 1 control law is described by

$$\underline{u}(t) = -C_1\underline{x}(t) - C_2 \int_0^t \left\{\underline{y}(\tau) - \underline{y}_d(\tau)\right\} d\tau - C_2\, \underline{\xi}_I$$

as shown in Fig. D-3. The integrator initial condition, $\underline{\xi}_I$, is chosen so that the initial control command, $\underline{u}(0)$, is the same as the actuator's starting position to eliminate mode switching transients. The Type 1 implementation is seen to be significantly different from the Type 0 version, in that there is no explicit shaping of pilot commands prior to the feedback summing point. Furthermore, it is desirable to form the command error in command coordinates, implying that the aircraft measurements should be processed by the nonlinear relationship between $\underline{x}$, $\underline{u}$, and $\underline{y}$ (Eq. D-31). (This is not a particular problem for the command vector -- a_n, p_w, and β -- used here, as a_n can be measured directly and the computation of p_w and β from p, r, w, and TAS is straightforward and shown in Appendix C.)

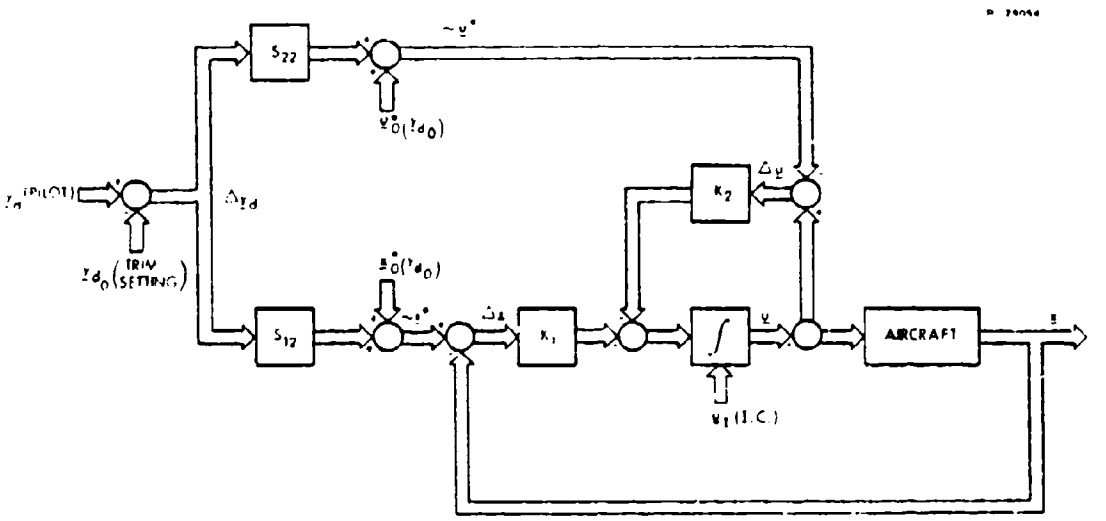

Figure D-2 Total-Value Type 0 DPCAS Structure

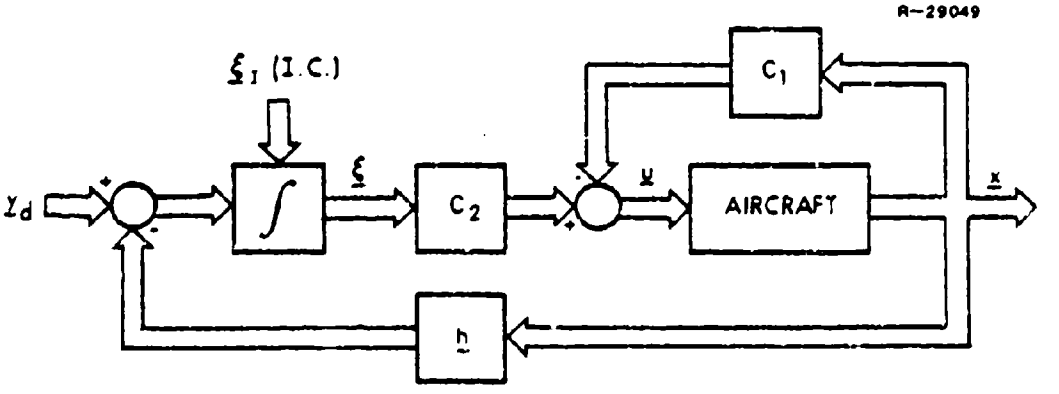

Figure D-3 Total-Value Type 1 DPCAS Structure